Doctoral Thesis

Optimized Merging of Search-Coil and Fluxgate Data for the Magnetospheric Multiscale Mission

DI David Fischer

Graz University of Technology
Signal Processing and Speech Communication Laboratory

In cooperation with

Space Research Institute Graz
Austrian Academy of Sciences

Thesis Advisor and Examiner:
Prof. Gernot Kubin
Signal Processing and Speech Communication Laboratory
Graz University of Technology

External Examiner:
Prof. Karl-Heinz Glassmeier
Institute for Geophysics and Extraterrestrial Physics
Technische Universität Braunschweig

Co-Advisor:
Dr. Werner Magnes
Space Research Institute Graz
Austrian Academy of Sciences

Graz, October 18th, 2018

Abstract

The main objective of the Magnetospheric Multiscale (MMS) mission is to characterize fine-scale structures in the Earth's magnetotail and magnetopause. These dynamic structures traverse the MMS spacecraft formation at high speed and generate magnetic field signatures that cross the sensitive frequency bands of both search-coil and fluxgate magnetometers. An improved understanding of these events is only possible by combining data from both instrument types for magnetospheric event analysis.

This combination is done using a model-based sensor fusion approach that merges data from both instrument types to a virtual instrument with flat gain curve, linear phase and known timing properties as well as the highest sensitivity and lowest noise floor. The generation of the underlying instrument models requires precise knowledge of the instrument frequency responses and timing. This knowledge was obtained in a dedicated end-to-end measurement campaign using a purpose-built magnetic field source tightly coupled to the MMS time standard.
Sensor fusion is embedded in a carefully designed setup that minimizes processing artefacts and which is suitable for automated execution. This setup uses the instrument models for frequency response compensation and merges the data using complementary filters based on instrument sensitivity and noise floor.

The precision of the resulting merged data set has been demonstrated by comparison of in-flight data. This comparison shows an unchanged DC and low frequency gain, an AC gain accuracy that is better than 1% for higher frequencies and a phase delay uncertainty below 100 µs.

The models, filters and data processing algorithms developed in this thesis are applied in the generation of the official fluxgate-search-coil merged data product, which is available for public use at the MMS science data center.

With the work done in this thesis, MMS is the first space mission that is able to provide a high precision merged magnetic field data product. It is an excellent tool to answer questions that are on the borders of knowledge in current plasma science, e.g., the existence of reconnection in the turbulent magnetosheath or the properties of dipolarization fronts with associated whistler mode wave emissions.

Kurzfassung

Das Ziel der Magnetospheric Multiscale (MMS) Mission ist die Charakterisierung von feinen Strukturen in der Magnetopause und im Magnetschweif der Erde. Diese dynamischen Strukturen passieren die Formation der MMS-Satelliten mit hoher Geschwindigkeit und erzeugen magnetische Signaturen, die jeweils nicht ganz in den empfindlichen Frequenzbändern von Search-Coil und Fluxgate Magnetometern abgebildet werden können. Ein verbessertes Verständnis dieser Strukturen kann nur durch die Analyse eines kombinierten Datenproduktes aus beiden Instrumententypen erreicht werden.

Diese Kombination wurde mit einem modellbasierten Datenfusionsansatz durchgeführt, der Daten von beiden Instrumententypen zu einem virtuellen Instrument mit flachem Amplitudengang, linearer Phase und definierten Zeiteigenschaften kombiniert und dabei die höchste Empfindlichkeit erreicht und das niedrigste Rauschniveau verwendet. Die Generierung der dazu benötigten Instrumentenmodelle kann nur mit exaktem Wissen über den Frequenzgang und die Zeiteigenschaften der Instrumente durchgeführt werden. Diese Eigenschaften wurden in einer Messkampagne mit einer für diesen Zweck entworfenen Stromquelle vermessen, die auf den Zeitstandard der MMS-Satelliten referenziert ist und damit eine Endpunkt-zu-Endpunkt-Vermessung ermöglicht.

Die Fusion der Sensordaten ist in einem sorgfältig entworfenen Prozess eingebettet, der mögliche unerwünschte Verarbeitungs-Artefakte minimiert und eine automatisierte Anwendung ermöglicht. Dieser Prozess nutzt die Instrumentenmodelle zur Kompensation des Frequenzgangs und kombiniert die Daten mit komplementären Filtern. Diese Filter wurden basierend auf der Empfindlichkeit und den Rauschniveaus der Instrumententypen entworfen.

Die Genauigkeit des kombinierten Datenprodukts wurde durch einen Vergleich von In-Situ Messdaten demonstriert. Dieser Vergleich zeigt, daß die Verstärkung für konstante und niederfrequente Magnetfelder unverändert ist, daß der relative Verstärkungsfehler für höherfrequente Wechselfelder unter 1% liegt und daß die Phasenlaufzeitdifferenzen weniger als 100 µs betragen.

Die Modelle, Filter und Datenverarbeitungsalgorithmen, die in dieser Arbeit entwickelt wurden, werden in der Produktion des offiziellen Fluxgate-Searchcoil-Datenprodukts verwendet, das im MMS-Datenzentrum für die Allgemeinheit zur Verfügung gestellt wird.

Basierend auf diese Arbeit ist MMS die erste Weltraummission, die ein hochgenaues kombiniertes Magnetfeld-Datenprodukt zur Verfügung stellen kann. Dieses Produkt ist ein hervorragendes Werkzeug, um Fragen an den Wissensgrenzen der Weltraumplasma-Wissenschaft zu beantworten, wie zum Beispiel die Existenz von Rekonnektion in der Magnetosheath oder was exakt die Eigenschaften von Dipolarisationsfronten mit dazugehöriger Whistler-Wellenemission sind.

Outline

The introductory section of this document (chapter 1) sets the stage for this thesis, which is the Magnetospheric Multiscale Mission (MMS), its mission goals, scientific questions as well as examined phenomena and the magnetic field instruments used. In addition, also previous work on sensor fusion is briefly discussed both generally and with respect to magnetic field measurements. This background information summary results in a concise design goal definition for the merged data product at the end of the chapter.

These goals were then used along a development path in chapter 2 that starts with a brief introduction of modeling and system identification methods, continues with the design of the measurement environment and the conducted measurements and ends with a presentation of the generated models and merging process elements. The measurement description includes the design overview of a novel synchronized current generator. The data from measurements was then used for the first generation of precise magnetic field instrument models that specify frequency response and timing based on high quality end-to-end measurements.

After the launch of MMS, the instrument models and the merging process were applied on in-flight data and compared relative to one another as well as to ground measurements. The findings of this comparison and the successful application of models and process are summarized in chapter 3 and are in line with the initially targeted goals. With the developed models and methods, it is possible to conclude (chapter 4) that MMS is the first mission featuring a regular merged magnetic field data product that combines fluxgate and search-coil data. Finally, chapter 5 contains a few recommendations that could be used for future work on this topic.

Many chapters of this thesis require some knowledge about digital filtering and sampling. Plenty of information about this topic is available in Oppenheim et al. (1998) or other books about digital signal processing. A short introduction about digital filters is available in appendix A.1 and some basics about resampling are explained in chapter 2. The appendix also contains a derivation of a sensor matrix transfer function that could be used in future applications.

Table of Contents

Preface

Acknowledgment

Awarding a doctorate's degree to one single person does not, in my opinion, reflect the conditions and work that stand behind the thesis and the doctoral candidate. Every thesis is based on numerous conditions that cannot be taken for granted and it is also dependent on the work and support of many other people who do not receive the degree. The following pages are therefore dedicated to the expression of my gratitude.

I am grateful that I was born in a country with educational opportunities, that I was gifted with the necessary talents to use them and that I was raised in a family that supported and encouraged me to take these opportunities. Thanks, Mom and Dad for raising my interest in engineering and space science quite early. Who would have thought I would get as close to space as I am today!

During the work for and writing of this thesis, the main support workload was placed on the shoulders of my wife Uli, who has encouraged and supported me the complete time. She took over a lot of work that I normally should have done, both in bringing up our daughters and in many things that I failed to do due to the workload. Thanks for your love and support. I love you.

My daughters Annika and Miriam had to forgo a lot of time that I was not able to spend with them, but was looking at a computer screen instead. Thanks for your understanding that I was not always available when there were wishes to discuss and problems to solve.

My group leader Werner accompanied me through the complete project as well as most travel and spent many hours commenting on my thesis despite his high workload during that time. This really helped me to bring the text of this thesis to a form that is more complete, concise and clear.

Christian accompanied me through my studies and as colleague at the Space Research Institute. We spent hours in debugging the current generator and he wrote the Labview Software to control it from the PC side.

My other colleagues at IWF helped in many small things and definitely received additional workload due to my "absence" for writing this thesis. Thanks Aris, Irmi, Gerhard and Ferdinand.

The hardware team at the University of New Hampshire (Mark Chutter, Ivan Dors and Jerry Needell) supported me during the FIELDS integration and test measurements, conducted the later measurements with remote support and were always available for discussions about timing and data formats. They also pointed out that looking at flowing screens of hex numbers is not normal, so we should definitely stop doing that!

Olivier Le Contel and Laurent Mirioni supported my understanding of the search-coil in many discussions and teleconferences. Together with Matthew Argall we also had a lot of discussions about the merged data product and its implementation. Thanks for the great collaboration.

Matthew Argall implemented the software for production of the merged data product in the science data center and improved it by contributing a merging filter based on in-flight measurements. Thanks for doing the hard work of complying with all the formal process requirements there.

Rebecca Zillinger had a look at this thesis from a native speaker's perspective and provided a lot of words that are not part of my usual vocabulary.

Gernot Kubin, my supervisor at the Graz University of Technology, who read through this whole thesis, provided many comments and pointed out a few mathematical issues that required a second glance.

The dedication and expertise of the Magnetospheric Multiscale (MMS) development and operations teams are greatly appreciated. Work at Johns Hopkins University Applied Physics Laboratory, University of California Los Angeles, University of New Hampshire and Southwest Research Institute was supported by the National Aeronautics and Space Administration (NASA) contract number NNG04EB99C. The French involvement (search-coil magnetometer) in MMS is supported by Centre National d'Études Spatiales (CNES) and Centre National de la Recherche Scientifique (CNRS).

I acknowledge the use of burst L1A data from digital and analog fluxgate magnetometers and search coil magnetometers. The data are stored at the MMS Science Data Center https://lasp.colorado.edu/mms/sdc/ and are publicly available.

The Austrian part of the development, operation and calibration of the digital fluxgate magnetometer as well as the work towards the merged data product was financially supported by a rolling grant of the Austrian Academy of Sciences and the Austrian Space Applications Programme with the contract number FFG/ASAP-844377.

Notes for the Reader

This thesis was published in a refereed article (Fischer et al., 2016) that covers most parts of this thesis, with significantly less detail.

Statutory Declaration

I declare that I have authored this thesis independently, that I have not used other than the declared sources / resources, and that I have explicitly marked all material which has been quoted either literally or by content from the used sources.

EIDESSTATTLICHE ERKLÄRUNG

Ich erkläre an Eides statt, daß ich die vorliegende Arbeit selbstständig verfasst, andere als die angegebenen Quellen/Hilfsmittel nicht benutzt, und die den benutzten Quellen wörtlich und inhaltlich entnommenen Stellen als solche kenntlich gemacht habe.

Graz,..... .....

1. Introduction

1.1. The Magnetospheric Multiscale Mission

1.1.1. Scientific Objectives

The Magnetospheric Multiscale (MMS) mission is a four-satellite NASA mission with the target of measuring plasma processes in the Earth's magnetosphere. The main mission goal is the exploration of magnetic reconnection which is a dynamic process in plasma environments that causes rapid changes in field configuration and plasma particle properties.

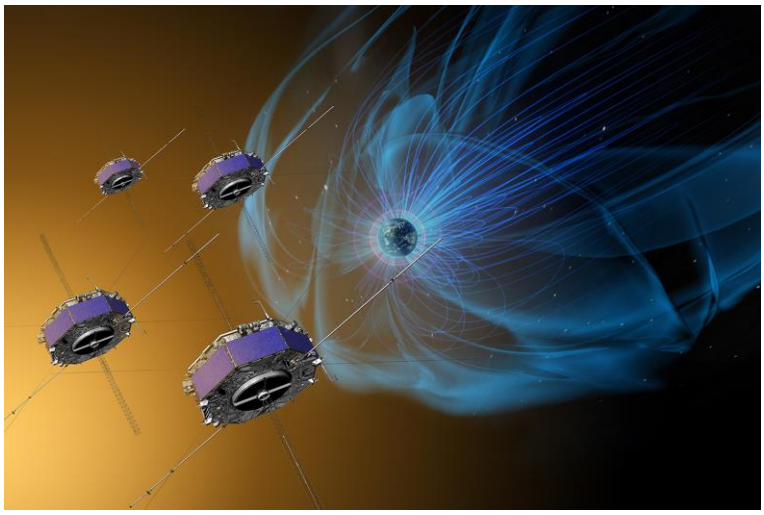

Figure 1–1 Artist's Concept of MMS in the Plasma Environment of the Earth (© NASA[1])

This chapter gives a basic explanation of the plasma environment (Baumjohann et al., 1997) and a summary of the scientific objectives of the MMS mission (Burch et al., 2016).

Plasma processes in the Earth's magnetosphere are created by the interaction of the solar wind with the Earth's magnetic field. The solar wind is a constant stream of particles that is emitted by the Sun, with rates in the order of million tons per second. These emitted particles are in plasma state and are composed of ionized hydrogen (protons and electrons), small amounts of Helium isotopes (a few percent) and traces of other materials. The particle stream expands outwards from the Sun in a radial direction, with speeds of several hundred kilometers per second. The positive and negative charges in this stream carry a "frozen" magnetic field that is still connected to the Sun. This way the solar magnetic field is expanded far out into the solar system to the Heliopause, which marks the border between the solar influence and the interstellar medium.

The interaction of the plasma with the Earth's magnetic field creates a complex structure of areas with different particle properties (density, energy) and associated magnetic and electric field conditions. This structure is called the magnetosphere (see figure 1–2). The outermost area of influence is the bow shock, where the plasma is compressed and slowed down to subsonic speeds. This compression is ultimately caused by the Earth's magnetic field, which poses an obstacle to the particles of the solar wind. The region downstream from the bow shock is called magnetosheath. In this region, the solar wind particles flow around the inner magnetosphere where the Earth's magnetic field is dominant.

The magnetopause is the boundary between the magnetosheath and the inner magnetosphere. Charged particles cannot pass this boundary directly, but exert pressure on it. Because of this pressure,

[1] © NASA, https://www.nasa.gov/feature/goddard/2016/nasas-mms-celebrates-a-year-in-space

the Earth's magnetic field is compressed on the dayside and elongated on the night side. The area of elongation is called the magnetotail.

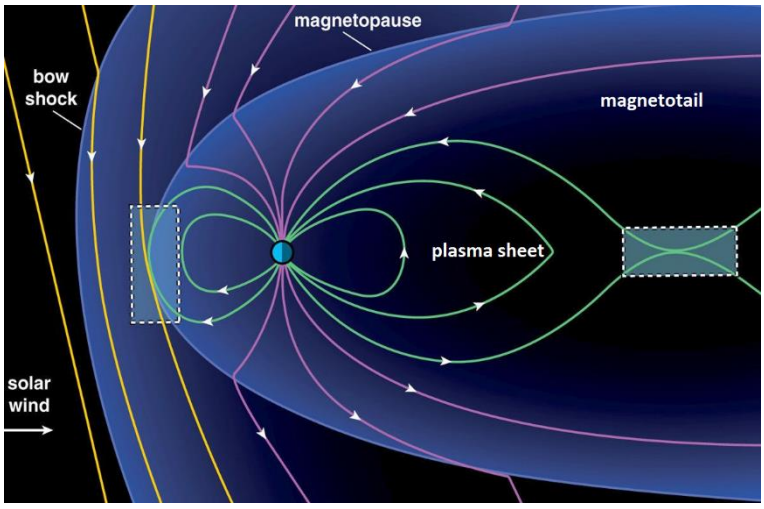

Figure 1–2 Simplified illustration of the Earth's Magnetosphere and Regions of Reconnection (© CC 4.0, Edited Labels, Original in Burch et al., 2016 [2])

The only way solar wind particles can enter the inner magnetosphere is by means of reconnection, which happens at the magnetopause and in the magnetotail (dashed boxes in figure 1–2). In both situations, the magnetic field has anti-parallel components (figure 1–3, 1) which point in opposite directions in adjacent areas. This anti-parallel configuration implies the presence of a perpendicular current between the opposite fields (figure 1–3, 2). This current is carried by moving plasma particles, which are both limited in quantity (plasma density) and acceleration (inertia). If the magnetic field configuration changes, the plasma is in some cases unable to support the required current change, which means that some current is "missing." In principle, this can be modeled using an anti-current (figure 1–3, 3) that results in a new magnetic field configuration (figure 1–3, 4). The resulting field configuration is highly bent and experiences magnetic tension that snaps the field back to a less bent configuration. The contained plasma particles are accelerated in the direction of the magnetic tension force, towards the magnetotail.

The result of this reconnection at the magnetopause is that the magnetic field of Earth and Sun become disconnected from their original magnetic domains (figure 1–2 yellow and green field lines, respectively) and are reconnected to other domains (purple field lines). Particles can then move towards the magnetotail along the reconnected magnetic field.

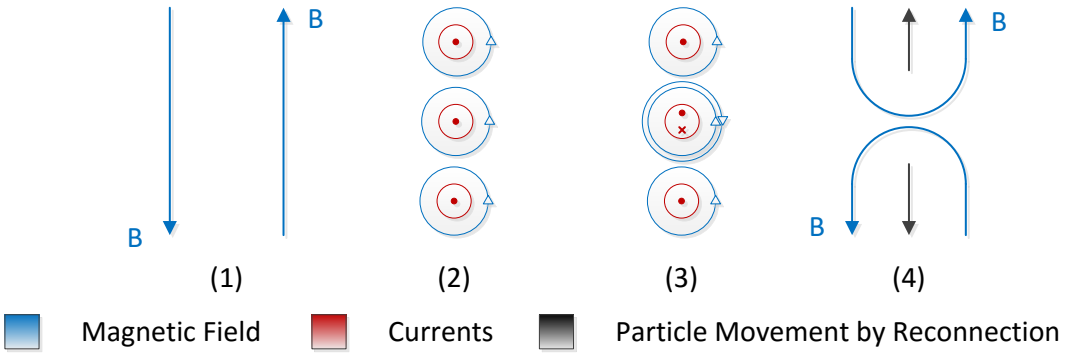

Figure 1–3 Simplified Model of Reconnection with resulting Field Configuration

[2] Creative Commons 4.0, http://creativecommons.org/licenses/by/4.0/

The same mechanism of reconnection occurs within the magnetotail where the field connected to the solar wind is stretched as the solar wind moves on. Reconnection in the magnetotail disconnects the magnetic fields of the Earth and Sun and accelerates particles both towards the Earth's plasma sheet and away from the Earth. Particles in the plasma sheet can move freely along the magnetic field and can therefore propagate towards Earth. Some of them penetrate the atmosphere and create auroras at the North and South poles.

Although considerable research has already been conducted on this subject, e.g., using in-situ data from previously launched missions like CLUSTER (Escoubet et al., 1997) or THEMIS (Angelopoulos, 2008), fundamental details of the reconnection process are not yet fully explained and require further data and research (Burch et al., 2016). Especially the explanation of the kinetic processes within reconnection requires more detailed measurements on the electron gyro-scale, with a spatial and time resolution that supports the resolution of electron properties on length scales smaller than the local electron gyro-radius. With this resolution, electrons can be treated as kinetic particles rather than using the more global treatment as fluid. This need for further measurements and research was summarized in the main goal of the MMS mission:

To understand the microphysics of magnetic reconnection by determining the kinetic processes occurring in the electron diffusion region that are responsible for collisionless magnetic reconnection, especially how reconnection is initiated. (Burch et al., 2016)

1.1.2. Mission Design of MMS

This mission goal can only be reached by delivering measurements of plasma properties with unprecedented time and spatial resolution. For this purpose, four spin-stabilized spacecraft were equipped with an identical set of the most advanced plasma and electromagnetic field instruments available for space application.

A high spatial resolution is achieved by flying the four spacecraft in a tight tetrahedron formation with distances of around 10 km and a positional accuracy of 100 m within the region of interest (ROI, the regions where reconnection occurs). The spin rate of the spacecraft is about 50 mHz.

The high time resolution was achieved by improved instrument design with high data rates (e.g., 30 ms, for 3D electron distribution measurements) and by using a selective downlink concept. This selective concept was developed, as effective time resolution is not only defined by the instruments, but also by the available data rate of the downlink system. Low rate Data is sent completely, but high rate data is stored in an onboard mass memory and only sent if it is relevant for scientific analysis (e.g., occurrence of reconnection). This relevance is determined either based on the automated onboard estimation or by the assessment by scientists in the loop (SITL) that review both onboard estimation results and low rate data.

Figure 1–4 MMS Spacecraft Stack (© NASA/Chris Gunn[3])

Measurements on MMS are done using electric and magnetic field instruments and multiple particle instruments for electron and ion velocity distribution as well as ion composition analysis. The electromagnetic fields are measured by the FIELDS instrument suite (Torbert et al., 2016), which contains the axial double probe (ADP), the analog Fluxgate magnetometer (AFG), the digital Fluxgate magnetometer (DFG), the electron drift instrument (EDI), the search-coil magnetometer (SCM) and the spin plane double probe (SDP). The FIELDS suite is described in more detail in chapter 1.1.3.

Particles are detected by multiple instrument suites: The Hot Plasma Suite contains the hot plasma composition analyzer (HPCA, Young et al., 2016) and the fast plasma investigation (FPI, Pollock et al., 2016), which is composed of dual ion sensors (DIS) and dual electron sensors (DES). The energetic particle detector (EPD, Mauk et al., 2016) contains the fly's eye energetic particle sensor (FEEPS) and the energetic ion spectrometer (EIS).

The particle measurements are supported by the active spacecraft potential control system (ASPOC, Torkar et al., 2016) which uses an ion gun to neutralize the electric potential of the spacecraft relative to the plasma so that the speed of charges is not influenced when they approach the spacecraft. Figure 1–5 shows a picture of the MMS instrument deck. Some of the instrument suites in this plot are shown as separate subunits.

[3] © NASA/Chris Gunn, https://mms.gsfc.nasa.gov/mms_spacecraft/spacecraft_008.html

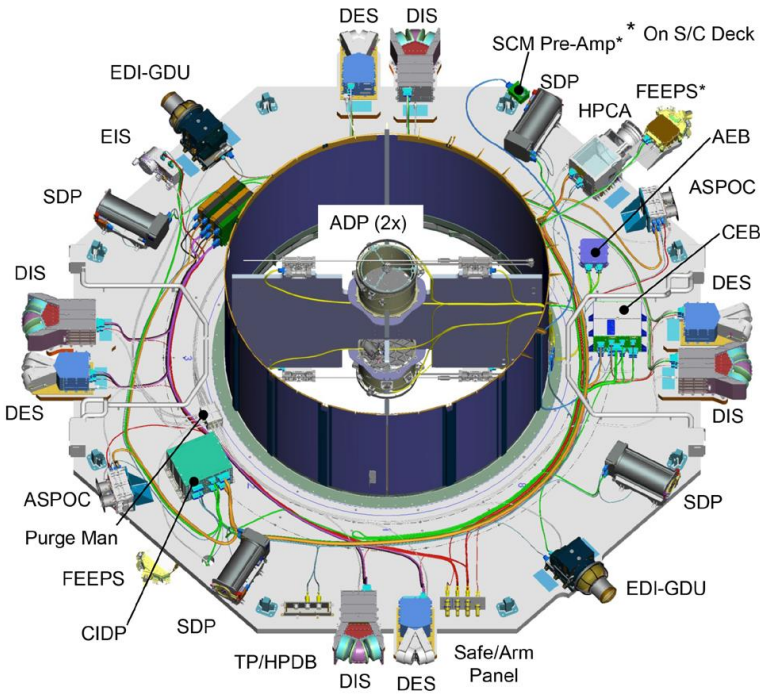

ADP	Axial Double Probe (FIELDS)	EDI/GDU	Electron Drift Instrument / Gun Detector Unit (FIELDS)
AFG	Analog Fluxgate Magnetometer (mounted on boom, FIELDS)	EIS	Energetic Ion Spectrometer (EPD)
ASPOC	Active Spacecraft Potential Control	FEEPS	Fly's Eye Energetic Particle Sensors (EPD)
CEB	Central Electronics Box (FIELDS)	HPCA	Hot Plasma Composition Analyzer
CIDP	Central Instrument Data Processor	IDPU	Instrument Data Processing Unit (FPI)
DES	Dual Electron Spectrometer (FPI)	SCM	Search-Coil Magnetometer (mounted on boom, FIELDS)
DFG	Digital Fluxgate Magnetometer (mounted on boom, FIELDS)	SDP	Spin Plane Double Probe (FIELDS)
DIS	Dual Ion Spectrometer (FPI)	TP/HPDB	Test Panel Heater / Power Distribution Box

Figure 1–5 Layout of MMS Instrument Deck
AFG, DFG and SCM Sensors are Mounted on Booms Outside of the Deck
(© CC 4.0, Burch et al., 2016 [4])

Figure 1–6 shows a picture of one MMS satellite with folded magnetometer booms. Most of the instruments in the picture are hidden below red protective covers to avoid damage and contamination.

[4] Creative Commons 4.0, http://creativecommons.org/licenses/by/4.0/

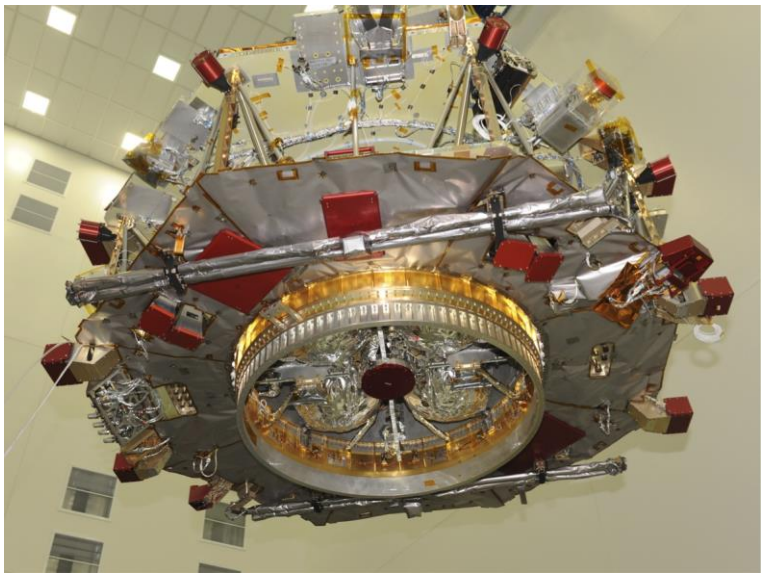

Figure 1–6 MMS Satellite
(© NASA [5])

The orbit of the MMS spacecraft is highly eccentric and was designed to cross regions of frequent reconnection during its apogee phase. As the speed at apogee is minimal, also the time of residence within these regions is maximized. The examined region of reconnection is defined by the science phases. During phase 1 (09/2015-01/2017) the apogee was around 12 Earth radii and reconnection was examined at the magnetopause. During phase 2 (02/2017-03/2018) the apogee was raised up to 25 Earth radii and reconnection is examined in the magnetotail.

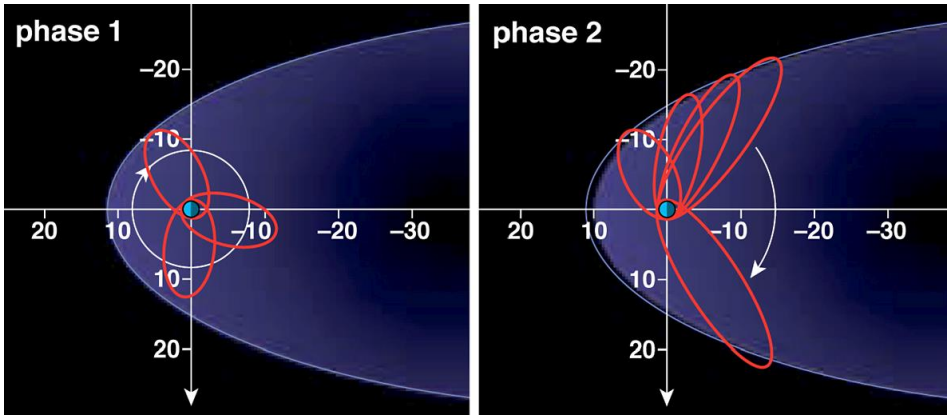

Figure 1–7 MMS Main Science Phases and Example Orbits
(© CC 4.0, Burch et al., 2016 [6])

[5] © NASA, no online source of image available at time of thesis publication, image received by personal communication within MMS team
[6] Creative Commons 4.0, http://creativecommons.org/licenses/by/4.0/

The science phases and their goals are presented in more detail within the mission profile paper (Fuselier et al., 2016). The MMS satellites were launched on March 12, 2015 from Cape Canaveral. Commissioning of the FIELDS magnetic field instruments started just a few days later. Since that time, the instruments have delivered valuable data for the scientific community.

Figure 1–8 MMS Launch
(© NASA [7])

[7] © NASA, https://www.nasa.gov/content/launch-begins-mms-mission-in-spectacular-fashion

1.1.3. FIELDS Instrument Suite

1.1.3.1. FIELDS Design

The FIELDS instrument suite is conducting in-situ electric and magnetic field measurements. It is a combination of magnetic and electric field sensors with supporting electronics for data processing, time stamping and power supply. This chapter includes summarized information from the FIELDS paper (Torbert et al., 2016). Figure 1–9 shows a block diagram with all major subunits of FIELDS.

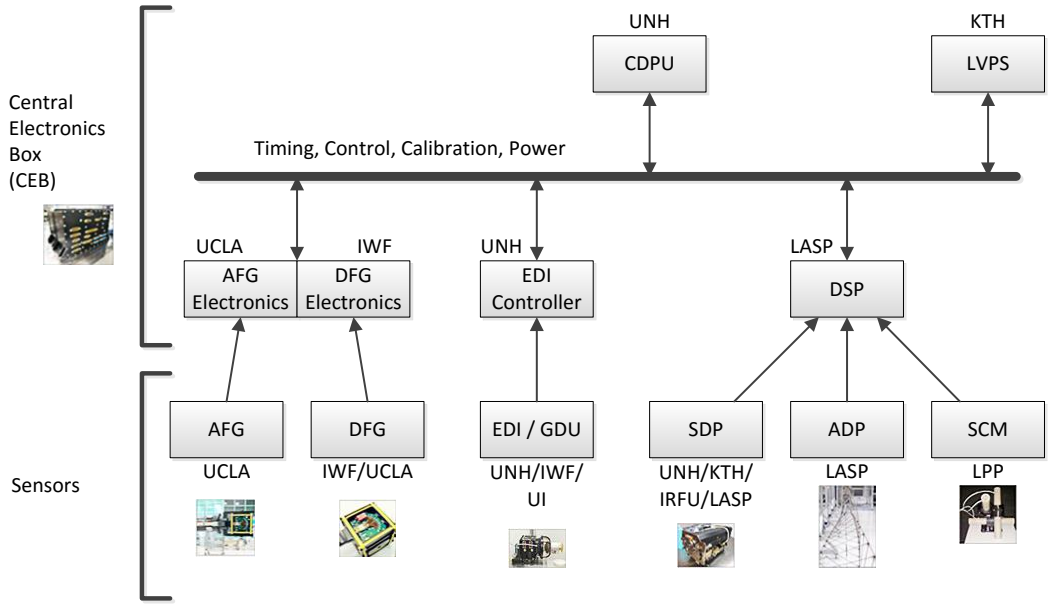

Figure 1–9 Block Diagram of the FIELDS Instrument Suite
(© CC BY 1.0, modified to improve Image Quality, Original in Torbert et al., 2016 [8])

The DC and low frequency magnetic field is measured by the analog fluxgate (AFG) magnetometer and the digital fluxgate (DFG) magnetometer with a maximum sampling frequency of 128 Hz. The search-coil magnetometer (SCM) measures the magnetic field at higher frequencies with a maximum nominal sampling frequency of 16,384 Hz. The functional principle of these magnetometers is discussed in more detail in chapters 1.1.3.3 and 1.1.3.4.

The electric field is measured by the spin plane double probe (SDP) and the axial double probe (ADP). The ADP (Ergun et al, 2016) is a double antenna that is extended along the spacecraft axis by roughly 15 m on each side. The SDP (Lindqvist et al, 2016) uses 4 antennas in the spacecraft spin plane that are extended to 60 m each by centrifugal force. The maximum nominal sampling frequency for both instruments is 16,384 Hz.

The electron drift instrument (EDI, Torbert et al., 2016) measures both the electric and magnetic field by using a weak beam of electrons that is emitted to space and returns to the spacecraft after one or more gyrations. The EDI has a maximum measurement rate of either 125 or 1,024 Hz, depending on the selected mode.

The mounting of the FIELDS sensors on the MMS spacecraft is shown in figure 1–10. The magnetic field sensors of AFG, DFG and SCM are mounted on 5 m long deployable booms to decrease the magnitude of magnetic stray fields generated by the spacecraft by increasing the distance to potential field sources.

[8] Creative Commons Attribution 1.0 Generic (CC BY 1.0), https://creativecommons.org/licenses/by/1.0/

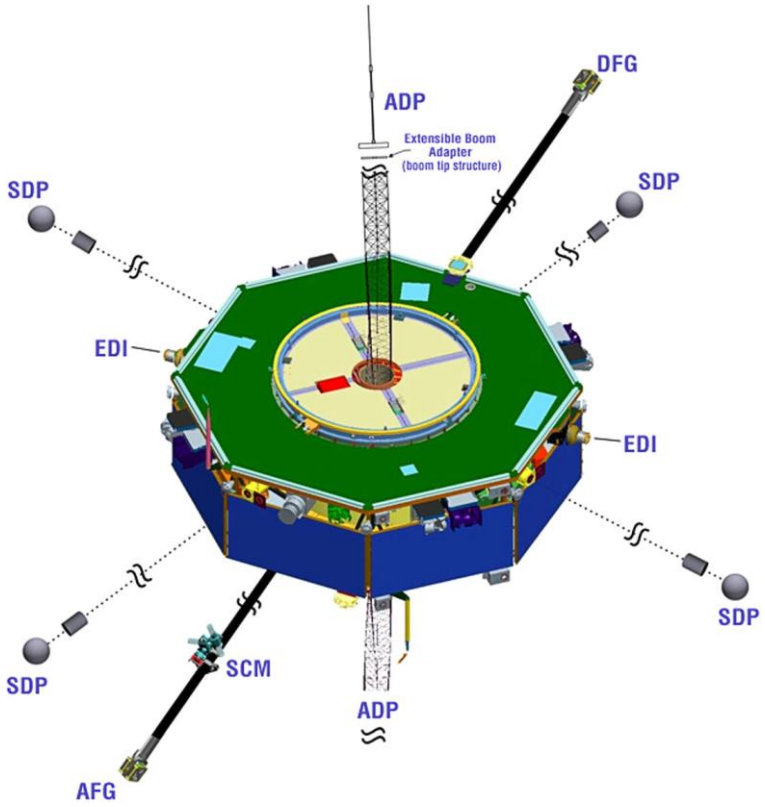

Figure 1–10 FIELDS Sensors on a MMS Spacecraft
(© CC BY 1.0, Torbert et al., 2016 [9])

The common electronics for most of the sensors is located in the central electronics box (CEB). AFG, DFG and EDI use their own electronics boards for digitization, while SDP, ADP and SCM are sampled by the digital signal processing unit (DSP, Ergun et al., 2016), which is available in redundant configuration (DSP-A and DSP-B). The maximum sampling frequency of the DSP unit is 262,144 Hz if only one sensor component is sampled and 16,384 Hz if data is sampled from all connected sensors.

Data from all FIELDS sub-instruments is collected in the central data processing unit (CDPU, Torbert et al., 2016, see figure 1–11), which is responsible for instrument synchronization, data time stamping, packetization, compression and instrument commanding. The CDPU is in turn connected to the MMS central instrument data processing unit (CIDP) which collects data from all instrument suites and distributes onboard time (see chapter 1.1.3.2) and commands. The last, but indispensable element of the CEB is the redundant low voltage power supply (LVPS), which provides the electric power for all instruments and the CDPU.

[9] Creative Commons Attribution 1.0 Generic (CC BY 1.0), https://creativecommons.org/licenses/by/1.0/

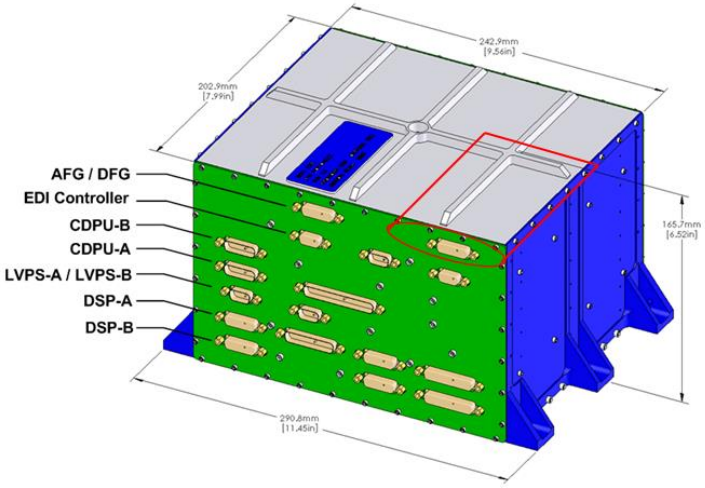

Figure 1–11 Drawing of FIELDS CDPU with DFG Location (red)[10]

Although FIELDS can in principle deliver various data rates, only a few of them are used during normal operation. Operation along the orbit is split into two different modes. Slow survey mode is active outside the region of interest (ROI) and delivers data at low rates. Both, fast survey and burst mode are active along the ROI, but only fast survey mode data are downlinked completely. Burst data are stored in the onboard mass storage and selected for download by scientists in the loop. Figure 1–12 shows a sketch of the distribution of modes along the orbit path. More detailed information is available in Fuselier et al, 2016.

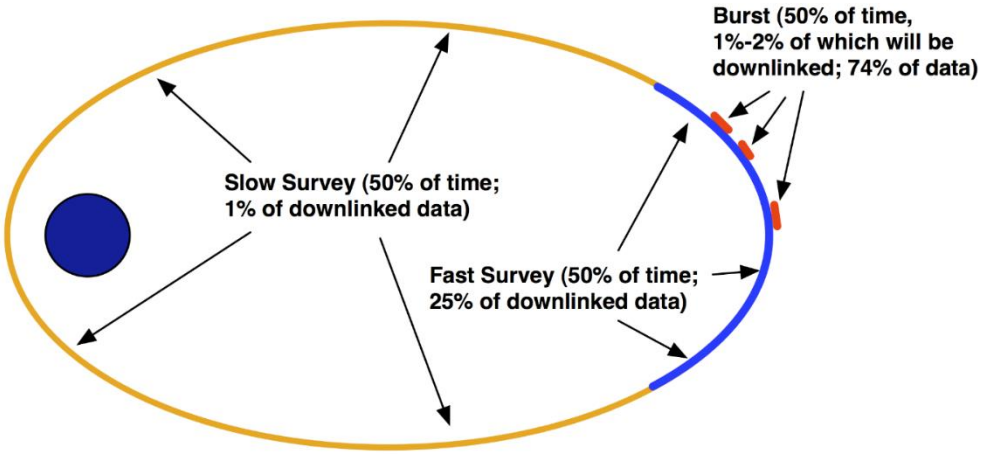

Figure 1–12 Sketch of MMS Orbit with ROI (blue) and Burst Intervals (red)
(© CC 4.0, Burch et al., 2016 [11]*)*

[10] Image Credits: University of New Hampshire
[11] Creative Commons 4.0, http://creativecommons.org/licenses/by/4.0/

The data rates of the instruments for the different operating modes are given in table 1-1. The data rate of EDI is not constant, since sampling depends on the flight time of electrons, which is dependent on the external field conditions.

Instrument	Slow Survey	Fast Survey	Burst
	Samples/s		
EDI	~16	~16	~125
AFG	8	16	128
DFG	8	16	128
EDP	8	32	8,192
ADP	8	32	8,192
SCM	8	32	8,192

Table 1-1 FIELDS Modes and Data Rates

Data rate reduction for AFG, DFG and EDI is done within the CDPU, while EDP, ADP and SCM data rate is reduced in the DSP unit.

1.1.3.2. Data Sampling and Time Stamping within FIELDS

The high time resolution of the multiple instruments in FIELDS is a challenge in terms of sampling and time stamping. Data samples from multiple instruments can only be used together if the timing relation of these samples to one another is known well enough. Even if this relation is known, working with this data can be complicated. Many standard methods used for data analysis can only be applied to synchronous data sets, which means that the available data must be brought to a common synchronous time standard, e.g., by interpolation. For asynchronous instruments, it is then necessary to interpolate data to this synchronous standard by using non-integer interpolation ratios that must be adjusted dynamically to catch sampling clock drifts (e.g., by temperature).

The FIELDS team has therefore spent considerable efforts in instrument design and verification to establish an isochronous sampling clock standard for most of their instruments (see Torbert et al., 2016). An isochronous clock standard means that the sampling of the instruments does not happen at the same time, but with a common sampling grid. In FIELDS, this sampling grid consists of sampling frequencies of 2^N Hz. The only exception is EDI, which cannot be operated at a constant sampling rate due to its operational principle.
This isochronous sampling grid is established by the CDPU (see figure 1–13), which provides one common logic clock and multiple 1 Hz synchronization pulses to the instruments that define the sampling phase. The 1 Hz pulses are individually adjusted so that each instrument provides data at the rising edge of the CDPU's own 1 Hz pulse (see figure 1–14).
With these mechanisms in place, the instruments deliver isochronous data streams that can be converted to one sampling frequency by resampling with a factor of 2^N. The small residual time shifts can either be ignored (for low frequency calculations) or be resolved with small time shifts (see chapter 2.6.2).

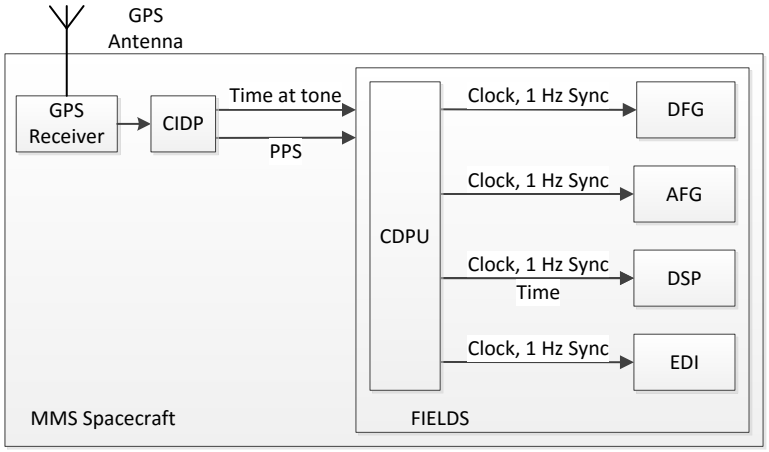

Figure 1–13 Real-Time and Clock Distribution for FIELDS

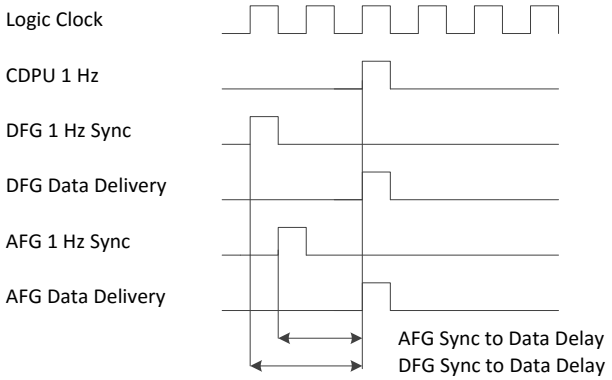

Figure 1–14 Example of FIELDS Data Synchronization

Although isochronous sampling delivers a solid base for synchronization, even isochronous data require time stamping to line up data from the various instruments. The real-time clock reference for MMS is derived from the time distributed by the global positioning system (GPS) satellites. Each spacecraft uses a military grade GPS receiver (see figure 1–13) that synchronizes the CIDP clock based on the GPS signal. GPS time is based on the temps atomique international (TAI, international atomic clock standard), but differs by a few leap seconds from this standard. The GPS time is propagated to the CDPU using a "time at tone" mechanism, which means the time stamp is announced beforehand and set valid with a separate "tone" pulse. This time pulse occurs once per second and is called the one pulse per second (PPS) signal.

Between the PPS pulses, the CDPU real-time clock runs on its internal clock frequency and therefore slowly drifts relative to the GPS time. Data from AFG, DFG and EDI is then time stamped using the CDPU real-time clock. DSP has its own real-time clock, which is synchronized to the CPDU using a 1 Hz sync pulse and the data interface. Since both the CDPU and the DSP use the same logic clock, their real-time clocks are perfectly synchronous and merely need synchronization to the PPS pulse.

With all these measures in place, the FIELDS design and synchronization is in good condition and provides a solid hardware base for exact timing. However, the presented mechanisms are only the ideal case and a few sources for delay and jitter remain. These sources are identified and discussed in chapter 3.1.1.

1.1.3.3. Fluxgate Magnetometers

Fluxgate magnetometers measure the magnetic field at DC and low frequencies, typically below 100 Hz. The principle of fluxgate instruments was invented by H. Aschenbrenner and G. Goubau in 1936 and was modified by F. Förster in 1937 (Musmann et al., 2010). The first major application was, as expected during this period, one of a military nature. Fluxgate instruments were and still are used for detecting submerged submarines, as their large ferromagnetic hulls cause measurable disturbances of the Earth's magnetic field.

In the civilian world, fluxgate instruments are used for geomagnetic measurements as well as in applications that employ the disturbance of the Earth's magnetic field for detecting materials. Disturbance measurements are, e.g., used for prospecting, archeology, detection of metal deposits (e.g., World War 2 remnants or old waste dumps) or finding building remnants.

In space applications, fluxgate instruments can be considered as the main workhorse for vectorial magnetic field measurements. This is due to the fact that fluxgate instruments deliver a combination of good measurement performance, low power requirements, low weight, long lifetime and high robustness that (up to now) has not been achieved with other types of magnetometers.

Functional Principle

A basic fluxgate sensor setup consists of a core of soft magnetic material and up to three coils that are wound around this core.

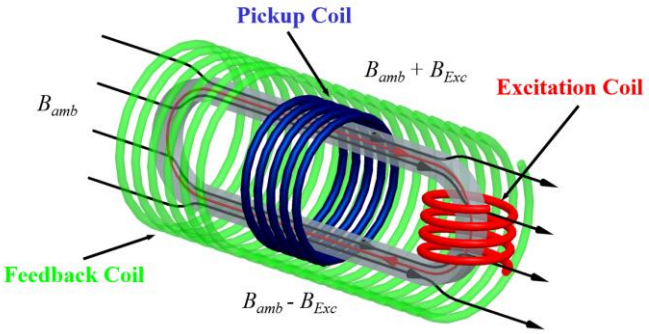

Figure 1–15 Single Axis Fluxgate Sensor
(Adapted from Auster, 2008, with the permission of the American Institute of Physics[12])

The excitation coil system is used to generate a periodic excitation field H in the core. The nonlinear dependency between H and magnetic field B of the magnetization curve (see figure 1–16) causes a saturation of B for higher excitation fields. The resulting induction in the pickup coil is still periodic, but contains odd harmonics of the excitation frequency (see figure 1–17).
An additional ambient magnetic field adds a bias in excitation, as this field and the excitation field are superposed within the sensor. This means that the relation between excitation and induction is no longer symmetric, because one field polarity reaches higher saturation than the other. This asymmetry introduces additional even harmonics of the excitation frequency f_{exc} in the induction B inside the core (see even harmonics depicted in red in spectrum plot of figure 1–17). In addition, these even harmonics also appear as asymmetry in the stray field caused by higher saturation in the core.

[12] Adapted from Auster, H.U.: How to Measure Earth's Magnetic Field, Physics Today (2008), Vol. 61 Iss. 2, pp. 76-77, Figure 1 https://doi.org/10.1063/1.2883919, with the permission of the American Institute of Physics

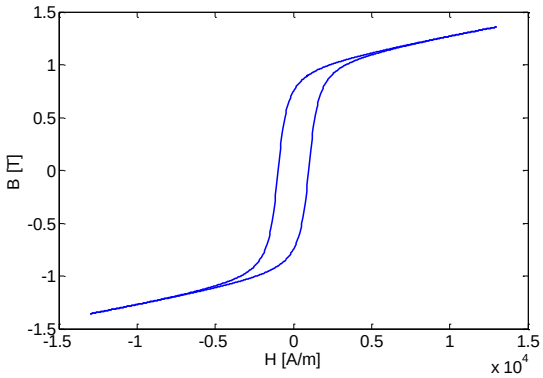

Figure 1–16 Exemplary Magnetization Curve of a Ferromagnetic Material

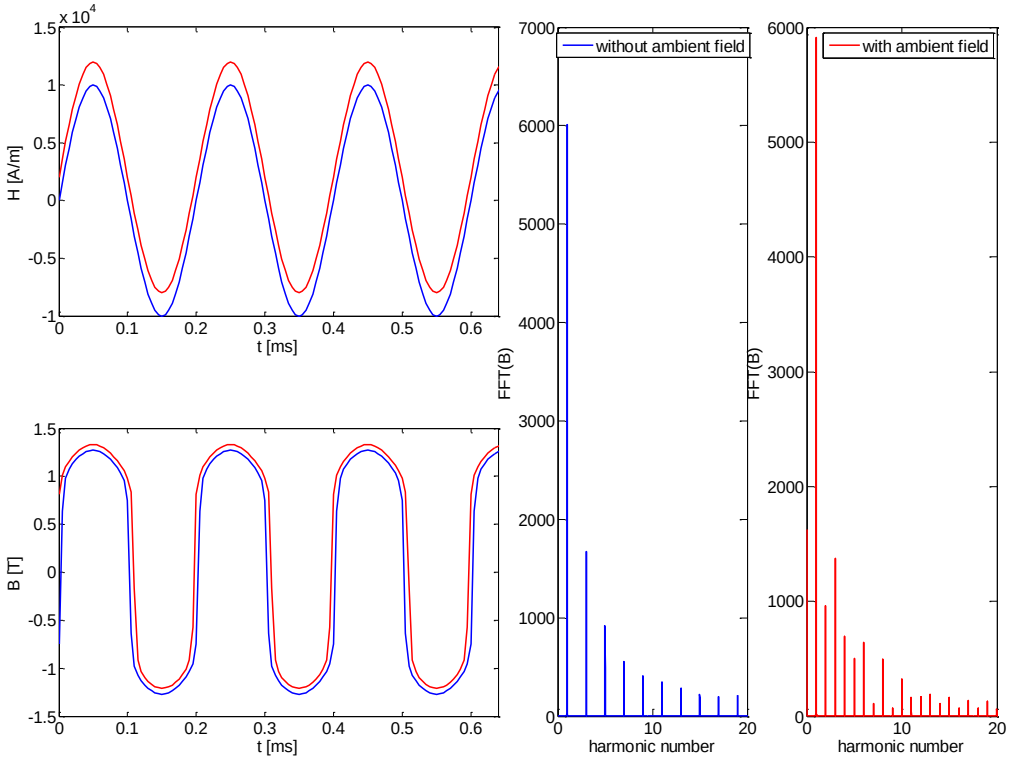

Figure 1–17 Fluxgate Induction with and without Ambient Magnetic Field

This mixture of harmonics can now be measured by an additional pickup coil. The induced voltage is proportional to the induction.

$$U = N\frac{d\phi}{dt} = N \cdot \vec{A} \cdot \frac{d\vec{B}}{dt} \qquad \textit{Equation 1-1}$$

The amplitude and phase of even harmonics within the measured voltage give information about the strength and polarity of the ambient magnetic field. This information can be extracted by synchronous demodulation with the respective multiples of the excitation frequency.

The connection between the harmonic amplitudes and the ambient magnetic field is nonlinear and dependent on the magnetization curve of the core. To eliminate this nonlinear connection, an additional feedback coil is added for the compensation of the ambient magnetic field. This changes the measurement from a direct nonlinear measurement to a null-detection control loop that is only dependent on the feedback. The magnetic field is detected by adjusting the feedback current until

even harmonics vanish. The value of the feedback current that is needed to remove the even harmonics is proportional to the ambient magnetic field. A block diagram of the complete mechanism is shown in figure 1–18.

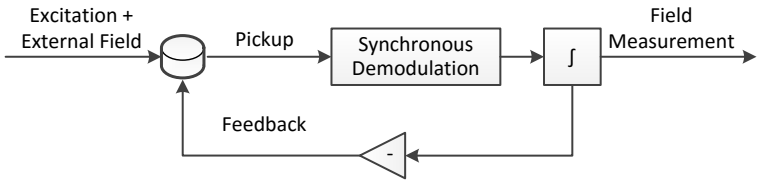

Figure 1–18 Feedback Mechanism of Fluxgate Instruments

This approach can then be expanded to three dimensional core/coil systems that can measure the induction in three directions. Figure 1–19 shows a mechanical drawing of the 3-axis fluxgate sensor that was used on MMS for both AFG and DFG.

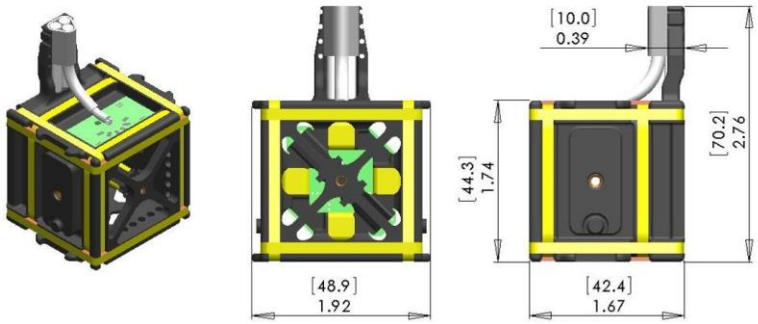

Figure 1–19 Drawing of MMS Fluxgate Sensor[13]
(dimensions in inch [mm])

The presented mechanisms are common to all fluxgate instruments, but individual instrument designs do implement them in quite different ways. Possible implementations can, for example, use rod cores or multi-axis ring cores, coils can be shared (e.g., common pick-up and feedback), pickup coils can measure direct field on the core or the surrounding stray field and feedback and demodulation can be implemented in either the analog or the digital domain. In addition, many power-saving mechanisms are used, e.g., the excitation field is typically not sinusoidal but more impulse-like (Janosek, 2017).

Frequency Properties

All of the elements presented above influence the frequency response of fluxgate instruments, both in amplitude and phase. The most relevant part of this influence is generated by the elements within the feedback loop and the need to regulate this loop in a stable manner.

The induction principle (see Equation 1-1) creates a -90° phase shift as well as an increasing gain vs. frequency response. This shift is also modified by the small influence of parasitic capacities and resistances of the coil. Another phase shift is caused by the demodulation system, but this is highly dependent on the actual implementation. Furthermore, every synchronous demodulator design needs some kind of bandwidth limitation to restrict the result to the parts of the spectrum that contains the even harmonics of the excitation frequency.

The feedback control system closes the control loop across all phase shifting elements. A stable feedback regulation can only be designed taking into account all the phase shifts within the loop and ensuring that no positive feedback occurs. This cannot be guaranteed for all frequencies (e.g., compare

[13] Image Credits: UCLA

to the current generator in 2.3.2.1) and is therefore enforced using bandwidth-limitation in the feedback. Typically, this is done with a first order low-pass filter that dominates the frequency behavior of the control loop. In addition, some designs choose a loop behavior that can also serve as anti-aliasing filter for later digitization.
The generated feedback is then driven through the feedback coil by either using a control voltage or a current source. In both cases, an additional phase shift will occur.

Figure 1–20 shows the gain curve of CLUSTER FGM (Balogh et al., 1997), which is a representative fluxgate instrument for space missions.

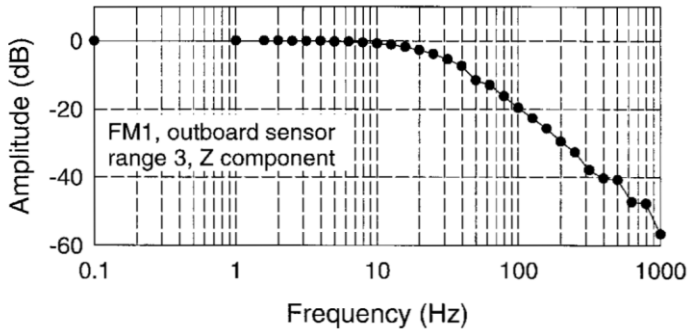

Figure 1–20 Frequency Response of CLUSTER FGM FluxGate Instrument
(© Kluwer Academic Publishers, Balogh et al., 1997[14])

Apart from the frequency response influences by the measurement principle itself, data reduction filters must also be taken into account. The FIELDS CDPU reduces data rates using multiple decimation steps that change the data rate by a factor of two each. Before each decimation, a 17-tap hamming windowed sinc filter (see chapter A.1) is applied to the data to avoid aliasing.

The Digital Fluxgate Magnetometer

The digital fluxgate magnetometer (DFG) on MMS is an implementation of the fluxgate principle that uses a sigma-delta loop across the sensor (Magnes et al., 2003 and 2008).

Figure 1–21 Electronics Board of MMS DFG

The principle of sigma-delta loops is to apply low-resolution quantization at high speeds. It is in fact quite similar to the principle of the fluxgate, as also here feedback and an integrator are used. Sigma-delta modulation uses feedback of the quantization value to push quantization noise towards higher frequencies and to change its correlation to the input signal. The output is a single bit stream with an

[14] Permission granted by Rightslink request May 30,2018

average value that corresponds to the input value. This average value is typically extracted by removing the high frequency quantization noise with a low pass filter. An example for a first-order sigma-delta loop is shown in figure 1–22. More information about this topic can be found in Schreier et al., 2017.

The advantage of sigma-delta converters is that conversion effort is shifted from the amplitude domain to the time domain. With this method, linearity is no longer defined by multiple quantization levels, but by just two of them.

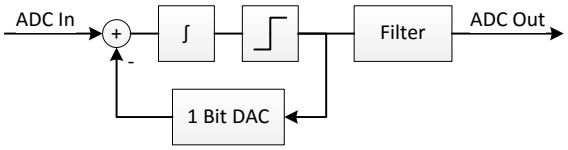

Figure 1–22: First-Order Sigma-Delta Analog-to-Digital Converter

The DFG uses this principle and applies a one-bit feedback to the sensor (see figure 1–23). This feedback alternates between the positive and negative maximum values, with an average that tracks the input value. The sigma-delta loop is in this case closed using magnetic coupling within the sensor. More detailed information on the actual structure and used modulator type can be found in Magnes et al., 2008.

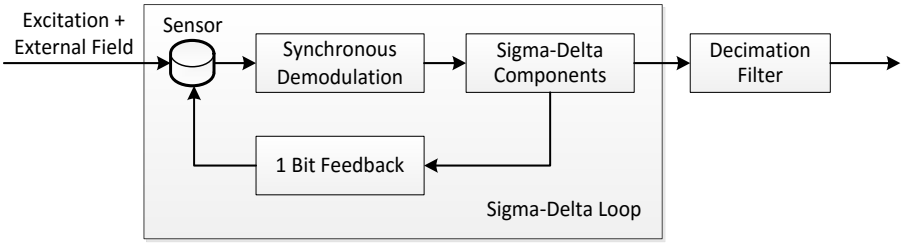

Figure 1–23: Simplified Block Diagram of the DFG Sigma-Delta Loop

The general advantage of sigma-delta modulators is that on-chip integration is simplified, since all the typical implementation problems of regular analog-to-digital and digital-to-analog converters (ADC and DAC) are avoided (e.g., the need for laser trimming of resistors).

With the possibility of on-chip implementation of fluxgate electronics, all the advantages of integrated designs can be exploited. The design of the DFG has therefore high temperature stability, low noise, low size and uses less power than comparable magnetometers.

The price for this gain is an increased nonlinearity for high magnetic fields, as the feedback toggles across the nonlinear part of the magnetization curve. For higher field values, this feedback toggling results in asymmetries that causes a nonlinear gain curve. In addition, the one-bit feedback generates a small distortion field that can be measured by other instruments.

The frequency response of the DFG is mainly defined by the sigma-delta loop and the used anti-aliasing filters for data decimation. The sigma-delta loop includes the fluxgate sensor components, the sigma-delta converter and a synchronous demodulator that is used for extracting the even harmonics. The influence of this loop on the final measurement is small, since it only affects frequencies in the kHz range, while the output data rate is 128 Hz.
Anti-aliasing filters are used in data decimation from the raw data rate of 8,192 Hz to the output rate of 128 Hz (a decimation factor of L=64). This decimation is done using a 4-stage cascaded integrator comb filter (CIC, Hogenauer et al., 1981) shown in figure 1–24. More information about basic filter structures is discussed in appendix A.1.

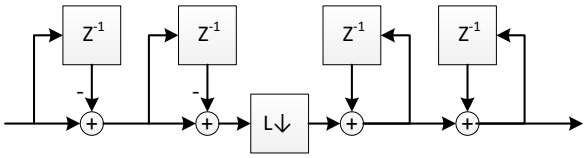

Figure 1–24: Example of a two Stage CIC Decimation Filter

This CIC filter can be operated in two modes. In DEC32 mode, the CIC filter is used to decimate from 8,192 to 256 Hz and the final decimation to 128 Hz is done by decimation with full aliasing. The effect of this aliasing is ignored, since higher frequencies typically have very low amplitude. This filter mode was introduced to generate data with low output delay. This data is used by the EDI instrument, which requires onboard knowledge about the magnetic field for steering the electron beam direction. In DEC64 mode, the CIC filter is used to get from 8,192 to 128 Hz with full anti-aliasing filtering. This also results in a lower noise floor, as in DEC32 the instrument noise from 64 to 128 Hz is also aliased into the 0 to 64 Hz band.

The DFG on MMS is able to measure the magnetic field in two measurement ranges, in low range (±650 nT) and high range (±10500 nT).

The Analog Fluxgate Magnetometer

The analog fluxgate (AFG) magnetometer on MMS uses a traditional design approach that implements the fluxgate principle in analog domain (details in Russell et al., 2016). Figure 1–25 shows the AFG electronics board. The gap at the lower right is allocated for the DFG electronics.

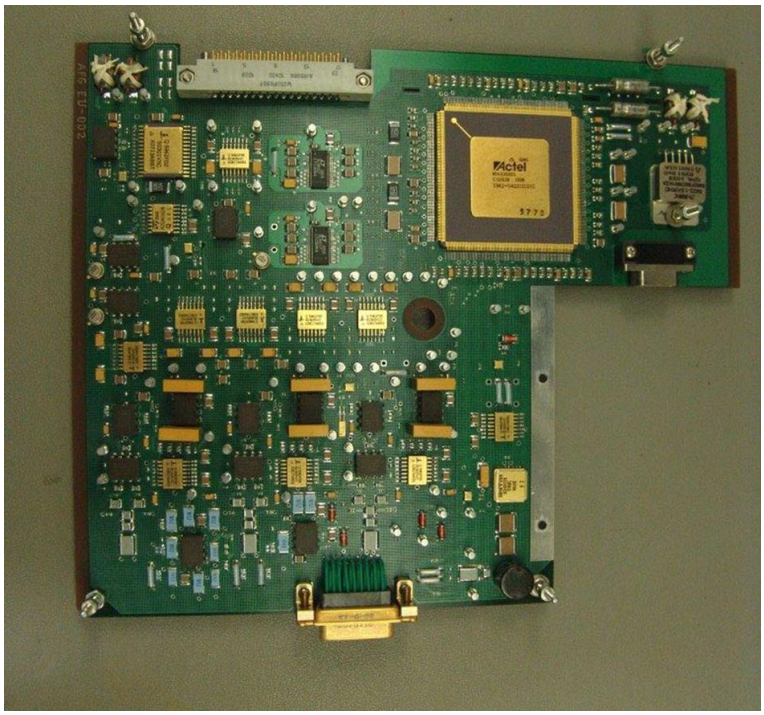

Figure 1–25 AFG Electronics Board for MMS
(© CC BY 1.0, Russell et al., 2016 [15])

A block diagram of this design is shown in figure 1–26. An initial bandpass-filter extracts the second harmonic. The resulting signal passes a synchronous demodulator and is integrated to deliver the feedback and measurement voltage. The measurement value is then amplified and sent to the analog to digital converter (ADC). The feedback voltage is converted to a current that drives the feedback coil.

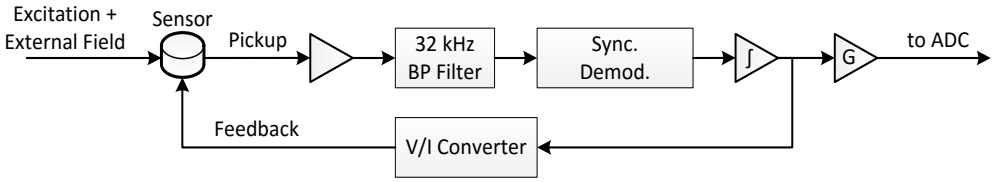

Figure 1–26: Simplified Block Diagram of AFG.
For full Diagram, see Russell et al, 2016

The ADC samples the measurement signal at 262,144 Hz using a 16-channel multiplexer. The resulting 16,384 Hz data is decimated to 2,048 Hz using a 16-point boxcar filter and further decimated to 128 Hz using two identical 16-point boxcar filters. For redundancy purposes, the ADC was added to the circuit twice. The two ADCs are identified as ADC A and B.

The frequency response of the AFG is mainly dominated by its analog components and is also subject to variations caused by the tolerances of the analog parts. The measurement range of the AFG is ±510 nT in the low range and ±8200 nT in the high range. Range switching is done by changing the output gain G, which has no influence on the frequency response.

[15] Creative Commons Attribution 1.0 Generic (CC BY 1.0), https://creativecommons.org/licenses/by/1.0/

1.1.3.4. Search-Coil Magnetometers

The MMS search-coil magnetometer (SCM, Le Contel et al., 2016) is a magnetometer that is based on direct magnetic induction in a coil and is therefore only suitable for measuring AC magnetic fields.

Functional Principle

The principle of magnetic induction (see equation 1-1) was discovered by M. Faraday in 1831 and is in fact the operating principle of electric power generators. Besides the use for power generation induction in coils, it is also used for power transmission (e.g., radio frequency identification or RFID, Qi Charging) and data transmission/reception like radio antennas. One common antenna type in these applications is the loop antenna (see figure 1–27), which just uses a coil with an application dependent number of windings to receive radio signals.

Figure 1–27 Shortwave Loop Antenna
(© Trixt [16])

This antenna can be improved by inserting a ferromagnetic core that is used as a concentrator for the magnetic flux. These antennas are typically used in compact amplitude modulation (AM) radio receivers or DCF77 time standard receivers. In principle, the search-coil magnetometer is quite similar to these AM antennas, but differs by the number of windings and the frequency sensitivity. Due to this similarity, the search-coil sensors are sometimes also referred to as "antenna." In fact early versions were sometimes developed by telecommunication companies. Search-coil magnetometers have been used in space for quite a long time, both for military applications (detection of nuclear explosions via their electromagnetic signatures) and for scientific applications similar to MMS. They provide excellent sensitivity for frequencies of up to hundreds of kHz and are typically built with three axes to measure the vector AC magnetic field.

[16] https://commons.wikimedia.org/wiki/File:Loop_antenna.jpg,
Creative Commons Share-Alike 3.0 (CC BY-SA 3.0), https://creativecommons.org/licenses/by-sa/3.0/

MMS Search Coil Magnetometer

The search-coil magnetometer used on MMS (see Figure 1–28) is a coil wound over a ferromagnetic core. Three of these coil/core assemblies are then combined to form a sensor for 3D measurement. The sensitivity of the coils is increased by placing many windings on the core with a wire length in the km range.

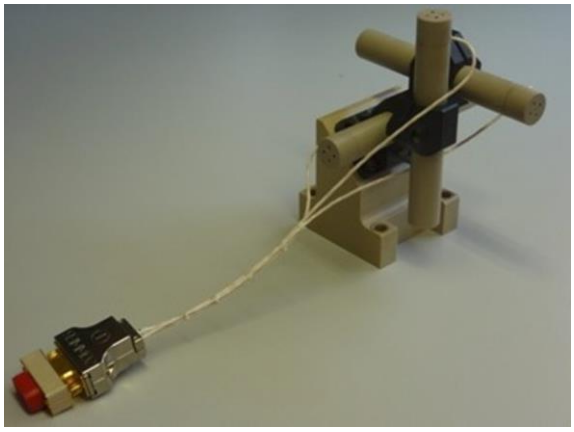

Figure 1–28 3D SCM Sensor for MMS
(© Springer Science+Business Media Dordrecht, Le Contel et al., 2016[17])

The resulting large number of windings generates large parasitic effects such as capacity between single windings, capacity between winding layers and ohmic resistance. Due to these parasitic contributions, search-coil sensors will show distinct resonance effects which are compensated by using a feedback coil system (see coil L2, Figure 1–29).

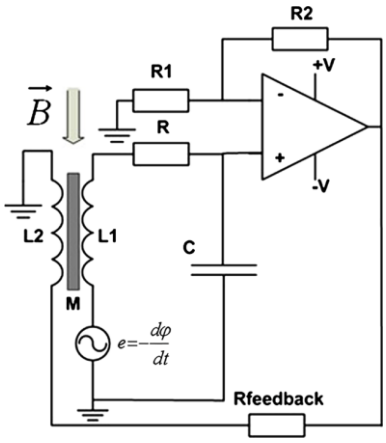

Figure 1–29 Feedback Circuit for MMS Search-Coil
(© Springer Science+Business Media Dordrecht, Le Contel et al., 2016[18])

In addition to the inherent properties of the sensor, also low and high pass filters are used to limit measurement bandwidth and remove DC offsets.

The resulting signal is then sent through a preamplifier and sampled by the digital signal-processing unit (DSP, Ergun et al., 2016). This sampling is done in an interleaved way, meaning the same ADC is used for all SCM axes using a multiplexer. The raw sampling frequency is 262,144 Hz for 16 channels which results in a maximum per-channel frequency of 16,384 Hz. The remaining channels of the multiplexer are used for sampling the electric field sensors.

[17] Permission granted by Creative Commons, https://creativecommons.org/
[18] Permission granted by Creative Commons, https://creativecommons.org/

Frequency Properties

The main contributor to the search-coil frequency response is the sensor itself, with coil inductivity, resistance and parasitic capacity. Further influence is generated by the feedback circuit and by DC removal filters. Figure 1–30 shows an exemplary frequency response of the search-coil from CLUSTER (Cornilleau-Wehrlin et al., 1997). This response includes the sensor, the feedback circuit, the pre-amplifier and the DC removal filter which attenuates frequencies below 0.2 Hz.

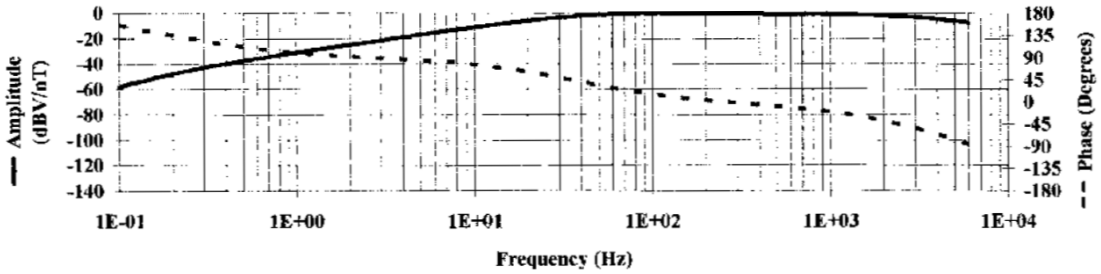

Figure 1–30 Frequency Response of CLUSTER Search-Coil
(© Kluwer Academic Publishers, Cornilleau-Wehrlin et al., 1997[19])

In addition, there is also some influence by the analog anti-aliasing filter before analog to digital conversion and by decimation filters in the digital domain that are used for reducing the data rate to the desired output rate. In the DSP on MMS, this decimation is done using a multiple stage digital filter and resampling process. Each stage uses a seven-tap hamming windowed sinc-filter (see chapter A.1), a three-tap triangular filter and data decimation by a factor of two. The minimum output sampling rate is 4 Hz.

[19] Permission granted by Rightslink Request May 30,2018

1.2. Merged Magnetic Field Data

1.2.1. Definition and Relevance

The aforementioned magnetic field instruments are well suited to measure the magnetic field in their sensitive frequency bands and to fulfill the requirements derived from their respective scientific objectives. A possible measure to compare the performance of the instruments is the noise equivalent magnetic induction (NEMI).

The NEMI combines all different noise sources, such as sensor and electronics noise, to a virtual magnetic noise source that is added to the external magnetic field. The additive noise and the external magnetic field are then measured by a theoretically noise-free instrument. The NEMI is affected by the instrument sensitivity, as frequency bands with lower sensitivity require higher virtual noise to achieve the actual instrument noise levels. This higher virtual noise is present, e.g., in the low frequency range of the SCM and towards the Nyquist frequency for both fluxgates and SCM.

Figure 1–31 shows a comparison of the Nyquist frequencies and the NEMIs of both DFG and SCM. The NEMI crossover frequency is at about 8 Hz.

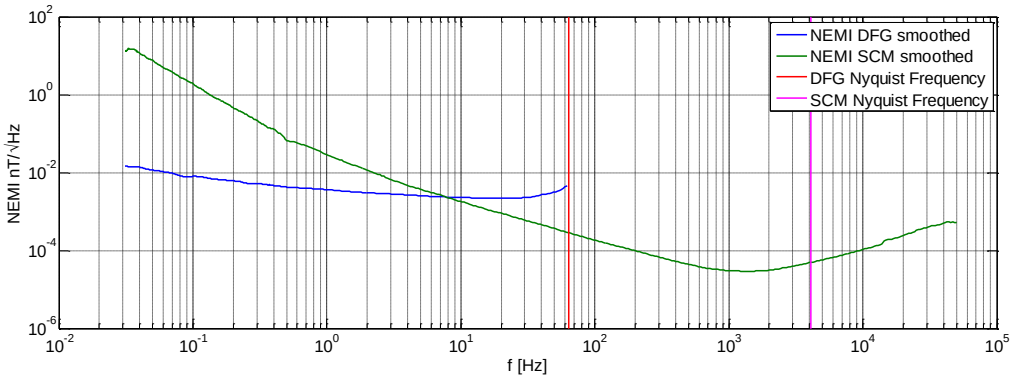

Figure 1–31 Comparison of DFG and SCM NEMI

The NEMI performance of DFG is better below and that from SCM is better above this crossover frequency. This means that an analysis of magnetic field events that include the frequency band around 8 Hz cannot rely on the best possible signal-to-noise ratio, as traditional waveform analysis needs to decide for one instrument type and its related NEMI level.

This fact triggers an obvious question: Why is there no data product that covers the whole frequency range? From the perspective of instrument design, the answer to this question is quite simple. To date, there is no instrument type that is able to fulfill this request with comparable performance features such as accuracy, noise floor and robustness for space applications. However, this request can be fulfilled with appropriate data processing based on sufficient information about the design and frequency characteristics of the instruments and with which data from both instruments can be merged into a common data product. The combined data product can profit from the best available noise floors of both instrument types which enables a single data set to cover the entire frequency range from DC to 4,096 Hz.

The advantage of a merged product from fluxgate and SCM data in the context of MMS is stated in the FIELDS instrument suite paper (Torbert et al., 2016):

"Electron diffusion regions and thin current sheets pass over the MMS spacecraft in time intervals of 0.5 to 2 seconds because a typical region size of 5 to 20 km moves with a boundary speed of 10 to 100 km/sec. (……) The frequency range of 0.5 to 20 Hz transitions from a low-frequency boundary where the SCM has little signal to a high-frequency one where the FG loses its ability to accurately track fields

that vary this fast. Thus, on MMS, it is critical to have algorithms to combine these two measurements in this overlapping frequency band into one accurate data series."

With the availability of a merged data product, events like this can be analyzed with just one single data set that takes into account the frequency properties of both magnetometers.

This is also beneficial for the analysis of events at higher frequencies which are normally based on SCM data but for which also the DC background field is typically required for data interpretation. For such cases, fluxgate data must be loaded and checked in parallel. A combined product already includes this background field information and no extra effort for additional data loading or processing is needed.

Besides the advantages in event analysis, also potentially hidden inaccuracies within single instrument data sets can be avoided with a combined data product. Due to the high quality of ground and in-flight calibration, fluxgate data is quite often considered as flawless and well calibrated, regardless of the frequency band. As opposed to the search-coil, the gain curve of a fluxgate instrument with its low pass characteristics (see figure 1–20) is, in most cases, not compensated for gain drops towards higher frequencies which can cause misinterpretation of the magnetic field data in this frequency range.

The gain curve of the fluxgates could be corrected in a similar way as it is done for the search-coil, but this would result in a problem that is in fact shared with the compensated search-coil. A frequency dependent gain correction will not only amplify the measured magnetic field, but also any noise present in frequency bands with reduced gain. The amplified noise includes not only the analog noise of the instruments but also the quantization noise introduced in the multiple-stage digital filters used for data rate reduction.
The NEMI presented in figure 1–31 is equivalent to the noise floor after gain correction, with the instruments operated at their maximum sampling frequencies and without further data rate reduction filters. The actual signal-to-noise ratio is finally dependent on the magnetic field strength which is typically in the sub-nT range for frequencies above 30 Hz.

Another source for misinterpretation can be caused by anti-aliasing filters (see chapter 2.6.1) used for data rate reduction in most instrument implementations. These filters normally have limited tap length with the consequence that the attenuation of aliasing frequencies is far from being perfect. Mirror frequencies of signals above the Nyquist frequency can therefore appear with amplitudes comparable to real signals and could result in erroneous interpretation. Occasionally, this artefact was even used as an "instrument feature" for detecting whistler waves at Venus (Russell et al., 2007) which were only visible due to the aliased spectrum.
Overall, it can be summarized that using SCM data below 1 Hz and using fluxgate as well as SCM data above half of their respective Nyquist frequencies could lead to potential misinterpretation and should only be used with care.

A combined data product helps avoiding such problems, as it includes proper gain and phase corrections and replaces the higher frequency fluxgate data by that from SCM, thus avoiding aliasing problems and a reduced signal-to-noise ratio. However, also this data product is not totally faultless towards its own Nyquist frequency, but at least the frequency range below half the Nyquist frequency can be considered as close to being perfect.

1.2.2. Previous Work in Data Merging

1.2.2.1. Sensor Fusion and System Identification

The combination of data from multiple sensors, also referred to as sensor fusion, has been used for determining measurement quantities and system states in a wide field of applications. Sensor fusion uses various sensors, sensor types and even different measurement quantities with the aim of obtaining information about one or more desired quantities. This additional information is then combined using a-priori knowledge like system models and estimates of measurement error. The goal of this combination is to obtain a more complete picture of this quantity, e.g., by achieving higher time resolution, better spatial resolution, improved signal-to-noise ratio, removal of distortion, higher bandwidth or estimations of otherwise inaccessible quantities.

One common application is the estimation of position and movement based on sensor readings from gyroscopes, inertial sensors, compass sensors, positional systems data and cameras. One of the most prominent research areas for these types of estimations is unmanned aerial vehicles or drones which require position and attitude information to stabilize their flight (da Silva et al., 2016; Mao et al., 2007).

A second example of sensor fusion is virtual reality applications (LaValle, 2018; Welch, 2009). Virtual reality headsets attempt to estimate head position and movement to synchronize screen contents with real movement. A mismatch between movement and screen can result in virtual reality sickness, which seriously impairs the customer experience. This application uses gyroscopes, compass sensors and cameras that track markers or laser grids.

A quite simple approach for sensor fusion in time-invariant systems is that of complementary filters (Osder et al., 1973). These filters are designed with the assumption that different sensors have different spectral probabilities, i.e., that some sensors provide better noise performance in specific frequency bands than other. This behavior is then reflected by designing complementary filters that create a sum of the "best" data of the available sensors using a frequency-weighted sum (see figure 1–32). The filters' transfer functions are designed such that their sum is either one or simply a delay.

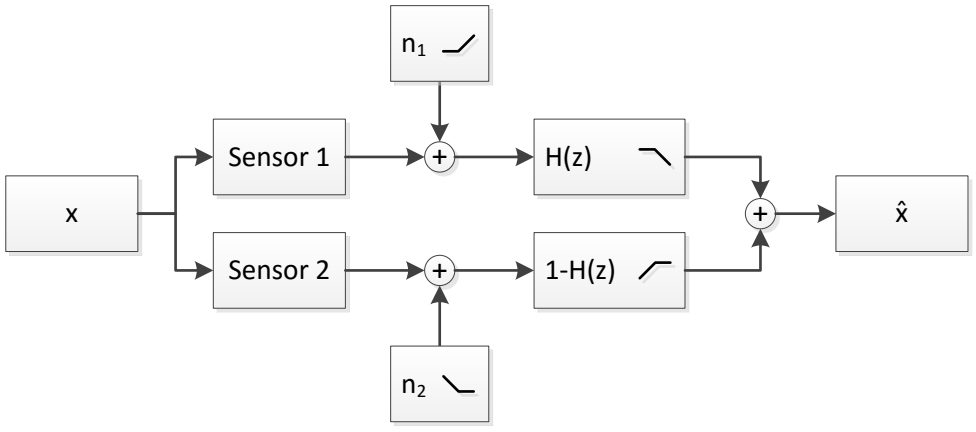

Figure 1–32 Block Diagram of a Complementary Filter

Complementary filters are designed using a-priori noise assumptions and are therefore not subject to an initial convergence phase. The number of computations is low, as no online estimation for variance states is required. In principle, the design of these filters is only dependent on the spectral properties of the measurement noise.

Because of this a-priori design approach, complementary filters are used in many applications. They are considered a sensor fusion method that is easy to program and requires little modeling effort (Jan, 2018; Leurent, 2018, OlliW, 2018, Alegiaco, 2018).

The standard approach for sensor fusion are Bayesian estimators such as the Kalman filter (Kalman, 1960) or particle filters (Del Moral, 1997). Most of these estimators use system and/or noise models (both possibly time varying) to estimate a measurement quantity or system state in a dynamical system. A disadvantage of these types of estimators is that spectral properties of the noise are not taken into account and only noise power statistics are used for estimation (e.g., covariance matrix). It is assumed that the observation noise of all used sensors is white (Simon, 2006, p. 130). In case of non-white noise within the modeled process, an adaptation of the system model is required, that replaces this noise with a more complex model with white noise input. The frequency properties of the non-white noise are in this case mapped into the system model.
In addition, Kalman filters have an impact on the spectrum of the measured signal that is dependent on the system model and noise model assumptions (Costello, 1980; Benmouyal, 1992). This influence must be taken into account in measurement applications that require a true representation of the signal spectrum.
Both, non-white noise and the wish for a true signal spectrum representation require a highly complex setup and result in a high number of calculations for variance estimation.

For time-invariant systems, complementary filters are therefore a more adequate approach and in fact, they are not that different from Kalman filters in this application case. For time-invariant systems, the Kalman filter will converge towards a time-invariant solution, the “steady state” (Simon, 2006, pp. 193ff). This solution is equivalent to a regular filter with static coefficients. If the Kalman filter system matrices and noise assumptions are designed in the right way, this solution is identical to the complementary filter (Higgins et al., 1975). It is even possible to generate a complementary filter by calculating the steady-state solution of the Kalman filter (Carreira et al., 2015).

Both, complementary and Kalman filters do not care about the frequency response of the sensors (see A.1.1), but assume that especially the magnitude responses are flat and all frequency dependencies are already represented in the setup of the Kalman and complementary filter, respectively.

It is therefore necessary to identify and compensate (or equalize) this frequency response before statistical merging is done. In principle, also this frequency response identification can be considered as statistical estimation. In this case, it is not about the estimation of quantities or system states, but about the estimation of system models based on measurement data.
The identification and compensation of a frequency response is used in many applications like control systems, channel and sensor equalization as well as loudspeaker and microphone equalization. This identification and compensation can be done in an adaptive way or by using static models, both based on a-priori knowledge of the identified system. Algorithms for this purpose are widely available in literature (e.g., Keesman et al., 2011; Hars, 2003) and can so be considered a standard technique.

The actual challenge is therefore in most cases not the design of an algorithm but the selection, tuning and application to a given problem. This also involves the design of the environment conditions to execute the algorithm, e.g., providing a suitable measurement environment for measuring the data required for the modeling.

1.2.2.2. Multi-Instrument Analysis of Magnetic Field Data

Numerous studies used both, search-coil and fluxgate magnetometer data. However, in most cases, event analysis was conducted using separate data products. Examples of this separated approach include Alexandrova et al. (2013), Chaston et al. (2008), Bruno et al. (2017), Vörös et al. (2011), Roux et al. (2011) among others.
In many cases, the authors stated their awareness of the limitations caused by the use of multiple data products such as different sensitivities and noise floor, e.g., Alexandrova et al. (2013) and Bruno et al. (2017) noted the increasing noise of the fluxgate instruments towards higher frequencies.
In addition to event analysis, Robert et al. (2014) used CLUSTER fluxgate data (Balogh et al., 1997) to cross-calibrate the gain of the search-coil (Cornilleau-Wehrlin et al., 1997). This was done using low frequency data (up to 6 Hz) that is less influenced by the frequency response of the fluxgate.

A fusion of search-coil and fluxgate data to common spectra and waveforms for event analysis was only conducted in a few cases. Alexandrova et al. (2004) used the wavelet transform to merge CLUSTER data by applying a crossover function that is dependent on the wavelet scaling factor. This analysis used gain and phase compensated search-coil data, but uncompensated fluxgate data. An almost identical method was also used by Chen et al. (2010) and Kiyani et al. (2013).

Torbert (2010) presented a fusion process for CLUSTER fluxgate and search-coil data to advertize the potential of a merged product for the MMS mission. This process was based on a gain and phase compensation in the frequency domain, using a combination of ground-based gain response measurements and an in-flight estimation of frequency response and delays. This combination was also presented by Argall et al. (2012) using data from CLUSTER and RBSP.
However, in all these cases, there was no dedicated ground based calibration of absolute time, gain and phase response. Data combination was therefore based on limited calibration data and in-flight estimations of these quantities, which can only deliver a relative calibration between the instruments, since it is limited to an order of roughly 10% in gain and several 100 µs in phase delay by the available signal-to-noise ratio of natural signals (see chapter 3.2.2).

A completely different approach was suggested by Han et al. (2012), who proposed an analog fluxgate search-coil hybrid that combines both principles in one instrument. This design uses an analog crossover filter to combine data from the two sensors. This type of design still requires a full characterization of the gain and phase response, but it automatically guarantees synchronous sampling. The disadvantage of this hybrid instrument is a higher noise floor caused by design trade-offs and magnetic interaction between the instruments. In Han et al. (2012), the fluxgate noise level is 8 pT/√Hz at 1 Hz and 4 pT/√Hz from 10-200 Hz, approximately twice the noise of AFG/DFG and about an order of magnitude larger than that of SCM.

1.3. Task Definition

The task of this thesis was to generate a merged data product from fluxgate and search-coil data measured aboard the four MMS spacecraft with minimal influence on gain and phase within the target bandwidth.

The task of merging can be considered as combining the two instrument types to a virtual instrument, which should ideally have flat gain response and a linear phase. The virtual instrument should thus be equivalent to a simple delay that can be fixed by adjusting the time stamps. The noise floor of this virtual instrument is then defined by the lowest possible noise floor that can be obtained by merging data of the individual real instruments.

The design goals for this virtual instrument are driven by the requirements of the FIELDS instrument suite, which again were flown down from the MMS mission requirements.

The time stamping accuracy requirement of FIELDS is 200 µs relative to the PPS signal. On top of this, a goal of 1 µs relative time stamping accuracy between the sub-instruments has been defined. The time stamping requirement of 200 µs can be directly mapped to a phase delay requirement for the merged data product, which means that the phase delay of every frequency should not exceed 200 µs relative to the time stamps.

Table 1-2 gives an overview of the accuracy requirements of the FIELDS magnetic field sub-instruments. The measurement error requirement of the fluxgate instruments is only given for DC fields, but in fact, this requirement is also valid for low frequencies up to 100 mHz. The gain error requirements for the fluxgate instruments AFG and DFG were computed from the absolute error requirements and the related instrument measurement ranges.

Instrument	Range	Range	Absolute Error	Gain Error
SCM	1-6000 Hz	-	-	< 2%
AFG	DC	High Range	< 1 nT	$< 1.22 \times 10^{-4}$
		Low Range	< 0.5 nT	$< 0.98 \times 10^{-3}$
DFG	DC	High Range	< 0.5 nT	$< 0.48 \times 10^{-4}$
		Low Range	< 0.5 nT (goal < 0.1 nT)	$< 0.76 \times 10^{-3}$

Table 1-2 Accuracy Requirements for FIELDS Magnetometer Instruments

The accuracy goals for the virtual instrument were derived from these requirements. In this context, it must be considered that the accuracy of gain and phase is subject to theoretical constraints, as it is not possible to modify gain and phase arbitrarily close to the Nyquist frequency. Furthermore, any amplification at frequencies close to Nyquist means in fact amplifying data that was attenuated by the anti-aliasing filter and which is subject to measurement and quantization noise. These frequencies will therefore suffer from increased noise floors.
Based on this restriction, it was defined that the merged data product shall meet the gain and time requirements of the instruments up to 75% of the Nyquist frequency of the merged data product.

The target sampling frequency of the merged data product was specified with 1,024 Hz instead of the theoretically possible 8,192 Hz. This choice was a compromise between time resolution and produced data volume at the MMS science data center. As the length of high frequency burst data intervals is highly limited by data downlink restrictions, the designed algorithms and models shall be fit for processing of short data intervals.

In summary, it was the task of this thesis to merge fluxgate and search-coil data to a common data product with a sampling frequency of 1,024 Hz, without introducing DC gain errors of more than 0.5×10^{-4} and AC gain errors of more than 2% up to 384 Hz, with a frequency independent time

stamping error of less than 200 µs (also up to 384 Hz) and with the lowest possible noise floor across the entire frequency range. Furthermore, the merging process needed to be designed to operate on short time intervals with just several minutes of burst data.

2. Approach

A merged data product can only be realized in multiple steps, which lead from model and method selection over measurements and model estimation to the realization of a complete merging process with all necessary elements. The following chapters follow this path and describe the necessary elements.

The required steps on this path are as follows:

- Select a suitable model type for each of the two types of instruments (chapter 2.1)
- Examine and select methods to identify the parameters of the selected model (chapters 2.1.1 to 2.1.3)
- Design the required measurement environment to support identification (chapter 2.2)
- Conduct the identification measurements (chapter 2.3)
- Identify the parameters using the measurement data (chapter 2.4)
- Verify the resulting models against previous tests and theoretical knowledge (chapter 2.4)
- Examine the instrument noise floor and design merging filters (chapter 2.5)
- Design a process for applying the instrument models and the merging filters on the data without violating the design goals (chapters 2.6 to 2.7)
- Verify the merging output of the process on in-flight data (chapter 3.2)

2.1. System Model and Identification Methods

The first step towards a merged data product is to classify the magnetometers into a matching system category for modeling. This categorization is based on the magnetometer system properties.

In general, both magnetometer types must be considered mixed signal systems, as they contain both analog and digital elements. In both cases, data is band-limited by internal low pass filters that either are required by functionality or are used for anti-aliasing in analog to digital conversion. The output of these mixed signal systems is provided as digital time stamped samples that are referenced to the FIELDS internal time, which is in turn defined by the PPS signal. All further data processing, including the preprocessing for a merged data product, is done in the digital domain. It is therefore reasonable to also choose a digital domain model for the magnetometers.
Although both magnetometer types contain nonlinearities, they either are designed to work in the linear range (SCM) or are linearized using feedback (AFG and DFG). The remaining nonlinearities are very small (e.g., for DFG a polynomial approximation yields a 2^{nd} order term of 10^{-7} for high range and no measurable nonlinearity for low range) and the magnetometers can therefore be considered linear.

Both magnetometer types are slightly time variant, as their parameters change, e.g., with temperature or by aging. Nevertheless, these changes are in general slow and covered by in-flight calibration. The magnetometers can therefore be modeled as time invariant.
The system properties listed above categorize the magnetometers as linear and time invariant systems that can be modeled in the digital domain. Commonly used model types for this purpose are finite (FIR) or infinite impulse response filters (IIR, see chapter A.1). However, the initial explanations in this chapter are done using continuous time systems, as the principles are similar and the presentation in the complete mixed signal view would introduce unnecessary complexity.

Identification of a filter is typically done by exciting the system with an input signal x(t) and measuring the output response y(t). In principle, this could already be solved by exciting the system with the Dirac impulse input $x(t)=\delta(t)$, which would result in an output that is in fact the impulse response h(t).

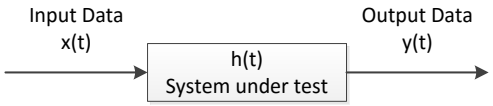

Figure 2–1 Input and Output of a Linear Time-Invariant Filter System

$$y(t) = h(t) * x(t) = h(t) * \delta(t) = h(t) \qquad \textit{Equation 2-1}$$

This approach is, for example, used in acoustics for room impulse response measurements. The impulse is in these cases generated by a clap or an explosive charge. One disadvantage of the impulse response method is that the complete excitation energy must be applied in one single moment, which is difficult to achieve in many systems. This also puts a limit on the possible signal-to-noise ratio of the measurements.

$$y_{noisy}(t) = y(t) + n(t) = h(t) * k \cdot \delta(t) + n(t) \qquad \textit{Equation 2-2}$$

$$SNR = \frac{\frac{1}{T}\int_T y(t)^2 dt}{\frac{1}{T}\int_T n(t)^2 dt} = \frac{\int_T \left(h(t) * k \cdot \delta(t)\right)^2 dt}{\int_T n(t)^2\, dt} = \frac{k' \int_T h(t)^2 dt}{\int_T n(t)^2\, dt} \qquad \textit{Equation 2-3}$$

For a given system h(t) with a given noise floor $n^2(t)$, the signal-to-noise ratio is highly dependent on the scaling factor k of the input pulse, which is equivalent to the pulse energy. The higher the energy of the pulse, the better the signal to noise ratio.

A further disadvantage is that all realizable methods for impulse generation are band limited and no Dirac impulses can be generated in practice. The resulting convolution therefore contains the non-ideal (wider) impulse given by the function p.

$$y(t) = h(t) * p(t) \qquad \textit{Equation 2-4}$$

This result can still be used with only minor impact if the bandwidth of the system h(t) is much smaller than that of the impulse p(t). In this case, the result of the convolution integral is almost identical to a multiplication with a constant:

$$y(\tau) = \int_{t=-\infty}^{\infty} h(t)p(\tau - t)dt \approx h(\tau) \int_{t=-\infty}^{\infty} p(t)dt \qquad \textit{Equation 2-5}$$

The allowed bandwidth of h(t) is therefore restricted by the achievable bandwidth in p(t). The target for an improved system identification is therefore to increase the signal-to-noise ratio and to eliminate the bandwidth limitation. One approach is to apply test signals for a longer time and to extract the impulse response mathematically. This increases the excitation energy and includes inherent averaging. The disadvantage is that the impulse response is convolved with the input signal (see equation 2-1) and is therefore no longer available directly, but requires some sort of computation. Potential test signals for this case are, e.g., chirp or noise signals. Noise signals apply all desired frequencies at the same time, while chirps sweep through all the frequencies. The difference between these signals is therefore mainly the distribution of the total energy per frequency band over time. This distribution has to be adapted to the actual situation, e.g., to slew rates in the signal generator or signal-to-noise ratio in specific frequency bands.

2.1.1. Sine Based Transfer Function Estimation

A quite simple method for model estimation is to use sine signals at different frequencies as input signals (see Keesman, 2011, pp. 24ff). The gain and phase shift of the respective output signals gives information about the frequency response of the system under test. This frequency response can then be used to determine the impulse response of the system. This can be done by either constructing a conjugate complex frequency domain kernel and using an inverse Fourier transform or by tuning an impulse response until its frequency response has identical gain and phase behavior. Figure 2–2 shows an example of a single test signal that is used to measure the gain difference ΔG and phase shift ϕ_{est} at one frequency.

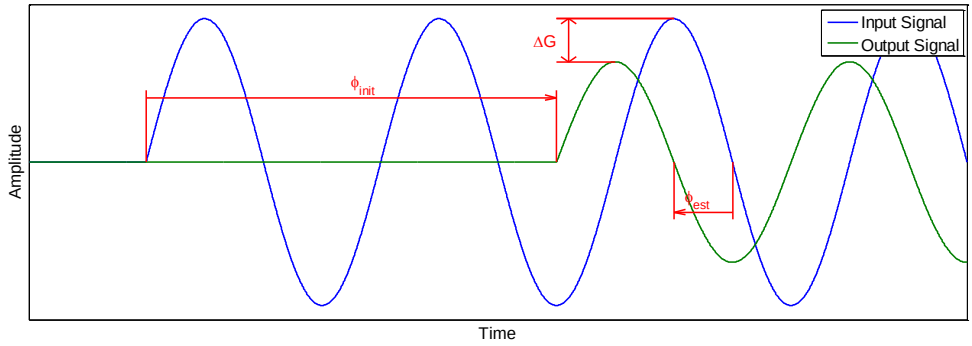

Figure 2–2 Phase and Gain Estimation with Sine Signals

One problem of this method is that the phase information is ambiguous. Any information about phase could as well be shifted by multiples of 360° or, if no information about polarity is included, even by multiples of 180°. This ambiguity is also present in figure 2–2, as the values of the estimated shift ϕ_{est} and the real shift ϕ_{init} differ by 720°. It is therefore necessary to exploit other information about the system to narrow down the possible interpretations of the phase shift to the correct 180° window. This can be accomplished, for example, by using a-priori system models that restrict the possible phase values or by including an initial phase measurement, which identifies the start delay of the sine signal. Only low precision is needed for this initial measurement, as it is just required to restrict the phase value to the correct 180° window.

The estimation of gain and phase can be done by fitting a sine signal to both signals and measuring gain and phase differences (see figure 2–3). This is done by using a least mean square error fit.

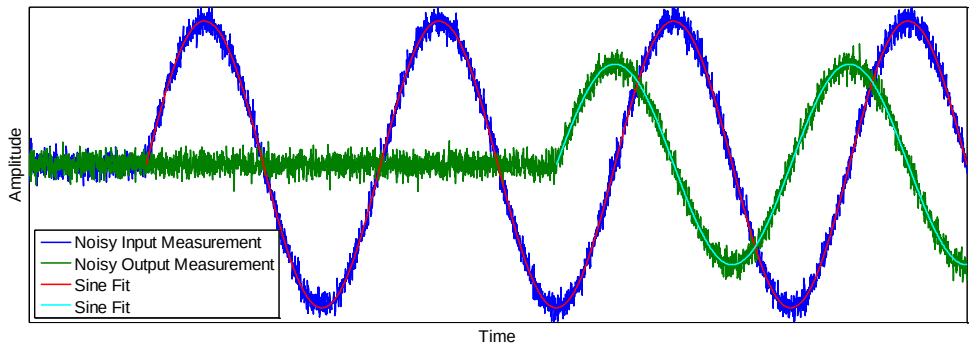

Figure 2–3 Phase and Gain Estimation with Noisy Sine Signals

The advantage of the sine fit method is that the limitation to one sine frequency is equivalent to a very narrow bandwidth filter which also reduces the measurement noise to a very small frequency band. The influence of all out of band noise is therefore reduced. On the other hand, this also results in a

very high sensitivity to distortion in this band; e.g., it would not be a advisable to use sine test signals at multiples of the power grid frequencies (50 Hz in Europe and 60 Hz in the US).
The main disadvantage of this method is that every measurement merely offers one point of the frequency response. This means that the desired frequency resolution defines the number of measurements and the needed time for the complete measurement.

2.1.2. Power Spectral Density Based Transfer Function Estimation

The power spectral density method does not rely on test signals with discrete frequencies, but on a mixture of multiple frequencies that cover the complete frequency range of interest. A derivation of this standard method (see Keesman, 2011, pp. 54ff) is provided, since the method actually used deviates from the standard to reduce computation power (see chapter 2.4.2). In addition, the derivation also gives information about the proper choice of a test signal.

The output y(n) of a discrete-time, linear and time-invariant system is given by the convolution of the input signal x(n) with the system's impulse response h(n).

$$y(n) = h(n) * x(n) \qquad \textit{Equation 2-6}$$

The instrument impulse response is then calculated by deconvolution. This can be done using the discrete time Fourier transform (DTFT, equation 2-7) which transforms a discrete time signal to the continuous frequency domain.

$$X\left(e^{j\omega}\right) = \sum_{n=-\infty}^{\infty} x[n]\, e^{-j\omega n} \qquad \textit{Equation 2-7}$$

This transformation converts the deconvolution operation to the simple division

$$H\left(e^{j\omega}\right) = \frac{Y(e^{j\omega})}{X(e^{j\omega})} \qquad \textit{Equation 2-8}$$

However, the result can only be calculated if the sum operation in equation 2-7 converges. This convergence is achieved for absolutely summable signals (= energy signals) and, in a few cases, for non-summable signals (= power signals), e.g., sine signals.

In theory, this convergence can be achieved by selecting a proper input signal x(n), as y(n) is in this case absolutely summable for most systems of practical interest, i.e., finite or stable infinite impulse response filters.

Unfortunately, all real-world signals involved in this deconvolution operation are subject to noise. It is therefore necessary to expand the convolution operation in equation 2-6 with input (n_x) and output noise (n_y).

$$y(n) = \big(x(n) + n_x(n)\big) * h(n) + n_y(n) \qquad \textit{Equation 2-9}$$

As long as the noise variables are uncorrelated to each other, one can simply combine all additive noise into one variable. Since the contribution of the input noise n_x is subject to convolution with h, the autocorrelation of the combined noise n_t is no longer a Kronecker delta.

$$y(n) = x(n) * h(n) + n_t(n) \qquad \textit{Equation 2-10}$$

The measurement noise is usually the result of a stationary random noise process and is therefore considered a power signal which is only windowed by the duration of the observation. For this reason, it is no longer possible to measure and calculate the true spectrum, but only a spectral estimate based on a limited observation time. The spectrum is usually expressed using the power spectral density (PSD) which is the DTFT of the autocorrelation sequence.
Using PSD estimates, the deconvolution in equation 3-8 can be expressed using the PSD estimate S_{XX} and the cross power spectral density estimate S_{YX} (CPSD, Fourier transform of the cross-correlation function).

$$\hat{H}(e^{j\omega}) = \frac{\hat{S}_{YX}(e^{j\omega})}{\hat{S}_{XX}(e^{j\omega})} \qquad \textit{Equation 2-11}$$

With included noise, this equation changes to

$$\hat{H}_N(e^{j\omega}) = \frac{\hat{S}_{YX}(e^{j\omega}) + \hat{S}_{NX}(e^{j\omega})}{\hat{S}_{XX}(e^{j\omega})} = \hat{H}(e^{j\omega}) + \frac{\hat{S}_{NX}(e^{j\omega})}{\hat{S}_{XX}(e^{j\omega})}. \qquad \textit{Equation 2-12}$$

The estimate of the frequency response is subject to two errors. The first error is caused by the noise term in the result of equation 2-12. The second error is the PSD estimation error in all used spectral densities.

A first approach to improve the estimate quality is to reduce the influence of the noise term S_{NX}/S_{XX} by modifying the input signal x which is the only selectable variable in this equation. The choice of the input signal is arbitrary, as long as it contains all relevant frequencies (S_{xx} is non-zero) and is uncorrelated to the noise. The error term is in fact equivalent to a transfer function $H_{X\to N}$ that uses the input signal x and delivers an output signal that is the noise within the currently observed window.

$$\hat{H}_N(e^{j\omega}) = \hat{H}(e^{j\omega}) + \hat{H}_{X\to N}(e^{j\omega}) \qquad \textit{Equation 2-13}$$

One criterion for a good estimate of the original transfer function H is to have a constant relative error power across all frequencies. This goal can be expressed using

$$\frac{\left|\hat{H}(e^{j\omega})\right|^2}{\left|\hat{H}_{X\to N}(e^{j\omega})\right|^2} = const. \qquad \textit{Equation 2-14}$$

The squared gain of a transfer function can also be calculated using the PSDs of the input and output signal.

$$\left|\hat{H}_{X\to N}(e^{j\omega})\right|^2 = \frac{S_{NN}(e^{j\omega})}{S_{XX}(e^{j\omega})} \qquad \textit{Equation 2-15}$$

$$\frac{\left|\hat{H}(e^{j\omega})\right|^2}{\frac{S_{NN}(e^{j\omega})}{S_{XX}(e^{j\omega})}} = const \qquad \textit{Equation 2-16}$$

This can then be translated to a design goal for the chosen input signal.

$$S_{XX}(e^{j\omega})\left|\hat{H}(e^{j\omega})\right|^2 \sim S_{NN}(e^{j\omega}) \qquad \textit{Equation 2-17}$$

In fact, this is a quite intuitive solution, as it simply states that the input signal should produce a sufficiently large output signal in comparison to the output noise for all frequencies.

A possible signal choice is to use white noise that is changed ("colored") in its frequency properties using a filter H_{color}.

$$S_{xx}(e^{j\omega}) = \left|H_{color}(e^{j\omega})\right|^2 \cdot {\sigma_W}^2 \qquad \textit{Equation 2-18}$$

With the design goal in equation 2-17, this filter can be designed using

$$\left|H_{color}(e^{j\omega})\right|^2 \sim \frac{S_{NN}(e^{j\omega})}{\left|\widehat{H}(e^{j\omega})^2\right|} \qquad \textit{Equation 2-19}$$

The next step for improving the estimate quality is to examine the estimation errors of the PSD. These estimates are calculated using the discrete Fourier transform (DFT, Oppenheim et al., 1998, pp. 541ff), which uses a limited size analysis window, assuming that the signal is periodic with the length of this window. The DFT analysis equation for a window length N is given by

$$X(k) = \sum_{n=0}^{N-1} x(n) W_N^{kn} \qquad \textit{Equation 2-20}$$

which is expressed using the the "twiddle factor"

$$W_N = e^{-j\frac{2\pi}{N}}. \qquad \textit{Equation 2-21}$$

The DFT is limited in frequency resolution by the window length N. The bandwidth of each DFT bin is given by

$$\Delta f = \frac{f_s}{N}. \qquad \textit{Equation 2-22}$$

The limitation to this window length is also equivalent to a multiplication with a window function w(n) in the time domain. In the absence of a user selected explicit window function, this window function is the implicit rectangular window. The multiplication can be expressed with

$$x_W(n) = x(n) \cdot w(n) \qquad \textit{Equation 2-23}$$

This time domain multiplication is equivalent to a frequency domain convolution.

$$X_W(k) = X(k) * W(k) \qquad \textit{Equation 2-24}$$

The combination of convolution and frequency resolution defines the effective resolution of the spectrum, as even with sufficient resolution small peaks or notches might be hidden by convolution. It is therefore important to match DFT length and window type to the actual application.

The CPSD and PSD estimates that are calculated with this transform suffer from a window dependent bias and estimation variance (Oppenheim et al., 1998, pp. 731ff). The simplest PSD estimate is the periodogram, which is calculated using

$$\hat{S}_{XX}(k) = \frac{1}{NU} X_W(k) X_W^*(k) \qquad \textit{Equation 2-25}$$

$$\hat{S}_{XY}(k) = \frac{1}{NU} X_W(k) Y_W^*(k) \qquad \textit{Equation 2-26}$$

In addition to convolution, the used windows also cause a gain bias in CPSD and PSD estimates. For single CPSD/PSD estimates this gain bias is handled adjusting the scaling factor U, which can be calculated using

$$U = \frac{1}{L}\sum_{n=0}^{L}(w[n])^2 \qquad \textit{Equation 2-27}$$

The estimation variance is in many cases as big as the squared spectrum itself.

$$var[S_{xx}(n)] \cong S_{xx}(n)^2 \qquad \textit{Equation 2-28}$$

This variance can be reduced by averaging multiple CPSD and PSD estimates, by using Bartlett's method (which uses non-overlapping data segments) and Welch's method (using overlapping data segments).

$$\hat{S}_{XX\ avg}(k) = \frac{1}{M}\sum_{i=0}^{M-1}\hat{S}_{XXi}(k) \qquad \textit{Equation 2-29}$$

Both Bartlett's and Welch's methods trade variance against spectral resolution, as data length is fixed and so defines the possibilities for overlap, number of averages and frequency resolution (= DFT window length N). Furthermore, the amount of overlap cannot be chosen arbitrarily, as the improvement in variance is a non-monotonic function (Barbe et al., 2010).
The complete estimation of frequency response can then be done using these averaged CPSD/PSD estimates. In this case, the scaling factor U is identical for both estimates and cancels out.

$$H(k) = \frac{\hat{S}_{YXavg}(k)}{\hat{S}_{XX\ avg}(k)} \qquad \textit{Equation 2-30}$$

2.1.3. Parametric Approach to Transfer Function Estimation

The power spectral density approach presented above uses non-parametric PSD estimators, as they do not use any model assumptions other than the used DFT transform length N. A different approach to transfer function estimation applies parametric PSD estimators (e.g., see Stoica et al., 2004), which assume that the given output data y is the output of a linear system with white noise input. The estimator then tries to find the parameters of this linear system to match the properties of the output data. The advantage of this method is that prior knowledge about the identified system can be used to improve the quality of the estimation, as distortion that does not fit to the model is automatically attenuated. The disadvantage is, of course, that the choice of the model is crucial for the quality of the result.

2.1.3.1. Wiener Filter

A similar approach to parametric PSD estimators is the Wiener filter (Haykin, 2002), that can be used to estimate the parameters of a linear system given its output and input signals.
The discrete Wiener filter is calculated using the Wiener-Hopf equations that are based on the auto-correlation of the input signal r_{XX} and the cross-correlation of output and input r_{XY}. These sequences are assembled to matrices R and p with dimensions defined by the order N of the linear system h.

$$\begin{bmatrix} r_{xx}[0] & r_{xx}[1] & \cdots & r_{xx}[N] \\ r_{xx}[1] & r_{xx}[0] & \cdots & r_{xx}[N-1] \\ \vdots & \vdots & \ddots & \vdots \\ r_{xx}[N] & r_{xx}[N-1] & \cdots & r_{xx}[0] \end{bmatrix} \begin{bmatrix} h_0 \\ h_1 \\ \vdots \\ h_N \end{bmatrix} = \begin{bmatrix} r_{yx}[0] \\ r_{yx}[1] \\ \vdots \\ r_{yx}[N] \end{bmatrix} \qquad \textit{Equation 2-31}$$

$$Rh = p \qquad \textit{Equation 2-32}$$

The linear system can then be calculated in a least mean square error sense by solving for h.

$$h = R^{-1}p \qquad \textit{Equation 2-33}$$

In fact this solution is not too far off from the power spectral density method in equation 2-30, as it follows a similar approach in the time domain. The Wiener Hopf method uses an implicit rectangular window that is defined by the system order N. Furthermore, the PSD method uses error averaging rather than the mean square error principle, therefore error statistics will vary.

The Wiener Hopf method works quite well, as long as the linear system does not have any frequency bands with low gain that include relevant system features. The problem in this case is that also the noise and resulting model errors in these bands are small in comparison to the noise in bands with higher gain. This means that optimization tends to "fix" the noise in frequency bands with high gain, while those with low gain are ignored. This behavior is problematic for a system like the search-coil, which has characteristic features in a frequency band with very low output gain (see frequencies below 1 Hz in figure 2–51).

2.1.3.2. Frequency Response Matching

An alternative approach for this case is to use the output of PSD based deconvolution (see equation 2-30) and to optimize a selected instrument model to produce a similar gain and phase response. The advantage of this approach is a free choice in model type (also IIR models can be used easily) and the possibility to weigh different frequency bands with different importance weights.

An initial guess is to simply match the complex gain H (see equation 2-30) by variation of the instrument model parameters p (e.g., filter cut-off frequencies) using a mean square difference as error criterion.

$$p_{1\ldots n} = \underset{p_{1\ldots n}}{\operatorname{argmin}} \left(\sum_k |H_{model}(k, p_{1\ldots n}) - H_{FFT}(k)|^2 \right) \qquad \textit{Equation 2-34}$$

Unfortunately, this approach still shares the problem of the Wiener Hopf method, as it is also sensitive to measurement noise. All frequency bands with high noise and distortion level will have higher impact in the error criterion. Furthermore, the error criterion minimizes the absolute error rather than the relative one, as a gain error of 100% at a gain of 0.1 and a gain error of 10% at a gain of 1 are equally important. This situation can be improved by adding frequency dependent weights for the error:

$$p_{1\ldots n} = \underset{p_{1\ldots n}}{\operatorname{argmin}} \left(\sum_k |H_{model}(k, p_{1\ldots n}) - H_{FFT}(k)|^2 \cdot W(k) \right) \qquad \textit{Equation 2-35}$$

These weights are then designed using a trade-off between the frequency dependent noise and a desired relative gain error.

2.2. Setup for the System Identification

The presented methods for system identification in chapter 2.1 are based on comparison of input and output signals and require a known time relation between these signals. Figure 2–4 shows the application of this principle on the FIELDS test setup.

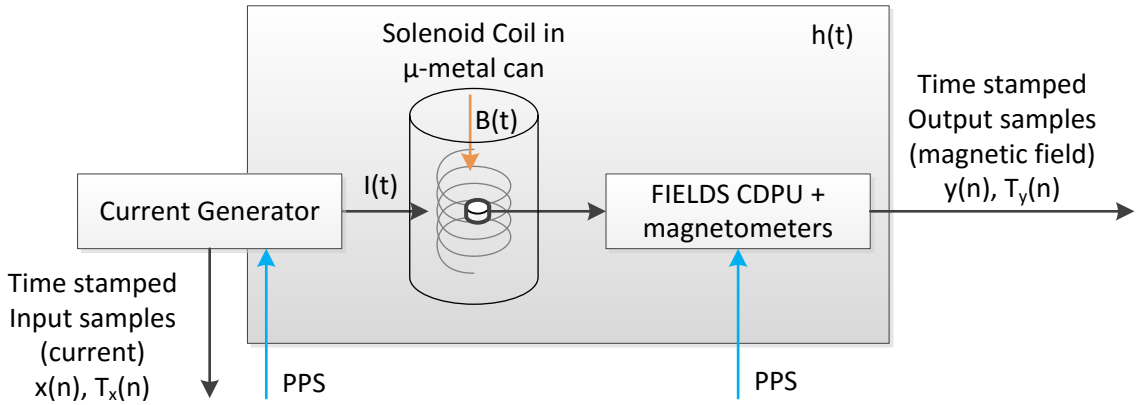

Figure 2–4 Simplified Block Diagram of System Identification with Current Generator

The input signal is a current I(t) which generates a magnetic field B(t) within the solenoid coil. This current is measured and time stamped within the current generator (x(n), T_x(n)). The magnetic field is measured by the fluxgate and search-coil magnetometers and is provided as time stamped data (y(n), T_y(n)) by the FIELDS CDPU. All time stamps are referenced to the PPS signal (see chapter 1.1.3.2).

The relation between input and output signals can therefore only be established if the magnetic field is also referenced to the PPS signal. One task of this thesis was therefore to design a current generator which is able to drive a PPS referenced current through a solenoid coil, thus generating a PPS referenced magnetic field signal. The design of this current generator is described in more detail in chapter 2.2.2.

The solenoid coil system was placed in a 3-layer µ-metal shielding can which is suitable to shield both the Earth's magnetic field and surrounding disturbances (e.g., any magnetic stray fields from a current consuming device). This µ-metal can is constructed of a metal with high permeability which acts as a path with low magnetic resistance. The magnetic field follows this path of least resistance along the circumference of the can and the influence of the external magnetic field within the can is thus significantly reduced.

Since both the current generator and coil system are located between input x(n) and the output y(n) of figure 2–4, any influence of coil and generator on the frequency response along this path would also change the identified system response h. It is therefore important to design this measurement setup with minimal or at least known influence on the signals.

2.2.1. Overview

The initial concept for frequency response measurements using the current generator (see figure 2–4) was embedded in the setup required for the FIELDS integration and test (FIT) campaign. Figure 2–5 shows an overview of the test setup used for the campaign. This setup was not only used to conduct the frequency response measurements, but also to support the delivery tests of the actual flight versions of the FIELDS sub-instruments, their integration into the FIELDS central electronics box as well as their functional verification testing in fully integrated configuration.
In this setup, the FIELDS instrument suite is in flight configuration and the test is therefore fully representative for the actual situation on the satellite. Unfortunately, this flight configuration did not

include any checkout connectors. The access to the internal clocks and time reference signal was therefore limited to the PPS signal, which was generated by a high precision frequency generator and provided to FIELDS via a central instrument data processor (CIDP) simulator unit. Two separate host PCs were used for control, as well as non-realtime data provision and retrieval for current generator and CIDP.
The setup presented in figure 2–5 was modified during the process to simplify the required calculations (see chapter 2.3.2).

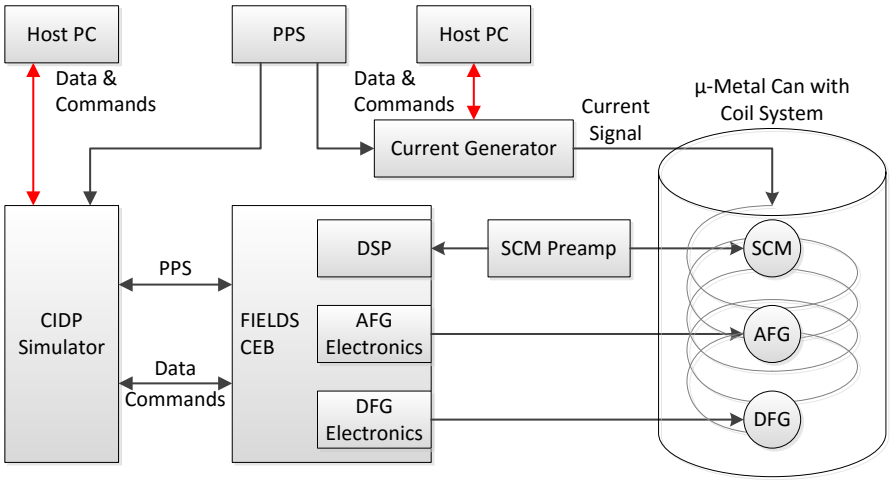

Figure 2–5 Initial Design of FIT Campaign Setup

2.2.2. Current Generator

The MMS current generator (see figure 2–6) used in the FIT campaign is a mixed signal system (digital/analog) that provides an analog current, which is generated using a digital control signal that is synchronized to the FIELDS time standard (PPS, see 1.1.3.2). This current is converted to a magnetic field signal using the solenoid coil system.

Figure 2–6 Front View of MMS Current Generator

Generation of this current requires several hardware blocks in the digital and analog domains. This chapter explores the most relevant blocks and their functionality.

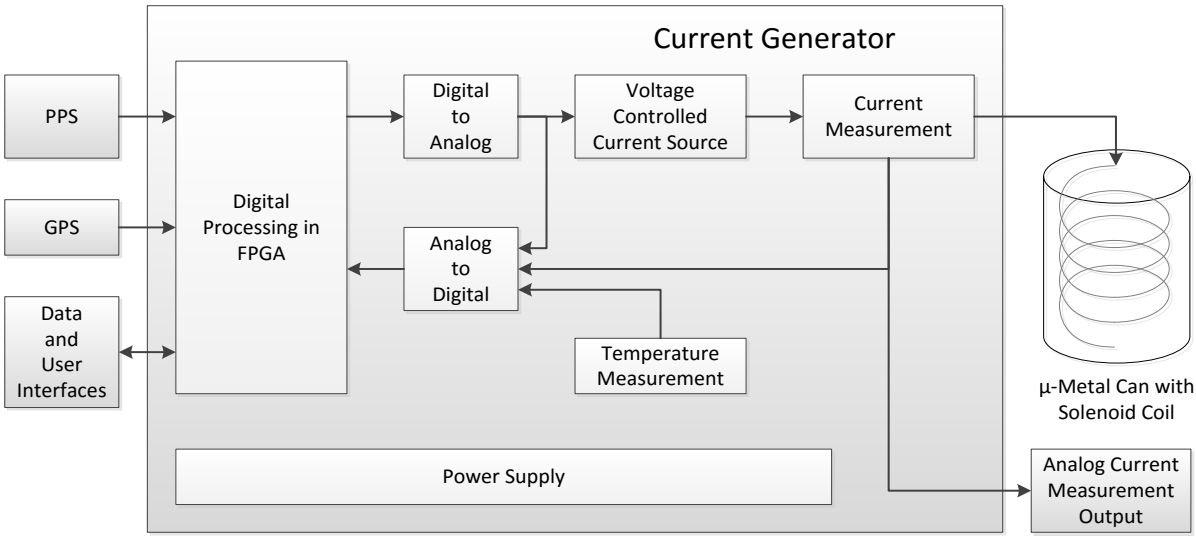

Figure 2–7 Block Diagram of Current Generator

Figure 2–7 shows the basic blocks of the current generator. Test data and control signals are provided via the data and user interfaces. The input data is provided as waveform files that simply contain a series of samples. A field programmable gate array (FPGA) contains a Leon 3 CPU with modules for the interfaces and synchronization (PPS and GPS). Digital test data is converted to a voltage using a digital to analog converter (DAC). This voltage is in turn converted to a current. To overcome non-idealities along the signal path, both generated voltage output and current output are measured to retrieve information about the real quantities rather than the expected ones. This measurement is provided at a monitor output and is also sampled using an internal analog to digital converter (ADC). To ensure temperature changes do not influence the measurement, also temperature is measured and sampled.

A low noise floor is achieved by using a low noise power supply with galvanic isolation which allows establishing a grounding concept that avoids noise being induced by grounding loops.

2.2.2.1. Design Targets

The design target of the current generator is to generate a current within the solenoid coil. This current should have a known timing relation to the PPS signal and the subsequent FIELDS time stamps. Knowledge about the exact amplitude of the current is not necessary, as the frequency response estimation only requires knowledge about the relative changes over frequency. The connection to the absolute calibration can be established using data points from the reference calibration campaigns completed by the instrument teams.

The required accuracy is in principle given by the design goals in chapter 1.3, but these goals are valid for the overall processing chain from measurement to modeling and application. The design target for the current generator was therefore to use only a part of the possible "error budget."

With this in mind, the current generator was designed with the specifications outlined in table 2-1.

	Merged data product goals	Current generator goals
Amplitude accuracy	DC gain error $<10^{-4}$ AC gain error <2%	≥16 bit digital resolution ~90 dB signal-to-noise ratio
Time/Phase accuracy	Time stamping error <200 µs, with a goal of 1 µs	1 µs
Bandwidth	512 Hz	≥ 1,024 Hz

Table 2-1 Top Level Requirements and Current Generator Design Goals

The digital to analog converter (DAC) is used to drive the current source, which in turn drives a current through a large coil. The achievable noise floor in such a system is not only a matter of part selection, but also of system size. The larger a system is, the larger the possibility of picking up other signals is. The large coil used for producing the magnetic field, in this case, also acts as pickup antenna for external noise and distortion.

Although this distortion is uncorrelated to the test signal, it will still set a limit on the measurement quality. Signal-to-noise ratio is therefore limited by the instrument's measurement range on one side and the noise and distortion floor on the other side. Generating test signals with matching magnitude across the whole spectrum is therefore more important than the low quantization noise level of DACs with high resolution.

2.2.2.2. Analog Frontend

Voltage Controlled Current Source

The magnetic field is generated by driving a current I through the solenoid coil. For a simplified geometry, neglecting boundary effects, the magnetic field along the center of a solenoid coil with N windings and length l can be expressed as a function of the current I_{coil}:

$$B = \mu_0 \mu_r \frac{N I_{coil}}{l} \qquad \textit{Equation 2-36}$$

The geometry and permeability of the used coil can be combined to the coil constant k_{coil}. The resulting field is

$$B = k_{coil} I_{coil} \qquad \textit{Equation 2-37}$$

The coil constant was measured as

$$k_{coil} = 1256.64 \frac{nT}{mA} \qquad \textit{Equation 2-38}$$

The magnitude of the coil current is subject to the applied voltage U and the coil impedance Z_{coil}, which is in turn frequency dependent.

$$I_{coil} = \frac{U_{coil}}{Z_{coil}} \qquad \textit{Equation 2-39}$$

The coil impedance is dependent on the coil inductivity L as well as as the ohmic resistance of the copper wire and a parasitic capacity between windings. This is modeled by the equivalent circuit in figure 2–8.

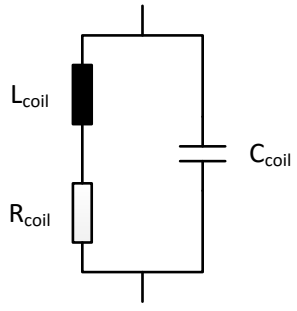

Figure 2–8 Equivalent Circuit of Solenoid Coil with Parasitic Influence

The impedance of this circuit is given in equation 2-40:

$$Z_{coil} = \frac{R_{coil} + j\omega L_{coil}}{1 + j\omega C_{coil} R_{Coil} - \omega^2 C_{coil} L_{coil}}$$ *Equation 2-40*

with R_{coil} = 120.7 Ω, C_{coil} = 6 nF and L_{coil} = 44 mH. The magnetic field is given by

$$B = k_{coil} \cdot \frac{U_{coil}}{R_{coil} + j\omega L_{coil}}$$ *Equation 2-41*

This generated field is frequency dependent. Precise knowledge of the magnetic field can be achieved either by controlling the current (rather than the voltage) or by measuring the generated current.

The current generator employs a mixed approach that uses a voltage controlled current source and measures the real current generated by this source. The advantage of this dual approach is that the current is almost frequency independent, while any remaining non-ideal behavior of the current source is covered by the current measurement. Such non-idealities include problems like offset and gain drifts, frequency response of the current source itself and the limitation in current amplitude and slope caused by a limited supply voltage.

The used current source is a standard non-inverting operational amplifier with ungrounded load (see figure 2–9, design from Tietze et al., 2002, pp. 795ff). This design has low output resistance and the resistor R_M can also be used as the resistor for the current measurement. In addition, the number of used electronic parts is very small and does not require resistor matching like, e.g., the Howland current pump. The disadvantage of this current source is that the load is not referenced to ground. Fortunately, the grounding topology of the current generator in fact uses floating ground potentials and the current can therefore be referenced to an arbitrary potential. The used grounding topology is discussed later in this chapter.

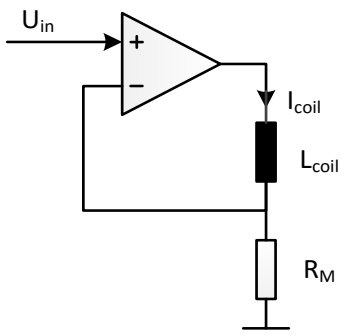

Figure 2–9: Basic Circuit of Current Source

The theoretical current output of the selected current source is defined by:

$$I_{coil} = \frac{U_{in}}{R_M}$$ *Equation 2-42*

The resistor R_M was implemented as switchable resistor array, which allows multiple current ranges. The values that were actually used are 511 Ω, 5,470 Ω and 34,096 Ω. With a maximum input voltage of ±2.048 V, this results in a generated magnetic field of ±5,036 nT (high output range), ±570 nT (medium output range) and ±75 nT (low output range).

The actual current through the coil is influenced by the parasitic capacity of the coil, the non-idealities of the operational amplifier and the available supply voltage, which limits the current slope.

An approximate value for the slope limitation caused by the limited supply voltage can be calculated using

$$\left(\frac{di}{dt}\right)_{max} = \frac{U_{supply} - I_{coil}R_M}{L_{coil}} \qquad \textit{Equation 2-43}$$

This relation introduces the requirement to limit changes in current, which in turn requires a reduction of the amplitude with increasing frequency and a limit to these changes while static currents are present. If the changes are not limited, the expected and actual current will not match. Although this mismatch is logged using the current measurement, this still means that higher frequencies might be attenuated and signal-to-noise ratio at these frequencies may degrade.

The influence of parasitic elements can be derived by solving the equations for the complete circuit, which is shown in figure 2–10.

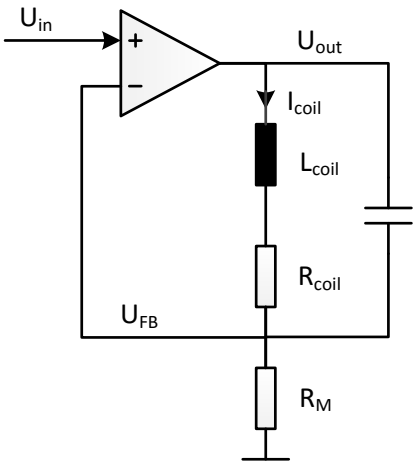

Figure 2–10 Equivalent Circuit of the Non-ideal Current Source

The current with this influence can then be expressed as

$$I_{coil} = \frac{U_{in}}{R_M(1 + j\omega C_{coil}R_{Coil} - \omega^2 C_{coil}L_{coil})}. \qquad \textit{Equation 2-44}$$

A further topic to examine is the possible instability of an operational amplifier in closed loop operation. This instability occurs, if the feedback of a sine signal has enough phase delay to cause positive instead of negative feedback.

Stability analysis is done by calculating the frequency response of the feedback signal and analyzing gain and phase values in open loop condition. A stable system needs to have loop gains smaller than one for phase conditions that result in positive feedback, when the feedback signal is in phase with the input signal (Tietze et al., 2002, pp. 518ff). The phase of the input signal is influenced by the feedback circuit, the operational amplifier itself and the feedback sign, which causes another 180° shift if negative feedback is used. Since negative feedback is typically used in operational amplifier circuits, these 180° are already added to the stability condition. An operational amplifier is therefore stable when the feedback is not in anti-phase, meaning the phase shift is not at ±180°.
The distances from unity gain and 180° phase shift are called gain and phase margin and give information about the stability and transient response of the feedback loop. Typically, a phase margin of 45° or more is desirable, as lower phase margins will result in overshooting step responses, also called "ringing."

For analysis of the gain and phase changes, also relevant influences by non-ideal parts within the circuit need to be taken into account. The major contributor to this non-idealities is the coil with its parasitic influences.

The open loop feedback gain β is the relation between output and feedback voltage:

$$\beta = \frac{U_{FB}}{U_{out}} = \frac{R_M}{R_M + \frac{R_{coil} + j\omega L_{coil}}{1 + j\omega C_{coil} R_{Coil} - \omega^2 C_{coil} L_{coil}}} \qquad \textit{Equation 2-45}$$

The influence of the operational amplifier itself is given by the open loop gain/phase diagram in the data sheet shown in figure 2–11.

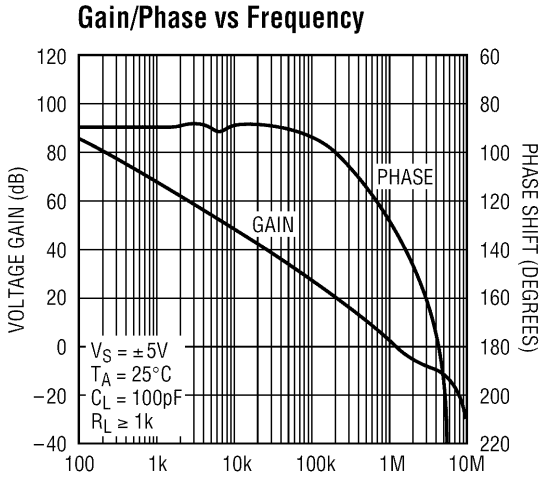

Figure 2–11: Open Loop Gain and Phase Curve of LTC1050 (LTC1050 Data Sheet[20])

The phase curve in the data sheet shows the phase value with a negative sign and a delayed phase is therefore represented by a positive phase value. Unity gain of the operational amplifier is obtained at roughly 1 MHz with a phase shift of around -130°. Until 100 kHz, the phase shift is nearly constant at around -90°.

An LTSpice circuit simulation of the feedback gain and the amplifier results in the overall gain/phase curves shown in figure 2–12. These curves are given for the operational amplifier itself, the external feedback circuit (U_{FB}/U_{out}) and the sum of both. The black lines show the borders of the stability limit, where the gain must be below one if the phase is close to 180°.

[20] LTC1050 data sheet revision fb, last retrieved 2018/03/08, http://www.linear.com/product/LTC1050

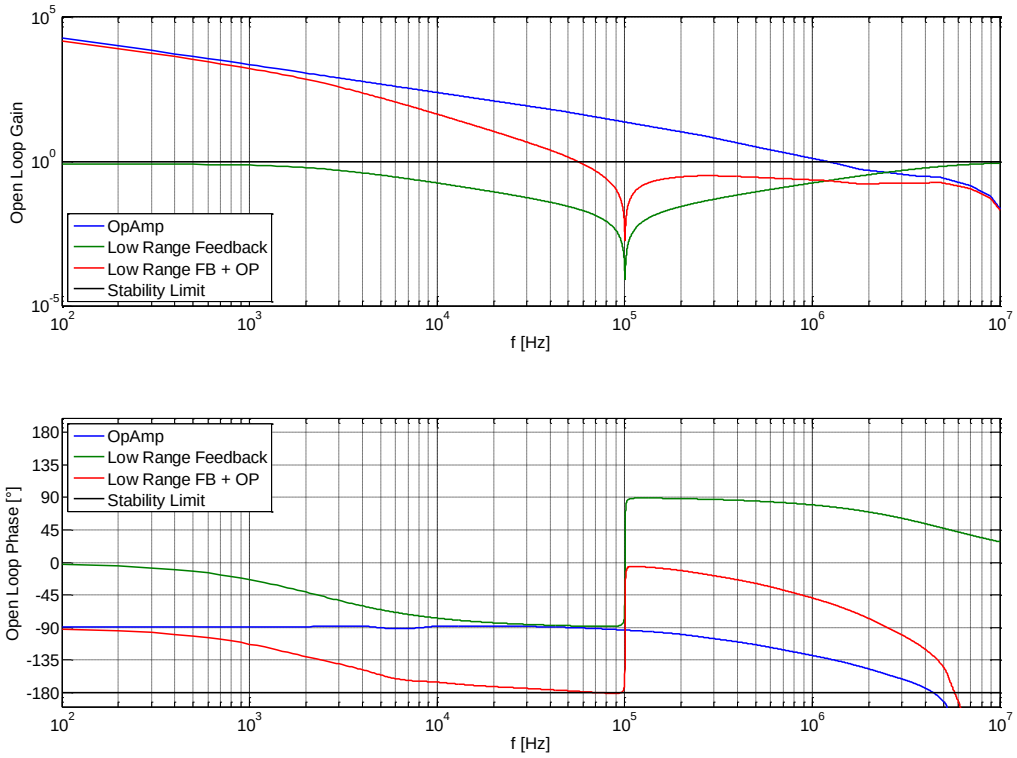

Figure 2–12 Open Loop Gain and Phase of Current Source (unstable version)

Although the circuit is stable for high frequencies, instability is possible due to the coil resonance at 100 kHz. At around 50 kHz, the gain is well above 1, while the phase shift is almost 180°. With these conditions, the circuit will suffer from heavy output ringing. Furthermore, any additional parasitic capacity in cables, electronic parts or the circuit board could cause instability.

The 90° phase contribution of the operational amplifier cannot be improved, as all frequency-compensated amplifiers have low pass characteristics and show similar phase behavior. Uncompensated amplifiers have less phase influence at the resonance frequency, but have a lower gain drop-off and will therefore simply move the problem towards higher frequencies.
The only possibility is therefore to modify the phase response of the feedback circuit to avoid a 180° shift at the coil resonance. A simple solution is to add another capacitor in parallel to the solenoid coil.

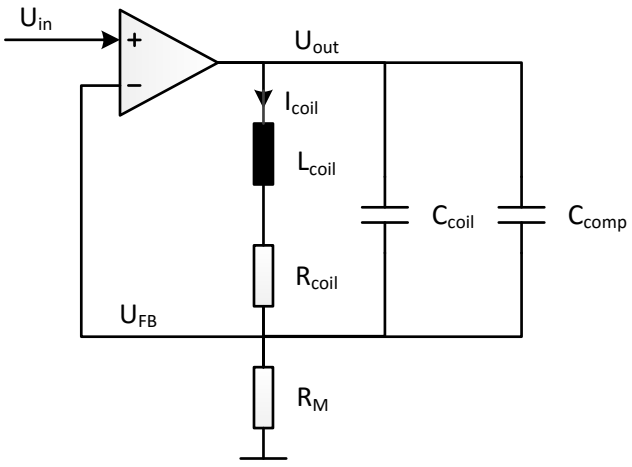

Figure 2–13 Current Source with additional Capacitor

With this additional capacitor C_{comp} (10 nF) the open loop feedback gain is

$$\beta = \frac{U_{FB}}{U_{out}} = \frac{R_M}{R_M + \dfrac{R_{coil} + j\omega L_{coil}}{1 + j\omega\left(C_{coil} + C_{comp}\right)R_{Coil} - \omega^2\left(C_{coil} + C_{comp}\right)L_{coil}}}$$

Equation 2-46

The resulting stabilized gain/phase curve with this capacitor is shown in figure 2–14. The phase margin for high output range is 40°, which results in some ringing at high frequencies. For the low output range, a phase margin of 15° is achieved, which results in acceptable ringing. In both cases, this ringing is also present in the current through R_M and is therefore visible both in the magnetic field and in the current measurement. The amplitude of this ringing depends on the size of changes in the control signal. These changes can be reduced by introducing a limitation of amplitude for higher frequencies. This limitation was acceptable, since it is also needed to handle the high sensitivity of the SCM (see chapter 2.2.4).

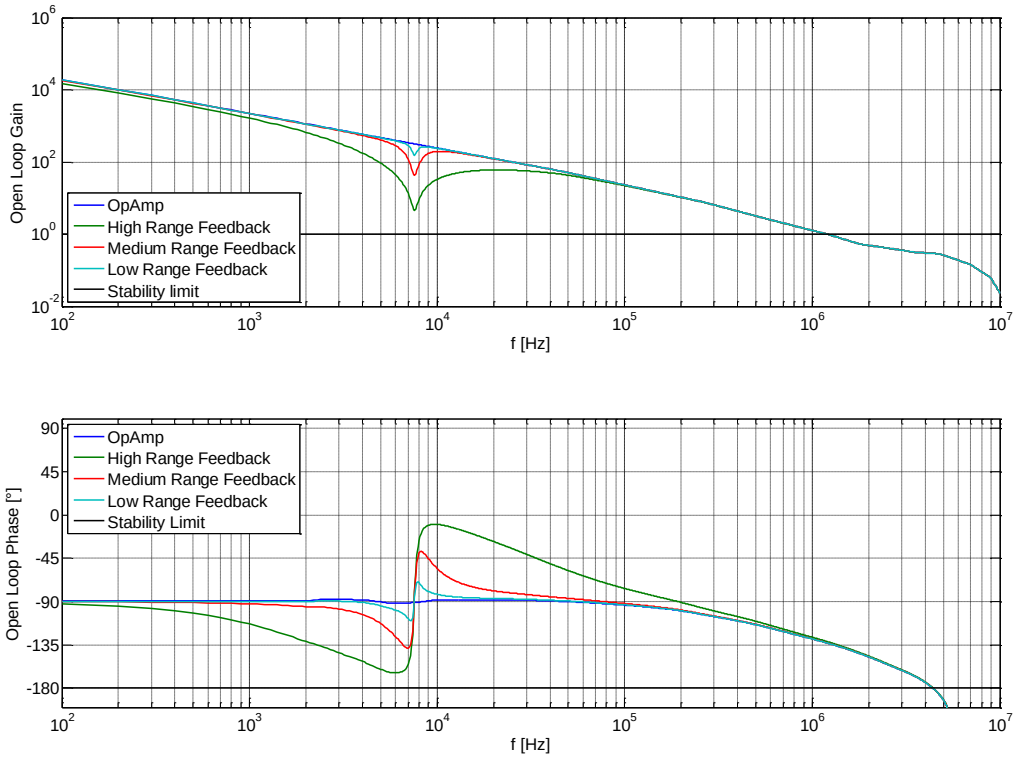

Figure 2–14 Stabilized Open Loop Gain and Phase with additional Capacitor

Both, the parasitic and the additional capacitor will divert a part of the current generated by the source. The ratio of the remaining coil current vs. the control voltage U_{in} can be calculated using

$$\frac{I_{coil}}{U_{in}} = \frac{1}{R_M\left(1 + j\omega R_{coil}\left(C_{coil} + C_{comp}\right) - \omega^2 L_{coil}\left(C_{coil} + C_{comp}\right)\right)}$$

Equation 2-47

This causes a frequency dependent gain error and phase shift between the current in R_M and the coil current I_{coil} that generates the magnetic field. The error influence was simulated in LTSpice and is shown in figure 2–15. The gain error is less than 1% across the complete frequency range and zero at DC. The phase shift corresponds to an almost constant group delay of 1.9 µs between coil and current

source current. Both gain and phase error are almost independent from the value of R_M for lower frequencies and only differ at high frequencies in the MHz range. For these high frequencies, also the non-idealities of the operational amplifier (e.g., input capacities) would result in small differences. Since the current generator only operates in the kHz range, these limitations can be considered as irrelevant.

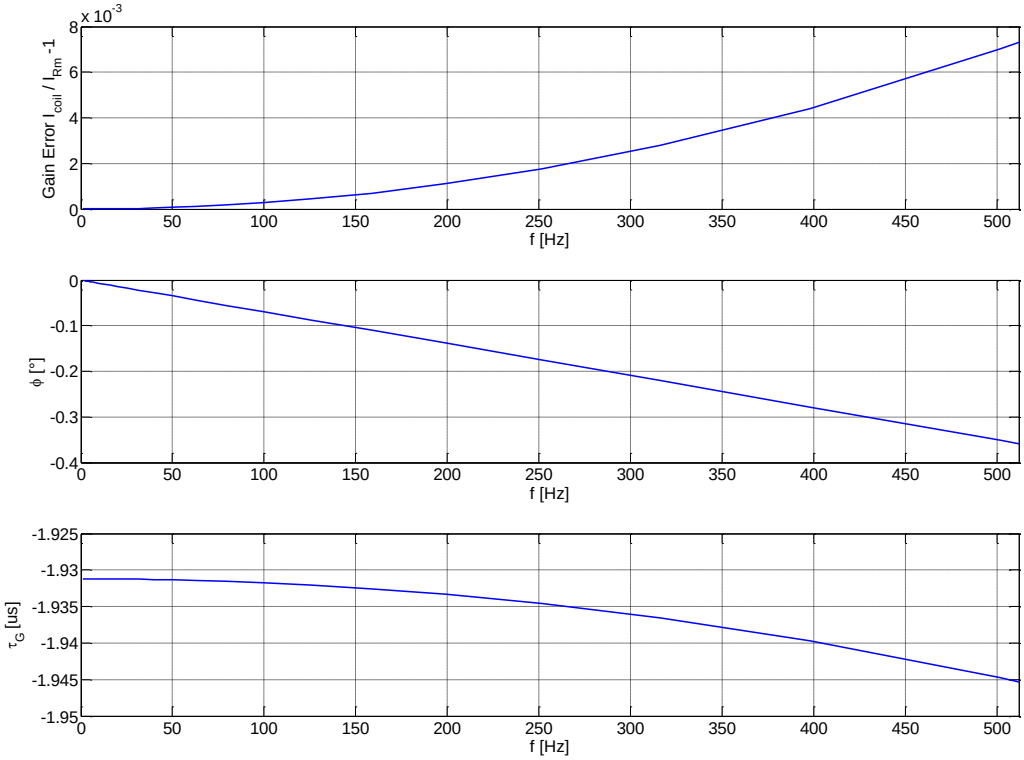

Figure 2–15 LTSpice Simulation of Gain, Phase and Group Delay Error caused by additional Capacitor

A further small circuit was needed for the protection of the current source, since accidental disconnection of the coil, power-off of the current generator or electromagnetic induction in the coil can result in high voltage spikes at the coil terminals. These spikes were suppressed by adding a set of transient voltage suppressor (TVS) and Zener Diodes in parallel to the coil contacts of the current generator. This multi-diode approach was necessary because Zener diodes are too slow to catch the faster spikes or onsets while TVS diodes are unsuitable to suppress higher energies due to their limited thermal capacity. In addition, the Zener diodes also limit the output voltage in case of failure in order to provide protection for the other devices used in the measurement setup.

Current Measurement

The voltage across the resistor R_M is buffered using an instrumentation amplifier and the resulting signal is provided as external current measurement output and forwarded to an ADC for internal current measurement (see figure 2–16).

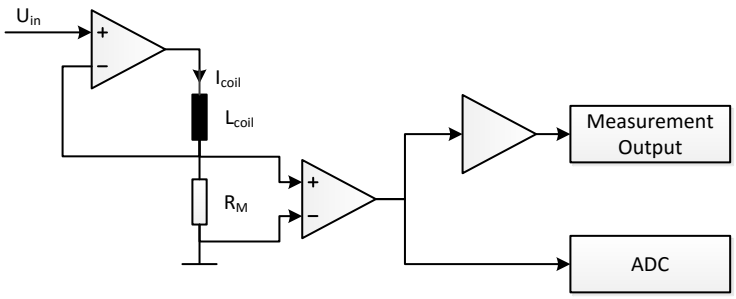

Figure 2–16 Current Measurement within the Current Generator

The measurement output of the current generator was protected using the same combination of diodes used for the coil output.

Power Supplies and Grounding Concept

A precise frequency response measurement also requires high quality supply voltages as well as a well-considered grounding concept. Both supply voltage and grounding can be a major source of noise and distortion.

The amount of induced noise and distortion caused by grounding is directly connected to the grounding topology and the resulting loop area of any cable/connection meshes. The induced voltage in a loop is proportional to the enveloped area (see equation 1-1). It is therefore most beneficial to implement a star-like topology that avoids loops and meshes. If such loops cannot be avoided, cables need to be placed closely to the ground path of the involved pieces of equipment (see figure 2–17) to reduce the loop area.

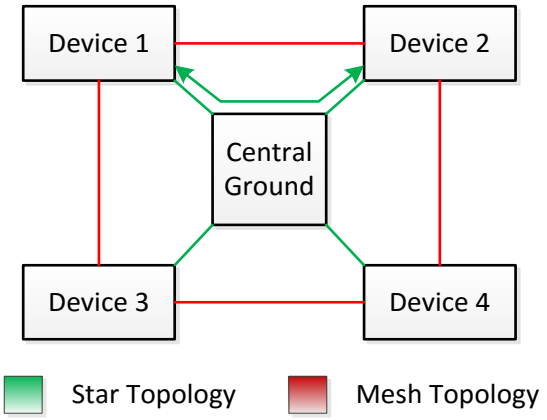

Figure 2–17 Star and Mesh Grounding Topologies

The grounding concept for the frequency response measurements was therefore designed using a star-like topology and one central grounding point with low ohmic connection to the FIELDS central electronics box. All other equipment was only connected to this central grounding point using a single ground connection. Data and signal connections were placed close to their respective ground connections to minimize the size of induction loops. Figure 2–18 shows the application of the star grounding topology in the initial FIT block diagram already presented in figure 2–5. The central point in this star grounding topology is the FIELDS CEB.

The only problematic component in this diagram is the current generator, as it is connected to multiple other devices. Grounding loops can only be avoided if galvanic isolation between the different connections is maintained.

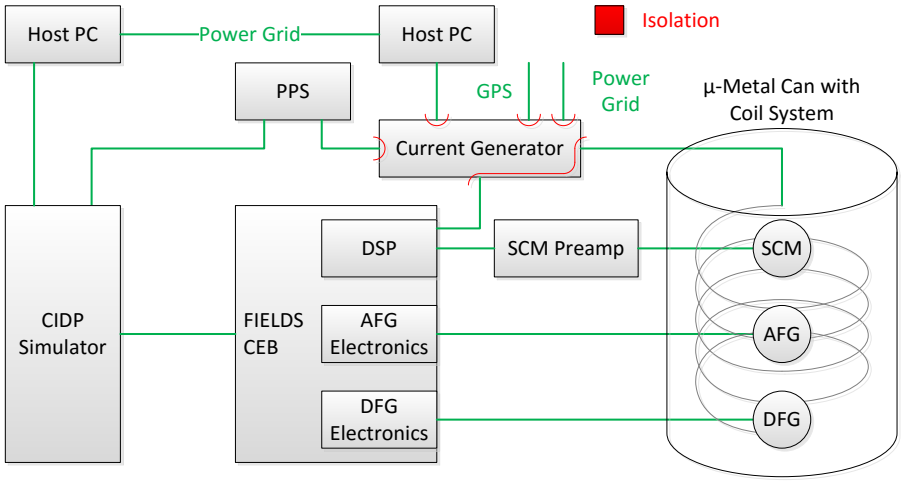

Figure 2–18 Grounding Topology for FIT Measurements

This was already considered during the design phase of the current generator. The different domains of the current generator were therefore isolated using DC/DC converters and high-speed magnetic data couplers (see figure 2–19). With these domains, it was possible to connect to the other devices without creating additional grounding loops. In addition, also conducted emission between analog and digital circuitry was reduced, as only a reduced number of digital components are in the same ground domain as the analog components.

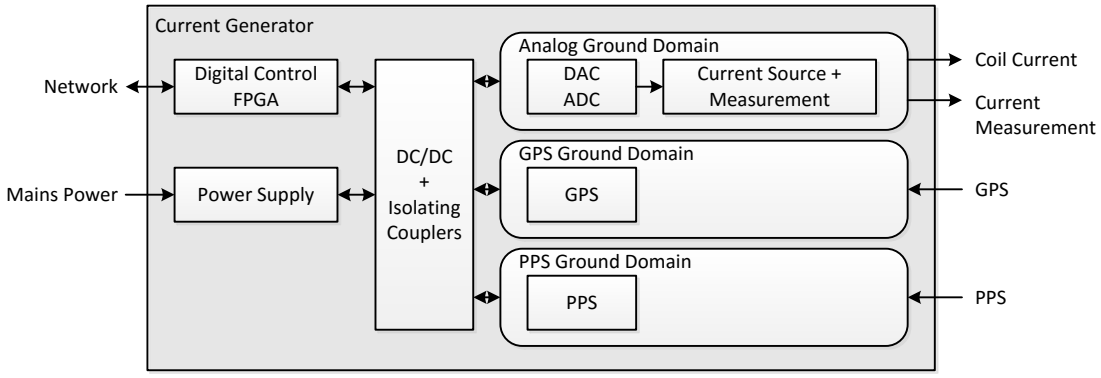

Figure 2–19 Grounding Domains of Current Generator

The disadvantage of this method is the introduction of discrete frequency noise generated by the DC/DC converters which is caused by the switching frequency at 300 kHz. This was mitigated by selecting low noise DC/DC converters and adding buffering capacitors as well as voltage regulators for the analog supply voltages, which attenuate the effects in the measurement bandwidth below the regular measurement noise.

2.2.2.3. Time Synchronization

The synchronization of samples taken by the current generator and the FIELDS instrument suite is essential for determining the frequency response and delay. The available time references during ground testing were the GPS time and the PPS signal.

Although the GPS time could in principle deliver a time signal with very high precision, its practical usability for this project was limited by the artificial limitation in time precision that is implemented in all commercial grade GPS receivers. High time precision can only be achieved by using military GPS receivers, but their price range was definitely above the financial limits of this project and they are also subject to export regulations, leading to significant complication.

In addition, a pure GPS time based approach increases the complexity of comparing data, as data is

not only sampled at different rates, but also time stamped on different time bases (FIELDS PPS and GPS based time). Interpolation of the data to one common equidistant time grid would therefore require building an interpolation filter that compensates both the differences and drift of all involved sampling rates and time bases.
The design of such a filter is dependent on the ratio and time shift between the different clock and time rates. This ratio cannot be considered as fixed, but slowly drifts due to temperature changes. Although this drift is negligible for short measurement times, it must be taken into account for a longer measurement campaign. If the drift is ignored, even a low drift may sum up to a larger error. For a sampling frequency of f_S=2,048 Hz, a low clock drift E_{CLK} of 1 ppm and a measurement duration T_{meas} of 5 minutes, the relative shift between sampling instants could be

$$\Delta N = f_S \cdot T_{meas} E_{CLK} = 2{,}048 Hz \cdot 300 s \cdot 10^{-6} = 0.6144\ samples \qquad \textit{Equation 2-48}$$

Clock rate changes in this order of magnitude could be easily caused by temperature variations of a few degree Centigrade. It would therefore be necessary to re-estimate the required interpolation ratios for every measurement and to create a new interpolation filter for every data set during the FIT campaign. Although this approach would be possible, it is definitely not desirable and was therefore dismissed.

Sampling Clock

A more convenient approach is to synchronize the sampling of the current generator to the FIELDS time stamping using the PPS signal (see 1.1.3.2) and to use GPS time only as a coarse real-time reference. During ground testing, the PPS signal is generated by a high precision signal generator and is available at both the FIELDS instruments and the current generator with negligible time difference. The sampling frequency used for signal generation and measurements of the current generator can therefore be derived from the PPS signal using an all-digital phase locked loop (ADPLL). With this sampling frequency, the sampling of the current generator is synchronous to the time base of the CDPU, but not to the sampling of the instruments.

In general, phase locked loops are used to generate a secondary clock with fixed phase relation to the primary clock using a regulation circuit. The phase of the two clocks is measured and then used as input for the regulator that accelerates or decelerates the secondary clock to match the primary clock, e.g., to generate a clock signal with double frequency. This principle is used in the analog domain (e.g., Tietze et al., 2002, pp. 1155ff) and has also been used in the digital domain with various approaches (Al-Araji et al., 2006)

The current generator ADPLL uses an internal 2^{25} Hz master clock f_{CLK} (roughly 32 MHz) which is used both for operation and for uniformly sampling the PPS signal. Clock interpolation is done using a digital counter that is accelerated or decelerated dependent on changes in the sampled PPS signal.
This method can be classified as a uniformly sampled version of a lead-lag (also called binary quantized) ADPLL, but includes a few modified elements that make it fit for a high interpolation rate.

Figure 2–20 shows the ADPLL realization used in the current generator. It uses two counters, one for the measurement of the clock frequency (counter 1) and the other for generating the interpolated clock (counter 2).

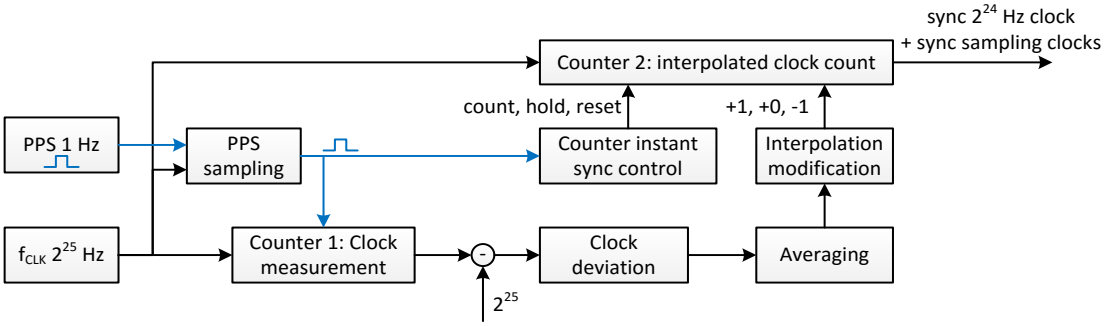

Figure 2–20: Block Diagram of ADPLL

The initial sampling of the 1 Hz PPS signal with f_{CLK} adds an uncertainty of up to one f_{CLK} cycle, as the edge of a PPS pulse might arrive just after sampling.

The master clock drives two counters. The first counter is used to measure the number of master clock cycles between two PPS pulses. Ideally, for a synchronous PPS and f_{CLK} configuration, the result would be 2^{25}. Any deviation from this number gives information about the difference between the two clocks.

The second counter is used as an interpolated phase counter that generates the necessary sampling clocks for the ADCs and DACs by using one of the counter bits as its clock source. The counting rhythm of this counter is modified according to the deviation result of the first counter and is also changed by the arrival of a PPS pulse.

The deviation result of the first counter is averaged over 16 PPS cycles. This averaged value is then rounded down and used to modify the second counter by extending or skipping counting cycles. This is based on the assumption that the clock rate deviation was estimated correctly and predicting that clock rates will change very slowly or not at all. We can, e.g., assume that the first counter delivers a value of 2^{25}+2. For this deviation of +2 cycles, one counting cycle is extended at 2^{23} and $3 \cdot 2^{23}$ (see figure 2–21 upper part). This way the deviation between the ideally interpolated PPS signal and the counter value is reduced to a half master clock period.

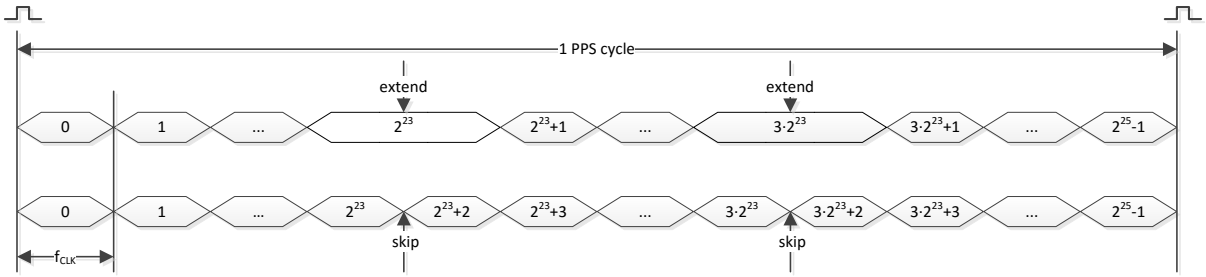

Figure 2–21: Interpolated Clock Counter for Extending (upper part) and Skipping 2 Cycles (lower part)

The presented mechanism quantizes the PPS cycle with a precision of 1 f_{CLK} cycle, using a round-down mechanism. Any deviation below this precision will result in an uncorrected error that is integrated over time and will eventually cause an additional cycle. With a clock rate of, e.g., 2^{25}+0.5 this would produce an alternating series of counter values switching between 2^{25} and 2^{25}+1. This could be used for increasing clock sampling resolution, but this information cannot be used within the ADPLL, as no half clock cycles can be modified. Nevertheless, averaging can be used to reduce the effect of clock jitter. The averaged result is, in turn, simply rounded down so that the counter value typically lags behind the real clock rate.

To catch up with the remaining clock deviation and to track slow drifts, synchronization also needs to be done on the fly. For this purpose, the second counter is paused if the PPS pulse does not arrive at the expected time or accelerated (reset) if the PPS pulse arrives ahead of time (see figure 2–22). This instant synchronization mechanism, of course, causes a larger error, as the distance between the DAC clock and the PPS pulse is integrated over the course of one second and only corrected at the end. To minimize the need for this final instant synchronization, tracking and averaging of the first counter is continued in parallel.

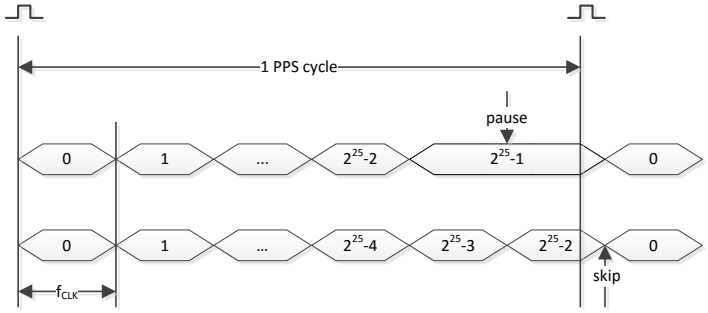

Figure 2–22: Current Generator Instant Clock Synchronization for Late (upper part) and Early PPS Arrival (lower part)

With these mechanisms, it is possible to create a counter that delivers an interpolated version of the PPS signal. The generated clock has a fixed deviation from the PPS signal that is defined by the processing delay of the ADPLL, which is subject to limitations in digital design resources (e.g., number of available clock networks). In the actual implementation, this delay was 4 f_{CLK} cycles or 120 ns.

In addition to this delay, there are clock deviations, often referred to as jitter. The sampling of the PPS cycle results in an uncertainty of one f_{CLK} cycle. The extension/skip mechanism can cause another half f_{CLK} cycle. In addition, the mapping of a clock deviation to an extension/skip pattern can create a small jitter, as inserting/skipping is only possible at discrete clock cycles. The possible error of this mapping is the total number of deviation cycles divided by 2^{25}, which is the amount of PPS deviation normalized to one f_{CLK} cycle. The overall worst-case jitter is therefore between 1.5 and 2 f_{CLK} cycles.
However, all of these jitter considerations are only valid for pseudo-static clock relations. As soon as clock rate changes are too large, clock synchronization mainly happens based on instant synchronization, which causes much larger jitter. Fortunately, these kinds of fast clock changes are only possible during initial equipment warm-up phases and can be mitigated by merely switching on equipment at a set time before testing.

The generated synchronization jitter is not the same as the usual randomly varying jitter, which is typically a normal distribution around the ideal sampling time, caused, e.g., by thermal noise within a quartz clock. Synchronization jitter is an accumulating time shift that persists for a longer time and parts of the signal are shifted by the currently accumulated value. The resulting amplitude error is defined by the maximum change of amplitude within the jitter time, but due to the longer persistence of the error, the resulting error energy can be larger than pulses generated by conventional jitter.

This kind of jitter is pseudo-periodic, as a fixed ratio between master clock and PPS would result in a periodic signal. In reality, this ratio is slowly drifting (e.g., due to temperature variation) and periodicity might not appear at all or last only for a few periods.
The error caused by synchronization jitter should therefore not be considered as noise, but as a synchronization distortion signal.

The impact of this synchronization distortion can be analyzed by calculating the possible amplitude error. This maximum error is generated with a sine with maximum signal frequency (512 Hz) and an amplitude of ±0.5 full scale (FS). It appears around the zero crossings of this signal. With a jitter time of

$$t_{jitter} = 1.5 \cdot 2^{-25} s \qquad \textit{Equation 2-49}$$

the amplitude error is

$$E_{sync} = 0.5 \sin\left(\omega_{max} \frac{t_{jitter}}{2}\right) = 36 \cdot 10^{-6} FS \qquad \textit{Equation 2-50}$$

Relative to the full-scale value FS, this error can be expressed in the form of an effective distortion free bit-resolution of

$$\log_2 E_{sync} \approx 14.76\ bit \qquad \textit{Equation 2-51}$$

This distortion free bit-resolution was calculated for the worst-case scenario. In the FIT application, the amplitude of the signals was reduced for higher frequencies (see chapters 2.2.4 and 2.3.3) and so the distortion from the jitter and the synchronization was well below the 16-bit resolution.

In general, synchronization distortion could be reduced by using a higher base clock f_{CLK}, but this is in turn limited by the type of FPGA type and the complexity of the FPGA module design. High clock speeds and multiple clock domains result in design restrictions that allow less flexibility for module placement and result in lower possible utilization of FPGA resources.

In addition to the effect of the jitter on conversion time, also conversion mechanisms in the ADCs and DACs need to be able to cope with these clock variations that are much bigger than the usual jitter of quartz oscillators (see chapter 2.2.2.4).

Time Synchronization

In addition to clock synchronization, the current generator also provides an internal real-time 24-hour clock for time stamping of samples as well as the occurrence of synchronization signals.

This real-time clock can also be synchronized to external clock sources using the same mechanism as used for conversion clock synchronization. It is possible to select one of three different synchronization sources: GPS time, PPS time and internal time. If external synchronization is used (GPS or PPS), the expected time at the next sync impulse is calculated and set at the arrival of the sync pulse.

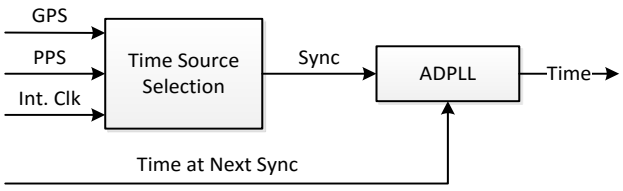

Figure 2–23 Real-Time Clock Synchronization of Current Generator

The internal real-time source uses the internal clock frequency and receives initial time synchronization via Ethernet by a support PC or by GPS.

GPS time is acquired using an IT321 integrated module[21] which is delivering both a time message and a one second time tick. The time tick is delivered at the full second with a precision of ±1 µs relative to the GPS time standard, while the time message arrives within 100 ms after the tick and gives the full GPS time at this tick. As this message is given in human readable format, a conversion to a common binary format (e.g., Unix time or TT2000) would require knowledge about leap seconds or years. As this would increase complexity in the software and would also require regular updates for leap seconds, it was decided to reduce the clock range to 24 hours and use additional date information added by the support PC. This additional date information is only added during data saving. In principle, also a network time server could be used for synchronization, but this was not implemented in the software. If the absolute time is not provided via GPS, initial time synchronization can also be provided by the support PC.

2.2.2.4. Analog to Digital and Digital to Analog conversion

The desired current signal is provided as a digital waveform via the host PC. This waveform is then converted to an analog voltage that is fed into the current source. The generated current is measured and converted to a voltage, which is then converted back to digital values that are in turn provided to the host PC.

The process of conversion from digital to analog domain and back is influenced by clock jitter. The effect of this jitter on timing and amplitude is dependent on the converter architecture actually used and is discussed in the following paragraphs.

Digital to Analog Conversion

The main criteria for selecting the digital to analog convert (DAC) were a matching signal-to-noise ratio (see 2.2.1) and the ability to cope with the large jitter of the synchronized clock (see 2.2.2.3).

The DAC that was chosen for this purpose is the 16 bit DAC8831ICD from Texas Instruments[22], which is based on an R-2R network. This architecture does not use sub-clocks and is therefore impervious to clock jitter. In addition, this DAC achieves better than 15 bit accuracy for all common DAC quality measures as well as low drifts over large temperature ranges. Although an accuracy of 15 bit may appear low in this day and age, a more detailed examination reveals that most modern 24 bit DACs are only better in some aspects and cannot achieve better quality across the full parameter range.

The low temperature drift of 0.1 ppm/°C allows combining two DACs to a cascade, using a secondary DAC with lower range as compensation (or even range extension) for the primary one. This requires a high precision ADC for calibrating the DACs. Although this possibility was foreseen in the design, initial tests showed that the added precision was not necessary for frequency response measurements and it was therefore deactivated.

[21] IT321 data sheet, revision 1.2, retrieved 2009, no longer available in 2018 due to acquisition of fastrax by u-blox; SIRF NMEA Reference manual for IT321, revision 2.2, last retrieved 2018/03/08, https://www.element14.com/community/docs/DOC-13410/l/sirf-nmea-reference-manual

[22] DAC8831 data sheet revision SLAS449D, last retrieved 2018/03/08, http://www.ti.com/product/DAC8831

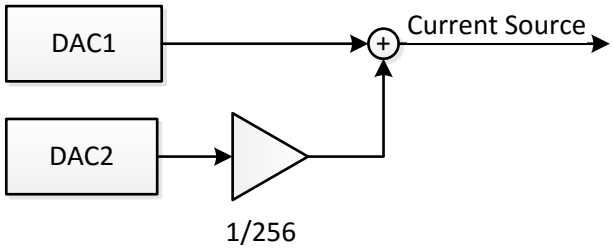

Figure 2–24: DAC Cascade for Improved Resolution

DAC timing is mainly defined by the settling time which is specified with 1 µs for a full scale jump. As this settling time is mainly used for loading parasitic capacities, the settling time for lower jumps (at lower frequencies) is within the few 100 ns range and therefore sufficient for the desired timing accuracy.

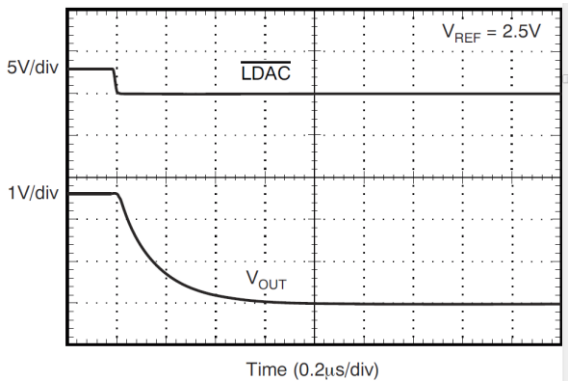

Figure 2–25: Settling Time of DAC8831 Output (DAC8831 Data Sheet, Revision SLAS449D)

The DAC is using a zero order hold output stage which keeps the output value constant until the next value is set. This stage is impervious to jitter and the generated synchronization distortion is therefore equal to the one given in equation 2-51.

Analog to Digital Conversion

Most current high precision analog to digital converters (ADCs) with sampling frequencies in the kHz range are sigma-delta ADCs. Typically used resolutions are 24 bit, although the overall measurement precision, including temperature drift, is usually more in the 14-16 bit range. Higher precision ADCs are possible (see calibration ADC in this chapter), but are limited in sampling frequency.

Using the sigma-delta conversion principle with the current generator's synchronized clock requires special consideration, since this type of ADC uses switched capacitor input stages. These stages are built on charge balancing and are therefore more sensitive to jitter. Since the implementation of these stages is different for each ADC type, the effect of jitter must be assessed for the actually selected ADC.

The selected ADC was the ADS1271[23] built by Texas Instruments with an overall quality of roughly 16 bit, excluding the expected temperature drift. The current generator operates this ADC at a synchronized clock frequency of 2 MHz that results in a sampling rate of f_S=4,096 Hz.

[23] ADS1271 data sheet, revision SBAS306F, last retrieved 2018/03/08, http://www.ti.com/product/ADS1271

The switched capacitor at the input of this ADC is charged and discharged for an integration time that depends on this sampling frequency (from data sheet).

$$t_{int} = \frac{2}{f_S \cdot 512} \qquad \textit{Equation 2-52}$$

The jitter caused by the ADPLL causes not only a synchronization distortion signal in the ADC (see 2.2.2.3), but also a variation in the integration time. In a first approximation, the charging process of a switched capacitor can be considered as linear, as it does not approach exponential saturation. With this linearization, the charging process can be replaced by voltage averaging over the charging time.

$$U_{avg} = \frac{1}{T_{avg}} \int_0^T u(t)dt \qquad \textit{Equation 2-53}$$

The worst-case error is in this case generated by a constant signal at +0.5 full scale (FS). In this case, the error in the integrated voltage is:

$$E_{sync} = 0.5 \frac{t_{int} + t_{jitter}}{t_{int}} - 0.5 = \frac{t_{jitter}}{2t_{int}} = 1.5 \cdot 2^{-6} FS \qquad \textit{Equation 2-54}$$

This error is then reduced by downsampling the oversampled data by a factor of 128.

$$E_{sync\ downsampled} = 1.5 \cdot 2^{-13} FS \qquad \textit{Equation 2-55}$$

Relative to full scale, this error caused by the ADPLL jitter can be expressed as a reduction of effective resolution to

$$\log_2 \frac{E_{sync}}{1} = 12.4\ bit \qquad \textit{Equation 2-56}$$

This error will generate short spikes in the sampled signal and is added to the regular synchronization distortion from synchronization. These spikes have an impulse length of one 4,096 Hz sample and are therefore outside of the bandwidth of interest. Also here, the calculation was done for the worst case of a synchronization happening during the charging cycle while the signal has full scale value.

For calibration purposes, an additional LTC2410[24] ADC was used. This low speed and high precision ADC runs asynchronously and can therefore only be used for DC calibration of both ADC and DAC. It achieves an analog precision of more than 18 bit in all parameters, including integral nonlinearity and temperature drifts.

2.2.2.5. Temperature Measurement

The case temperature of the current generator is monitored during operation using a PT100 temperature dependent resistor in a Wheatstone bridge and an LTC2410 ADC. This was done to identify phases with high temperature drifts, which would result in changes of the quartz clock frequencies in the ppm range. During the measurement campaign, it turned out that only initial warmup drifts are relevant and the changes during operation phases are not large enough to cause relevant clock drifts. It was therefore decided to switch on the current generator at least 30 minutes before measurements to ensure a stable operating temperature of around 35°C at a room temperature of 20°C.

[24] LTC2410 data sheet, last retrieved 2018/03/08, http://www.linear.com/product/LTC2410

2.2.2.6. Digital Part

The digital functionality of the current generator was implemented using a GR-XC3S-1500 field programmable gate array (FPGA) development board from Pender Electronics/Gaisler[25]. This board is designed to support the development of modular processors within FPGAs. It features a Xilinx XC3S-500 FPGA and peripheral components that support the development of embedded systems. Analog functionality was added using a piggyback board placed on the external connectors (I/O) of the FPGA board.

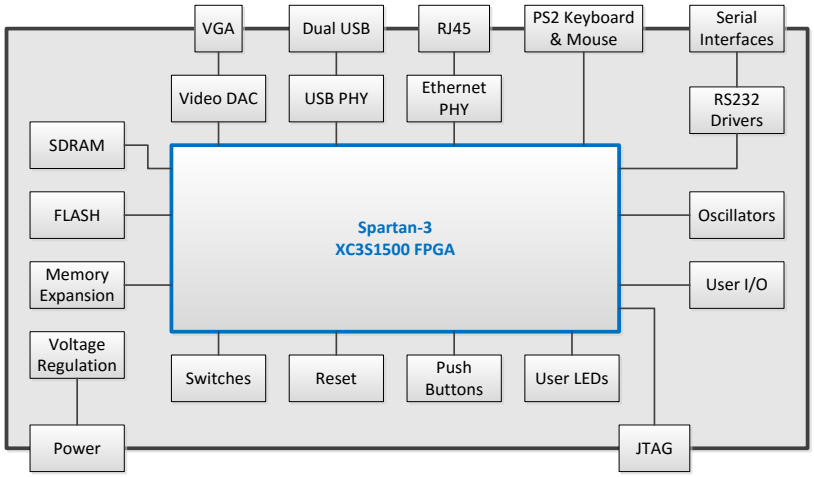

Figure 2–26: Block Diagram of GR-XC3S-1500 Development Board

The current generator FPGA design is based on a softcore library by Gaisler Research[26]. This library provides the Leon3 Sparc V8 processor as well as predefined modules for all the peripherals and memories of the development board. Additional user-defined modules can either be directly connected to these modules or attached to the on-chip bus (Advanced Microcontroller Bus Architecture AMBA). The AMBA bus provides two interfaces for additional components, the AMBA host (AHB) and peripheral bus (APB). The host bus is typically used for applications with high data rate, as it provides bus-master direct memory access (DMA). The user-defined modules of the current generator were attached to the APB, as data rate is limited and communication overhead was reduced using buffering within the modules.

[25] Gaisler/Pender GR-XC3S-1500 development board, last retrieved 2018/03/08, http://www.pender.ch/products_xc3s.shtml

[26] Leon3 Processor and GRLIB IP library by Gaisler Research (currently Cobham Gaisler), version 1.0.21-b3848, this obsolete version was removed from http://www.gaisler.com/index.php/downloads/leongrlib

An overview of the functional blocks and relevant connections is given in figure 2–27. Although this diagram shows many blocks, only the ones marked in red were implemented during this work and are explained briefly in the following paragraphs. All other modules can be found in the GRLIB IP reference guide.

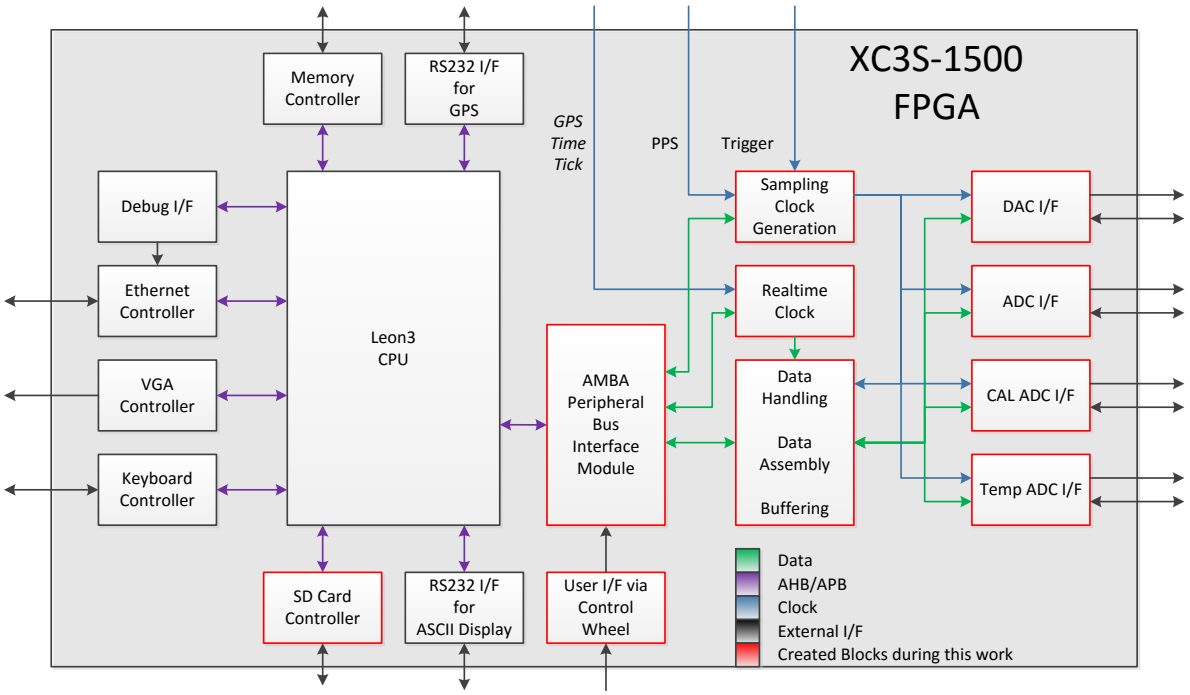

Figure 2–27 Functional Blocks within the FPGA

General FPGA Considerations

FPGAs use special clock networks ("trees") for distributing clocks within the chip. These networks are optimized for low latency, but their number is limited. The design of the current generator required many different clock signals like the GPS time tick, the PPS signal and the various sampling clocks of ADCs and DACs. It was therefore necessary to switch from asynchronous clock networks to synchronized clocks using logic state signals, thus using a lower number of clock trees.

All incoming clock signals are sampled using the master clock and converted to synchronous logic state clocks. All logic circuits that use additional clock signals (blue lines in figure 2–27) are operated using the master clock, but logic state updates are only permitted after a 0/1 transition of the respective synchronous logic state clocks.

Using this method, logic state changes are still dependent on the relevant clock, but happen synchronously to the master clock. This allows the use of multiple independent clocks without using up all the clock trees. This introduces a known delay and a jitter, as both clock sampling as well as detection of the 0/1 transition requires some time. The delay is roughly 30 ns per FPGA clock cycle and the jitter is up to 30 ns. As the initial time precision target is in the µs range, both jitter and delay delay are considered acceptable.

Sampling and Real-time Clock

The functionality presented in chapter 2.2.2.3 is implemented within these modules. In addition, these modules provide time tags for the PPS signal as well as the clock offset and drift values per PPS cycle. These values are then used for averaging and slowly adapting the added/subtracted cycles to clock drifts using software. Furthermore, these values are forwarded to the host PC for storing.

This module also includes a trigger module that is used to control the start of the actual sampling

operation. Sampling is started at the next PPS pulse after the trigger was armed by software or using a hardware button.

ADC and DAC interfaces

These interfaces take care of the various types of serial communication used by the ADCs and DACs. In addition, the sampling clock is reduced to the clocks needed for (over)sampling and communication. This interface provides measurement data at a rate of about 544 kbytes per second.

Data Handling, Assembly and Real-time Data Buffering

This module provides data to the DACs and takes care of assembly and time stamping of ADC and DAC data samples. Although DAC output and ADC measurements happen simultaneously, this data is not available at the same time due to processing times. The data-handling module uses intermediate buffering to collect the associated DAC and ADC samples as well as their time stamps to one data packet. The assembled sample packet is then buffered again and delivered to the processor in groups of 8 to 16 packets using interrupt-based communication.

SD-Card and User Interface

In combination with the serial ASCII display, these modules provide the basis for stand-alone operation. The user interface records the signals of the control wheel and passes them on to the software. The SD card interface is operated using the royalty-free serial peripheral (SPI) communication mode and provides a hardware basis for storing and retrieving data.

Although these interfaces are present in hardware, they were not used in the software version employed for MMS tests, as VGA screen, keyboard and network interfaces provided sufficient functionality to control the current generator. Figure 2–28 shows a screenshot taken during one of the MMS tests.

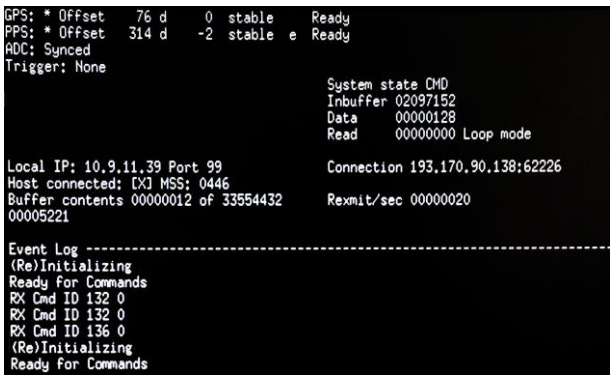

Figure 2–28 VGA Output of MMS Current Generator

2.2.2.7. Software

The higher-level functions of the current generator are controlled using software running on the Leon 3 processor. This software was written in C and uses simple state machines. An operating system was not considered due to the simplicity of the software and the fact that real-time operation with operating system usually requires higher effort. The main functionality blocks are shown in a simplified block diagram in figure 2–29. This block diagram only shows the main data path from current input and output samples, as an exact representation of all data paths would result in a quite confusing block diagram.

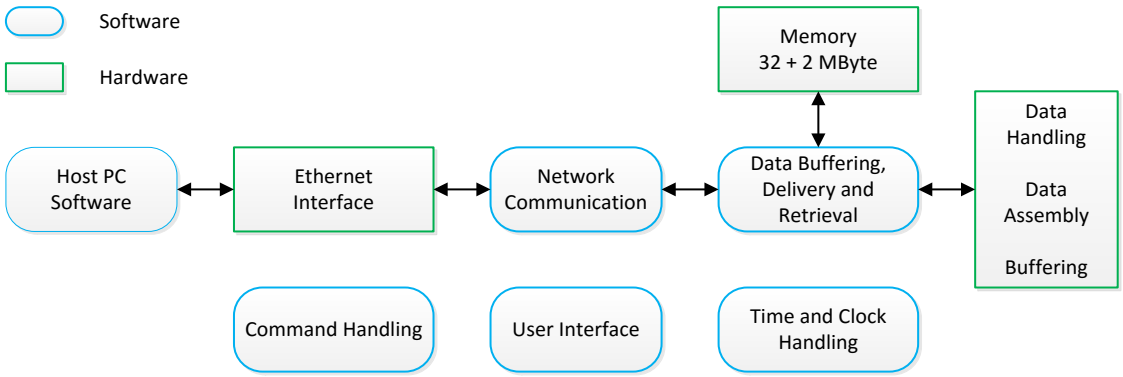

Figure 2–29 Current Generator Software Modules

Time and Clock Handling

The averaging of clock and time deviation is handled in software, as it only happens every second and is therefore not time critical. Furthermore, handling this in hardware would use valuable resources (e.g., the number of adders within an FPGA is limited). In addition, the control loop of the ADPLL can be adapted in software which requires considerably less effort than adapting FPGA firmware.

The software routines also take care of the initial synchronization and provide a warning message if the clock drift increases during operation. Furthermore, the time at the next sync pulse is calculated dependent on the selected time source (PPS or GPS time). If the internal time source is used, no time update is provided. Information about the clock rate variation is provided in housekeeping data.

Data buffering, delivery and retrieval

These routines manage the retrieval and delivery of samples from and to the hardware buffers. This data is composed of current measurement samples, the corresponding output waveform samples as well as measurements of the temperature. The handling of these samples must be done with real-time priority to avoid overflow or empty buffers. It is therefore done using interrupt-based communication that triggers the software routines before such problems can occur. Buffer handling on the network side is done using a normal round-robin scheme.
The allocated memory buffer size for measurement data is 32 Mbytes which is enough for about one minute of data. The buffer for waveform data uses 2 Mbytes of memory which is equivalent to about two minutes of output data. The output data buffer can be operated in loop configuration to repeat the output waveform. The fill status of the buffer is provided as housekeeping data via network and user interface.

Command Handling Module

Command handling interprets the commands received via user and network interface, triggers the required reactions and provides feedback about the executed commandos on both interfaces. Basic commands are, e.g., starting/stopping of signal generation, resynchronization and buffer clearing.

User Interface

The user interface software controls the text mode VGA display and a keyboard interface. Information about the current operation status, such as buffer fill status, network status or clock synchronization, is provided on the VGA display.

Network Communication

During normal operation, the current generator is controlled using a host PC. Data communication to this PC is handled using a TCP/IP connection. The current generator acts as a server that provides a data stream to the connecting client PC and accepts commands as well as input waveforms. Input waveforms can only be uploaded in inoperational mode before the start of a measurement. During a measurement, all data as well as status information is provided to the support PC in buffered real-time communication. This means that measured data is provided to the support PC as fast as possible, but data is buffered if communication is too slow.

TCP stack handling was done using the open source micro-IP stack (uIP[27]) which is optimized for small processors and memory footprints. Although this choice was not optimal for speed reasons (see below), the achievable data rate was high enough to support longer measurement times with intermediate buffering of unsent data.

The TCP protocol handled by the uiP stack uses bidirectional communication to acknowledge the arrival of each packet at its destination. The uIP stack only permits one unanswered packet ("in-flight" packet) and therefore waits for an acknowledge message before sending another packet.
This behavior limits the data rate, as packet sending is limited by the network latency (also called "ping"). This latency consists of the actual latency caused by low-level network communication and the processing time that is needed by each of the systems to handle and answer the involved packets. For low-end architectures (such as the current generator) this latency is typically in the order of 10-30 ms. This results in a packet rate of less than 100 packets per second. Together with the maximum segment size (MSS) of 1500 bytes per network packet, this results in a maximum data rate of roughly 150 Kbytes/second.

In addition to this primary limitation, there are further issues resulting from another speed optimization present in most TCP stacks which is the TCP delayed acknowledgement technique (RFC 1122[28]). The TCP delayed acknowledgement technique tries to reduce the protocol overhead of acknowledge messages by gathering them for 200 to 500 ms, dependent on the operating system, and sending all of them in one collective packet.

In combination with the single in-flight packet limitation of the uIP stack, this means that packets are only acknowledged after this time and data throughput would be limited even more. Fortunately, most modern operating systems allow deactivating delayed acknowledgment per application or even globally.

With immediate acknowledgement and a direct cable connection, it was possible to increase the data rate to roughly 450 Kbytes/second which means that some data could not be transferred as fast as it was generated and the internal buffers were slowly filled. This resulted in a limited measurement time of about 5 minutes until buffers were full. Fortunately, this time was more than enough for the measurements required for MMS.

[27] uIP TCP/IP stack, version 1.0, last retrieved 2018/03/08, http://dunkels.com/adam/software.html https://github.com/adamdunkels/uip
[28] RFC1122, last retrieved 2018/03/08, https://www.rfc-editor.org/info/rfc1122

For future applications, data transfer could be improved by using the lightweight IP stack (lwIP[29]) which supports a higher number of in-flight packets. This stack was already tested during this thesis, but the change was not applied since the current generator was already in use.
Even with this higher number of in-flight packets, another common speed optimization technique will interact with communication: Nagle's algorithm (RFC 896[30]). This algorithm tries to reduce protocol overhead by combining TCP packets until the maximum segment size (= maximum packet size on network) is reached or until all in-flight packets have been acknowledged. This reduces the number of sent packets, the overhead by the packet header and the effort for the handling of packet lists. Also this algorithm is present in most modern operating systems.

Together with delayed acknowledgement and a limited number of in-flight packets, this may again put a limitation on the data rate, as the allowed number of in-flight packets might be reached before the delayed acknowledgements are released. As a result, the application of delayed acknowledgement, Nagle's algorithm as well as the number of in-flight packets needs to be optimized for high throughput without creating large memory requirements for buffering.

A possible alternative is the use of UDP instead of TCP, which does not use acknowledge packets for data transfer at all. The disadvantage of UDP is that data completeness and packet order is not guaranteed and has to be handled on application level, which would increase the complexity of the software. The idea of using UDP was therefore dismissed.

Host PC Software

The software on the host PC was written in LabVIEW by a colleague (see chapter D). It is therefore not part of this thesis and was only added for the sake of completeness. The software is responsible for commanding, status information and data saving. The available measurement data of the current generator is displayed to support preliminary analysis of the noise floor. Figure 2–30 shows a screenshot of the software.

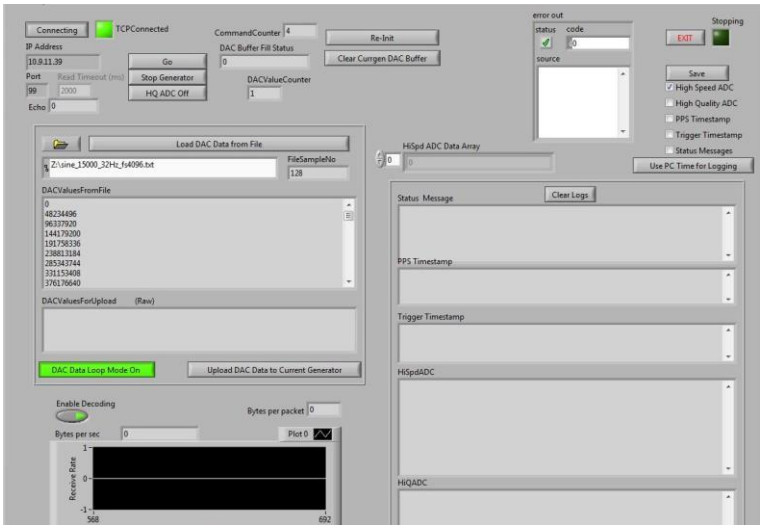

Figure 2–30 Screenshot of Current Generator Host PC Software

[29] lwip TCP/IP stack, version 1.4, last retrieved 2018/03/08, http://dunkels.com/adam/software.html http://savannah.nongnu.org/projects/lwip/
[30] RFC896, last retrieved 2018/03/08, https://www.rfc-editor.org/info/rfc896

2.2.3. Sensor Configuration

The sensors of all three instruments were mounted one above the other on a nonmagnetic rack (figure 2–31). This rack was then placed in a 3-layer µ-metal can with an included solenoid coil (figure 2–32). The sensor mounting plates of the rack were tilted by about 45° so that every sensor axis was able to measure the magnetic field with almost identical amplitude. The remaining amplitude difference by orientation can be neglected, as the target of the measurements is not the absolute gain but frequency dependent changes of the gain.

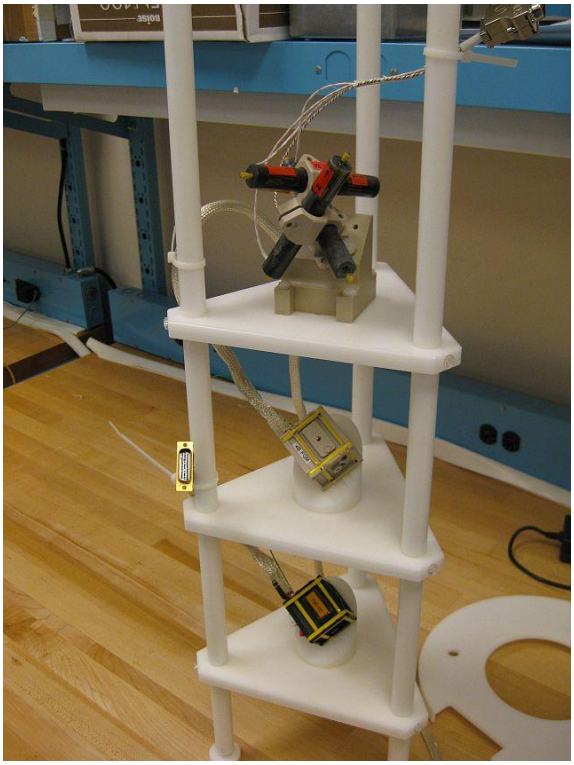

Figure 2–31 MMS Sensor Test Rack with SCM (top), AFG (center) and DFG (bottom)

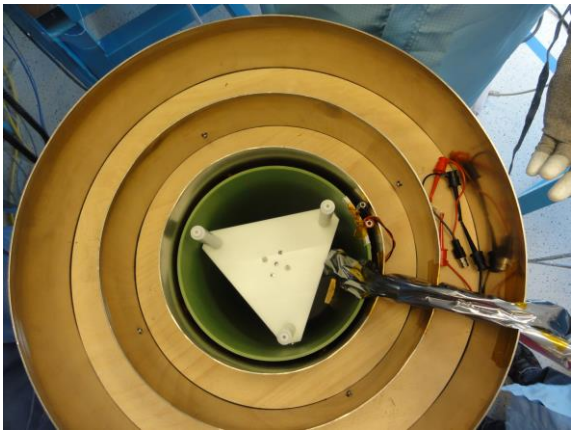

Figure 2–32 µ-Metal Can with Solenoid Coil and Sensor Test Rack

Since the generated magnetic field of a solenoid coil is most homogenous at the center of the coil, the sensors closer to the top and the bottom are exposed to a less homogenous field. However, since this homogeneity condition is not dependent on frequency and only results in a different absolute amplitude, also this effect can be neglected.

2.2.4. Test Signals

The quality of the frequency response determination is dependent on the signal-to-noise ratio (SNR) across the complete bandwidth. This SNR is in turn dependent on the instrument noise as well as the instrument gain, which both vary over frequency. The noise equivalent magnetic induction (NEMI) plot in 1.2.1 already includes the instrument gain and the SNR can therefore directly be found by relating the NEMI to the amplitude of a magnetic field test signal.

Figure 2–33 shows the change in SNR of SCM and DFG when using sine test signals with constant field amplitude. For the SCM, the SNR change reaches 110 dB at 512 Hz when taking the reference point of 0 dB at 30 mHz. The SNR of DFG changes by less than 20 dB.

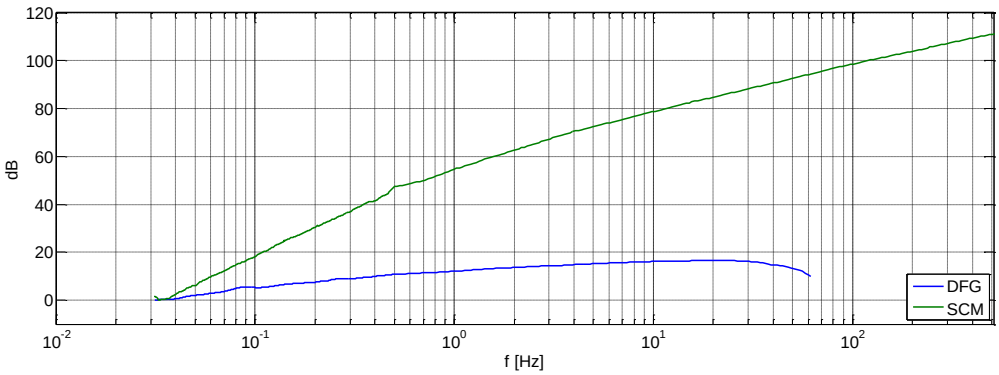

Figure 2–33 Variation of DFG and SCM SNR with Constant Amplitude Sine Signals

While using a constant amplitude signal is acceptable for DFG, using the same signal would result in a problem at the analog output of the SCM. The sensitivity of the SCM changes with the same curve as the SNR and therefore the dynamic range of the output signal would also be 110 dB. This dynamic range is opposed by the dynamic range of the 16-bit ADC used in the DSP (Ergun et al., 2016) which is only 96 dB. It is therefore necessary to reduce the dynamic range by scaling the test signal amplitude with frequency. One possibility is to scale this amplitude with the inverse SNR curve from figure 2–33. This would result in constant SCM analog amplitude as well as a constant SNR.
Unfortunately, this merely shifts the problem of the high dynamic range to the current generator which would then require a dynamic range of 110 dB or even more, if higher SNR were desired. Frequency dependent test signal scaling should therefore depend on the dynamic range and SNR of both instruments and current generator.

The frequency dependent scaling of sine test signals can easily be established, since sine testing is done using one frequency at a time (see chapter 2.3.3). It is therefore possible to change both the current generator output range and the digital test signal amplitude. With this scaling, a total signal range of approximately 120 dB can be covered by changing the amplitude of the test signal (~80 dB) and by switching the hardware ranges (another 40 dB). This results in a worst-case SNR of 10 dB for the frequency range from 30 mHz to 512 Hz.

For spectrum based and parametric estimation, all frequencies are applied at once and the switching of hardware ranges is impossible. Pink noise is a test signal that establishes an acceptable trade-off between SNR and dynamic range. This signal is generated by filtering white noise with a pink noise filter approximation (Smith, 2011, chpt. synthesis of 1/F Noise). This filter decreases the power of the noise inversely proportional to the frequency by scaling the noise amplitude changes with $1/\sqrt{f}$. For the frequency range of 0.05 to 512 Hz, the noise amplitude changes by about 40 dB, which means that the remaining current generator SNR is roughly another 40 dB. The overall SNR for a test with this signal is shown in figure 2–34.

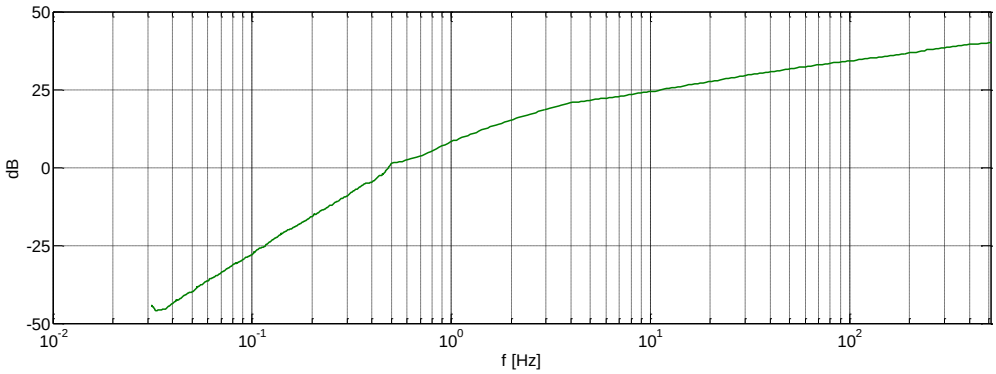

Figure 2–34 Variation of SCM SNR with Pink Noise Signal

A positive SNR can therefore only be guaranteed down to 0.5 Hz which is roughly the cutoff frequency of the SCM DC removal filter. The SNR for lower frequencies is negative and measurements can only be done with averaging, which reduces the noise floor.

In addition to pink noise filtering, all noise signals were also filtered to the necessary bandwidth for the test, i.e., to the Nyquist rate of the different data products at 4, 8, 16, 64 and 512 Hz as well as for a special test with 1,024 Hz. This was done using a 16,385-tap sinc filter with the desired cutoff frequency.

The test signals were generated at the current generator sampling frequency of 4,096 Hz and stored in waveform files. Sine data was designed to be used in a loop by cutting at zero crossings. Also pink noise data was used in a loop; therefore, special handling of the beginning and end of the data was required to avoid jumps. This was done by filtering three consecutive copies of the raw white noise signal with the pink noise and band limitation filter. The center copy was then used as output waveform signal. This approach avoids jumps when the waveform is played in a loop.

2.3. Measurement Campaign

2.3.1. Verification of Current Generator

The properties of the current generator were measured using different test signals and timing sources. figure 2–35 shows the spectrum of the current measurement output while the generator was operated with a 32 Hz sine with 1.87 V peak, which is a little less than half the output range of ±4.096 V.

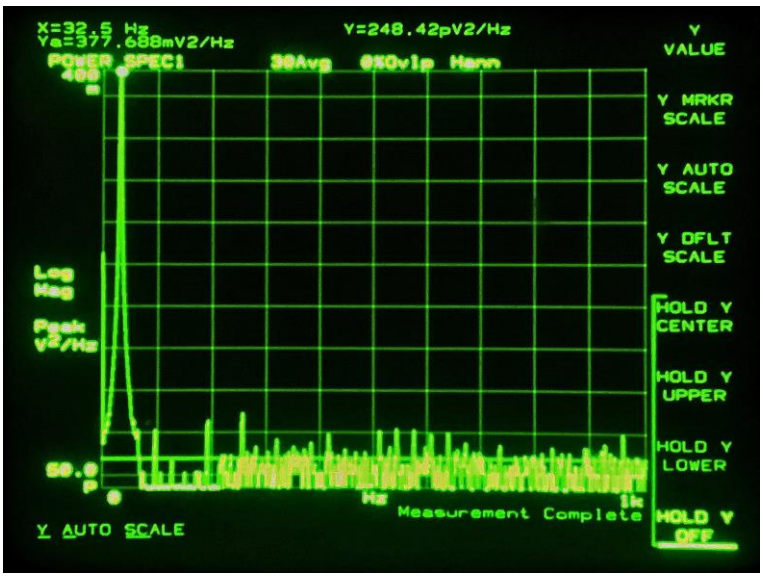

Figure 2–35 Noise of Current Measurement Output for 32 Hz Sine Output in the Frequency Band 0-1kHz

The signal-to-noise ratio in the bandwidth below 1 kHz can be approximated using an estimated average noise floor given by the marker line in figure 2–35.

$$SNR = \frac{P_{Signal}}{P_{Noise}} = 10\log_{10}\frac{(1.87\ V)^2}{248.42 \cdot 10^{-12}\frac{V^2}{Hz} \cdot 1000\ Hz} = 71.48\ dB$$

Equation 2-57

With a full-scale sine output signal, this SNR would improve by another 6 dB to roughly 78 dB. This corresponds to a noise-free resolution of 13 bit (assuming no headroom and a crest factor of 1), which is a little more than the predicted jitter-free resolution of 12.4 bit (see chapter 2.2.2.4).

The worst-case ratio between signal and distortion amplitude is 80 dB at the 8th harmonic of the test signal (at 256 Hz) and roughly 92 dB on average. With this distance, both sine and noise based measurements can be conducted with sufficient quality.

The timing of the current generator was verified by comparing the DAC output and the current measurement to a PPS tick using oscilloscope measurements. Figure 2–36 shows the PPS tick (blue, channel 2), the DAC output (green, channel 4) and the current measurement (pink, channel 3). The delay between the PPS tick and the output signals is approximately 1.5 µs or 50 clock cycles of the current generator. This delay is composed of the digital delays in clock synchronization as well as the DAC delay.
The analog transient response is caused by the anti-aliasing filter of the DAC. This response does not influence the measurements, as all later modeling processes are based on the real current delivered by the current measurement output.

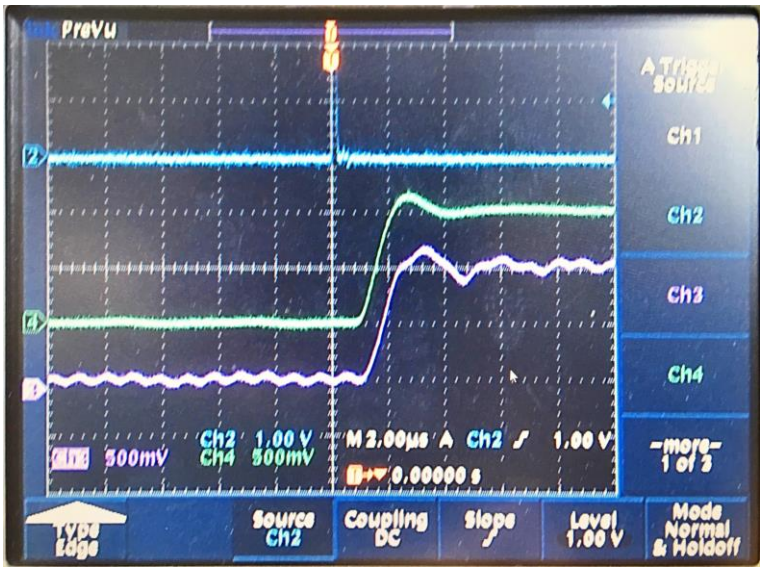

Figure 2–36 Timing Accuracy of Current Generator

Figure 2–37 shows a transfer function measurement of the current generator between the DAC output data and the current measurement data. This transfer function was calculated using equation 2-30 with Welch's method using 16,384 FFT points. Gain and phase were corrected for the influence of the DAC anti-aliasing filter, the zero-order hold characteristic of the DAC and the ADC delay. The gain and phase delay are flat within the required tolerances (see chapter 1.3) and the ADC measurements roughly confirm the 1.5 µs delay of the DAC output.

The increased variance in phase delay towards lower frequencies is a general property of phase delay calculation, as an almost constant phase noise is scaled by the division with the frequency in the phase delay calculation (see equation A-7). Thus, the standard deviation for lower frequencies becomes higher than that at high frequencies.

The presented result only gives the transfer function of the current measurement. The coil current itself is in addition changed by the bypass capacitor as shown in figure 2–15.

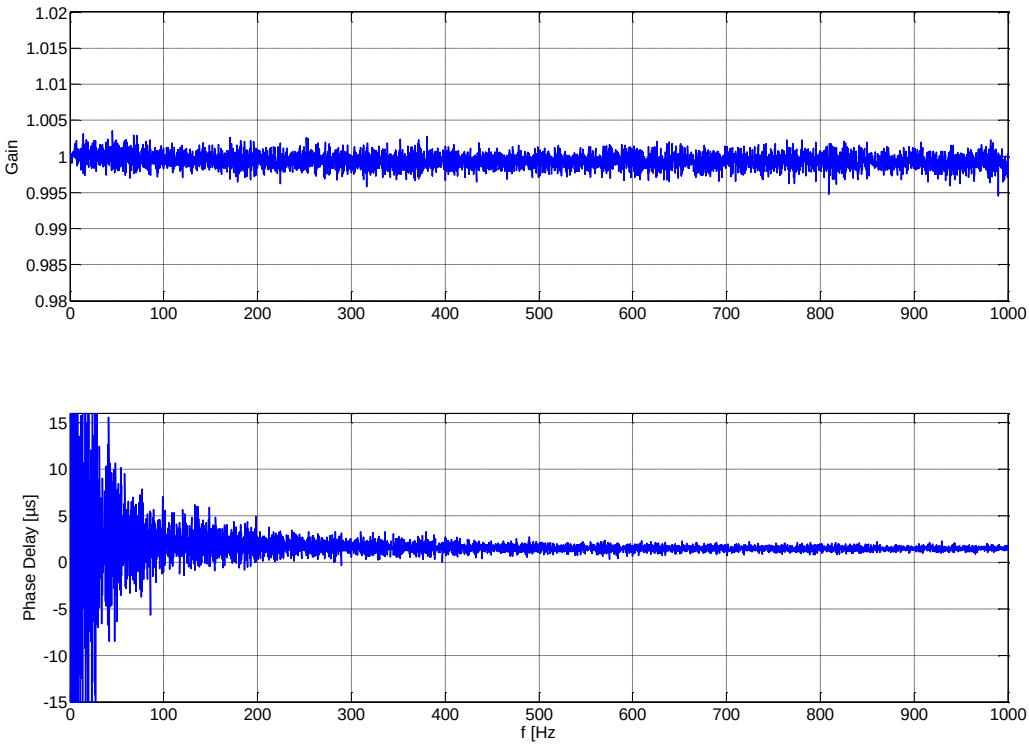

Figure 2–37 Current Generator Gain and Phase Delay

With these results, the current generator errors are far below the goals presented in chapter 1.3. The current generator can therefore be considered as a suitable tool for frequency response measurements of the MMS FIELDS instruments.

2.3.2. Simplifications of Setup

During the preparatory measurements it became evident that the measurements of the current generator are perfectly synchronous with the PPS signal, but different from the sampling clock of the FIELDS instruments which is in turn based on the master clock of the CDPU. It was therefore necessary to resample the current generator measurement data to the sampling grid of AFG, DFG and SCM which means high computational effort due to the large amounts of recorded data.

Fortunately, an approach with lower computational effort was possible by using a DSP voltage channel for current measurements. The used channel is called E56 (see figure 2–39) and is normally used for differential measurements of the electric field. The E56 channel is sampled with a rate of 16,384 Hz and is only subject to the anti-aliasing filters at the input. It is therefore possible to sample the measurement output of the current generator using these channels without relevant impact on the frequency response measurements. The data is in this case sampled with a sampling grid that is isochronous to that of the FIELDS instruments.

Naturally, this channel can only be used if its timing and frequency response relative to the measurement output of the current generator are well characterized. This characterization was done using a series of sine frequencies that was related to the current generator internal measurements. These measurements verified that the frequency response of the DSP voltage channel has almost flat gain and constant phase delay. The data of the voltage inputs can therefore be used with only a simple time correction.

As timing and frequency response could possibly change for different DSP models and/or software

updates, the sine frequency test was repeated during every single test of the FIT campaign. This test was only done in a feedforward configuration, just using the output data of the current generator instead of the current measurement data of the generator. Figure 2–38 shows a comparison of the E56 measurements and the expected gain and delays specified in the DSP design documents.

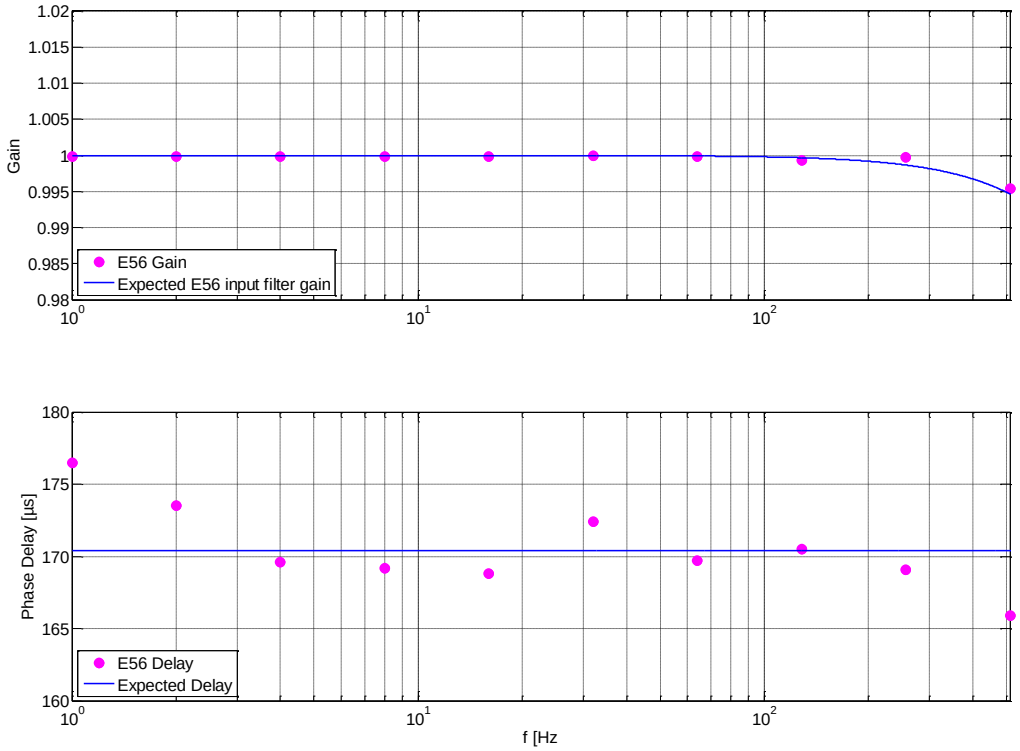

Figure 2–38 Comparison of DSP E56 Gain and Delay with the Expected Values from Design documentation

With this simplification, the measurement data was both generated with reference to the PPS signal, by the current generator and sampled synchronously to all instruments using sampling via the E56 channel. All further calculations only required time shifting and either divisions or multiplications of the sampling frequency by powers of two. The modified setup with this simplification is shown in figure 2–39.

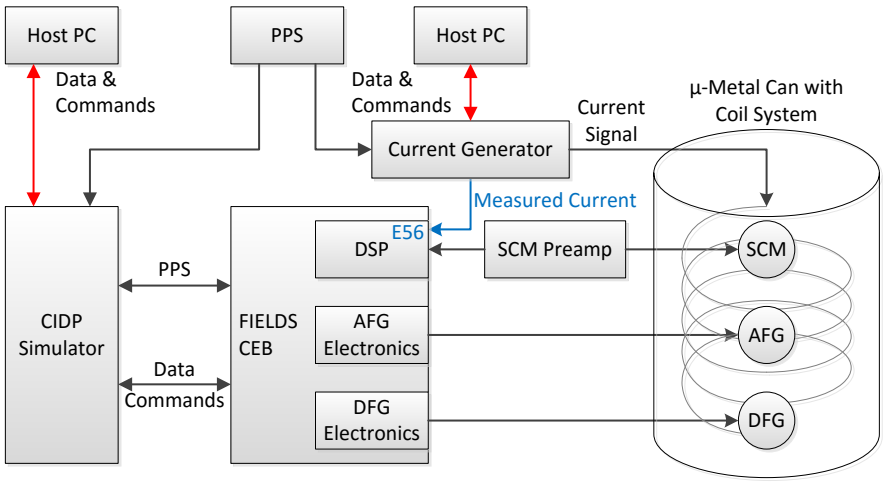

Figure 2–39 Modified Block Diagram for FIT Campaign with Additional E56 Current Measurement

2.3.3. Conducted Measurements

The measurements needed for the frequency response estimations were taken during the FIELDS integration and test (FIT) campaign. This campaign took place in the years 2012 to 2013 during the delivery of the four flight models for MMS 1 to 4.

The test was started with an initial measurement of instrument background noise with the current generator operating at constant zero output. This measurement was used to reveal problems in the ground connection topology and cable placement which typically resulted in an increase of noise and distortion. When the noise floor of this measurement was below ±0.1 nT peak, the other tests were conducted.

Different colored noise and sine signals were used to test the instruments in their various operational modes and sampling rates. These tests are summarized in table 2-2. In many cases, multiple outputs of the CDPU decimation chain were used and data was available at multiple sampling frequencies at the same time. SCM and DFG were not operated simultaneously, as the low separation in the μ-metal can and the sigma-delta feedback of the DFG would have caused noise within the SCM data.

<table>
<tr><th>Test #</th><th>Test Signal</th><th>Curr. Gen. Range</th><th>Fluxgate Range</th><th>AFG ADC mode</th><th>DFG filter mode</th><th>SCM mode</th><th>Sampling Frequency</th></tr>
<tr><td>1</td><td>Quiescent Noise Floor</td><td>MR</td><td>LR</td><td>ADCA</td><td>DEC32</td><td>DSP A</td><td>AFG: 128 Hz
DFG: 128 Hz
SCM: 16 kHz</td></tr>
<tr><td>2a</td><td>Pink Noise 64 Hz</td><td rowspan="7">MR</td><td>LR</td><td>ADCA</td><td>DEC32</td><td rowspan="15">Off</td><td rowspan="4">all: 128 Hz</td></tr>
<tr><td>2b</td><td>Pink Noise 64 Hz</td><td>LR</td><td>ADCB</td><td>DEC64</td></tr>
<tr><td>2c</td><td>Pink Noise 64 Hz</td><td>HR</td><td>ADCB</td><td>DEC64</td></tr>
<tr><td>2d</td><td>Pink Noise 64 Hz</td><td>HR</td><td>ADCA</td><td>DEC32</td></tr>
<tr><td>3a</td><td>Pink Noise 16 Hz</td><td>LR</td><td>ADCA</td><td>DEC32</td><td>all: 32 Hz</td></tr>
<tr><td>3b</td><td>Pink Noise 8 Hz</td><td>LR</td><td>ADCA</td><td>DEC32</td><td>all: 16 Hz</td></tr>
<tr><td>3c</td><td>Pink Noise 4 Hz</td><td>LR</td><td>ADCA</td><td>DEC32</td><td>all: 8 Hz</td></tr>
<tr><td>3d</td><td>Sine 0.1 Hz</td><td rowspan="2">MR</td><td>LR</td><td rowspan="6">ADCA</td><td rowspan="6">DEC32</td><td rowspan="6">all:
128/32/16/8 Hz</td></tr>
<tr><td>3e</td><td>Sine 2 Hz</td><td>LR</td></tr>
<tr><td>3f</td><td>Sine 2 Hz</td><td>HR</td><td>HR</td></tr>
<tr><td>3g</td><td>Sine 8 Hz</td><td rowspan="3">MR</td><td>LR</td></tr>
<tr><td>3h</td><td>Sine 32 Hz</td><td>LR</td></tr>
<tr><td>3i</td><td>Square Wave 8 Hz</td><td>LR</td></tr>
<tr><td>4a</td><td>Pink Noise 1,024 Hz</td><td rowspan="4">LR</td><td rowspan="4">-</td><td rowspan="4">Off</td><td rowspan="13">Off</td><td>DSP A</td><td>16k/8kHz</td></tr>
<tr><td>4b</td><td>Pink Noise 512 Hz</td><td>DSP A</td><td>16k/1kHz</td></tr>
<tr><td>4c</td><td>Pink Noise 1,024 Hz</td><td>DSP B</td><td>16k/8kHz</td></tr>
<tr><td>4d</td><td>Pink Noise 512 Hz</td><td>DSP B</td><td>16k/1kHz</td></tr>
<tr><td>5a</td><td>Pink Noise 16 Hz</td><td>LR</td><td rowspan="4">LR</td><td rowspan="8">ADCA</td><td rowspan="8">DSP A</td><td>all: 32 Hz</td></tr>
<tr><td>5b</td><td>Pink Noise 8 Hz</td><td rowspan="2">MR</td><td>AFG: 16 Hz
SCM: 32 Hz</td></tr>
<tr><td>5c</td><td>Pink Noise 4 Hz</td><td>AFG: 8 Hz
SCM: 8 Hz</td></tr>
<tr><td>5d</td><td>Sine 0.05 Hz</td><td>MR</td><td rowspan="5">AFG: 128/32 Hz
SCM: 16k/8k/1k/
32 Hz</td></tr>
<tr><td>5e</td><td>Sine 2 Hz</td><td rowspan="4">LR</td><td rowspan="4">LR</td></tr>
<tr><td>5f</td><td>Sine 8 Hz</td></tr>
<tr><td>5g</td><td>Sine 32 Hz</td></tr>
<tr><td>5h</td><td>Sine 128 Hz</td></tr>
</table>

Table 2-2 List of FIT Measurements and Respective Configurations
(LR/MR/HR corresponds to low/medium/high range)

2.4. Model Development

The measurement data generated during the testing campaign was used both immediately during the course of the measurements and in post-processing. Immediate processing was required to get a preliminary guess of the usability and credibility of measurement data. It resulted in the adjustment of both the used analysis methods and the measurements. The processes presented below have therefore not been developed in one shot, but are the result of a longer iteration process.
All generated models were normalized to a maximum gain of one which is the DC gain for AFG and DFG and the gain at 512 Hz for the SCM.

2.4.1. Sine Based Estimation

The sine based frequency response estimations were only done with a limited number of frequencies to save measurement time. The results are therefore not useable for the generation of a system model that is suitable for merging data. Nevertheless, the gained results were a valuable tool to confirm the results of the other methods and to also ensure the unchanged properties of the E56 channel based measurements (see 2.3.2). The result of the sine measurements are therefore not presented in this paragraph, but are included in the spectrum based estimation results in the next chapter.

2.4.2. Spectrum Based Estimation

Initial estimation of the instrument models was already conducted during the course of the testing campaign. Software development in this phase was therefore driven by the need for quick results using the available limited calculation power.
A boost in calculation power was achieved by using the graphic processor unit (GPU) that is supported via NVIDIA CUDA within the MATLAB environment. The GPU provides the possibility for massive parallel calculation that can, e.g., be used for FFT calculations. The drawback to these parallel architectures are restrictions in algorithm design and memory layout, e.g., not all operations available on a regular processor are also available on a GPU. Even if they are available, their execution times might be much larger.
In addition, the massive parallel computation also requires feeding the GPU with enough input data to actually take advantage of the parallelism. This requires taking the memory architecture of the GPU into account which provides large memories with low speed and small memories with high speed. The available GPUs at the time of the testing campaign had several tens of kilobytes of fast first level cache memory which was approximately enough to store a single FFT data set with 16 bytes per complex 64 bit floating point variable. Transferring any of these data sets to or from the larger GPU memory or even CPU memory increased the memory latency from a few to several hundred clock cycles.

The target of algorithm design was therefore to use the available optimized algorithms in MATLAB, to avoid recalculation and to avoid data saving outside the cache. This required a modification of the spectrum based algorithm in equation 2-30. Instead of dividing averaged PSD estimates, the algorithm was changed to average single frequency response estimates based on periodograms.

$$\widehat{H}_{single}(k) = \frac{Y_{noisy}(k)}{X(k)} = \frac{Y_{noisy}(k) * W(k)}{X(k) * W(k)} = \frac{FFT\left(y_{noisy}(n) \cdot w(n)\right)}{FFT\left(x(n) \cdot w(n)\right)} \qquad \textit{Equation 2-58}$$

$$\widehat{H}(k) = \frac{1}{M} \sum_{i=0}^{M-1} \widehat{H}_{single}(k) \qquad \textit{Equation 2-59}$$

The advantage of this approach is that the need to either store or recalculate X^* (used in S_{XX} and S_{YX}) is removed. The disadvantage is a change in the statistics of the frequency response estimate, as the order of division and averaging is interchanged in comparison to the PSD method.

In principle, with a Gaussian noise distribution for the periodogram estimates, the result of the division would be a Gaussian ratio distribution (see Hinkley, 1969). This distribution is both biased and asymmetric and influences the frequency response estimate. The amount of bias increases with the variance of dividend and divisor, therefore the FFT method suffers from an increased bias in comparison to the PSD based method. In addition, the division result is subject to a higher variance.

However, practical application shows that the resulting errors are acceptable. Figure 2–40 shows a simulated comparison of the simplified method using only FFTs and the regular PSD based method. This plot was done using a 129 point hamming windowed sinc filter (fc= 16 Hz, fs= 1,024 Hz) as the identified system and 10^5 samples of white noise input. Both PSD and FFT were calculated with a length of 16,384 points and an overlap of 87.5%. The FFT method shows a higher noise floor which is visible at around 40 Hz.

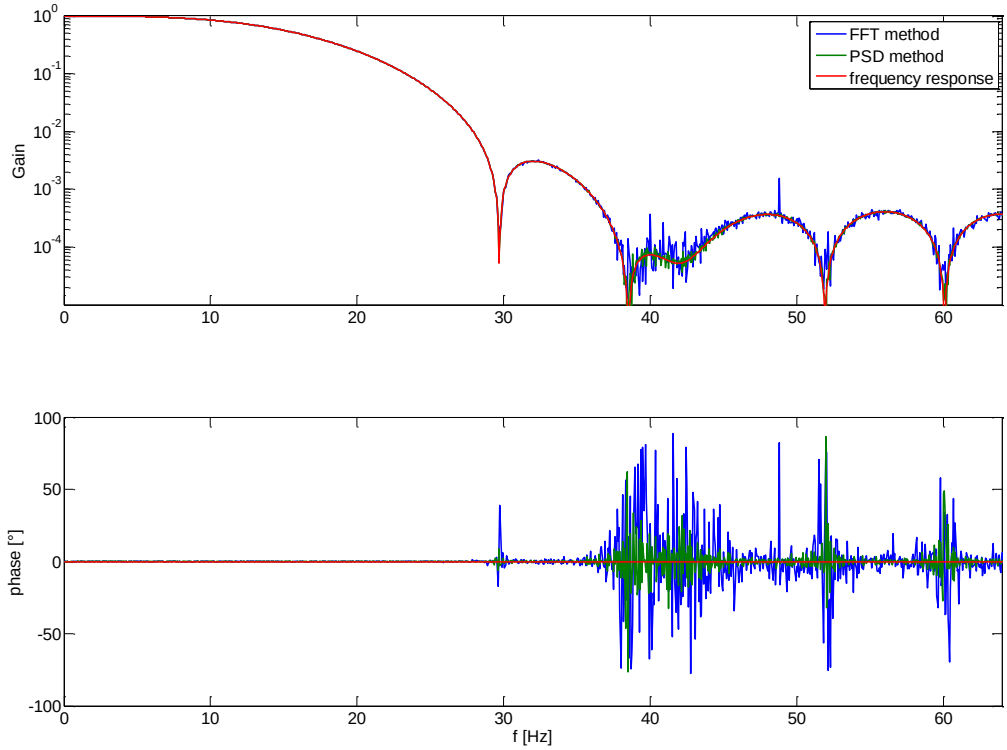

Figure 2–40 Comparison of the Noise Floor of FFT and PSD Based Frequency Response Estimation

In addition to this simulated example, also the comparison of sine based, spectrum based and parametric models are in line with each other, which means that the generated errors by bias and variance changes are negligible in this case.

The gain of the FFT method is a decrease in calculation time by 30% on modern computers. Table 2-3 compares the calculation times using GPU and CPU for both the PSD and FFT method. The used data set for this benchmark is a single measurement of SCM data with approximately 5 million PSD averages.

CPU		Core i7-3770K @ 3.5 GHz	Core i7-2670QM @ 2.2 GHz	Core 2 Quad Q9550 @ 2.83 GHz	Core 2 Duo SP9400 @ 2.4 GHz
GPU		Nvidia Geforce GTX 560 Ti	Nvidia Quadro 1000M	Nvidia Geforce GTX 560 Ti	-
Method	Hardware	Time			
FFT	CPU	57 min	120 min	147 min	~250 min
MATLAB PSD	CPU	120 min	-	441 min	-
tailored PSD	GPU	29 min	110 min	35 min	
FFT		20 min	90 min	24 min	

Table 2-3 Required Calculation Time for Different Frequency Response Estimation Methods

The resulting calculation times are highly dependent on the hardware type used. Furthermore, tailoring the algorithm to the actual problem results in a large improvement, as the tailored PSD algorithm is much faster than the MATLAB standard algorithm (version 2012b). The calculations during the initial measurements were done on even slower computers (Core 2 Duo) which resulted in even higher calculation times compared to the other CPUs.
With this knowledge, the calculations during the actual test were done in two steps. An initial estimate with low averaging numbers was calculated using the available notebooks (Core 2 Duo T4300). When this estimate was satisfactory, the detailed estimate was calculated by transferring data to remote controlled desktop PCs to use the available higher calculation power.

Figures 2–41 to 2–45 show the results of FFT based frequency response estimates from AFG, DFG and SCM. Also, these plots show the increase of phase delay noise towards lower frequencies discussed in chapter 2.3.1.
In all presented plots, the results of the sine fit match those from the spectrum-based estimation within the required limits (see goals in 1.3). All gains have been normalized to a maximum gain of one to get to comparable gain scales.

Figure 2–41 shows the gain and phase delay of the DFG flight model 4 in DEC32 mode and low range, sampled at 128 Hz. The individual axes are almost identical in gain and only show a small difference in phase delay which is due to the individual tuning of the sensor axes. These differences are small also for all other operation modes. Thus, only a comparison of the x-axis is shown in figure 2–42 for visibility reasons. Gain and delay are mainly dependent on the decimation mode (red/green) but independent from the range (cyan/blue and red/green). The results from high range measurements have a slightly increased phase delay noise level due to the higher instrument noise level in this range.

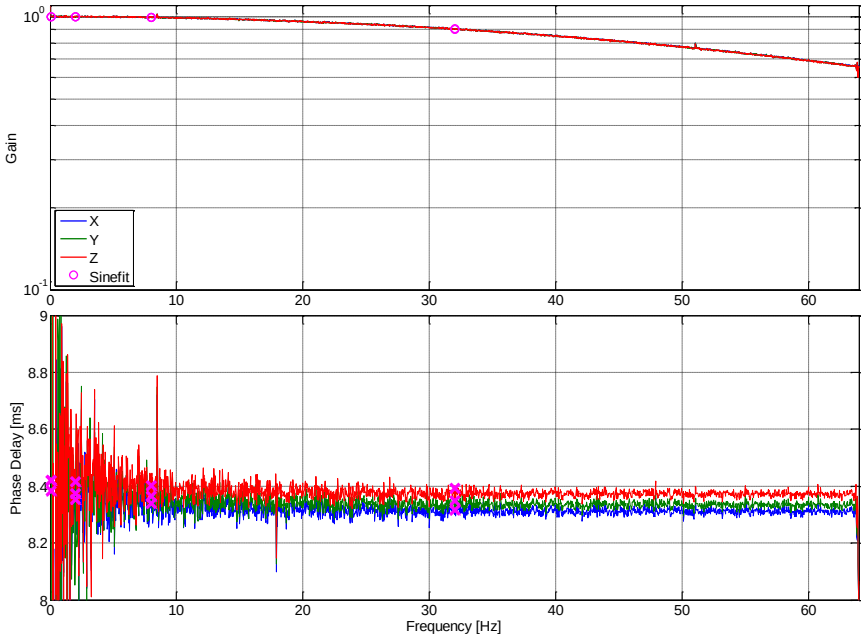

Figure 2–41 Gain and Phase Delay of DFG 128 Hz, DEC32, Low Range

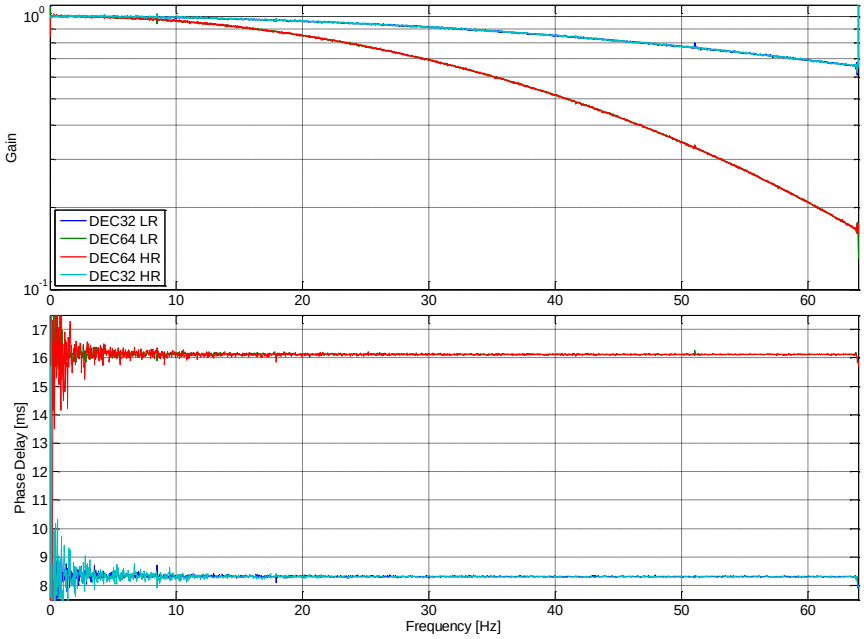

Figure 2–42 Comparison of Gain and Phase Delay for DFG X in Different Operating Modes

Figure 2–43 shows the frequency response of AFG flight model 4 using the primary ADC in low range with a sampling frequency of 128 Hz. Both gain and phase delay vary for the different axes which is caused by the tolerances of the analog parts and by the additional delay of the multiplexed ADC. All four possible modes of operation (low/high range, ADC A/B) show almost identical behavior (see figure 2–44), as a range change is only a gain modification (see chapter 1.1.3.3). The phase delay noise is in this case less dependent on the range, as the noise floor of the AFG in high range is lower than that of the DFG.

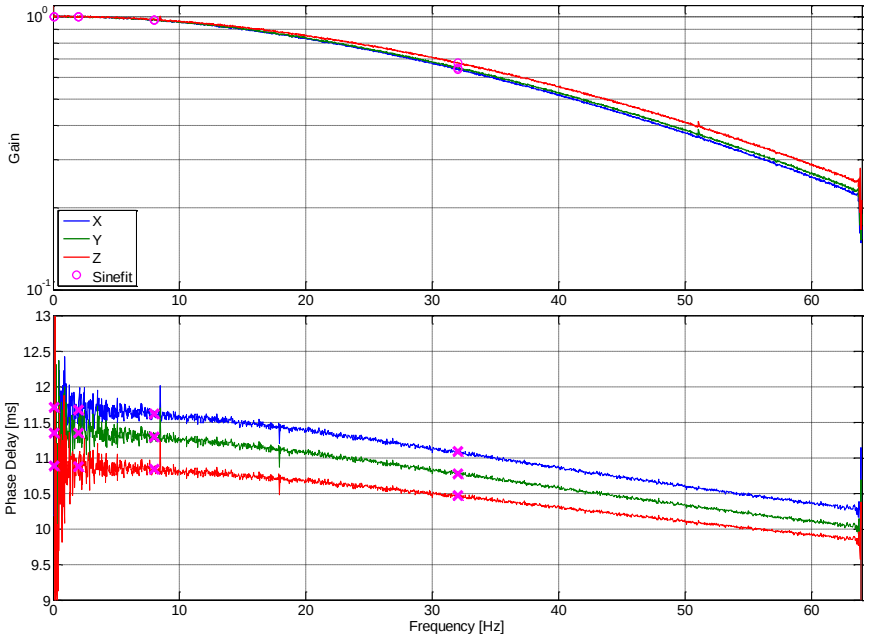

Figure 2–43 Gain and Phase Delay of AFG 128 Hz, ADC A, Low Range

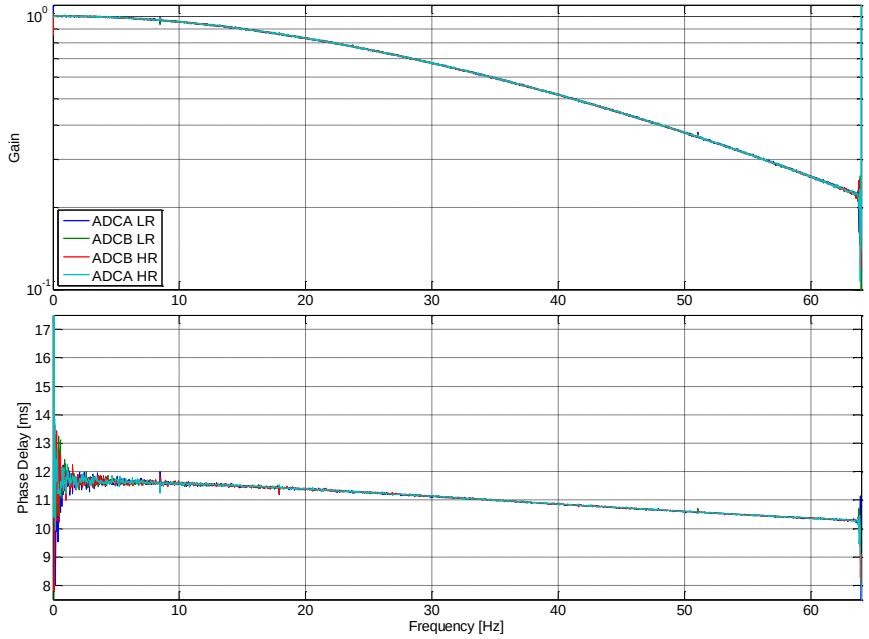

Figure 2–44 Comparison of Gain and Phase Delay for AFG X in Different Operating Modes

The frequency response of the SCM with a sampling frequency of 8 kHz is depicted in figure 2–45. In this case, the plot shows the phase rather than the phase delay, as the high pass property results in large changes of the delay over frequency that are less suitable for plotting.

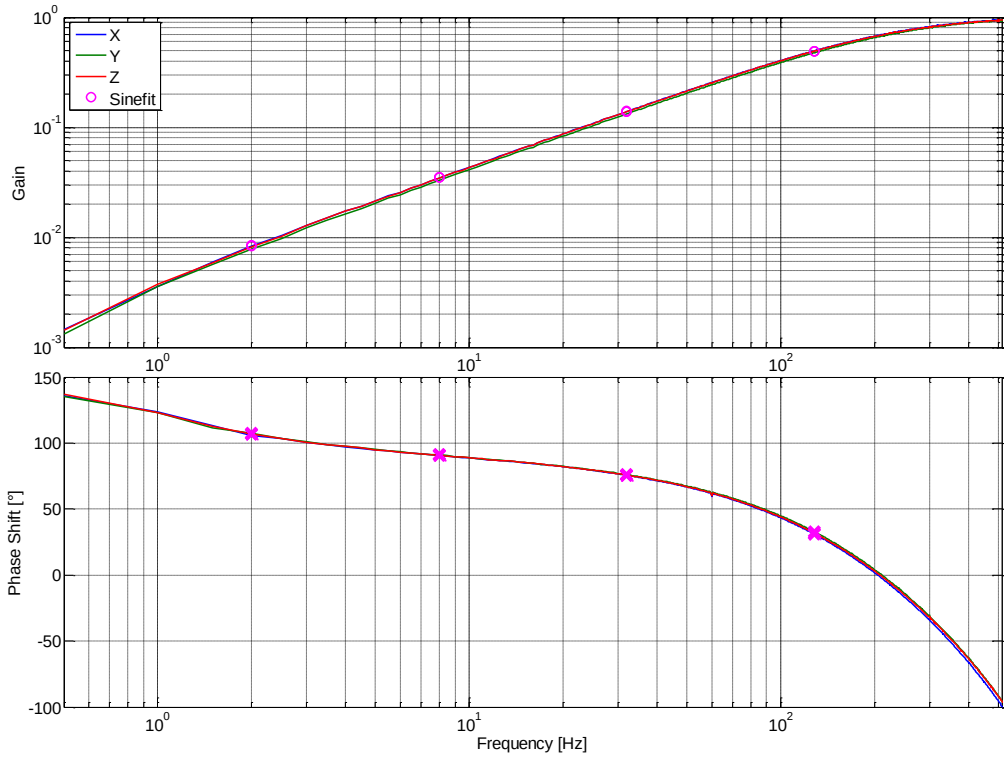

Figure 2–45 Frequency Response of SCM FM4

2.4.3. Parametric Estimation

2.4.3.1. Fluxgate Parametric Model

The models for AFG and DFG were found using the Wiener filter method introduced in chapter 2.1.3.1. This method was implemented in an inverse manner since the target of optimization was not to find an instrument model that converts the current measurements (input data x) to the generated fluxgate data (output data y), but a model that restores the current measurements (that are equivalent to the real magnetic field) based on the fluxgate output data. This merely requires swapping input and output variables and adding some delay in the current generator data. This delay is needed to compensate the delay of the fluxgate instruments, as any filter that could work without this delay would be acausal, as the estimated current measurement would be based on future fluxgate data.
The advantage of this inverse approach is that the resulting model can directly be used on the data regardless of the minimum phase property that would be required for an inverse filter (see chapter A.1.5).

The data flow for the Wiener filter calculation is shown in figure 2–46. All used low pass filters in this diagram are 16,385 tap hamming windowed sinc filters. The E56 samples are filtered before decimation to avoid aliasing. Both datasets are resampled to a common sampling frequency of 1,024 Hz and then filtered with a cut-off frequency of 64 Hz to remove any data that is above the Nyquist frequency of the fluxgate instruments.
The Wiener filter was then calculated using a 128th order FIR filter prototype and a delay of 60 to 81 samples, depending on instrument type and operation mode. This delay is composed of the delay of the instruments themselves and the group delay of the filter prototype.

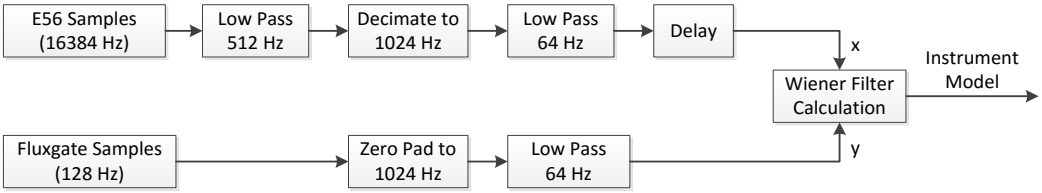

Figure 2–46 Data Flow AFG and DFG Model Calculation

The advantage of computing the Wiener filter at 1,024 Hz instead of the 128 Hz sampling rate is that delays can be chosen on a finer grid and that the relevant frequency band is, in this case, reduced to 1/8th of the Nyquist frequency, meaning the transfer function of the filter for frequencies above 64 Hz is irrelevant. This gives some degrees of freedom for the optimization process, even if models with low order like the 128th order filter are used.

Figure 2–47 shows examples of the filter coefficients for AFG and DFG. The calculated filters are not symmetric and therefore nonlinear phase, as the instruments either have non-linear phase (AFG analog transfer function) or include non-integer delays that require an asymmetric filter (DFG).

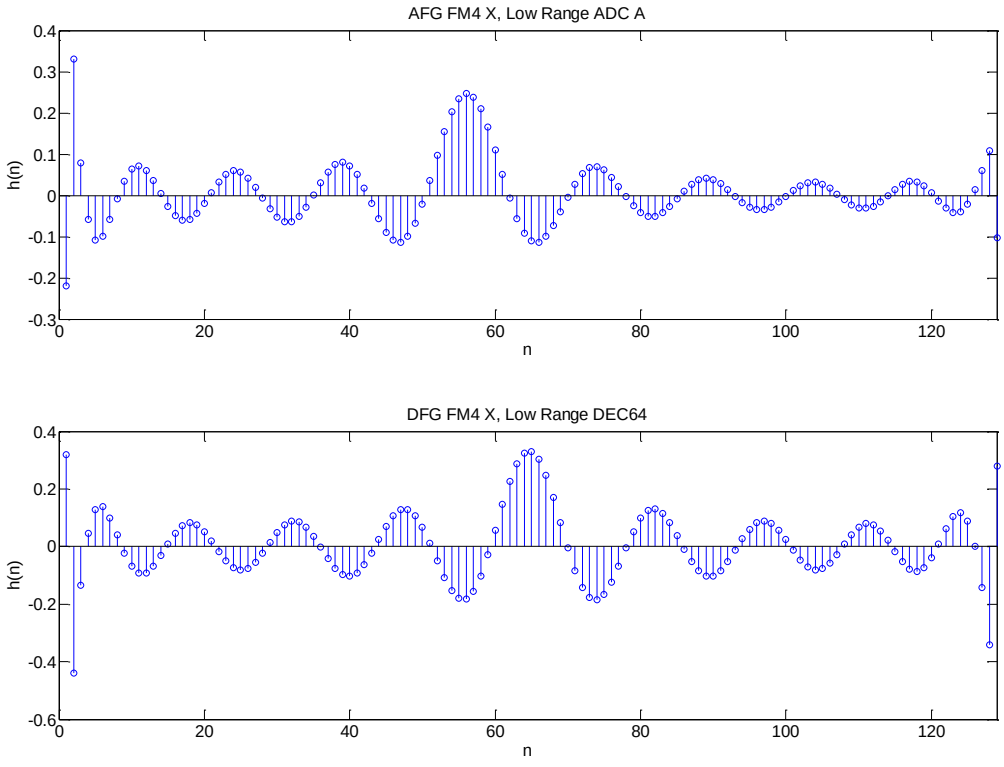

Figure 2–47 FIR-Based Inverse Model Examples for AFG and DFG

The gain and phase of the resulting models were then compared to the results of the spectrum-based estimation. Figures 2–48 and 2–49 show a gain ratio and phase delay difference plot.

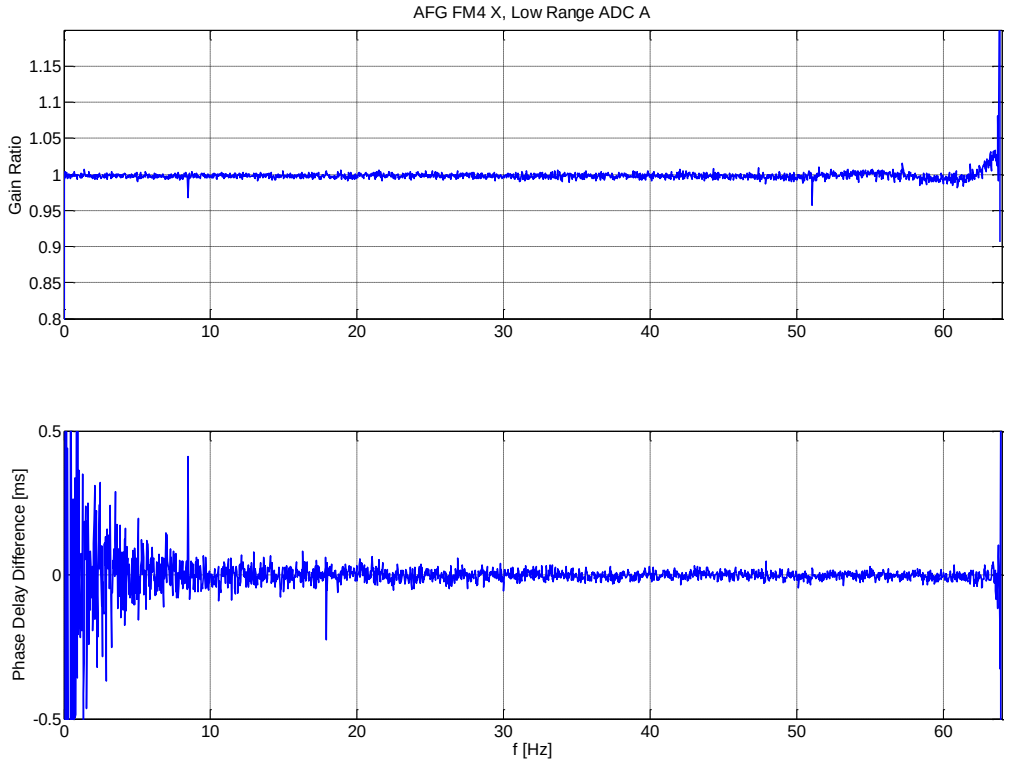

Figure 2–48 Gain Ratio and Phase Delay Difference between AFG Spectrum Based and Parametric Models

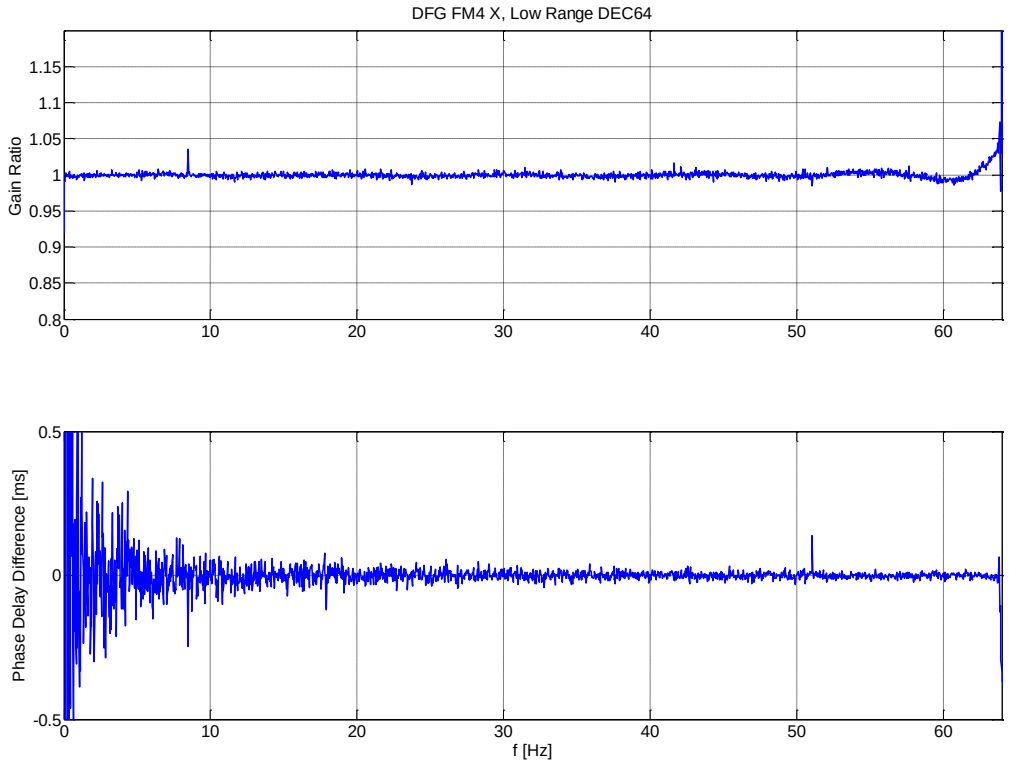

Figure 2–49 Gain Ratio and Phase Delay Difference between DFG Spectrum Based and Parametric Models

These plots show that gain and phase delay match very well with a few differences due to noise and distortion (e.g., at 51 Hz). There is a small deviation towards 64 Hz which is due to the limited length

of the filter model. In principle, this could be solved by increasing the model order, but at the cost of more lost data in the final data product due to filter settling. As the data close to 64 Hz are not used in the final data product (see chapter 2.5), this small difference can be considered as irrelevant.

Figure 2–50 shows the difference between the expected behavior of the DFG and the calculated model. The most prominent features of this difference are variations in gain and phase as well as a constant delay. The variations are definitely due to the model, as the CIC filter has constant phase delay and a monotonously decreasing gain within the passband.
The regular variations in gain are therefore caused by the modeling process and could be reduced by choosing a higher order model. The origin of the large difference in phase delay below 10 Hz and the phase delay offset are unknown. However, all remaining differences are within the accuracy goal of a 2% gain error and a 200 µs phase delay error and are therefore considered as acceptable.

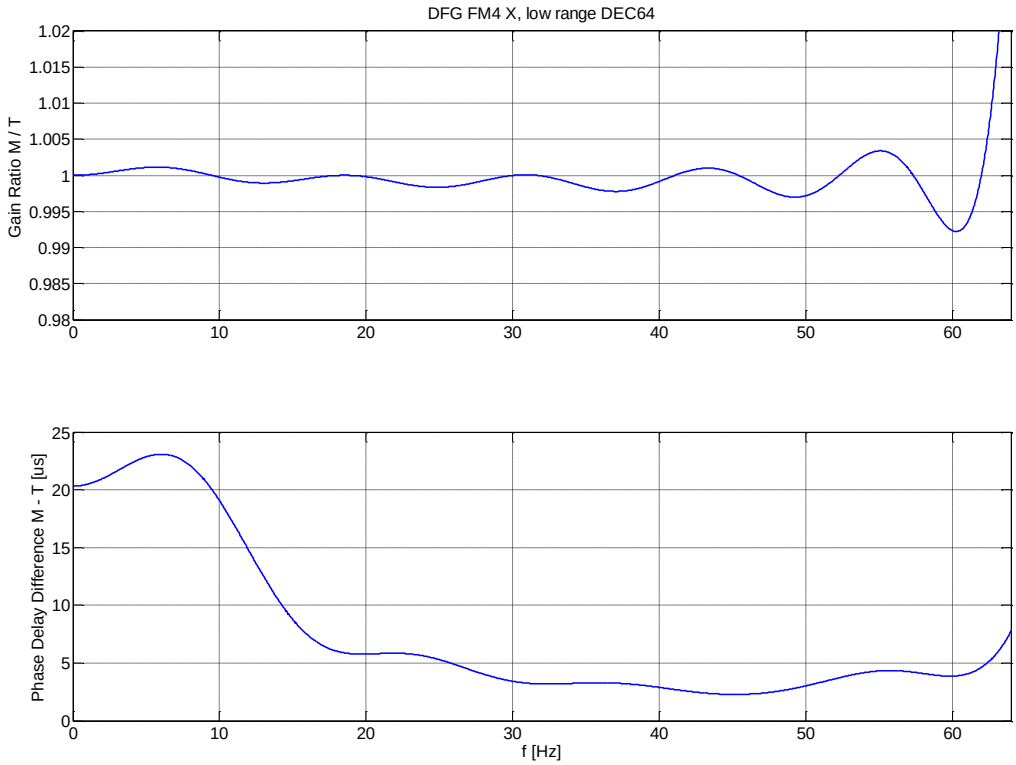

Figure 2–50 Comparison between DFG Model (M) and Theoretical Frequency Response (T)

2.4.3.2. Search-Coil Parametric Model

The analog domain model of the search-coil transfer function is derived in Le Contel et al., 2016. The overall transfer function is composed of the second order transfer function of the sensor and three first order filters within the preamplifiers. The system can therefore be modeled using high and low pass filters with five different cutoff frequencies. The result of the spectrum based estimation in figure 2–45 shows that only two of these five cutoff frequencies have a relevant impact on gain and phase within the bandwidth of interest for the merged data product. It is therefore possible to neglect the corner frequencies above 512 Hz and reduce the model to a second order high pass filter that is given as an analog transfer function in equation 2-60.

$$h(s) = \frac{s}{\omega_{c_1} + s} \cdot \frac{s}{\omega_{c_2} + s} \qquad \textit{Equation 2-60}$$

Unfortunately, this transfer function is not minimum phase, as the solutions of the numerator polynomial are zero. If this model is used for compensation by inverting the transfer function, the resulting compensation filter is therefore unstable. This is also visible in the spectrum-based estimate in figure 2–45 that shows that the gain of the SCM approaches zero for DC inputs. The inverse gain would therefore be infinite and unstable. A simple solution for this problem is to increase the DC gain of the transfer function by adding a small positive constant k. The resulting compensation filter will therefore also have limited DC gain.

$$h(s) = \frac{s + k_1}{\omega_{c_1} + s} \cdot \frac{s + k_2}{\omega_{c_2} + s} \qquad \textit{Equation 2-61}$$

The analog transfer function can then be transformed to the digital domain using the bilinear transformation (Oppenheim et al., 1998, pp. 450ff) with a sampling time T_s. Also, here the inverse filter is stable for any positive k, as the solutions of the numerator polynomial are inside the unit circle.

$$h_{model}(z) = \frac{z + \frac{T_s k_1 - 2}{T_s k_1 + 2}}{z + \frac{T_s \omega_{c_1} - 2}{T_s \omega_{c_1} + 2}} \cdot \frac{z + \frac{T_s k_2 - 2}{T_s k_2 + 2}}{z + \frac{T_s \omega_{c_2} - 2}{T_s \omega_{c_2} + 2}} \qquad \textit{Equation 2-62}$$

The cutoff frequencies ω_c in equation 2-62 were then found by minimizing the model error which is the difference between the complex frequency response of the model (H_{model}) and the result of the spectrum based estimation (H_{FFT}). This was done in a minimum mean square error sense.

$$\omega_{c_1}, \omega_{c_2} = \underset{\omega_{c_1}, \omega_{c_2}}{\operatorname{argmin}} \left(\sum_k \left| H_{model}\left(k, \omega_{c_1}, \omega_{c_2}\right) - H_{FFT}(k) \right|^2 \cdot W(k) \right) \qquad \textit{Equation 2-63}$$

The weighting factor W is needed to adjust the error criterion to the expected gain curve signal-to-noise ratio. A gain dependent weight is needed to ensure an equal contribution of the model error regardless of gain, otherwise the parts of the model with high absolute gain would have a much higher influence on the error sum. An equal weight of all errors can be achieved by setting the weights proportional to the inverse of the squared gain of SCM which is approximately the FFT result.

$$W_G(k) \sim \frac{1}{H_{SCM}(k)^2} \approx \frac{1}{H_{FFT}(k)^2} \qquad \textit{Equation 2-64}$$

With this scaling, all parts of the frequency response would become equally important. However, in this approach, the quality of the estimation result was not taken into account. This quality is dependent

on the measurement noise. For the SCM this noise is approximately inverse to the gain response (see Le Contel et al., 2016); therefore, the noise based weight factor is proportional to the squared gain response.

$$W_N(k) \sim \frac{1}{N_{SCM}(k)^2} \approx H_{FFT}(k)^2 \qquad \textit{Equation 2-65}$$

The gain and noise based weight factors are then multiplied to get the final weight factor:

$$W(k) \sim W_G(k) \cdot W_N(k) \approx \frac{H_{FFT}(k)^2}{H_{FFT}(k)^2} \qquad \textit{Equation 2-66}$$

The weight factor is practically one and could be removed from equation 2-63. Nevertheless, this simplification cannot be considered as universally valid as, e.g., cutoff frequencies in frequency bands with very high noise floor could still result in very low errors and could therefor, be ignored during optimization. This situation actually happened during the optimization of the model for SCM, as in some cases an optimal cutoff frequency was found close to the Nyquist frequency rather than its real value at around 0.6 Hz. This problem was solved by manual adjustment of the weight function, giving lower frequencies a little more weight.

Figure 2–51 shows a comparison of the modeled transfer function, the results of the FFT estimate and the reference measurements taken by the SCM team (Le Contel et al., 2016). The phase reference measurements were corrected for the already known digital delays. Model, spectrum estimate and reference measurements show no visible difference in the logarithmic scale. The DC gain of the generated model was limited to -220 dB (using the constant factor k_1 and k_2) in order to enforce the minimum phase property.

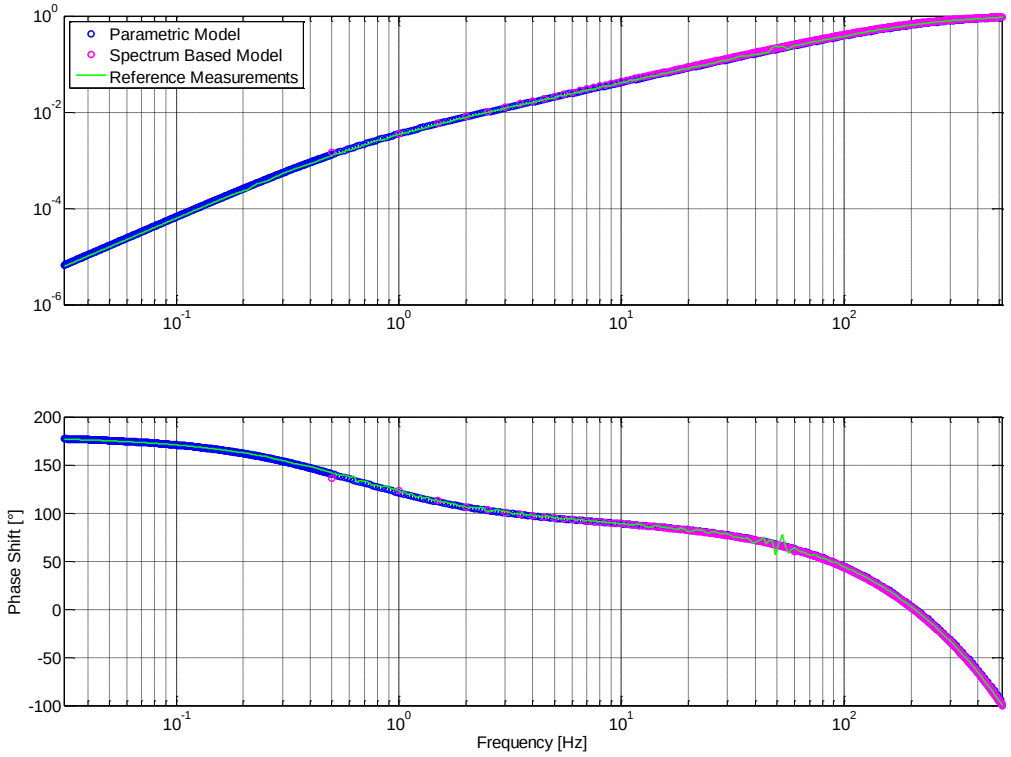

Figure 2–51 Comparison of Gain and Phase Shift using SCM Parametric Model, Spectrum based Estimates and Reference Measurements

The calculated differences are presented in figure 2–52 which shows the gain ratio and phase delay difference between the model and the reference measurements. The variations are due to noise in the reference measurements, as the model itself has smooth gain and phase curves. Furthermore, there is a large gain difference at 50 Hz due to the powerline tone in the reference measurements.
These differences caused by noise and distortion reveal an advantage of the parametric model. The parametric model limits the changes in frequency response to those that are actually possible within the model. This restricts the influence of noise and distortion to a minimum in comparison to all higher order non-parametric approaches, such as spectrum-based estimates or the SCM reference measurements.

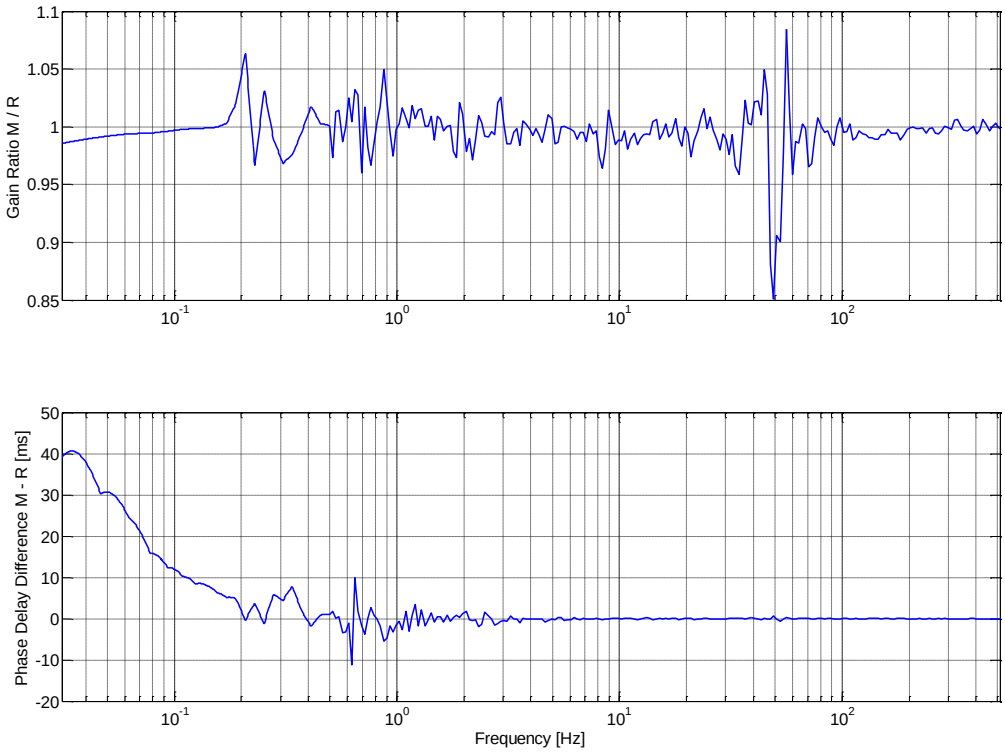

Figure 2–52 Gain Ratio and Phase Delay Difference between Model (M) and Reference Measurements (R)

In addition, there is a decrease in gain and an increase in phase delay for frequencies below 0.2 Hz. The origin of these changes is unknown and is actually hard to explain based on theory alone. It is not caused by the DC gain reduction for stability reasons nor by any possible change of cut-off frequencies in the model of the search-coil.
Fortunately, this change of gain and phase delay is located in a frequency range that has almost no influence on the final data product (see chapter 2.5) and the differences in gain and phase delay above 1 Hz (with more influence) are clearly due to the noise in the search-coil reference measurements.

Despite the small differences previously discussed, the designed model matches both the results of the reference measurements and the spectral estimates with high accuracy. These results can therefore be considered as a successful independent verification of the SCM analog measurements as well as the expected digital processing delays of the FIELDS DSP.

2.5. Crossover Filter

Data from AFG, DFG and SCM is merged with a crossover filter that weighs different spectral parts of the instrument signals according to their properties. An optimum crossover filter set would weigh the spectral components based on a comparison of instrument sensitivity, noise floor and possible distortion. These weights can be considered as a filter function with variations in the frequency domain.

For initial testing of the merged data product, a set of finite impulse response (FIR) low and high pass filters was used which was based on a hamming windowed sinc function. These filters used DFG/AFG data up to 8 Hz (crossing of the noise floor in figure 1–31) and SCM data above. The sinc function also provides the advantage that the design of the respective complementary filter is a simple subtraction from z^0=1. This means the sum of the two filters is unity gain. Furthermore, comparison to unfiltered signals is simple due to its constant group delay property.

Unsurprisingly, this initial filter pair was only a first guess, as the optimum noise floor can be achieved by having a filter that is based on the actual noise floor and sensitivity. It is therefore interesting to compare the used filter with this optimal filter and to design an improved filter using the knowledge from this comparison.

The principle of combining measurements with the purpose of getting a better data product is best explained by using multiple measurements of one quantity. Each measurement is defined by a measurement value and some assessment of the measurement uncertainty or noise. If the measurement noise is Gaussian, the distribution of the noise can be characterized using the mean value μ and the variance σ^2.

Assuming there are N noisy measurements of the same quantity, one can reduce the noise level by averaging the individual values x_i to get the mean value $\bar{x}$

$$\bar{x} = \frac{1}{N}\sum_{i=1}^{N} x_i \qquad \textit{Equation 2-67}$$

If the noise on each measurement is independent and identically distributed (i.i.d.) Gaussian noise, the variance after averaging is reduced to

$$\sigma_{\bar{x}}^2 = \frac{1}{N^2}\sum_{i=1}^{N} \sigma_i^2 \qquad \textit{Equation 2-68}$$

Using this property, one can see that in the best case with identical measurement variance, the resulting variance of the averaged measurement versus the best individual measurements is reduced by a factor of N^2.

This method can be employed for a non-identical variance by implementing a rough estimate of the noise levels for giving the "better" measurements a higher weight w_i:

$$\bar{x}_w = \frac{\sum_{i=1}^{N}(w_i x_i)}{\sum_{i=1}^{N}(w_i)} \qquad \textit{Equation 2-69}$$

The resulting variance will then be

$$\sigma_{\bar{x}_W}^2 = \frac{1}{\left(\sum_{i=1}^{N} w_i\right)^2}\sum_{i=1}^{N}(w_i\sigma_i)^2 \qquad \textit{Equation 2-70}$$

The optimal approach for this weighting is the maximum likelihood (ML) estimator (see Kay, 1993, pp. 157ff) that uses the inverse variance as weight:

$$\bar{x}_{ML} = \frac{\sum_{i=1}^{N}\left(x_i \sigma_i^{-2}\right)}{\sum_{i=1}^{N}\left(\sigma_i^{-2}\right)} \qquad \textit{Equation 2-71}$$

The resulting variance is

$$\sigma_{\bar{x}_{ML}}^2 = \frac{1}{\sum_{i=1}^{N}\left(\sigma_i^{-2}\right)} \qquad \textit{Equation 2-72}$$

This method can now be expanded from the single sample probability perspective to the spectral perspective. We assume that the instruments deliver a sample series of a constant magnetic field value x with additive i.i.d. Gaussian noise. One can then apply a filter bank to extract tiny frequency bands by using a set of narrow band FIR filters. These filters do a convolution of the signal x and the filter function h to get the output signal

$$y[n] = \sum_{m=-\infty}^{\infty} x[m]h[n-m] \qquad \textit{Equation 2-73}$$

This equation is in fact a scaled version of the weighted average in equation 2-69, but here the samples are not from different instruments, but realizations from the same instrument at different times. The variance of the output is then

$$\sigma_y^2 = \sum_{n=-\infty}^{\infty} (h[n]\sigma_x)^2 = \sigma_x^2 \sum_{n=-\infty}^{\infty} (h[n])^2 \qquad \textit{Equation 2-74}$$

which is simply a scaled version of the input variance, but this time the noise is limited in bandwidth. Going one step further, one can now apply the same filter bank on data from each instrument, calculate an ML average for every filtered sample based on the noise power in the respective band and sum up the bands using a reconstruction filter bank. This principle can now be refined by taking infinitesimally small filter bands for determining the weights which is equivalent to using the power spectral density S_{xx} of the instrument noise floor.

Instead of using the filter bank and summing up, it is now possible to create a filter that directly applies the weights on frequencies, thus creating a frequency dependent ML averaging filter. Its filter response for instrument i of N different instruments can be calculated using

$$H_i\left(e^{j\omega}\right) = \frac{\left(\hat{S}_{xxi}(e^{j\omega})\right)^{-1}}{\sum_{i=1}^{N}\left(\hat{S}_{xxi}(e^{j\omega})\right)^{-1}} \qquad \textit{Equation 2-75}$$

This filter is then applied to the individual input signals before summing up:

$$X_{ML}\left(e^{j\omega}\right) = \sum_{i=1}^{N} X_i(e^{j\omega}) \cdot H_i(e^{j\omega}) \qquad \textit{Equation 2-76}$$

Given this formula, the design of an optimal merging filter seems quite easy, but of course this requires having exact knowledge of the noise floor and its statistical properties. The optimal merging filter based on this formula is equivalent to the complementary filter discussed in chapter 1.2.2.1.

The total noise of the magnetic field instruments aboard MMS is generated by various sources: sensor noise, magnetic stray field noise by the spacecraft, electronics noise and quantization noise. The noise floor from ground measurements, which does not include spacecraft noise, is shown in figures 2–53 and 2–54. This noise floor was determined by placing the sensors in quiet field conditions (e.g., a shielding can) and measuring the instrument output. The following plots are limited to data from DFG and SCM, as this data is used in the merged burst product. The analysis for AFG can be done in the same way.

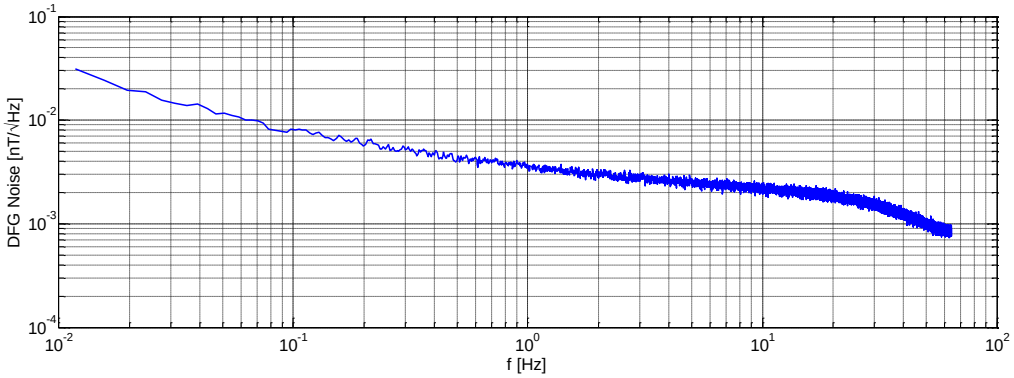

Figure 2–53 DFG Qualification Model Noise floor, X-Axis, from Ground Measurements

The noise floor of DFG (figure 2–53) is given in magnetic field units of nT/√Hz. This is due to the fact that fluxgate data is typically used without frequency response compensation. The sensitivity function is just a simple lowpass (see figure 2–41) that allows direct use of the data below 10 Hz with only small errors.

SCM has a more complex bandpass like sensitivity function (see figure 2–45) and cannot be used without frequency response compensation. The raw noise floor (figure 2–54) can therefore not be interpreted as a magnetic field and is still given in raw measurement units of V/√Hz.

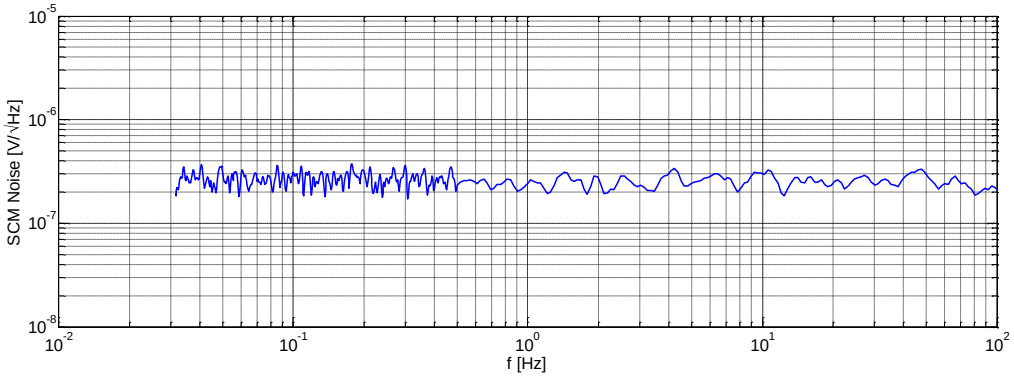

Figure 2–54 SCM Flight Model 1 Raw Noise Floor, X-Axis, from Ground Measurements
Data provided by O. Le Contel

The significance of the raw instrument noise floors is limited, as it is modified by the compensation of the instrument frequency response. This compensation not only amplifies the desired signal at frequencies with low sensitivity, but also lifts the noise floor by the same amount. It is therefore no longer meaningful to talk of magnetic sensor noise, but rather noise equivalent magnetic induction (NEMI, Le Contel et al., 2016). The NEMI gives the noise level after frequency response compensation, which is directly comparable to magnetic field amplitudes. Using these NEMI noise levels, the maximum likelihood (ML) filter frequency response can be calculated (see figure 2–55).

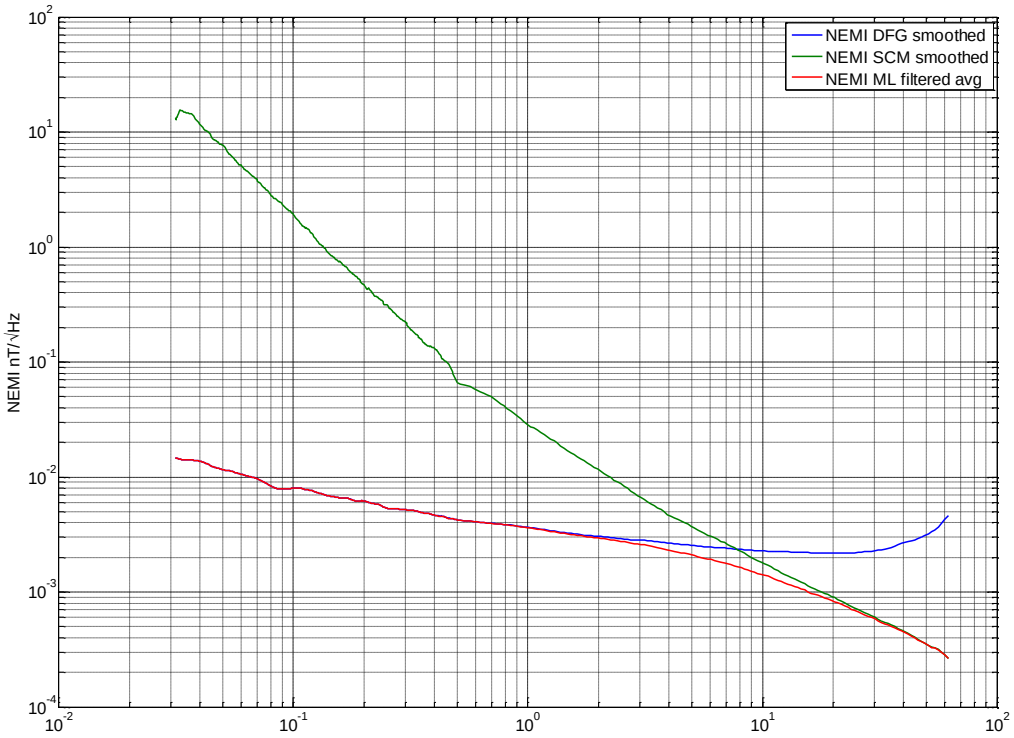

Figure 2–55 NEMI of DFG and SCM and Resulting NEMI of ML Filtered Merging

Even the smoothed NEMI curves still contain ripples from PSD calculation and measurement distortion (e.g., SCM NEMI at ~0.5 Hz). If this raw NEMI is used for estimating the ML filter, the ripples will also appear in the frequency response of the filter (see figure 2–56, e.g., between 15 and 20 Hz). One can get rid of these ripples by using a parametric PSD approach or by fitting a filter to the result of ML estimation. With this modeling approach, also further filter properties can be taken into account, like filter tap length (and the associated removal of filter settling times) and phase delay properties.

Besides the topic of ML estimation, a further consideration is necessary for designing the optimal filter. Fluxgate data requires upsampling and anti-aliasing filters (see 2.6.1). These filters have an increasing influence on gain, the closer the signal frequency gets to the Nyquist frequency (i.e., 64 Hz for AFG/DFG). This influence can be reduced if the merging filters are designed with a crossover frequency well below 64 Hz.

A compromise with good noise performance as well as high attenuation at 64 Hz is a windowed sinc filter with cutoff at 8 Hz. This filter is a symmetric FIR filter with constant phase delay which allows easy comparison and analysis of data sets without dispersion. Figure 2–56 shows a comparison of sinc filters with 129 and 513 coefficients with the ML filters.

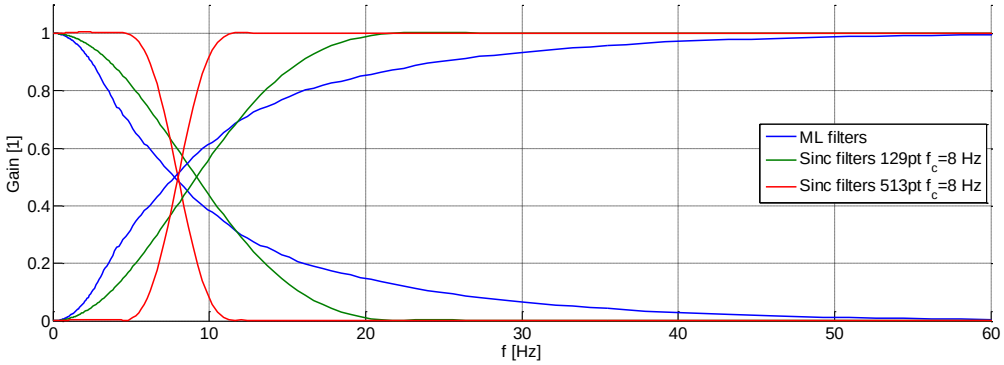

Figure 2–56 Gain Comparison of ML Filter, Sinc Filter and Initially Used Filter

Figure 2–57 shows the improvement in noise floor relative to the best noise floor if just a single instrument is used. The 129-tap filter delivers slightly more noise than the ML filter (e.g., a worst-case noise increase of 7% at 20 Hz). The low tap number of 129 also results in a low data loss due to filter settling (see filter basics in a.1). The 513-point filter delivers a better performance at the crossover frequency, but has a higher noise floor around it. This could, e.g., be further improved by using a Kaiser windowed filter, which includes a scaling parameter for the window shape that allows a better approximation o the ML filter function.

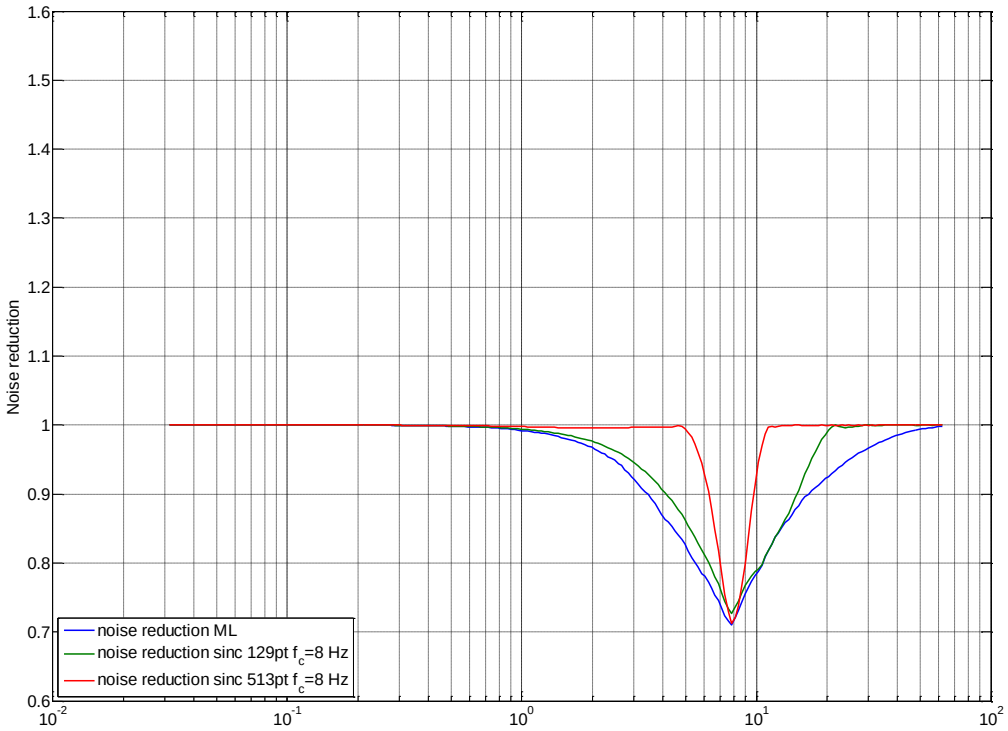

Figure 2–57 Comparison of Noise Floor Amplitude Improvement by ML Filter and Sinc Filters in Relation to the Best Noise Floor of Single Instruments

An alternative solution would be to approximate the ML filter by, e.g., least squares FIR filter design. In addition, an optimal method would not only use ground measured noise floors, but also attempt to estimate noise floors in orbit and adapt to possible onboard distortion sources, noise level change by temperature variations and more. This estimation of in-flight noise was outside the scope of this thesis and was researched by another member of the FIELDS team.

However, it should be noted that the improvement of using an optimal filter rather than a rough approximation is quite small. The differences between the 129-point sinc filter and the optimal filter are 7% in the worst case (20 Hz) which is in contrast to the noise improvement of 30% at 8 Hz granted by both filters. Furthermore, in both cases, the noise floor is increased by large numbers in comparison to using un-merged data (e.g., an improvement of 50 dB at 30 mHz or 20 dB at 60 Hz, see figure 2–55).

With these numbers, the optimal design of a merging filter can be seen in a quite relaxed way, as the gain of merging with a rough estimate is much larger than the disadvantage of using a non-optimal filter. It is therefore more important to consider the other relevant properties of the filter, i.e., tap length and the resulting removal of samples during initial filter settling. For routine processing, it is therefore more beneficial to use the shorter filter than to gain those last small percent of signal-to-noise ratio in a limited bandwidth window.
However, an optimal merging filter could still be applied in special situations when the signal feature of interest is just above the noise floor in the frequency band that can be improved by optimal merging.

2.6. Elements of the Merging Process

2.6.1. Resampling

Data products of AFG, DFG and SCM are generated at different sampling frequencies, dependent on the mode of operation. The standard sampling frequencies for MMS are 8, 16 and 128 Hz for AFG/DFG and 8, 32 and 8,192 Hz for SCM. The combination of data requires bringing these different data products to a common sampling frequency before merging.

Upsampling

Data from AFG and DFG require upsampling from 128 Hz to reach the target frequency of the merged burst data product at 1,024 Hz. The upper panel in figure 2–58 shows the power spectral density (PSD) of in-orbit measured magnetic field (MMS1, DFG, 20150922 07:35:04 UTC), sampled at f_s=128 Hz. The presented spectrum can be divided into different sections that are due to different effects in sampling and transformation.

The section from zero to the Nyquist frequency (0-64 Hz) is equivalent to the frequencies that are present in the analog measurement of the magnetic field. This section will be referred to as "**Nyquist spectrum**" in the following paragraphs.

Sampling is equivalent to a multiplication of the analog signal with a Dirac impulse train (Oppenheim et al., 1998, pp. 140ff). This multiplication is in turn equivalent to a convolution in frequency domain. As the Fourier transform of a Dirac impulse train is again a Dirac impulse train, spaced by the sampling frequency, this convolution introduces a **periodic spectrum**. The result of the Fourier transform of a sampled signal is therefore periodic and repeats at multiples of the sampling frequency.

The Fourier transform used in PSD estimation also introduces the concept of negative frequencies, as the solution of the Fourier transform integral is done by splitting up sine signals using Euler's identity. The resulting Fourier spectrum has exponentials with positive and negative frequency, which are the Nyquist spectrum and its negative counterpart. Due to periodicity, this negative spectrum is also visible as a **mirror spectrum** between the Nyquist and sampling frequency (64 to 128 Hz).

The process of upsampling is done by inserting zero samples between the existing ones until the desired sampling frequency is reached. This step simply increase the field of view on the same spectrum. For an upsampling factor of 8 (from f_s=128 Hz to 1,024 Hz) both the old mirror spectrum and 3 additional periods of the spectrum become part of the Nyquist spectrum (see middle panel panel of figure 2–58).
The added frequencies are called aliasing frequencies, as they are interpretations of the ambiguity of the original spectrum. If a signal is sampled at 128 Hz, it cannot be known if a sample sequence was caused by a sine of 16 Hz or its aliases at 112 Hz, 144 Hz or 240 Hz (and so on), as the sequence is identical in all cases. The restriction to a unique interpretation (e.g., the band from 0 to 64 Hz) is in fact based on previous knowledge, e.g., the input bandwidth restriction in analog to digital conversion. Upsampling results in more room for interpretation, as the increased bandwidth (0 to 512 Hz) allows presence of frequencies of up to 512 Hz without ambiguity. The process of adding zeroes interprets this ambiguity by assuming that all possible alias frequencies were indeed present in the original signal with equal amplitude. The process of anti-aliasing then restricts the ambiguity by selecting a single frequency band with the original bandwidth of 64 Hz. Since fluxgate data was restricted between 0 and 64 Hz, the ideal anti-aliasing filter removes all data outside this band.

The ideal anti-aliasing filter is a rectangular filter in frequency domain (see lower panel of figure 2–58) and is discussed in chapter a.1.4. As this filter removes a part of the spectral energy (the alias frequencies), overall signal power can only remain constant if a scaling factor is introduced, which is equal to the upsampling ratio (a factor of 8 in the plotted example).

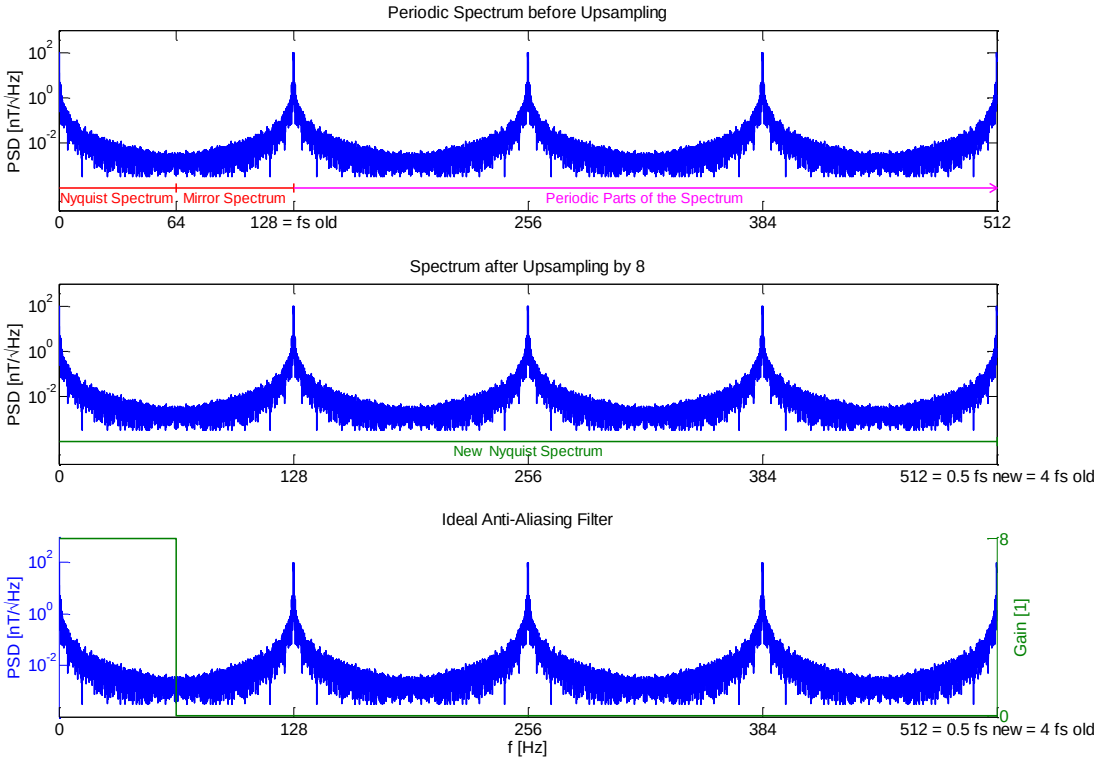

Figure 2–58 Upsampling in Frequency Domain

In time domain, this filter is defined by the sinc function. For an upsampling factor L this filter is defined as

$$h[z] = \sum_{n=-\infty}^{\infty} L \cdot sinc\left(\frac{2n}{L}\right) z^{-n} \qquad \textit{Equation 2-77}$$

It is clear that this infinitely long filter cannot be realized and the ideal filter can only remain a mathematical concept.

The real anti-aliasing filter needs to be designed having in mind both data properties and the application within the merged data product processing. Since no ideal filter is realizable, there will always be some influence on gain for frequencies close to the old Nyquist frequency. With the knowledge that these frequencies might be removed by the crossover filter regardless (see chapter 2.5), this gives some degrees of freedom in anti-aliasing filter design. The usually desired unity gain and linear phase in the passband are less relevant in frequency bands with low crossover filter gain.

Although the theoretical target is to remove all aliasing frequencies, in reality, it is only necessary to attenuate these frequencies below the noise floor of the SCM which is 20 fT/√Hz at the lowest point (see figure 1–31). Due to the low amplitude of the natural magnetic field at higher frequencies (see figure 2–58, upper panel), the requirements for attenuation can be relaxed for the frequency band between roughly 24 and 104 Hz, as amplitudes are already ~60 dB below the maximum level.

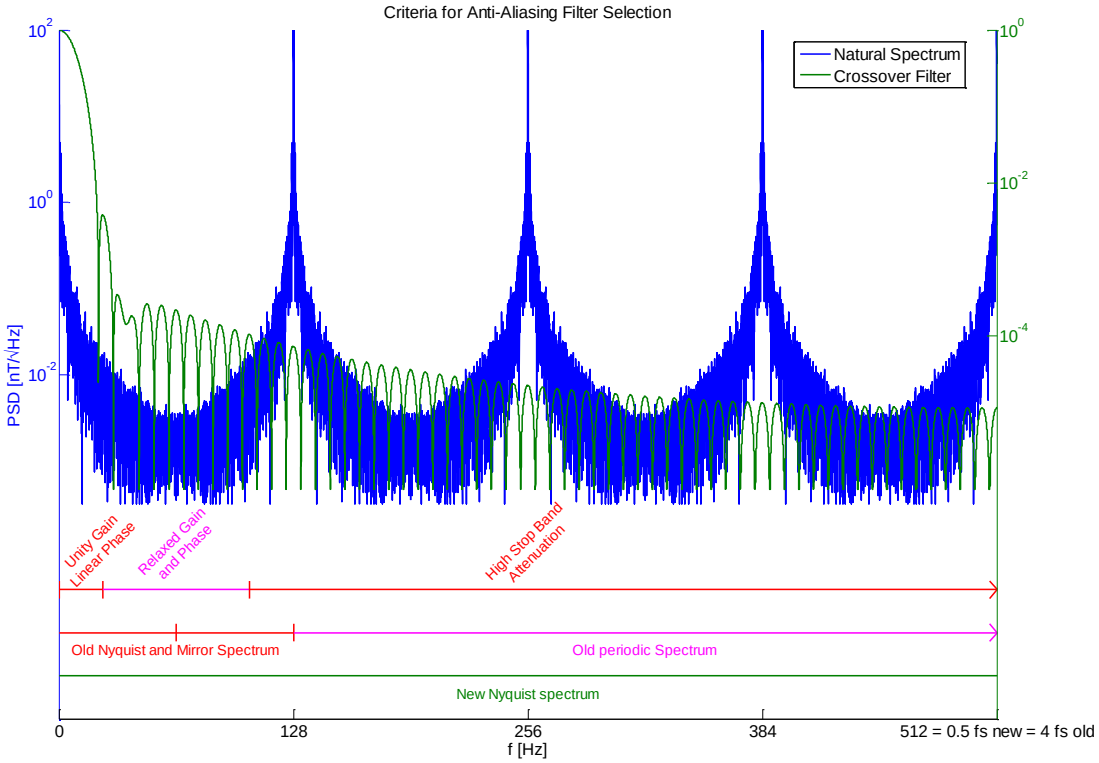

Figure 2–59 Selection Criteria for Anti-Aliasing Filter, Based on Signal Amplitude and Crossover Filter Gain

Figure 2–59 shows the frequency response of the 129-tap crossover filter, the signal spectrum and the resulting bands with different importance for gain, phase and attenuation. The band from 0 to roughly 20 Hz has a significant influence in the final data product and therefore unity gain and linear phase are important. From roughly 20 to 110 Hz both influence in the data product and signal amplitude are low, so gain and phase requirements can be relaxed. Above 110 Hz, the mirrored spectrum amplitude increases again, so high stop band attenuation is required.
Although these frequency response criteria would be sufficient for the production of a merged product, also in-flight verification of the merging process and the instrument models need to be considered. This verification is done by comparing data from all instruments in the frequency range of 1 to 60 Hz (see chapter 3.2). For this reason, the unity gain and linear phase criterion is desirable up to 60 Hz.

The requirement for unity gain and linear phase and the desire to reduce data loss due to filter settling (see filter basics in a.1) rules out IIR filters and only FIR filters are applicable. For FIR anti-aliasing filters, the desired properties of unity pass-band gain, steepness of transition region and stop band attenuation are dependent on the number of taps and the selected filter type (e.g., Schafer et al., 1973). For a given tap number, a tradeoff is required, because not all properties can be improved at the same time. This is visible in figures 2–60 and 2–61 which evaluate differently windowed sinc filters. To improve stop band attenuation at 64 Hz, the corner frequency was shifted to 48 Hz for these plots.

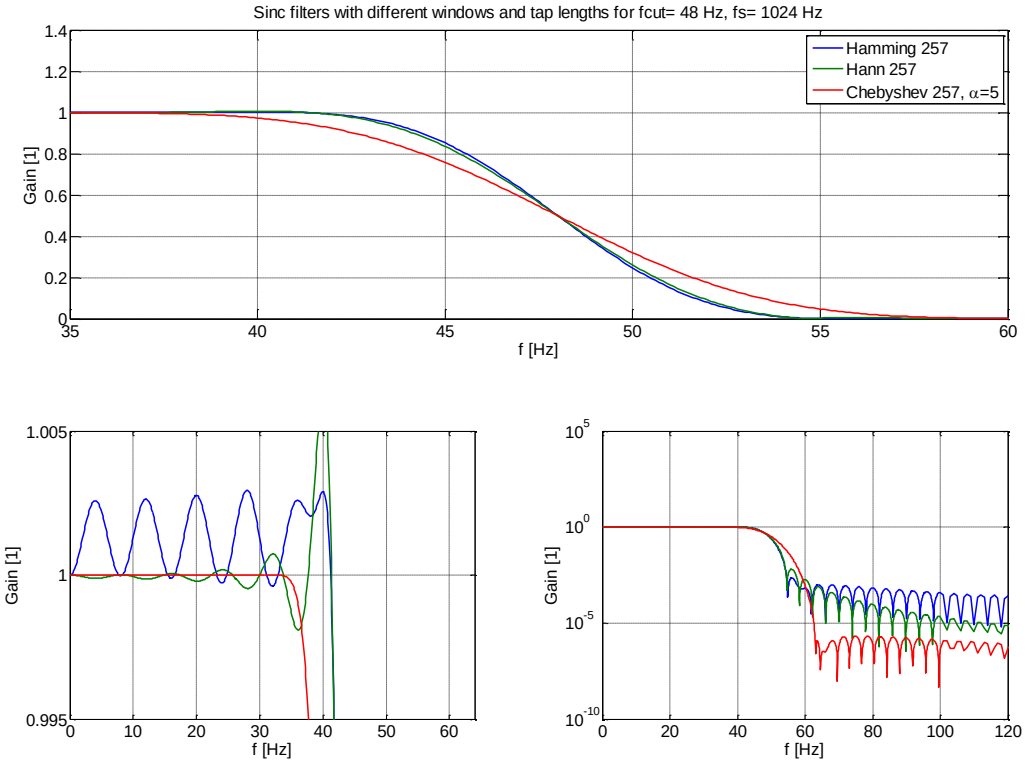

Figure 2–60 Comparison of Differently Windowed Sinc Interpolation Filters with 257 Taps

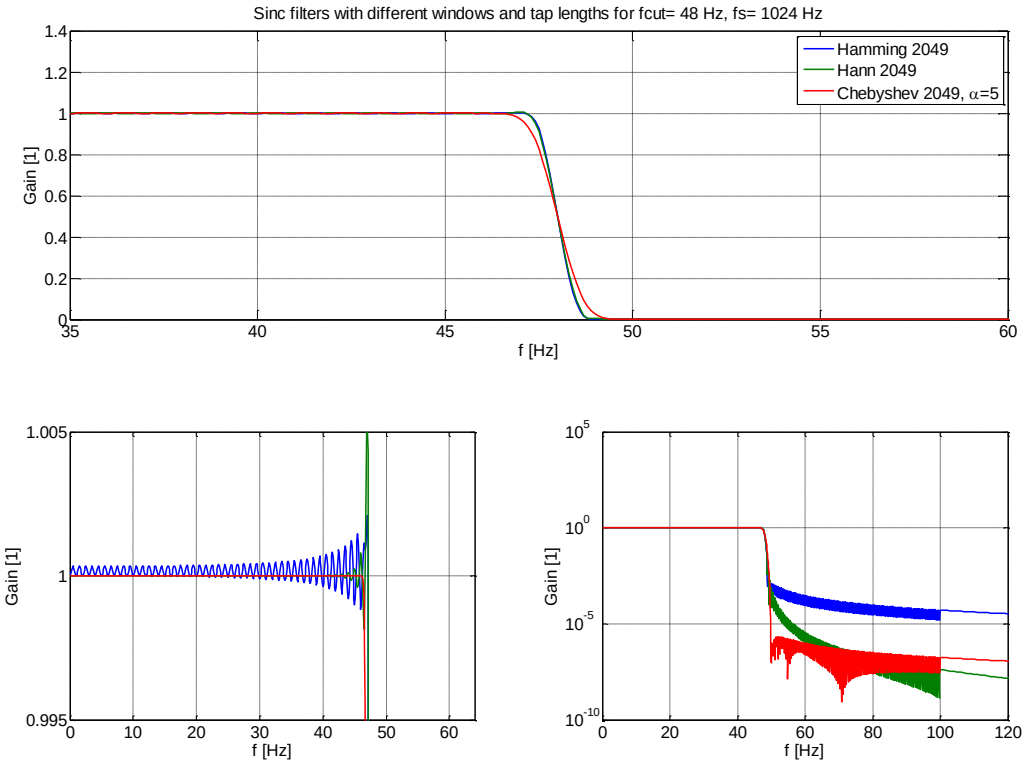

Figure 2–61 Comparison of Differently Windowed Sinc Interpolation Filters with 2049 taps

The Chebyshev window with 257 taps provides a very flat pass band and high stop band attenuation, but the transition from pass to stop band is quite slow. The 257-tap Hamming window delivers the

steepest initial slope, but has a moderate increase of stopband attenuation in comparison to the Hann window. If tap length is increased to 2049, all properties are improved, but the basic properties of the different window types remain the same.

The filter used for interpolation was selected depending on the application case. The preferred filter is the 2049 tap Chebyshev windowed sinc, which is most suitable for regular MMS operation with short burst periods. For the initial mission phases with longer burst periods, a 16,385 tap Hamming window was used, as the verification by comparison of instruments was more important during these initial phases and unity gain was desired up to a frequency of 60 Hz (see chapter 3.2).

Downsampling

SCM data at 8,192 Hz requires decimation before it is usable in the 1,024 Hz merged data product. When doing just decimation, all frequencies above the target Nyquist frequency of 512 Hz are folded into the remaining frequency band, similar to drawing the spectrum on a piece of transparent paper and folding it multiple times to achieve a desired width.

To eliminate of this effect, the frequencies above the new Nyquist frequency need to be removed before decimation. The requirements for this filter are similar to that for down-sampling, but with one exception: A drop in gain towards the Nyquist frequency is part of all data products of this world (even the raw SCM data) and is therefore less critical than a gain drop by upsampling which would end up in the mid frequencies of the merged product. The main topic is therefore not to have constant gain until the Nyquist frequency, but rather to document what the gain is.

The chosen filter in this case was a 16,385-tap sinc filter with Hamming window, as the raw data still have high sensitivity at 512 Hz and can be used until close to this frequency. The choice of this window is a tradeoff between transition band ripple, transition bandwidth and stop band attenuation. Due to the high sampling frequency, only 2 seconds of data need to be removed due to filter settling (see a.1.1).

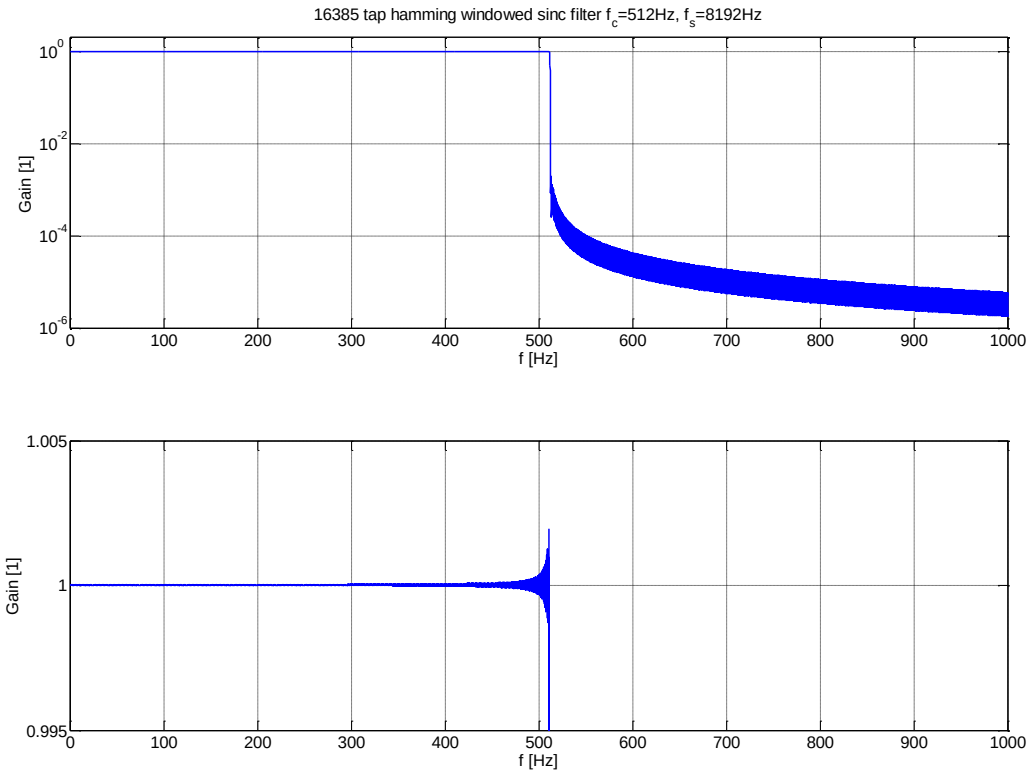

Figure 2–62 Hamming Windowed Sinc Filter for Downsampling

2.6.2. Time Shift

Although the sampling of SCM and AFG/DFG is synchronized, the time relation is in fact only isochronous. This means the sampling grid is identical, but there is a small constant time shift between the individual sampling times. This time shift can be calculated using the difference between data time stamps. The worst-case time shift for burst data is ½ sample of SCM 8,192 Hz data, which is roughly 122 µs. Before merging, it is therefore necessary to re-align data to the same time stamps by interpolation.

Time shifting is in fact similar to interpolation, as data is "interpolated" to intermediate time steps. The only difference is that no upsampling step happens beforehand and data is kept at its original sampling frequency. This means that the phase delay of the interpolation filter is no longer an integer multiple of samples, but is an arbitrary fraction of a sample. It is therefore no longer possible to create filters with constant phase delay, as the required symmetry to achieve this property cannot be achieved (Oppenheim et al., 1998, pp. 298ff).

One commonly used method for time shifting is the Lagrange filter which was published both by Waring and Lagrange (Waring, 1779, Lagrange, 1797). The Lagrange filter uses a polynomial interpolation scheme. If the order of this polynomial scheme is increased to infinity, the resulting interpolation function is again the sinc function. Its coefficients can be calculated (Smith, 2018, chpt. Lagrange Interpolation) using

$$h_\Delta(n) = \prod_{\substack{k=0 \\ k \neq n}}^{N} \frac{\Delta - k}{n - k} \qquad \textit{Equation 2-78}$$

The value Δ is the desired shift in samples, including a shift of N/2 samples caused by the length of the filter. The minimum deviation from unity gain and linear phase is achieved, when the distance from the center of the filter is minimized (e.g., for a filter with 17 taps, the delay should be between 8.5 and 9.5 samples). All further integer shifts can be realized using simple shifting without filtering.

The frequency response of this filter and its deviation from the ideal linear phase is dependent on the value of Δ and the number of coefficients. Since the shift itself is defined by the application, only the number of coefficients can be selected freely. A plot of the influence of different tap numbers on gain and phase delay is shown in figure 2–63.

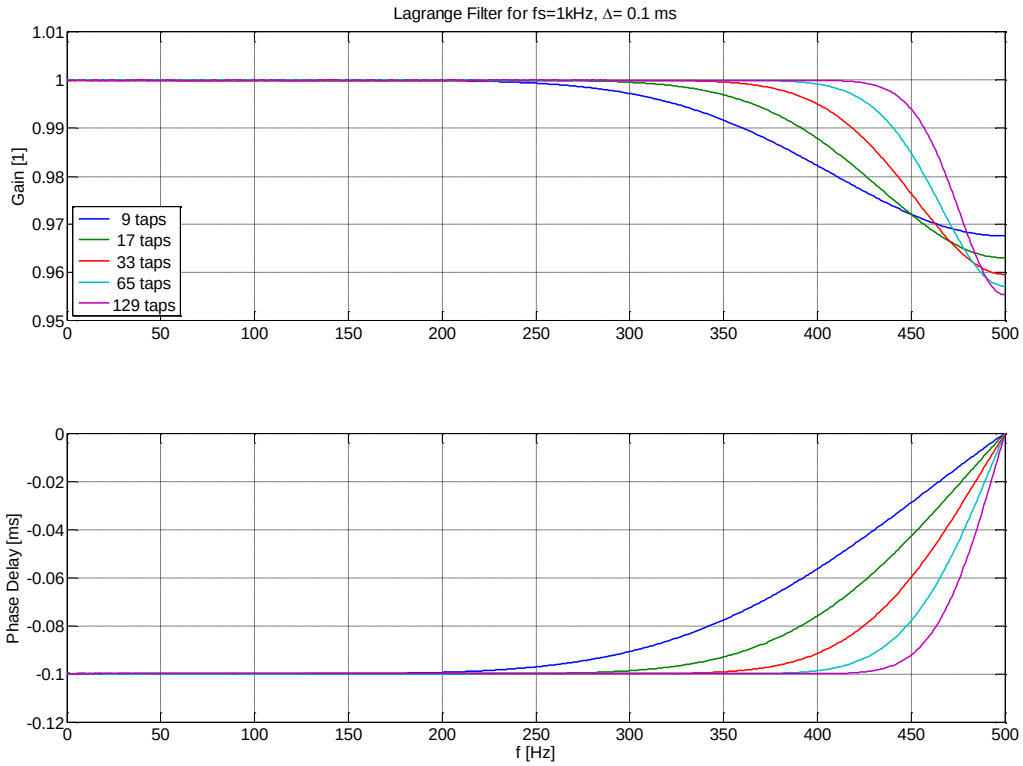

Figure 2–63 Effects of Tap Number in Lagrange Filters

The plot shows that the deviation from ideal behavior is small for low frequencies even for low tap numbers. The deviation is less than 10^{-3} from unity gain and less than 10 µs from constant group delay below 200 Hz. This already defines the way this filter should be used: As fluxgate data is only used at low frequencies, the non-ideal behavior of the Lagrange filter at higher frequencies is irrelevant. It is therefore beneficial to synchronize the AFG/DFG data to SCM time stamps and not vice-versa.

Figure 2–64 shows the influence of the shift Δ on gain and phase delay. For a constant tap number, a bigger shift results in a higher gain change and the deviation from constant phase delay starts a little earlier.

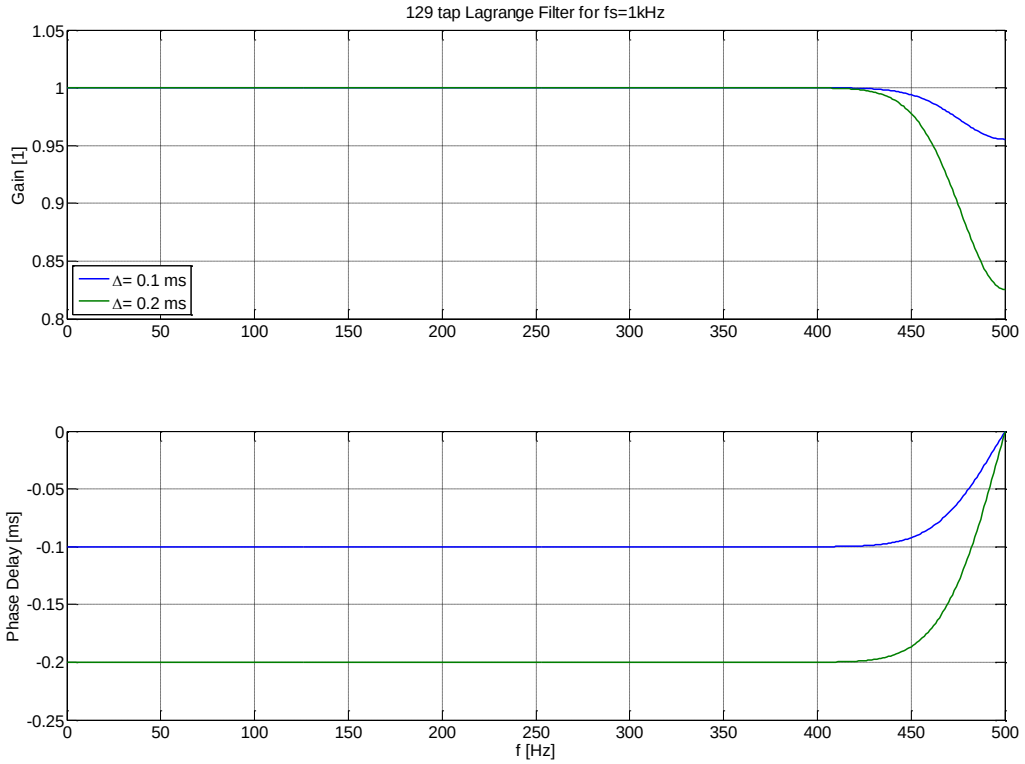

Figure 2–64 Lagrange Filter: Influence of Δ

The required shift is given by the time stamp distance between SCM and fluxgate data and cannot be selected, but it is possible to reduce the shift during downsampling from 8,192 Hz to 1,024 Hz. The sampling phase (the first remaining sample in the decimated product) needs to be chosen in a way to minimize the time distance to the first sample of fluxgate data.

The chosen filter for merging was a 17-tap Lagrange filter, as its influence on gain ($<10^{-3}$) and phase (<10 µs) is acceptable and therefore the decision was mainly driven by the low tap number that requires less data removal during filter settling (see chapter a.1).

2.7. Merging Process

The data flow from raw instrument data to the final merged data products not only includes the processing steps discussed in the previous chapters, but also regular in-flight calibration. In-flight calibration adjusts the DC gain, the sensor alignment and the orthogonalization of the sensors. The order of processing steps including this calibration has some degrees of freedom, but the outcome both on the data product quality and on the verification possibilities needs to be taken into account. An optimized flow chart of the merged burst data process is presented in figure 2–65.

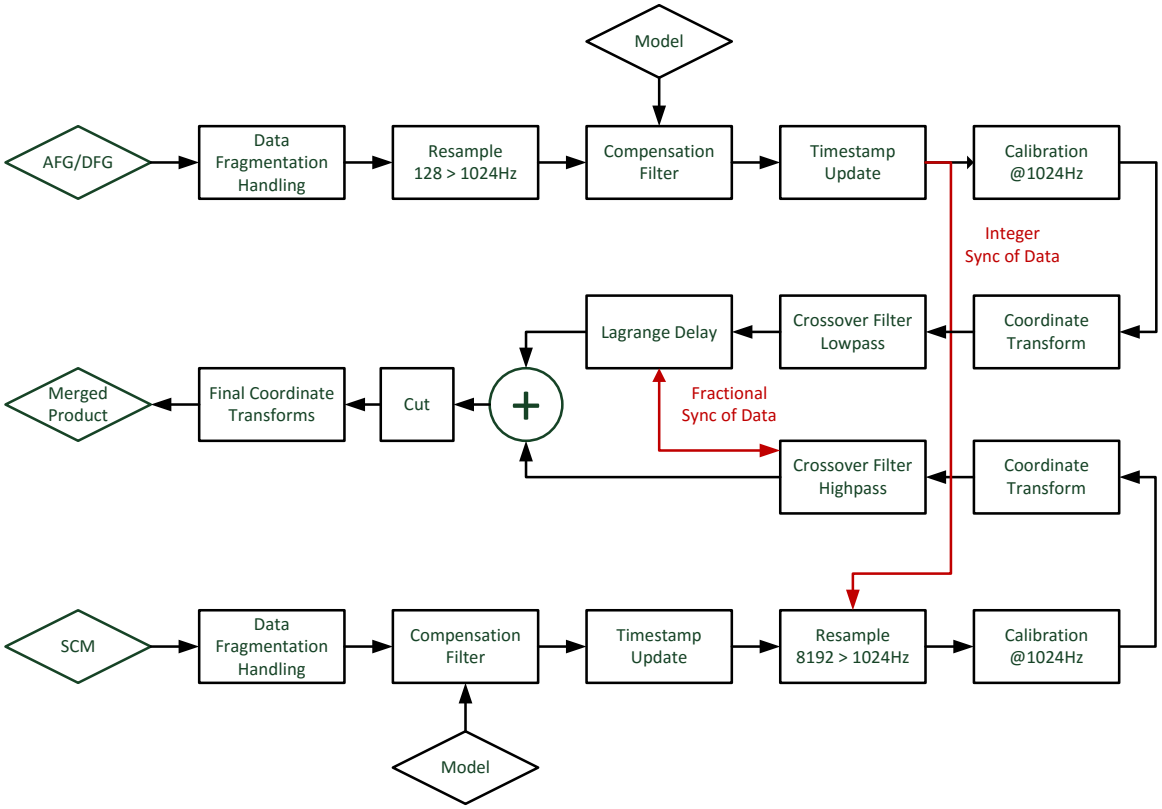

Figure 2–65 Flow Chart for Merging Burst Data

Data fragmentation handling is used to combine contiguous burst data files into one large data stream. This is necessary since burst data is not downlinked in one large block, but separated in small chunks with different download priorities. As the merging process includes filters, this means that data at the beginning and end of each chunk would need to be removed to eliminate the influence of filter settling. With fragmentation handling, data from contiguous neighboring files can be used to preload filters, so no data removal is necessary. This step must be completed before all other processing steps.

Resampling of data must be done in a way to ensure that the application of compensation filters happens at the data frequency these filters were designed for. For AFG and DFG, the compensation filters are applied at a sampling frequency of 1,024 Hz, for the SCM 8,192 Hz. The anti-aliasing filters for SCM need to be applied before resampling, those of AFG/DFG can be done at any position between resampling and merging, as all operations in between do not change their effect.

Model application and **time stamp updating** compensates the frequency response and removes known fixed time shifts that were part of modeling.

The target of **integer synchronization** is to reduce the amount of fractional sample time shifts in the Lagrange delay (see chapter 2.6.2). For a 1,024 Hz merged product, this shift is limited to ±0.125

samples by selecting the phase of decimation such that the remaining are the closest neighbors to AFG/DFG samples.

Calibration applies a gain factor and rotates the sensor axes to a spin-axis aligned orthogonal coordinate system. This rotation is needed to remove the influence of unavoidable mechanical imprecision as well as the changes of the spin axis relative to the body frame of the spacecraft. The rotation causes a mixture of data from different axes, which would also mix up frequency responses. The correct way is therefore to apply models before this rotation. However, since both, the required rotations and the difference between frequency responses are small, it is worth considering neglecting and moving both resampling and model application to a position after calibration. The advantage of this move is that this allows the use of the regular calibration process that is already used for non-merged data (see chapter 3.3).

Before merging, a **coordinate transform** to a common coordinate system could be necessary. Since this transform could involve rotation by larger angles, the mixture of frequency responses cannot be neglected. Fortunately, the MMS orthogonal mounted boom (OMB) coordinate system is considered as identical for all instruments and no coordinate transform is required.

The position of **crossover filters** in the processing chain depends on the type of selected filters. If a common filter is used for all axes, this filter can be applied at any position between data fragmentation handling and merging. If the filters are based on separate noise estimates for different axes, the filters need to be applied in the coordinate system in which the estimation was done.

The **Lagrange delay** aligns AFG/DFG samples to those from SCM. The required fractional delay is calculated from the time stamps of the instruments.

Merging becomes a simple addition of the resulting time series, using truncation to a common time frame. After addition, data that is influenced by filter settling times needs to be **cut** at the beginning and end of data.

The **final coordinate transform** is then provides the data in the non-spinning coordinate systems Geocentric Solar Ecliptic (GSE) and Geocentric Solar Magnetospheric (GSM). This process applies the standard rotation routines used also for all MMS magnetometer data products (Russell et al., 2016).

3. Verification and Application

3.1. Time Stamp Post-Processing

3.1.1. Time Stamp Jitter on MMS

Although the onboard time of MMS and the FIELDS CDPU is very accurate, there is still some remaining jitter on the time stamp. The sources of this jitter are the inaccuracy of the GPS time, the jitter introduced by onboard communication as well as jitter caused by clock differences.

The onboard GPS time standard is provided by a GPS receiver. Although the accuracy of military GPS receivers is quite high (<40 ns with fixed location receivers), this accuracy is limited by the fact that the MMS satellites have high orbits (700,000 km to 1,500,000 km) and move quite fast in comparison to ground based objects. This introduces an error in position estimation and therefore also an error in time. Unfortunately, the resulting error is only specified as a maximum error of 325 µs (Tooley et al., 2016) relative to TAI, but no information about the jitter is given. An estimate of jitter can be obtained using the accuracy of position determination, which is specified with 100 m. With the propagation speed of GPS radio waves (speed of light), this accuracy translates to a time jitter of 333 ns, which is much less than the specified overall accuracy of 325 µs.

The GPS time is distributed onboard using the PPS signal (see 1.1.3.2), which is used to set the onboard time sources to the correct time at the PPS signal edge. This distribution is done using shared communication lines, which are subject to communication collisions caused by other messages. In case of collision, an ongoing transmission on these lines cannot be interrupted and the sending of the PPS pulse is delayed until the line is free again. The other messages on the shared communication line can cause a delay of 35 µs every 20 seconds and a delay of 20 µs that could in principle occur at every PPS signal. However, a coincidence of the PPS and the other messages for a longer time is highly improbable.

The last source of jitter is the handling of the time within the CDPU. The CDPU sets its time to the specified value (the full second) at the arrival of the PPS signal. Between PPS signals, the CDPU clock drifts relative to the PPS standard dependent on the quartz clock frequency. This frequency is typically accurate to a few ppm and can change with temperature (a few ppm/K) and due to aging. The resulting jitter appears periodically, but has a constant jitter amplitude below 10 µs.

The most prominent mechanism that is visible in the data is the 35 µs jitter caused by PPS distribution.

3.1.2. Smoothing of Time

Time stamp post-processing on ground is done to minimize the effect of time stamp jitter by generating interpolated timelines using packetized data. Each data packet generated by the FIELDS CDPU only contains a single time stamp from the first contained sample. The time stamp of all further samples is calculated either using the nominal sampling rate (for standalone packets) or by interpolating the time across sections of contiguous packets.

One approach for interpolation is to calculate the sampling time t_s using the difference between first and last time stamp of an interval and dividing it by the number of sampling intervals between these time stamps.

$$t_s = \frac{t_N - t_0}{N} \qquad \textit{Equation 3-1}$$

The timeline can then be calculated using

$$t(n) = t_0 + t_s \cdot n \qquad \textit{Equation 3-2}$$

This approach generates a smooth timeline without jitter with an error that is dependent on the jitter of the first and last time stamp used for interpolation. Figure 3–1 shows the effect of jitter on a simulated time sequence. To increase the visibility of effects, a sampling frequency of 16,384 Hz was used. The upper panel shows the ideal interpolation using unjittered first and last time stamps. If, e.g., the first time stamp is jittered, this error is expanded across the complete timeline (see center panel) and the time stamp of all following samples is falsified by a decreasing amount.

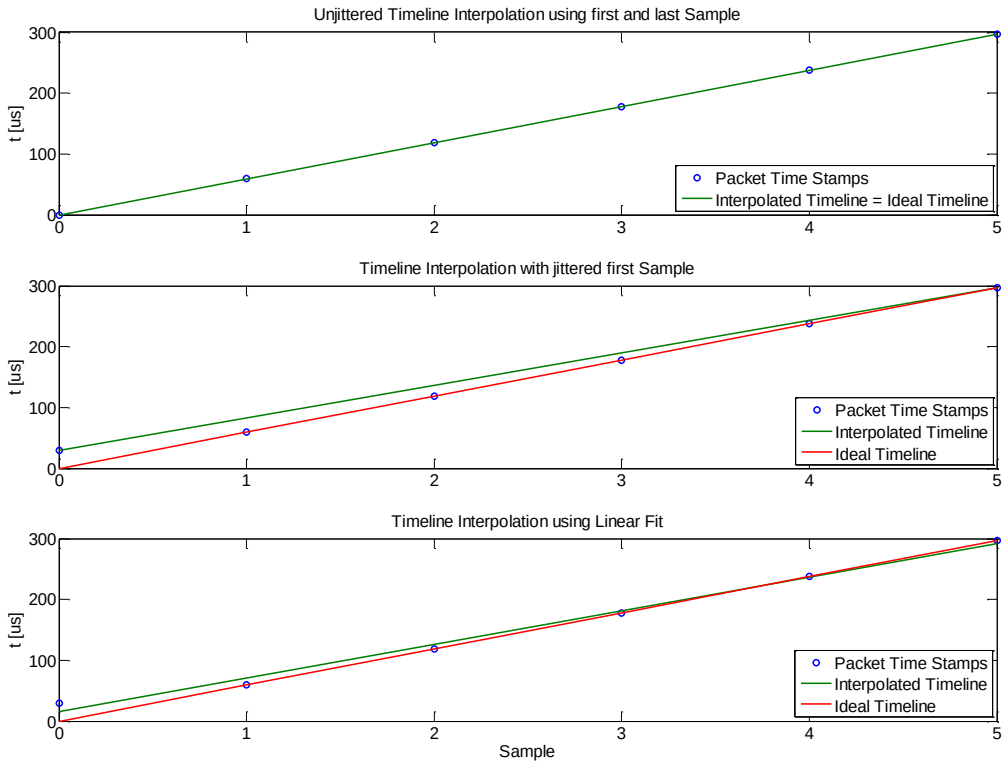

Figure 3–1 Simulated Effect of Jitter on Time Stamp Interpolation.

A different approach is to interpolate the timeline using a linear least mean square error fit (see equation 3-3 and figure 3–1 lower panel).

$$(k,d) = \underset{k,d}{\operatorname{argmin}} \left(\sum_i \left(t_i - (k \cdot i + d) \right)^2 \right) \qquad \textit{Equation 3-3}$$

The time is then calculated using

$$t(n) = k \cdot n + d \qquad \textit{Equation 3-4}$$

This approach is less sensitive to the single jitter values at the start and end of the interval, but is more sensitive to a bias (average delay) of the jitter. This bias can be caused by both collision jitter and clock drift. Collision jitter causes a positive bias (the average collision delay of the complete data set), while the clock drift bias can have both signs.

A third approach includes jitter categorization. The jitter caused by clock drift is periodic and changes quite slowly, while the communication jitter varies in appearance and value. It is therefore possible to categorize time stamps as potentially more or less jittered. The previously presented methods of linear interpolation and least mean square error fit can then be applied using the less jittered samples only and the residual error in smoothing is reduced.

For MMS FIELDS data processing, it was decided to apply the first approach using first and last time stamps, as it is computationally less expensive.

Any of the presented time smoothing methods generates a small residual error that is distributed across the complete data set. Unfortunately, this residual error can be different for data that is time stamped in the CDPU (AFG and DFG) and the DSP (SCM). This difference is either caused by data sets with different length (which could mean an additional PPS synchronization within the data) or by a PPS synchronization that occurs right between CDPU and DSP time stamping.
In both cases, the difference in residual error appears as an erroneous time shift between AFG/DFG and SCM data. The worst-case value of this time shift is dependent on the residual value of collision jitter, as clock drift jitter changes slowly and is therefore almost identical in AFG/DFG and SCM data.

The time shift caused by the residual error difference reduces the phase delay precision of the merged data product to the worst-case jitter amplitude of the collision jitter, which is 35 µs. This error was considered as acceptable.

3.2. Verification of Merged Data

The developed instrument models as well as the complete merging process were verified using in-flight data from MMS. For this purpose, data from September to November 2015 was prepared for merging using a modified version of the process in figure 2–65. This process skips the crossover filters and stops just prior to merging. With this approach, the preprocessed data is fully compensated, time aligned and rotated to a common coordinate system, but is still available with its original bandwidth.

This bandwidth is then restricted to a frequency band between 1 and 60 Hz using fourth order Butterworth filters. This common frequency band is available in the data set of both instrument types with acceptable noise floor.

The following paragraphs give an overview of the verification approach. For simplicity, the plots only show the comparison of DFG and SCM on MMS 1.

3.2.1. Gain Comparison

Figure 3–2 shows a small interval of preprocessed DFG and SCM data (see above) as well as data from the MMS SCM L1b data product, which is an MMS standard data product prepared by the SCM instrument team. The main findings of this plot are that DFG and SCM gain are obviously different and that the differences between the two SCM data sets are minimal.

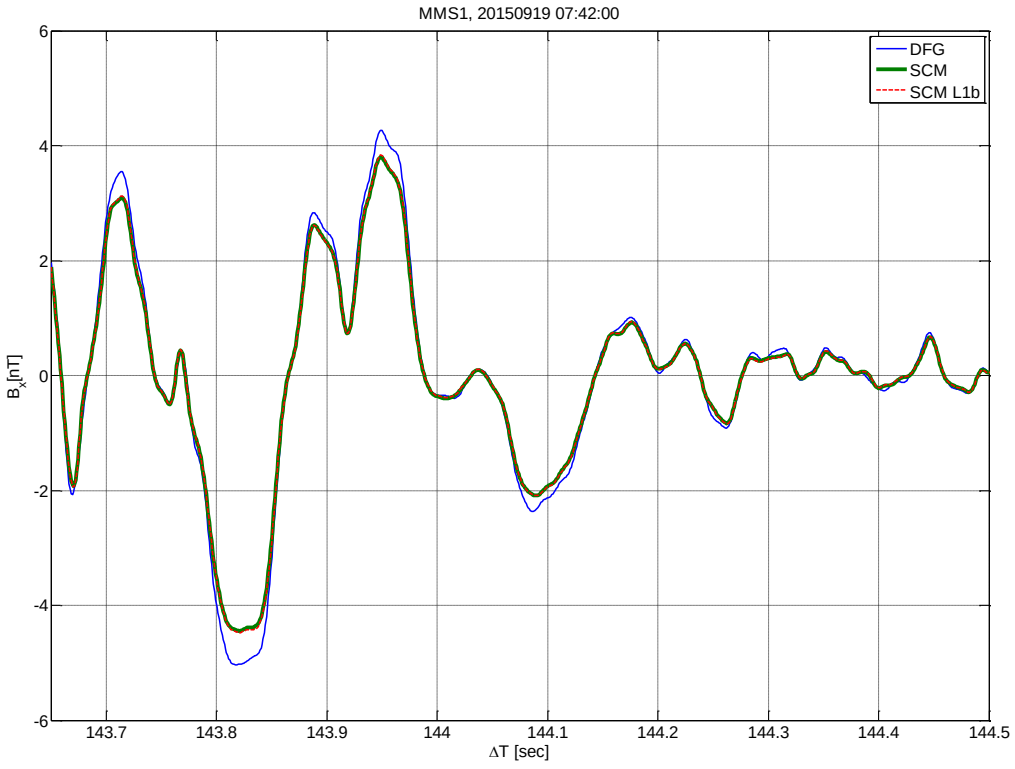

Figure 3–2 Comparison of Band Limited DFG and SCM Data

Further comparison of multiple data sets showed that the gain of SCM differs by about 13% from the DFG and the AFG in all data sets. This gain difference was also verified for frequencies down to 0.1 Hz, as it is visible even with the low signal-to-noise ratio of the SCM at these frequencies. This difference is therefore unaffected by the frequency response of AFG and DFG and is a real difference in gain. The AFG and DFG gain for DC and low frequency was verified by in-flight calibration to an accuracy of 10^{-4} and is not affected by instrument models, upsampling or merging filters. The difference is therefore caused by a change in the SCM gain. The SCM team calculated a similar result and the gain calibration factor was adjusted accordingly for all SCM instruments. This adjustment was done by comparing the

SCM team results with the estimates of the gain that were calculated during orthogonality and alignment calibration (see chapter 3.2.3).

3.2.2. Spectral Comparison

The approach already applied in frequency response estimation (see 2.1.2) was also used for computing a "cross frequency response" between SCM and the fluxgate instruments. The data from SCM was considered as output data Y and the data from DFG was used as input data X.

$$H(k) = \frac{\hat{S}_{SCM-DFG}(k)}{\hat{S}_{DFG-DFG}(k)} \qquad \textit{Equation 3-5}$$

The result of this frequency response estimation is the virtual filter that is needed to make the SCM data identical to that from DFG. If the complete modeling and merging process was done correctly, no further change should be required. The ideal frequency response result should have unity gain and zero phase, which corresponds to a time domain transfer function of 1.

The frequency response estimation was done using the data preprocessing described in chapter 3.2.1 on data segments with a length of approximately 10 minutes. The achievable quality of the estimate depends on the amplitude of the magnetic field in relation to the instrument noise floor. It was therefore necessary to restrict the used data to intervals with sufficiently high SNR. Figure 3–3 shows a comparison of the signal level in the selected intervals with the instrument noise floor. The selection criterion was an average signal level of more than 20 pT/√Hz in the frequency band from 30 to 50 Hz. This preselection reduced the useable intervals to about 10 % of the original data. Each blue dot represents one PSD bin of one of the 10-minute intervals.

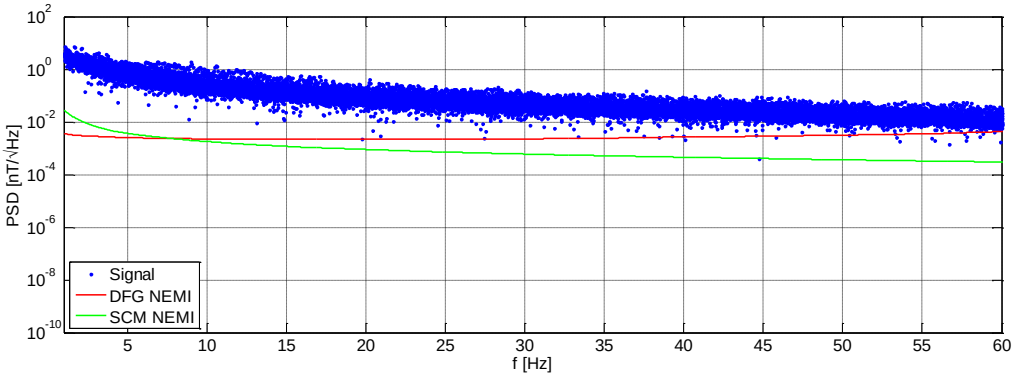

Figure 3–3 Power Spectral Density of Used Intervals for Cross Frequency Response Estimate

Figure 3–4 shows the resulting cross frequency response estimates. The error bars of these estimates were calculated using an expected SNR, which is given by the average signal power in figure 3–3 in relation to the instrument noise floor (see figure 1–31).
The gain error bar is directly dependent on the SNR, as the estimation treats the higher signal power of the noise as "higher" gain of the instrument. The phase error is based on the assumption that the worst-case noise signal with an amplitude given by the SNR is phase shifted by 90° relative to the natural signal. This results in a potential phase shift error of

$$\Delta\varphi = tan^{-1}(SNR) \qquad \textit{Equation 3-6}$$

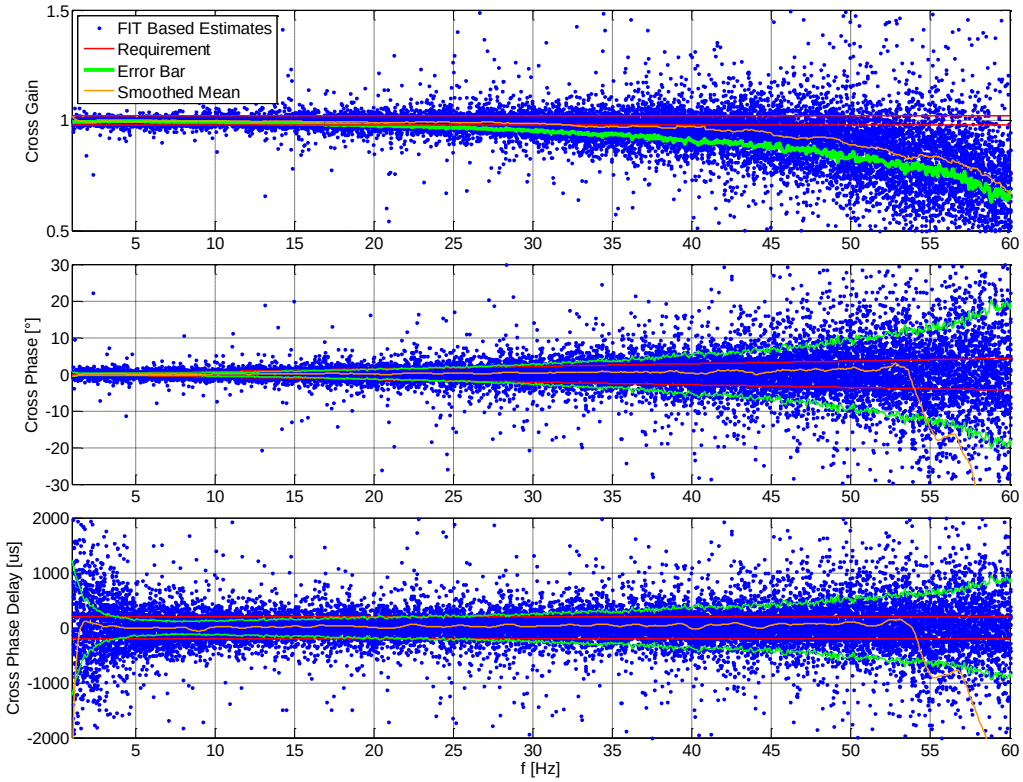

Figure 3–4 Cross Frequency Response from SCM to DFG

For comparison purposes, the same computation was repeated using the SCM L1b data from the SCM team (figure 3–5). This comparison shows a small increase in phase delay below 5 Hz, which is similar to that which was identified between FIT and SCM reference measurements (see figure 2–52). The correctness of the FIT based model is therefore verified by in-flight measurements and can even provide an improvement to the SCM calibration.

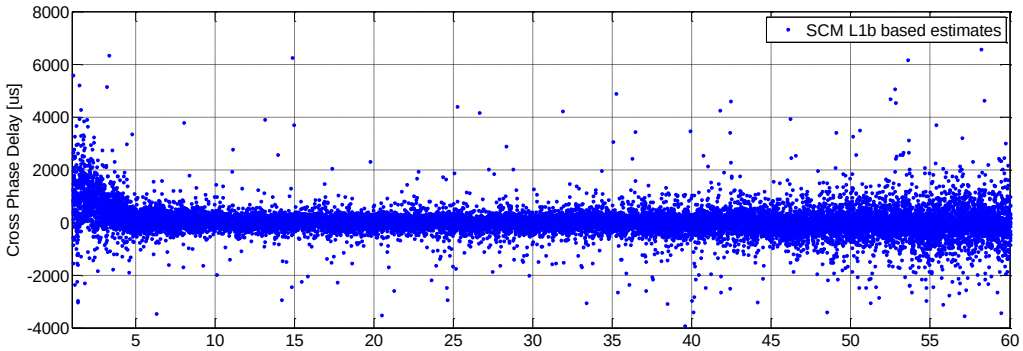

Figure 3–5 Cross Phase Delay using Data from the SCM Team

Conversly, the influence of this deviation on the merged data product is so small that both the FIT based and SCM reference calibration can be used without problems, as long as the gain correction of 13% is applied (see 3.2.1).

However, given the large error bars of in-flight estimation, the results are only representative in the frequency band from 5 to roughly 30 Hz, as, in this case, the mean values of gain and phase delay are within the specified goals for the merged data product (see chapter 1.3). In the other frequency bands, the verification is not possible due to insufficient magnetic field magnitude in the available data.

3.2.3. Cross Calibration of SCM Alignment and Gain

With the preprocessed data, it was also possible to analyze the gain and alignment of the SCM. Usually gain, orthogonality and most alignment parameters of the fluxgate magnetometers are estimated in-flight using the properties of the magnetic field measured on a spin-stabilized spacecraft (Kepko et al., 1996, Khurana et al., 1996). Any deviation from a coordinate system that is not orthogonal and aligned to the spacecraft spin axis generates characteristic signals at DC, the spin frequency and its harmonics.

Fluxgate in-flight calibration uses these characteristic signals to estimate a matrix that is used to rotate the sensor measurement data to the spin-aligned coordinate system. This method is infeasible for the SCM, as its signal-to-noise ratio at the satellite spin frequency (e.g., 50 mHz for MMS) is insufficient.

Fortunately, the alignment and gain of the SCM can be estimated by comparing the preprocessed SCM dataset with the calibrated DFG data. This is done by estimating a suitable transformation matrix T using equation 3-7. This matrix gives the coordinates of the non-orthogonal SCM coordinate system (123) within the calibrated and orthogonal DFG coordinate system (XYZ_{OMB}, orthogonal mounted boom system).

$$T = \underset{C}{\operatorname{argmin}} \left(\sum_{k} (T\, B_{DFG} - B_{SCM})^2 \right) \qquad \textit{Equation 3-7}$$

The transformation matrix estimate T is then converted to a better understandable representation of spherical and Cartesian coordinates. The Cartesian coordinates are added to avoid the discontinuity of a spherical coordinate system around its poles, where small changes of a vector direction can result in angle changes of 180°. Figure 3–6 shows the different angles and vectorial components within the OMB coordinate system. These variables are then combined to get to a calibration matrix C that converts data from the SCM sensor coordinate system (123) to the DFG OMB system (XYZ). This matrix is composed of a rotation matrix R and a diagonal gain matrix G that contains the individual axis gains $G_{1,2,3}$.

$$R = \begin{pmatrix} \sin\vartheta_1 \cos\varphi_1 & \sin\vartheta_1 \sin\varphi_1 & \cos\vartheta_1 \\ \sin\vartheta_2 \cos\varphi_2 & \sin\vartheta_2 \sin\varphi_2 & \cos\vartheta_2 \\ d_{3X} & d_{3Y} & \sqrt{1 - d_{3X}^2 - d_{3Y}^2} \end{pmatrix} \qquad \textit{Equation 3-8}$$

$$G = diag(G_1, G_2, G_3) \qquad \textit{Equation 3-9}$$

$$C = (GR)^{-1} \qquad \textit{Equation 3-10}$$

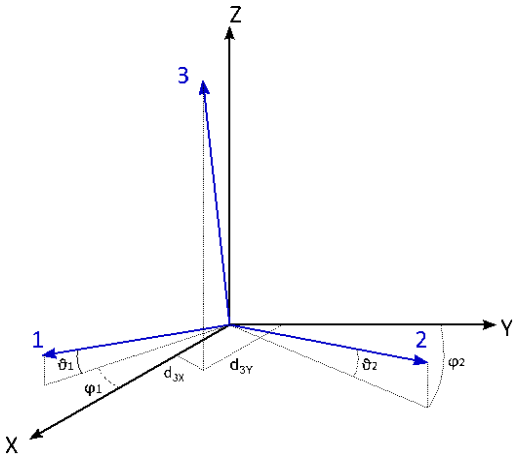

Figure 3–6 SCM Coordinate Transformation

Figure 3–7 shows the estimation results using a preprocessed 3-month long data set. Each dot represents a 16-second data segment. The x-axis gives the mean power of the magnetic field in the respective segment.

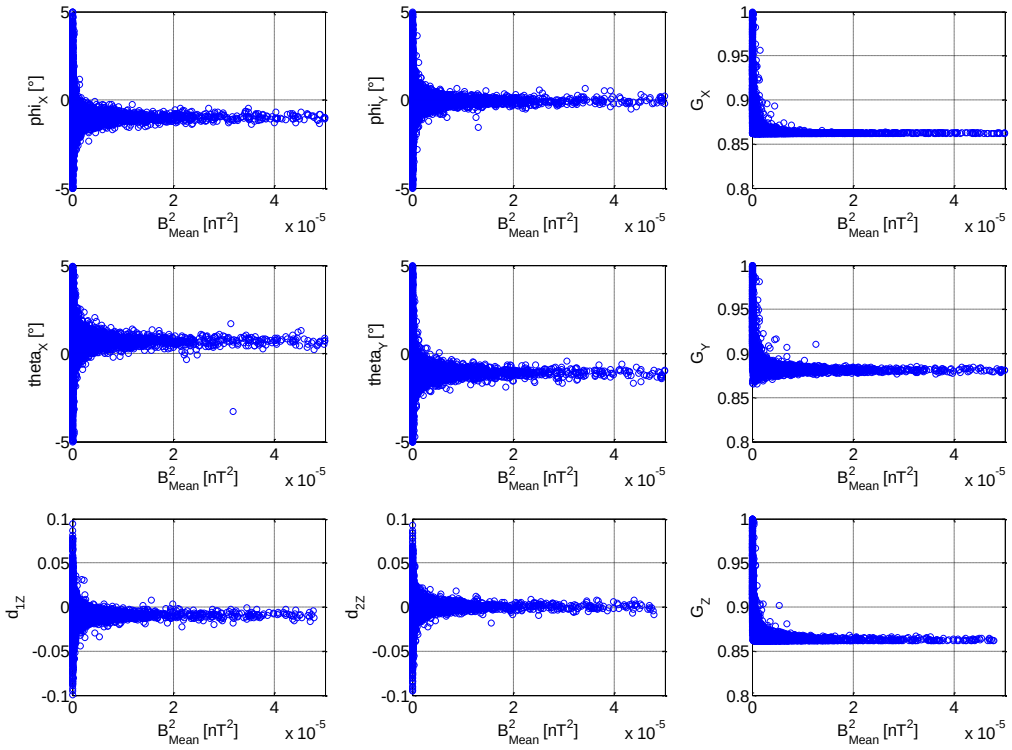

Figure 3–7 Components of Rotation and Gain Matrix

The matrix components converge to a smaller standard deviation for higher magnetic field power. Table 3-1 lists the average values of the components that were calculated using only segments with a magnetic field amplitude of more than 400 pT_{RMS} within the 16-second data segment.

φ_X	ϑ_X	G_X	φ_Y	ϑ_Y	G_Y	d_{1Z}	d_{2Z}	G_Z
-0.9243°	0.7319°	0.8727	-0.6790°	-1.1288°	0.9057	0.0092	-0.000487	0.8631

Table 3-1 Averaged Components of SCM Rotation and Gain Matrix for MMS 1

The frequency dependency of orthogonality was examined, but no major changes were found in the frequency band from 1 to 30 Hz. The method used by Cornilleau-Wehrlin et al. (1997) can therefore be improved by determining the SCM alignment in a frequency band with a good signal-to-noise ratio. With this method, the SCM in-flight calibration can be improved by linking it to the otherwise inaccessible methods used for fluxgate instrument calibration.

3.3. Final Application

The original merging process presented in figure 2–65 was modified to simplify processing at the MMS science data center. This work was conducted in a common effort by the SCM team (Olivier Le Contel, Laurent Mirioni), the UNH FIELDS team (Matthew Argall, Mark Chutter) and myself.

The modified flow reuses the fluxgate and search-coil standard calibration software, applies a different merging filter and is able to produce an 8,192 Hz data product. Figure 3–8 shows the modified data flow with major changes highlighted in blue and original blocks in black.

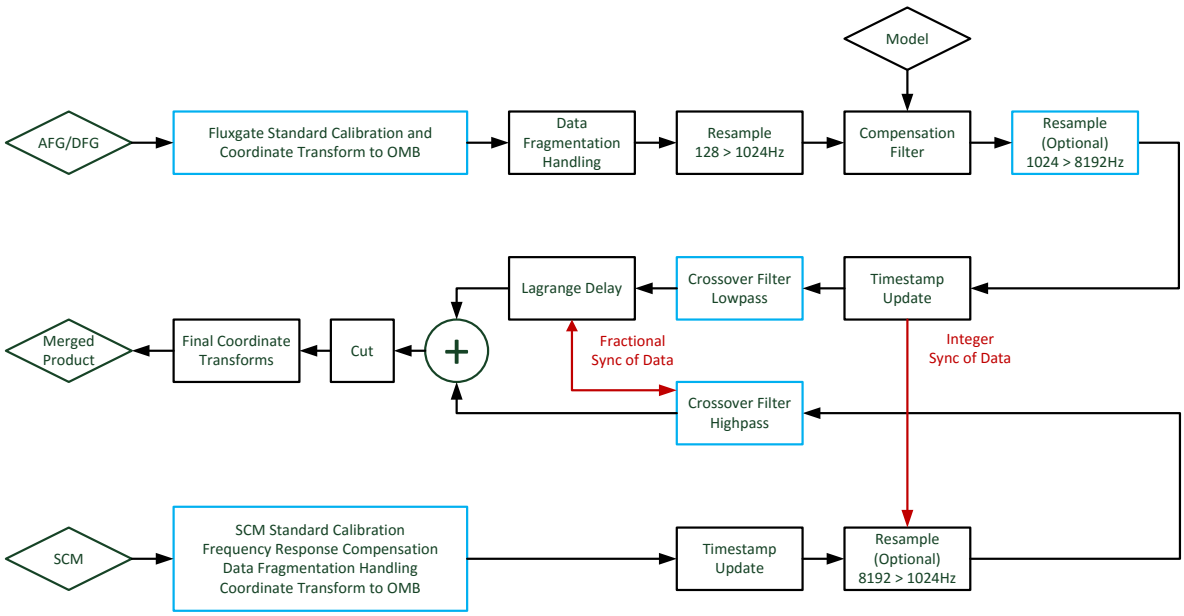

Figure 3–8 Modified Flow Chart for Merging Burst Data at the MMS Science Data Center

In this modified data flow, the standard fluxgate calibration is executed before frequency response compensation is applied. This means that the coordinate transform within this calibration mixes data from different sensors axes with their respective frequency response, which are then compensated with a single frequency response. This was considered as acceptable, as the differences between the frequency responses of the individual axes are quite small (see figures 2–41 and 2–42). In addition, the contribution of other axes in the transformation matrix is only in the order of 5‰, since the sensor and orthogonal mounted boom coordinate system are almost identical. The change introduced by this axis mixture is therefore negligible.

A further modification of the original data flow is the application of the SCM standard calibration and frequency response compensation. The gain adjustment found within this thesis (see 3.2.3) was merged into this calibration and the remaining differences in frequency response and timing (see figures 3–4 and 3–5) were considered as acceptable.

The use of fluxgate and SCM standard calibration software has two major advantages. The first advantage is that there is no need for additional software features in the calibration software, which would result in a separate software branch that would need to be supported over the entire lifetime of the MMS mission.

The second advantage is that a separate software branch would require intermediate data files in the order of 700 GByte per year in both, the main and backup data servers. This data amount is further increased if multiple data versions are generated that could be caused by changes in calibration parameters and software. The process presented here reuses already existing intermediate files and does not require additional storage beyond the merged data product.
In addition, the use of the SCM calibration software enabled a change of the merged data product sampling frequency from 1,024 Hz to 8,192 Hz. The original concerns of the MMS team that an 8 kHz product would only result in an unnecessary effort, both in storage and computation power for analysis, were no longer considered as valid at this time. The production of the merged data product is therefore done with the SCM standard calibration at 8 kHz. This calibration was verified for frequencies up to 512 Hz in this thesis.

The last modification is the introduction of a merging filter that is based on in-flight estimation of the instrument noise floor. The work on this improved filter was done under the lead of Matthew Argall (UNH FIELDS team) which will presumably be published in 2018 and is available as preprint (Argall et al., 2018).

The final process was implemented by the FIELDS team (Matthew Argall, Mark Chutter) who embedded the processing routines developed during this thesis in the framework required at the SDC. The produced software generates the fluxgate-search-coil merged (FSM) data product on a routine basis. The data is available for download at the SDC using the MMS standard data management software SPEDAS.

4. Conclusion

The common effort of the MMS FIELDS team allowed the generation of a merged data product from search-coil and fluxgate instruments. The presented approach combines both instrument types to a virtual instrument with constant gain, linear phase and known timing as well as the best sensitivity and lowest noise floor.

The virtual instrument is based on instrument models that were developed using data from a full end-to-end on-ground calibration campaign. In this campaign, the instruments were excited using magnetic field test signals synchronized to the MMS time standard. These signals were generated with a coil system and a purpose-built current generator that is able to produce currents with arbitrary waveforms. Precise knowledge about the amplitude and timing of the current was provided by measuring the actually generated current relative to the instrument's time standard.
The magnetic field measurements of the instruments and the current measurements were then used for the calculation of instrument models. The fluxgate instruments were modeled using finite impulse response filters based on a Wiener-Hopf solution, while the search-coil required an infinite impulse response model. The later model was based on a physical model of the search-coil which was needed to overcome the impact of high gain variation.
The generated models were cross checked with the previous reference measurements as well as available technical documentation. This comparison shows more congruency than the initially targeted accuracy of 2% for AC gain and 200 µs for phase delay.
The models were then applied in a carefully designed processing chain that merges data from both instrument types to a single product using a complementary filter approach.

The accuracy of the instrument models and the quality of the processing chain was evaluated by comparing in-flight magnetic field data in the common frequency range of fluxgate and search-coil instruments between 1 and 60 Hz.
This comparison of preprocessed data showed good agreement between the instruments and resulted in an updated absolute gain factor for the search-coil. Apart from this updated gain, the relative comparison shows a gain accuracy of 1% and a phase delay accuracy of 100 µs, both of which are better than the initially targeted accuracy levels. Strictly speaking, these accuracy levels are in fact not the real result, but simply a measure of the uncertainty in the accuracy estimate. This uncertainty is caused by the low signal-to-noise ratio in the compared frequency range, which is due to the low amplitude of the natural magnetic field signals. It is therefore only possible to conclude that the achieved accuracy is at least as good as the uncertainty of the result, but the actually achieved accuracy remains covered by noise.
The remaining limitations of the in-flight comparison also give the justification for the high effort spent in ground calibration of delays and frequency response. Any in-flight estimation of these quantities can only deliver relative information and is further limited in accuracy by the available natural signal levels.

The good relative agreement between the instruments gives confidence in the absolute accuracy of the instrument models used for frequency response compensation. This is supported by the fact that the independent calibration of the SCM team delivers identical results.

The data processing chain for the merged data product was further improved in a cooperation within the FIELDS team and is now used in routine processing at the MMS science data center. The resulting data product is available for download using the SPEDAS software tools.

Overall, the excellent design of MMS and FIELDS, the magnetic cleanliness level of the spacecraft, the quality of the instruments and their on-ground and in-flight calibration as well as the work done in this thesis allowed the generation of a new merged data product with unprecedented data quality. This

data product opens a new perspective on magnetospheric events has that already resulted in a number of publications (e.g., Plaschke et al., 2016, Vörös et al., 2017 and Yordanova et al., 2016), with many more to come. In addition to the data product itself, the steps toward this product also resulted in an improved understanding of the frequency and timing properties of both, search-coil and fluxgate instruments.

The usefulness of the merged data product for magnetospheric science as well as in instrument understanding is visualized with an example in figure 4–1. It shows a blurred image that only reveals a rough color structure, similar to low-pass filtered data from the fluxgate instruments. This image is complemented by a sharp view that gives the details of all edges, but is missing background context, similar to high-pass filtered search-coil data. Only a merged image of both data sets gives a more detailed view of MMS, its instruments and the surrounding magnetosphere.

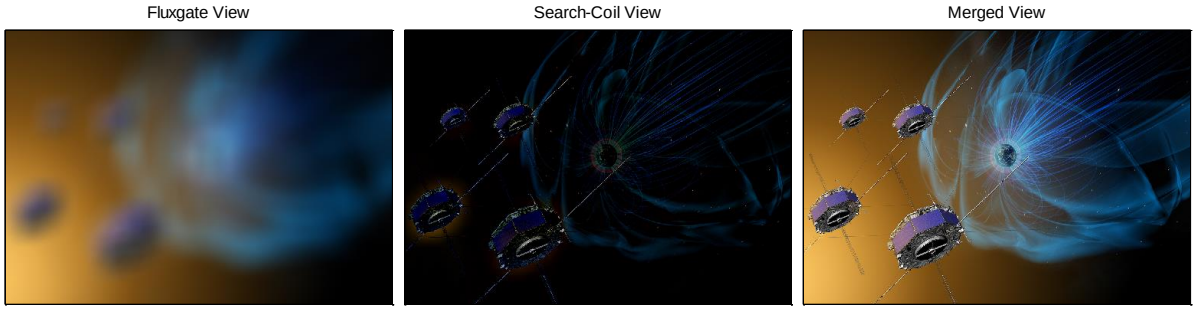

Figure 4–1 Visualization of the Advantages of a Merged Data Product (Modified from Original Image, © NASA[31])

[31] © NASA, https://www.nasa.gov/feature/goddard/2016/nasas-mms-celebrates-a-year-in-space

5. Outlook

Future Missions

The data product generated during this thesis resulted in an increased interest in merged data products. Currently, merged data products are being considered for several current and future missions. This includes Bepicolombo MMO (a mercury mission, launch October 2018), JUICE (a Jupiter mission, launch 2022), Parker Solar Probe (a mission to the Sun, launch August 2018) and Solar Orbiter (a mission to the Sun, launch 2019).

However, most of the aforementioned missions are already beyond the design phase that allow use of the approach presented in this thesis. In the case of MMO, Parker Solar Probe and Solar Orbiter the flight instruments are already integrated on the spacecraft and a measurement campaign like the MMS FIT measurements is no longer feasible. Furthermore, the approach to sampling and time synchronization used in these missions is quite different from that on MMS.

With the experience gained from this thesis, we are confident that an acceptable level of accuracy can be achieved by conducting similar measurements on available ground reference models and augmenting the gained data from these measurements with an in-flight comparison. However, this accuracy level will of course be lower than that achieved with the MMS measurements and needs to be discussed on a case-to-case basis in accordance with the respective mission accuracy goals.

Time Stamping in Synchronous Designs

In future missions with similar instrument suite design like MMS FIELDS, the time stamp smoothing methods described in chapter 3.1 could be improved by using two different time standards: an instrument internal clock without synchronization and the external synchronization pulse. Measurement data would be time stamped using the internal clock and real time correlation would be established by also time-stamping the arrival of the synchronization pulse with the internal clock.

With this mechanism, the information about sampling time and synchronization is preserved in its entirety without information loss thus avoiding problems such as those mentioned in chapter 3.1. The cost of this advantage is some change in hardware and/or software and a little data volume for sending the time stamps of the synchronization pulse.

Feedback, Orthogonality and their Connection to Frequency Response

Both, search-coil and fluxgate instruments use 3-axis sensors with magnetic feedback. This magnetic feedback causes crosstalk between the sensor-axes due to the unavoidable non-idealities in the sensor (e.g., small mechanical misalignments and magnetic crosstalk). Due to these non-idealities, the feedback of one axis will also appear in all other axes and results in an inter-axis dependency of the measurements.

For DC magnetic fields, the crosstalk contributions of one axis to the other will reach a static configuration after some initial settling time. This configuration can be modeled with a simple change of the orthogonality matrix.

For AC magnetic fields, these contributions are not constant, but result in a transfer function that spans across multiple axes. This can be modeled with a dynamic system with crosstalk as shown in figure 5–1.

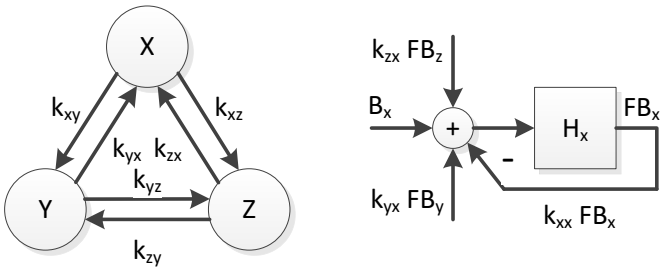

Figure 5–1: Dynamic Model of Feedback Crosstalk (left) and Model for Single Axis X (right)

The feedback of any axis N will influence another axis M with a crosstalk factor k_{NM}. The feedback crosstalk in axis M will result in some feedback in this axis, which will in turn influence the primary axis N. An exact modeling approach would therefore not only consider the scalar transfer function of one axis, but a matrix transfer function over all axes. A derivation of this matrix transfer function is provided in chapter A.2.

The effect of the matrix transfer function is a frequency dependent orthogonality matrix as well as an influence on frequency response estimates. The frequency dependent orthogonality matrix changes the amplitude and phase of AC signals. This also affects the spin-modulated magnetic field on satellites. The change in amplitude is in this case negligible, but the phase change influences the result of in-flight calibration that relies on accurate phase information.

The frequency response estimates in this thesis only used the scalar transfer function approach and measured the field in all axes in one go. The matrix contribution was neglected because the crosstalk factors are small (~1%) and the feedback bandwidth of all instruments is much higher than the bandwidth that was actually used in the merged data product. This means that the used frequencies in this product are “quasi-DC” in comparison to the feedback speed and the difference between scalar and matrix transfer function is strongly reduced.

However, this situation could change in future missions with crossover frequencies that are closer to the feedback bandwidth. In these cases, the matrix transfer function could be measured by applying the test signals to single axes and switching the other axes on and off. Of course, this would result in an increased measurement time, a higher model complexity and more effort in calculation.

A different approach is to reduce the influence of the matrix transfer function by hardware design. One way is, of course, the reduction of crosstalk, however, this is limited by mechanical and magnetic properties of the sensors. Another approach, previously hinted above, is to reduce the difference between matrix and scalar transfer function by using high feedback bandwidth.
Actually, this approach fits nicely with the DFG design with its fast sigma-delta feedback, even though this topic was not even considered during the DFG design phase

Another reduction can be obtained by using orthogonalized feedback. This feedback is no longer operated on a single axis, but is calculated using a transformation matrix that compensates some of the crosstalk and reduces the crosstalk factors k_{nm}. This requires simple matrix calculations before sending data to the feedback DAC.

Temperature Dependencies of Frequency Response

The change in SCM group delay (see figure 3–5) and gain (see figure 3–2) shows that there was a change in the frequency response of the SCM between reference calibration, FIT and in-flight situation. One possible reason for this change is a temperature dependency of the frequency response. This could be caused by mechanical changes in the sensor coil as well as the temperature dependency of the electronic components within the analog filters.

This influence of temperature on the frequency response is currently under investigation by the SCM team. For the fluxgate magnetometers, the change of the gain response was examined, but the phase was not measured in this configuration. It would be beneficial to include these measurements for all instruments in future campaigns for instrument modeling.

Current Generator Design

The presented current generator was well suited for conducting the FIT measurements. However, some improvements and new features are desirable for future application.

- In addition to the PPS interface, an interface for ESA's SpaceWire communication standard would be desirable, as this standard includes a time synchronization interface for onboard clocks.
- The jitter of the ADPLL could be reduced by using an increased FPGA master clock frequency. This can be done by changing to a faster FPGA family.
- The architecture of the analog current source could be changed by using a transistor based output stage with higher current limits. This source could then be used to drive bigger coil systems.
- The network interface should be changed to the lightweight IP stack to improve the speed of TCP/IP communication (see chapter 2.2.2.7)
- The possibilities for stand-alone operation should be improved, so that host computers are no longer mandatory.

Instrument Design

The quality of frequency response estimates could be improved by a few minor design changes in future magnetometers.

- The matrix transfer function can be measured, if all axes and their feedback can be operated independently. The intra-axis transfer functions can be measured by deactivating the other axis, while the inter-axis transfer functions can be measured by using programmable feedback signals in the other axes.
- The operation of the current generator could be improved if high frequency clocks and all sync signals were available on the checkout connectors of the instruments and data processing units. These connectors could be realized using small daughter boards with isolated data couplers. The primary side of these couplers would be connected to the flight hardware and would just cause an additional load on the clock signals. Electric power is only required on the secondary side. This way the flight instruments would remain isolated from all other test equipment.
- The DEC32/DEC64 data mode of the DFG should be replaced by a dual-path approach that provides one path with low group delay (to support other instruments) and another one with high quality anti-aliasing filtering (for regular instrument data). This would allow for high data quality and low delay at the same time.

A. Appendix

A.1 Digital Filtering

The text of this thesis uses many terms from the world of digital filters. This chapter shall therefore give an overview of this topic and introduce the necessary terms. More information can be found, e.g., in Oppenheim et al., 1989.

Digital filters use a combination of digital samples to modify the properties of a sample series, e.g., by introducing frequency dependent gains or delays. The filters used in this thesis are a subset of these filters, as they are linear, time-invariant and causal. They can be described using a difference equation that can be used to calculate the current output value.

$$y(n) = \sum_{i=0}^{N} b_i x(n-i) + \sum_{j=1}^{M} a_j y(n-j) \qquad \textit{Equation A-1}$$

This current output value at time n is calculated using N past input and M past output values, which are weighted with the filter coefficients a_i and b_j. A different representation of the difference equation can be achieved by applying the z transform

$$y(z) = \sum_{i=0}^{N} b_i X(z) z^{-i} + \sum_{j=1}^{M} a_j Y(z) z^{-j} \qquad \textit{Equation A-2}$$

and converting to a transfer function

$$H(z) = \frac{Y(z)}{X(z)} = \frac{\sum_{i=0}^{N} b_i z^{-i}}{1 - \sum_{j=1}^{M} a_j z^{-j}} \qquad \textit{Equation A-3}$$

Equation A-1 uses past output values as input for the current output, which means past outputs are fed back into the filter. This type of feedback creates the possibility for instability, as a bounded input value could potentially result in a permanently growing (unbound) or oscillating output value. A filter can be analyzed for stability by finding the roots of the denominator polynomial. The roots of this equation are called "poles." If the absolute value of these values is below one, the causal filter is stable. One method for representing the poles and also the zeros (the roots of the numerator polynomial) is the pole-zero diagram in the z-plane. Stability is achieved if all poles are within the unit circle with radius one.

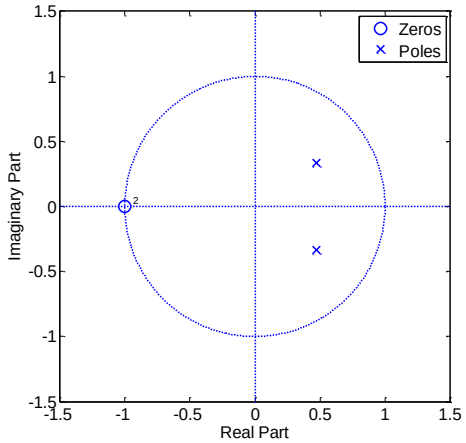

Figure A–1 Pole Zero Plot of a 2nd Order Butterworth Low Pass Filter

The presented digital filters can be divided into two categories: Finite and infinite impulse response (FIR and IIR) filters. This categorization expresses the reaction of the filter to a single pulse. If the filter output becomes permanently zero after a finite time, the filter is an FIR filter.
The simplest way of categorization is to look at the transfer function. If the numerator polynomial is finite and the denominator becomes one, the filter is an FIR filter. The inverse conclusion (identifying an IIR filter using the denominator) is not necessarily possible, as in some cases the polynomial division of the transfer function can be solved without remainder. In these cases, only a numerator remains and the transfer function can again be categorized as FIR filter.

A.1.1. Filter Properties

The desired functionality of a linear, time-invariant filter is to change signal properties like amplitude and phase, dependent on frequency. These properties are often illustrated using the frequency response which gives information about the effect of the filter on sinusoidal input signals. The frequency response can be calculated by evaluating the z-domain transfer function along the unit circle by setting

$$Hz = e^{j\omega} \qquad \textit{Equation A-4}$$

in equation A-3. The result is a complex function of the input frequency ω that can be reformulated to give information about gain and phase shift.

$$H\left(e^{j\omega}\right) = \left|H\left(e^{j\omega}\right)\right| \cdot e^{j\measuredangle\left(H\left(e^{j\omega}\right)\right)} \qquad \textit{Equation A-5}$$

Measurement systems like the instruments on MMS should have minimal influence on the measurement signal within the bandwidth of interest and the signal shape should not change. This behavior can be guaranteed if two conditions are met: The filter features unity gain and linear phase within the bandwidth of interest. Unity gain ensures that amplitudes do not change, whereas linear phase guarantees that individual signal components are not shifted relative to one another. Linear phase means that the phase shift is dependent on the signal frequency and some constant factor.

$$\measuredangle\left(H\left(e^{j\omega}\right)\right) = k \cdot \omega \qquad \textit{Equation A-6}$$

The resulting phase shift can be considered as time delay by relating the shift to a complete period of the signal.

$$\tau_\phi = -\frac{\measuredangle\left(H\left(e^{j\omega}\right)\right)}{\omega} \qquad \textit{Equation A-7}$$

This delay is also referred to as phase delay. The negative sign is introduced since a negative phase is equivalent to a positive delay. For a linear phase system, this equation changes to

$$\tau = -\frac{k \cdot \omega}{\omega} = -k \qquad \textit{Equation A-8}$$

This means the delay is constant and not dependent on frequency. A signal passing through the filter is only delayed in total and its subcomponents are not shifted relative to one another.

Another representation of the filter delay is the group delay, which does not look at the delay of single frequencies, but at the delay experienced by a wave packet that passes the filter.

$$\tau_g(\omega) = -\frac{d\measuredangle(H(e^{j\omega})}{d\omega}$$ *Equation A-9*

For linear phase filters, group and phase delay are identical and constant. These filters are therefore also called filters with constant group (or phase) delay.

Dependent on their frequency response, filters are categorized in low pass filters, high pass filters, band pass filters and band stop filters. The different characteristics are shown in figure A–2.

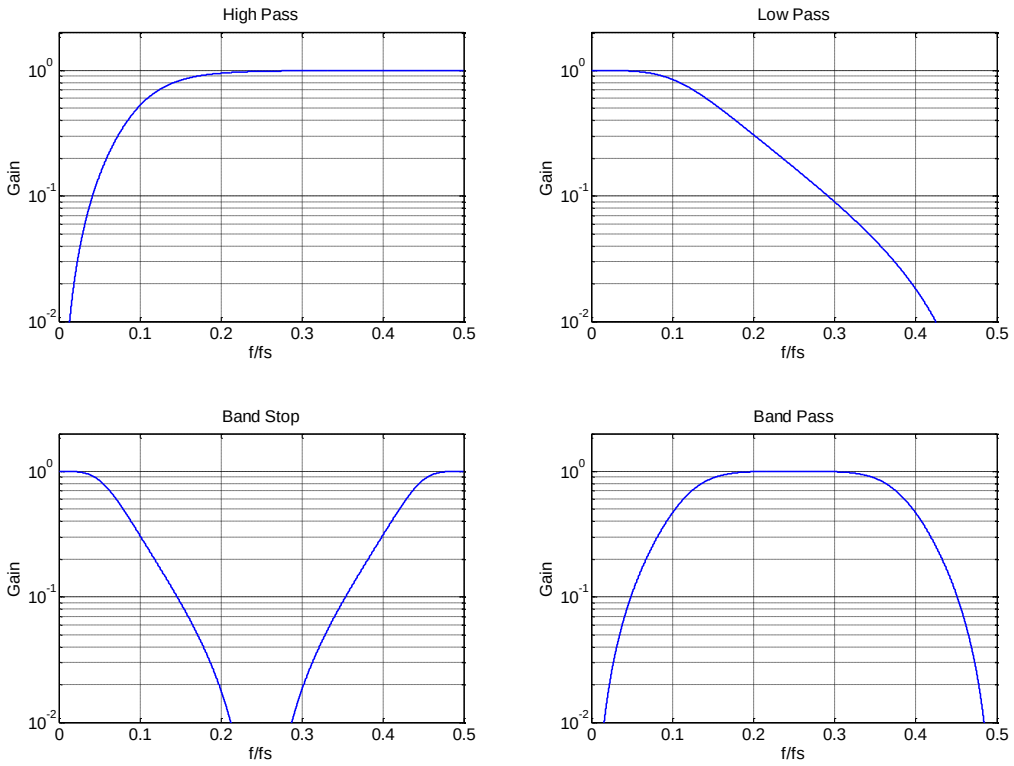

Figure A–2 Different Filter Frequency Response Categories

Figure A–3 shows the different frequency bands of a low pass filter, which are divided in pass band (the desired frequencies), stop band (the undesired frequencies) and transition band (the frequency region in between).

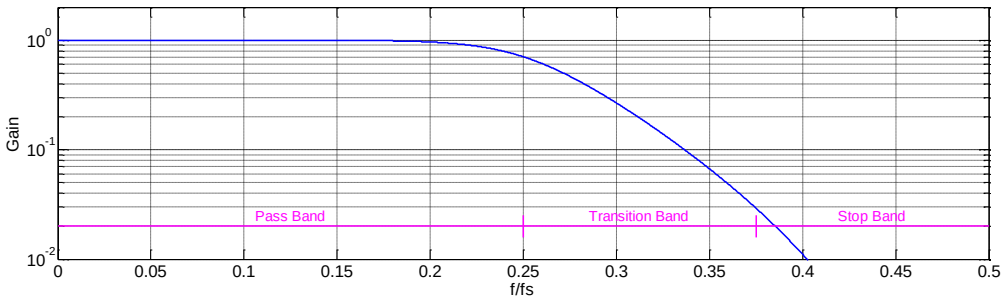

Figure A–3 Different Bands of a Low Pass Filter

A.1.2. FIR Filters

The most obvious property of an FIR filter is its limited length impulse response, which is due to the absence of feedback (with a few exceptions in a handful of special cases, see chapter A.1). A block diagram of an FIR filter structure is shown in figure A–4. Delay blocks are labeled with z^{-1}.

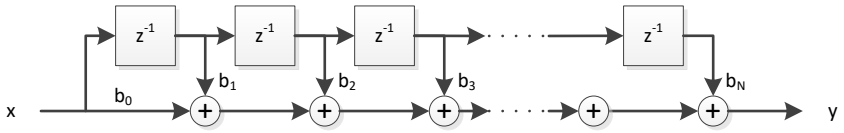

Figure A–4 Structure of FIR Filters

This impulse response length is N+1 and any reaction ends N samples after the last input excitation. The advantage of this limited impulse response is that the influence of any past input value will vanish completely after N+1 output values. This number of N+1 is also called the tap number. This limited impulse response is important in the context of missing data, which can appear, e.g., at the beginning of calculation (e.g., start of a data file or power-on of an instrument), in between (e.g., missing data, data corruption) or at the end (end of file or power-off of an instrument). In all these cases, only N+1 samples around the occurrence of missing data are influenced. This time of influence is also called "filter settling time."

This influence is not tolerable for measurement data, especially since MMS data is used by a wider audience that could perhaps be unaware of it. It is therefore necessary to remove this data, either by deleting it or replacing it with "not a number" (NaN) flags.

In the end, this means that the filter order gives information about potential data loss. It is therefore beneficial to use filters with the lowest possible order for a given task to reduce the amount of lost data and to keep computational complexity low.

A further result of this limited impulse response is that any FIR filter can be made causal by shifting it in time by adding a delay in front of it so that "future" values become available using this delay.

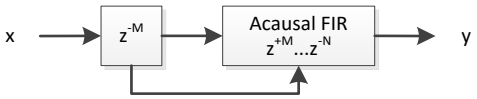

Figure A–5 Converting an Acausal FIR Filter

Another property of FIR filters is that they are always stable, since the denominator polynomial is always one and there is only a pole at z=0. Furthermore, FIR filters have a linear phase, if their coefficients are either symmetric or anti-symmetric around a center (see figure A–6).

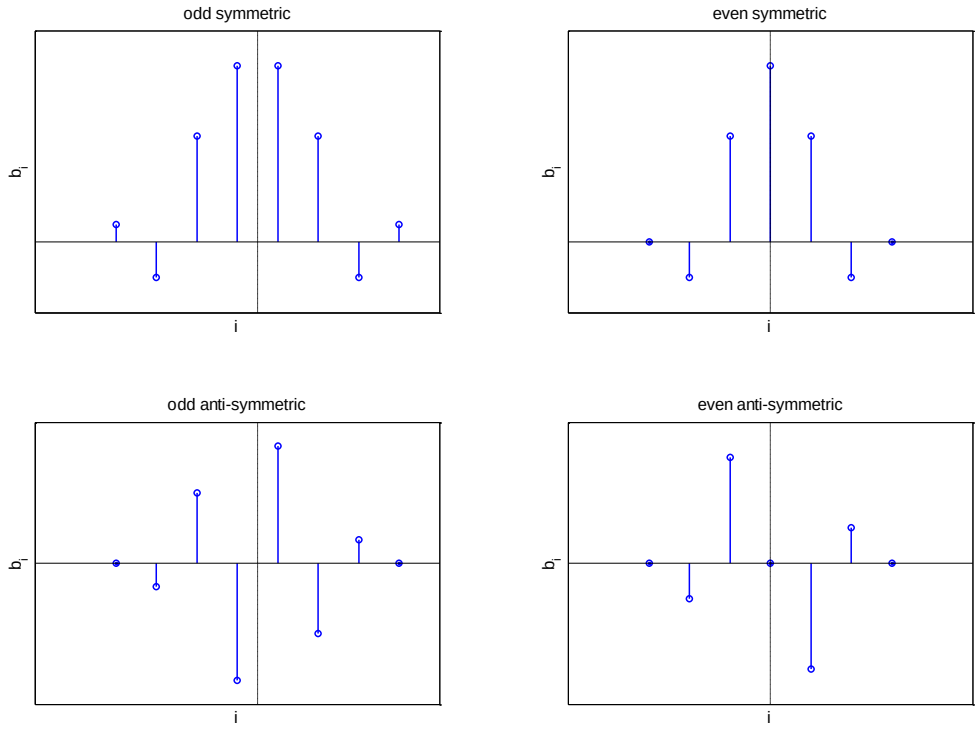

Figure A–6 FIR Filter Symmetry Examples

Naturally, having all these positive properties gives rise to the suspicion that there are also negative properties. For a given order, FIR filters deliver less flexibility in the design of the frequency response. This means FIR filters typically require higher order to achieve comparable attenuation or gain characteristics in comparison to IIR filters. This higher order results in higher computation power and memory requirements, as both the number of operations per output sample and the required memory for storing past samples are directly proportional to the filter order.
Some of this effort can be omitted by using fast convolution (Oppenheim et al., 1989, pp. 582 ff)) and by skipping zero coefficients. A further possibility for optimization is to use a feedback structure with finite impulse response (e.g., the CIC filter in figure 1–24).

A.1.3. IIR Filters

As their name implies, IIR filters have an infinitely long impulse response. This response is a result of their feedback structure, which uses previous output values.

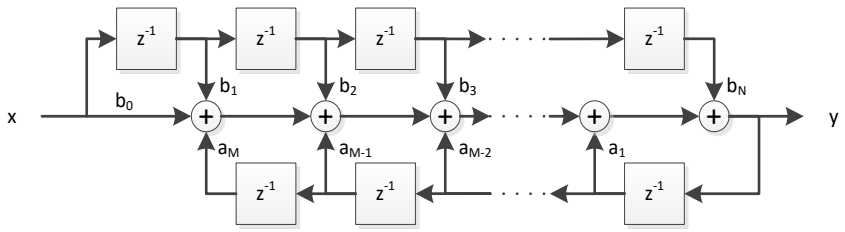

Figure A–7 Structure of IIR Filters

The advantage of IIR filters is a higher flexibility in frequency response design. Figure A–8 shows a comparison of 4th order IIR filter with a 4th and 8th order FIR filter. The IIR filter has a flatter passband, a steeper transition from passband to stopband and a higher stopband attenuation than the FIR filter.

In practical applications, IIR filters can therefore achieve good performance with low orders and the connected lower computational resources.

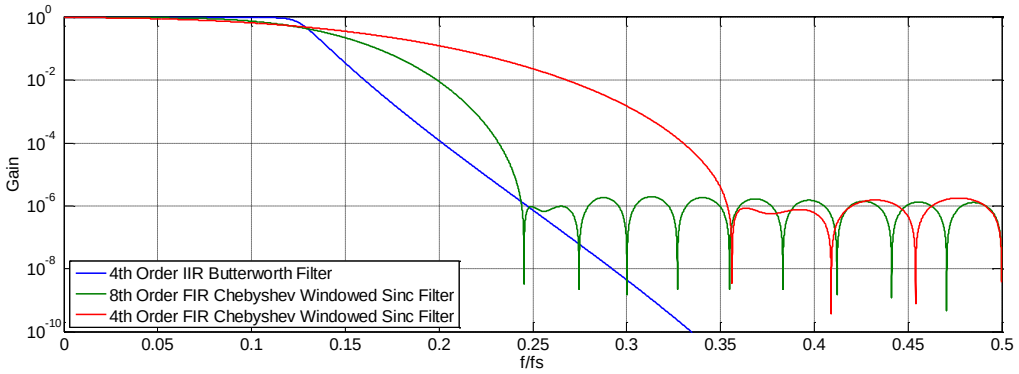

Figure A–8 Comparison of FIR and IIR Low Pass Filters with Cutoff at 0.125 fs

The disadvantages of IIR filters are their non-linear phase, the possibility for instability and their infinite impulse response. Past input values will influence the output for an indefinite time. Any data error (e.g., a gap or the beginning of a file) will influence the output for its entirety and the filters will (theoretically) have infinite filter settling time.

Fortunately, the requirement for stability and the property of an infinitely long impulse response interact if IIR filters are used in practical applications. A stable IIR filter will always have a decaying impulse response. In theory, the output value after an impulse input will continue decaying forever. However, in real signal processing systems, numerical precision is limited. This means at some time quantization will either result in a zero output value or the output will oscillate in a pattern defined by numerical precision that is more connected to the filter itself than the initial input pulse. In practical applications with real input signals, even the oscillation will vanish in general numerical noise. As a result, the influence of data errors will vanish after some time.
It is even possible to convert IIR filters to FIR filters by calculating the IIR impulse response to a certain extent and limiting its length by fading out to zero once the value of the impulse response approaches numerical precision limits. The disadvantage of this approach is an increase in computational complexity.

A.1.4. Ideal Low Pass Filtering

One of the filters used in this thesis is the Sinc-filter. This filter is based on an ideal rectangular transfer function in frequency domain.

$$|H(j\omega)| = \begin{cases} 1 & -2\pi f_c \leq \omega \leq 2\pi f_c \\ 0 & else \end{cases} \qquad \textit{Equation A-10}$$

The transform of this filter to the time domain results in the following function

$$h(t) = 2f_c \mathrm{sinc}(\pi f_c t) \qquad \textit{Equation A-11}$$

or its digital representation

$$h(n) = 2f_c \mathrm{sinc}(\pi \frac{f_c}{f_s} n) \qquad \textit{Equation A-12}$$

The disadvantage of this filter is that this filter has infinite order, as h(n) approaches zero only for infinite n. This can be changed by multiplying the filter with a window that limits the number of filter coefficients. Figure A–9 shows the results of applying a Chebyshev window to a sinc-filter.

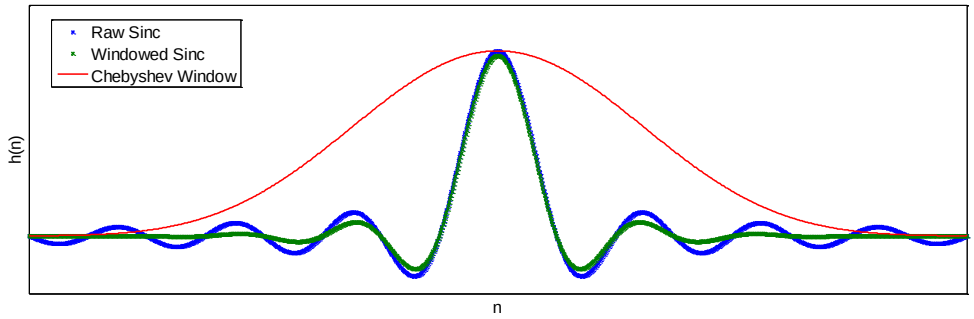

Figure A–9 Windowing of Sinc-Filter in Time Domain

This windowing in time domain is equivalent to a convolution in frequency domain. The filter is therefore no longer an ideal rectangular filter. The type of used window influences the properties of the non-ideality, e.g., stop band attenuation or pass band ripple. A few examples are shown in figure A–10.

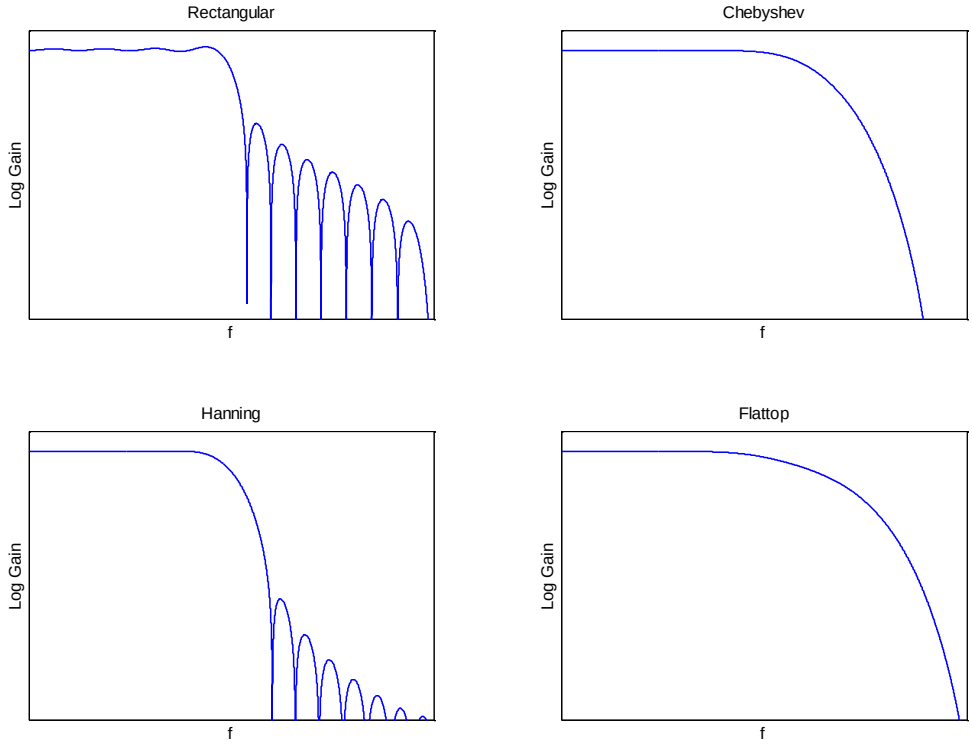

Figure A–10 Frequency Response of Windowed Sinc-Filters

A.1.5. Minimum Phase Filters

A minimum phase filter is a causal and stable filter with invertible transfer function. This means that numerator and denominator in equation A-3 can be swapped without running into stability problems by having poles outside the unit circle. A causal minimum phase filter will therefore have all poles and zeros within the unit circle.

The advantage of a minimum phase filter is that its frequency response can be compensated by an additional filter with swapped numerator and denominator. For causal filters, the convolution of the original filter H(z) and its inverse equivalent G(z) results in a pure delay function.

$$H(z) * G(z) = z^{-n} \qquad \textit{Equation A-13}$$

Unfortunately, not all systems that require frequency response compensation are minimum phase systems. The design of a filter that perfectly restores gain and phase is therefore not always feasible. Nevertheless, partial restoration can be achieved using all-pass filters (Oppenheim et al., 1998, pp. 280ff) or by designing compensation filters that only compensate the frequency response within a reduced bandwidth.

A.2 Matrix Transfer Function Derivation

The matrix transfer function of magnetic field sensors with feedback is set up using the block diagrams presented in figure 5–1. In this model, each axis influences the others with a crosstalk factor k_{NM}. This factor is in fact not a scalar value, but a complex transfer function that models magnetic and electric properties.

The following calculation uses s-domain transfer functions H(s), superposition and feedback across multiple axes to set up the matrix transfer functions. This calculation would also be possible in the z-domain, but in this case, all multiplications must be replaced with convolution operations.

The simple feedback transfer function for a field that is perfectly aligned to one ideal coil system is given by:

$$FB_{xx} = B_x \frac{H_x}{1 - k_{xx} H_x}$$ *Equation A-14*

In a situation with crosstalk across multiple axes, the feedback of axis x on itself (FB_{xx}) is subject to a feedback path across all other axes (see figure A–11).

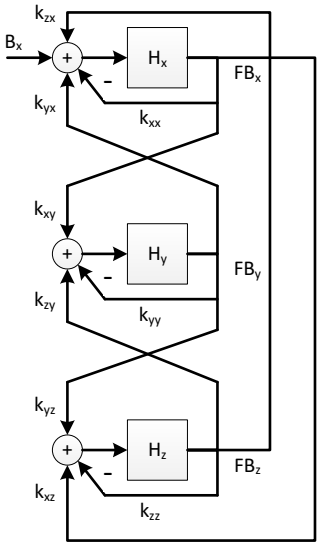

Figure A–11 Full Crosstalk Diagram for one Axis

Applying a similar structure for all axes, the feedback of every axis on itself can be expressed using

$$FB_{xx} = -B_x H_x \frac{(H_y H_z k_{yz} k_{zy} - 1)}{H_x\, H_y\, k_{xy} k_{yx} + H_x H_z k_{xz} k_{zx} + H_y H_z k_{yz} k_{zy} + H_x H_y H_z k_{xy} k_{yz}\, k_{zx} + H_x H_y H_z k_{xz} k_{yx} k_{zy} - 1}$$

$$FB_{yy} = -B_y H_y \frac{(H_x H_z k_{xz} k_{zx} - 1)}{H_x\, H_y\, k_{xy} k_{yx} + H_x H_z k_{xz} k_{zx} + H_y H_z k_{yz} k_{zy} + H_x H_y H_z k_{xy} k_{yz}\, k_{zx} + H_x H_y H_z k_{xz} k_{yx} k_{zy} - 1}$$

$$FB_{zz} = -B_z H_z \frac{(H_x H_y k_{xy} k_{yx} - 1)}{H_x\, H_y\, k_{xy} k_{yx} + H_x H_z k_{xz} k_{zx} + H_y H_z k_{yz} k_{zy} + H_x H_y H_z k_{xy} k_{yz}\, k_{zx} + H_x H_y H_z k_{xz} k_{yx} k_{zy} - 1}$$

Equations A-15

In addition, every axis will receive crosstalk that is generated by the feedback field of other axes:

$$FB_{zx} = FB_{xx} \frac{H_z k_{xz} + H_y H_z k_{xy} k_{yz}}{1 - H_y H_z k_{yz} k_{zy}}$$

$$FB_{yx} = FB_{xx}\frac{H_y k_{xy} + H_y H_z k_{xz} k_{zy}}{1 - H_y H_z k_{yz} k_{zy}}$$

$$FB_{xy} = FB_{yy}\frac{H_x k_{yx} + H_x H_z k_{yz} k_{zx}}{1 - H_x H_z k_{xz} k_{zx}}$$

$$FB_{zy} = FB_{yy}\frac{H_z k_{yz} + H_x H_z k_{yz} k_{zx}}{1 - H_x H_z k_{xz} k_{zx}}$$

$$FB_{yz} = FB_{zz}\frac{H_y k_{zy} + H_x H_y k_{xy} k_{zx}}{1 - H_x H_y k_{xy} k_{yx}}$$

$$FB_{xz} = FB_{zz}\frac{H_x k_{zx} + H_x H_y k_{xy} k_{zx}}{1 - H_x H_y k_{xy} k_{yx}}$$

Equations A-16

This can now be simplified into a matrix transfer function by moving the loop transfer function to the front and by collecting common terms. The matrix transfer function is given by

$$\overrightarrow{FB} = \vec{B} \cdot [H_x \quad H_y \quad H_z] \cdot H_{loop} \cdot \begin{bmatrix} (1 - H_y H_z k_{yz} k_{zy}) & H_y(k_{xy} + H_z k_{xz} k_{zy}) & H_z(k_{xz} + H_y k_{xy} k_{yz}) \\ H_x(k_{yx} + H_z k_{yz} k_{zx}) & (1 - H_x H_z k_{xz} k_{zx}) & H_z(k_{yz} + H_x k_{yz} k_{zx}) \\ H_x(k_{zx} + H_y k_{xy} k_{zx}) & H_y(k_{zy} + H_x k_{xy} k_{zx}) & (1 - H_x H_y k_{xy} k_{yx}) \end{bmatrix}$$

Equation A-17

and the loop transfer function is

$$H_{loop} == \frac{1}{H_x\, H_y\, k_{xy} k_{yx} + H_x H_z k_{xz} k_{zx} + \; H_y H_z k_{yz} k_{zy} + H_x H_y H_z k_{xy} k_{yz}\, k_{zx} + H_x H_y H_z k_{xz} k_{yx} k_{zy} - 1}$$

Equation A-18

The measurement value of the fluxgate sensor is calculated by replacing the vector transfer function $[H_x\ H_y\ H_z]$ in equation A-17 with the respective output transfer functions H_{out}.

$$\vec{M} = \vec{B} \cdot [H_{xout} \quad H_{yout} \quad H_{zout}] \cdot H_{loop} \cdot \begin{bmatrix} (1 - H_y H_z k_{yz} k_{zy}) & H_y(k_{xy} + H_z k_{xz} k_{zy}) & H_z(k_{xz} + H_y k_{xy} k_{yz}) \\ H_x(k_{yx} + H_z k_{yz} k_{zx}) & (1 - H_x H_z k_{xz} k_{zx}) & H_z(k_{yz} + H_x k_{yz} k_{zx}) \\ H_x(k_{zx} + H_y k_{xy} k_{zx}) & H_y(k_{zy} + H_x k_{xy} k_{zx}) & (1 - H_x H_y k_{xy} k_{yx}) \end{bmatrix}$$

Equation A-19

As already discussed in chapter 5, an application of this concept did not fall within the scope of this thesis, but could bring frequency response identification for future missions to an even more accurate level.

B. Open Source Contributions

During the design of the current generator, several open source libraries were used and modified. Since the current generator was and is still property of the IWF Graz, this was for internal use only and the software was not distributed to the public or customers.

Nevertheless, the used libraries should be mentioned, as they were of great use and greatly eased the work for this thesis.

- The GRLIB IP library by Gaisler Research
- The uIP TCP/IP by Adam Dunkels
- The lwIP TCP/IP stack by Adam Dunkels

In addition to the current generator software and VHDL code, also a few other open source software toolsets were also used during the development:

- The Eclipse Development Environment for C and C++
- The Leon C/C++ plugin for Eclipse
- Tortoise SVN for software version management
- The GNU C compiler for Leon3

C. Publication List

Thesis Related Publications

The content of this thesis was published with a much lower detail level in Geoscientific Instrumentation, Methods and Data Systems. All parts of this thesis are therefore based on this publication.

Fischer, D., Magnes, W., Hagen, C., Dors, I., Chutter, M. W., Needell, J., Torbert, R. B., Le Contel, O., Strangeway, R. J., Kubin, G., Valavanoglou, A., Plaschke, F., Nakamura, R., Mirioni, L., Russell, C. T., Leinweber, H. K., Bromund, K. R., Le, G., Kepko, L., Anderson, B. J., Slavin, J. A., and Baumjohann, W.: Optimized merging of search coil and fluxgate data for MMS, *Geosci. Instrum. Method. Data Syst.*, 5, 521-530, https://doi.org/10.5194/gi-5-521-2016 (2016)

Several publications used the merged magnetic field data that was generated as part of this thesis and cited the first author publication.

Le Contel, O., R. Nakamura, H. Breuillard, M.R. Argall, D.B. Graham, D. Fischer, A. Retinò, M. Berthomier, R. Pottelette, L. Mirioni, T. Chust, F.D. Wilder, D.J. Gershman, A. Varsani, P.-A. Lindqvist, Yu.V. Khotyaintsev, C. Norgren, R.E. Ergun, K.A. Goodrich, J.L. Burch, R.B. Torbert, J. Needell, M. Chutter, D. Rau, I. Dors, C.T. Russell, W. Magnes, R.J. Strangeway, K.R. Bromund, H.Y. Wei, F. Plaschke, B.J. Anderson, G. Le, T.E. Moore, B.L. Giles, W.R. Paterson, C.J. Pollock, J.C. Dorelli, L.A. Avanov, Y. Saito, B. Lavraud, S.A. Fuselier, B.H. Mauk, I.J. Cohen, D.L. Turner, J.F. Fennell, T. Leonard, A.N. Jaynes: Lower hybrid drift waves and electromagnetic electron space-ohase holes associated with dipolarization fronts and field-aligned currents observed by the Magnetospheric Multiscale mission during a substorm, *J. Geophys. Res.*, **122**, 12236-12257, doi: 10.1002/2017JA024550 (2017)

Plaschke, F., N. Kahr, D. Fischer, R. Nakamura, W. Baumjohann, W. Magnes, J.L. Burch, R.B. Torbert, C.T. Russell, B.L. Giles, R.J. Strangeway, H.K. Leinweber, K.R. Bromund, B.J. Anderson, G. Le, M. Chutter, J.A. Slavin, E.L. Kepko: Steepening of waves at the duskside magnetopause, *Geophys. Res. Lett.*, **43**, 7373-7380, doi: 10.1002/2016GL070003 (2016)

Vörös, Z., E. Yordanova, A. Varsani, K.J. Genestreti, Yu.V. Khotyaintsev, W. Li, D.B. Graham, C. Norgren, R. Nakamura, Y. Narita, F. Plaschke, W. Magnes, W. Baumjohann, D. Fischer, A. Vaivads, E. Eriksson, P.-A. Lindqvist, G. Marklund, R.E. Ergun, M. Leitner, M.P. Leubner, R.J. Strangeway, O. Le Contel, C. Pollock, B.J. Giles, R.B. Torbert, J.L. Burch, L.A. Avanov, J.C. Dorelli, D.J. Gershman, W.R. Paterson, B. Lavraud, Y. Saito: MMS observation of magnetic reconnection in the turbulent magnetosheath, *J. Geophys. Res.*, **122**, 11442-11467, doi:10.1002/2017JA024535 (2017)

Yordanova, E., Z. Vörös, A. Varsani, D.B. Graham, C. Norgren, Yu.V. Khotyaintsev, A. Vaivads, E. Eriksson, R. Nakamura, P.-A. Lindqvist, G. Marklund, R.E. Ergun, W. Magnes, W. Baumjohann, D. Fischer, F. Plaschke, Y. Narita, C.T. Russell, R.J. Strangeway, O. Le Contel, C. Pollock, R.B. Torbert, B.J. Giles, J.L. Burch, L.A. Avanov, J.C. Dorelli, D.J. Gershman, W.R. Paterson, B. Lavraud, Y. Saito: Electron scale structures and magnetic reconnection signatures in the turbulent magnetosheath, *Geophys. Res. Lett.*, **43**, 5969-5978, doi:10.1002/2016GL069191 (2016)

The work done for this thesis was also added to the FIELDS instrument paper. Chapters 4.2, 4.4 and the time domain method in chapter 5.1.2. are based on the work of this thesis

Torbert, R.B., C.T. Russell, W. Magnes, R.E. Ergun, P.-A. Lindqvist, O. Le Contel, H. Vaith, J. Macri, S. Myers, D. Rau, J. Needell, B. King, M. Granoff, M. Chutter, I. Dors, G. Olsson, Y.V. Khotyaintsev, A. Eriksson, C.A. Kletzing, S. Bounds, B. Anderson, W. Baumjohann, M. Steller, K. Bromund, G. Le, R. Nakamura, R.J. Strangeway, H.K. Leinweber, S. Tucker, J. Westfall, D. Fischer, F. Plaschke, J. Porter, K.

Lappalainen: The FIELDS instrument suite on MMS: Scientific objectives, measurements, and data products, *Space Sci. Rev.*, **199**, 105-135, doi:10.1007/s11214-014-0109-8 (2016)

MMS related Co-Authorships

These co-authorships resulted from my participation in the magnetometer calibration team. This participation is a result of my initial work in MMS frequency response calibration. In fact, the high quality of MMS magnetometer calibration also improves the quality of the merged data product.

Anderson, B.J., C.T. Russell, R.J. Strangeway, F. Plaschke, W. Magnes, D. Fischer, H. Korth, V.G. Merkin, R.J. Barnes, C.L. Waters, I.J. Cohen, J.H. Westlake, B.H. Mauk, H.K. Leinweber, D.J. Gershman, B.L. Giles, G. Le, R.B. Torbert, J.L. Burch: Electrodynamic context of magnetopause dynamics observed by magnetospheric multiscale, *Geophys. Res. Lett.*, **43**, 5988-5996, doi:10.1002/2016GL069577 (2016)

Breuillard, H., O. Le Contel, A. Retino, A. Chasapis, T. Chust, L. Mirioni, D.B. Graham, F.D. Wilder, I. Cohen, A. Vaivads, Yu.V. Khotyaintsev, P.-A. Lindqvist, G.T. Marklund, J.L. Burch, R.B. Torbert, R.E. Ergun, K.A. Goodrich, J. Macri, J. Needell, M. Chutter, D. Rau, I. Dors, C.T. Russell, W. Magnes, R.J. Strangeway, K.R. Bromund, F. Plaschke, D. Fischer, H.K. Leinweber, B.J. Anderson, G. Le, J.A. Slavin, E.L. Kepko, W. Baumjohann, B. Mauk, S.A. Fuselier, R. Nakamura: Multispacecraft analysis of dipolarization fronts and associated whistler wave emissions using MMS data, *Geophys. Res. Lett.*, **43**, 7279-7286, doi:10.1002/2016GL069188 (2016)

Chasapis, A., W.H. Matthaeus, T.N. Parashar, O. LeContel, A. Retinò, H. Breuillard, Y. Khotyaintsev, A. Vaivads, B. Lavraud, E. Eriksson, T.E. Moore, J.L. Burch, R.B. Torbert, P.-A. Lindqvist, R.E. Ergun, G. Marklund, K.A. Goodrich, F.D. Wilder, M. Chutter, J. Needell, D. Rau, I. Dors, C.T. Russell, G. Le, W. Magnes, R.J. Strangeway, K.R. Bromund, H.K. Leinweber, F. Plaschke, D. Fischer, B.J. Anderson, C.J. Pollock, B.L. Giles, W.R. Paterson, J. Dorelli, D.J. Gershman, L. Avanov, Y. Saito: Electron heating at kinetic scales in magnetosheath turbulence, *Astrophys. J.*, **836**, 247, doi:10.3847/1538-4357/836/2/247 (2017)

Le Contel, O., A. Retinò, H. Breuillard, L. Mirioni, P. Robert, A. Chasapis, B. Lavraud, T. Chust, L. Rezeau, F.D. Wilder, D.B. Graham, M.R. Argall, D.J. Gershman, P.-A. Lindqvist, Y.V. Khotyaintsev, G. Marklund, R.E. Ergun, K.A. Goodrich, J.L. Burch, R.B. Torbert, J. Needell, M. Chutter, D. Rau, I. Dors, C.T. Russell, W. Magnes, R.J. Strangeway, K.R. Bromund, H.K. Leinweber, F. Plaschke, D. Fischer, B.J. Anderson, G. Le, T.E. Moore, C.J. Pollock, B.L. Giles, J.C. Dorelli, L. Avanov, Y. Saito: Whistler mode waves and Hall fields detected by MMS during a dayside magnetopause crossing, *Geophys. Res. Lett.*, **43**, 5943-5952, doi:10.1002/2016GL068968 (2016)

Le, G., H. Lühr, B.J. Anderson, R.J. Strangeway, C.T. Russell, H. Singer, J.A. Slavin, Y. Zhang, T. Huang, K. Bromund, P.J. Chi, G. Lu, D. Fischer, E.L. Kepko, H.K. Leinweber, W. Magnes, R. Nakamura, F. Plaschke, J. Park, J. Rauberg, C. Stolle, R.B. Torbert: Magnetopause erosion during the 17 March 2015 magnetic storm: Combined field-aligned currents, auroral oval, and magnetopause observations, *Geophys. Res. Lett.*, **43**, 2396-2404, doi:10.1002/2016GL068257 (2016)

Le, G., P.J. Chi, R.J. Strangeway, C.T. Russell, J.A. Slavin, K. Takahashi, H.J. Singer, B.J. Anderson, K. Bromund, D. Fischer, E.L. Kepko, W. Magnes, R. Nakamura, F. Plaschke, R.B. Torbert: Global observations of magnetospheric high-m poloidal waves during the 22 June 2015 magnetic storm, *Geophys. Res. Lett.*, **44**, 3456-3464, doi:10.1002/2017GL073048 (2017)

Nakamura, R., T. Nagai, J. Birn, V.A. Sergeev, O. Le Contel, A. Varsani, W. Baumjohann, T.K.M. Nakamura, S. Apatenkov, A. Artemyev, R.E. Ergun, S.A. Fuselier, D.J. Gershman, B.J. Giles, Yu.V. Khotyaintsev, P.-A. Lindqvist, W. Magnes, B. Mauk, C.T. Russell, H.J. Singer, J. Stawarz, R.J. Strangeway,

B. Anderson, K.R. Bromund, D. Fischer, L. Kepko, G. Le, F. Plaschke, J.A. Slavin, I. Cohen, A. Jaynes, D.L. Turner: Near-Earth plasma sheet boundary dynamics during substorm dipolarization, *Earth Planets Space*, **69**, 129, doi:10.1186/s40623-017-0707-2 (2017)

Nakamura, R., V.A. Sergeev, W. Baumjohann, F. Plaschke, W. Magnes, D. Fischer, A. Varsani, D. Schmid, T.K.M. Nakamura, C.T. Russell, R.J. Strangeway, H.K. Leinweber, G. Le, K.R. Bromund, C.J. Pollock, B.L. Giles, J.C. Dorelli, D.J. Gershman, W. Paterson, L.A. Avanov, S.A. Fuselier, K. Genestreti, J.L. Burch, R.B. Torbert, M. Chutter, M.R. Argall, B.J. Anderson, P.-A. Lindqvist, G.T. Marklund, Y.V. Khotyaintsev, B.H. Mauk, I.J. Cohen, D.N. Baker, A.N. Jaynes, R.E. Ergun, H.J. Singer, J.A. Slavin, E.L. Kepko, T.E. Moore, B. Lavraud, V. Coffey, Y. Saito: Transient, small-scale field-aligned currents in the plasma sheet boundary layer during storm time substorms, *Geophys. Res. Lett.*, **43**, 4841-4849, doi:10.1002/2016GL068768 (2016)

Narita, Y., F. Plaschke, R. Nakamura, W. Baumjohann, W. Magnes, D. Fischer, Z. Vörös, R.B. Torbert, C.T. Russell, R.J. Strangeway, H.K. Leinweber, K.R. Bromund, B.J. Anderson, G. Le, M. Chutter, J.A. Slavin, E.L. Kepko, J.L. Burch, U. Motschmann, I. Richter, K.-H. Glassmeier: Wave telescope technique for MMS magnetometer, *Geophys. Res. Lett.*, **43**, 4774-4780, doi:10.1002/2016GL069035 (2016)

Narita, Y., R. Nakamura, W. Baumjohann, K.-H. Glassmeier, U. Motschmann, B. Giles, W. Magnes, D. Fischer, R.B. Torbert, C.T. Russell, R.J. Strangeway, J.L. Burch, Y. Nariyuki, S. Saito, S.P. Gary: On electron-scale whistler turbulence in the solar wind, *Astrophys. J. Lett.*, **827**, L8, doi:10.3847/2041-8205/827/1/L8 (2016)

Russell, C.T., B.J. Anderson, W. Baumjohann, K.R. Bromund, D. Dearborn, D. Fischer, G. Le, H.K. Leinweber, D. Leneman, W. Magnes, J.D. Means, M.B. Moldwin, R. Nakamura, D. Pierce, F. Plaschke, K.M. Rowe, J.A. Slavin, R.J. Strangeway, R. Torbert, C. Hagen, I. Jernej, A. Valavanoglou, I. Richter: The magnetospheric multiscale magnetometers, *Space Sci. Rev.*, **199**, 189-256, doi:10.1007/s11214-014-0057-3 (2016)

Russell, C.T., R.J. Strangeway, C. Zhao, B.J. Anderson, W. Baumjohann, K.R. Bromund, D. Fischer, L. Kepko, G. Le, W. Magnes, R. Nakamura, F. Plaschke, J.A. Slavin, R.B. Torbert, T.E. Moore, W.R. Paterson, C.J. Pollock, J.L. Burch: Structure, force balance, and topology of Earth's magnetopause, *Science*, **356**, 960-963, doi:10.1126/science.aag3112 (2017)

Schmid, D., R. Nakamura, M. Volwerk, F. Plaschke, Y. Narita, W. Baumjohann, W. Magnes, D. Fischer, H.U. Eichelberger, R.B. Torbert, C.T. Russell, R.J. Strangeway, H.K. Leinweber, G. Le, K.R. Bromund, B.J. Anderson, J.A. Slavin, E.L. Kepko: A comparative study of dipolarization fronts at MMS and Cluster, *Geophys. Res. Lett.*, **43**, 6012-6019, doi:10.1002/2016GL069520 (2016)

Zhao, C., C.T. Russell, R.J. Strangeway, S.M. Petrinec, W.R. Paterson, M. Zhou, B.J. Anderson, W. Baumjohann, K.R. Bromund, M. Chutter, D. Fischer, G. Le, R. Nakamura, F. Plaschke, J.A. Slavin, R.B. Torbert, H.Y. Wei: Force balance at the magnetopause determined with MMS: Application to flux transfer events, *Geophys. Res. Lett.*, **43**, 11941-11947, doi:10.1002/2016GL071568 (2016)

Other Publications and Co-Authorships

These are my few other publications, which are completely unrelated to this thesis and the work on MMS.

Auster, H.U., K.H. Glassmeier, W. Magnes, O. Aydogar, W. Baumjohann, D. Constantinescu, D. Fischer, K.H. Fornacon, E. Georgescu, P. Harvey, O. Hillenmaier, R. Kroth, M. Ludlam, Y. Narita, R. Nakamura, K. Okrafka, F. Plaschke, I. Richter, H. Schwarzl, B. Stoll, A. Valavanoglou, M. Wiedemann: The THEMIS fluxgate magnetometer, *Space Sci. Rev.*, **141**, 235-264, doi:10.1007/s11214-008-9365-9 (2008)

Fischer, D., G. Berghofer, W. Magnes, T.L. Zhang: A lossless compression method for data from spaceborne magnetometer. In: *Proceedings of the Sixth International Symposium on Communication Systems, Networks and Digital Signal Processing*, TU Graz, Graz, 326-330 (2008)

Fischer, D.: Design study of a low noise and radiation tolerant sigma-delta digital-to-analog converter for space application, Diploma Thesis, Technische Universität Graz, 101 pages (2006)

Magnes, W., D. Fischer, A. Valavanoglou, G. Fremuth: Design of a radiation hard and low power 16-bit digital-to-analog converter based on sigma-delta modulation, *EGU General Assembly 2006*, Vienna, Austria, Apr 2006.

D. Formal Requirements

The constitution of the doctoral school of electrical engineering at Graz University of Technology is available at (link validated 2018/03/08):
https://www.tugraz.at/studium/studienangebot/doktoratsstudien/doctoral-school-elektrotechnik/

This constitution requires a publication list and their relation to this thesis (see appendix C) and a list of cooperators as well as their work, sorted by contribution. This includes all cooperators listed in my publication (Fischer et al., 2016)

- Werner Magnes, Ferdinand Plaschke, Christan Hagen: Commenting on this thesis and the paper
- Werner Magnes: project lead at IWF Graz for the MMS magnetometers (including the merged data product)
- Christian Hagen: Labview Software of the current generator (see chapter 2.2.2.7) as well as direct cooperation in electronics debugging
- Mark W. Chutter, Ivan Dors, Jerry Needell: The FIELDS hardware team. They provided a lot of technical information about FIELDS and operated FIELDS during the FIT measurements (see chapter 2.3). Ivan Dors conducted the last two FIT measurements by himself and I merely confirmed that the data is usable.
- Olivier Le Contel, Laurent Mirioni: They were my contact persons at the SCM team and provided vital information about the SCM. They provided the reference measurement data (see chapter 2.4.2) and took part in all discussions about gain and alignment (see chapter 3.2) by comparing my results to their own results from the onboard calibration circuit.
- Werner Magnes, Aris Valavanoglou: They are the designers of the DFG and provided all information about this instrument.
- Kathryn M. Rowe: She was my main information source about the AFG analog design
- Ferdinand Plaschke, Rumi Nakamura, Christopher T. Russell, Hannes K. Leinweber, Kenneth R. Bromund, Guan Le., Lawrence Kepko, Brian J. Anderson, Werner Magnes, Olivier Le Contel, Laurent Mirioni and myself: This is the MMS magnetometer calibration team that provides the MMS magnetometer calibration that is used for producing data that is not off by tens of nT. This data is the basis for the onboard-comparison.
- Matthew Argall implemented the software for the production in the MMS science data center and improved it by generating an improved merging filter based on in-flight statistics.
- Jim Burch: Project lead for MMS. Without him there would be no MMS and no thesis.
- Roy B. Torbert: Project lead for FIELDS. He had the initial idea for data merging and luckily required someone else that was able to do it.
- Wolfgang Baumjohann: My institute director at IWF Graz
- Gernot Kubin: My supervisor at TU Graz: commenting on this thesis and the paper

E. Acronyms

AC	Alternating Current (or other quantities that change with a frequency)
AD/DA	Analog to Digital/Digital to Analog
ADC	Analog to Digital Converter
ADP	Axial Double Probe
ADPLL	All Digital Phase Locked Loop
AFG	Analog FluxGate magnetometer
AM	Amplitude Modulation
ASCII	American Standard Code for Information Interchange
ASPOC	Active Spacecraft Potential Control system
CDPU	Central Data Processing Unit
CEB	Central Electronics Box
CIC	Cascaded Integrator Comb Filter
CIDP	Central Instruments Data Processor
CLUSTER	actually no acronym
CPSD	Cross Power Spectral Density
CPU	Central Processing Unit
DAC	Digital to Analog Converter
DC	Direct Current (or other quantities that are constant)
DEC32/64	DFG Decimation Modes
DES	Dual Electron Spectrometer
DFG	Digital FluxGate magnetometer
DFT	Discrete Fourier Tranform
DIP	Dual In-line Package, a chip package size in electronic board design
DIS	Dual Ion Spectrometer
DMA	Direct Memory Access
DSP	Digital Signal Processor
E56	Electric Field Input E56 of DSP
EDI	Electron Drift Instrument
EFW	Electric Field and Wave experiment (CLUSTER instrument)
EIS	Energetic Ion Spectrometer
EPD	Energetic Particle Detector
FEEPS	Fly's Eye Energetic Particle Sensor
FFT	Fast Fourier Transform
FG	Fluxgate
FGM	Fluxgate Magnetometer
FIELDS	actually no acronym
FIR	Finite Impulse Response
FIT	FIELDS Integration and Test
FLASH	No acronym, a term how fast writing this non-volatile memory is.
FPGA	Field Programmable Gate Array
FPI	Fast Plasma Investigation
FS	Full Scale
FSM	fluxgate-search-coil-merged data product at the MMS science data center
GNU	GNU is not Unix, Term for free software
GPS	Global Positioning System
GPU	Graphics Processing Unit (of a PC)
GRLIB	Gaisler Research Library
GSE	Geocentric Solar Ecliptic coordinate system
GSM	Geocentric Solar Magnetospheric coordinate system
HPCA	Hot Plasma Composition Analyzer
HR	High Range

I/O	Input/Output Connectors
IDPU	Instrument Data Processing Unit
IIR	Infinite Impulse Response
IP	Intellectual Property (in GRLIB) or Internet Protocol (Network)
IWF	Institut für Weltraumforschung
JTAG	Joint Test Action Group, a connector standard for hardware debugging
LabVIEW	A graphical programming language
LED	Light Emitting Diode
LR	Low Range
LVDS	Low Voltage Differential Signalling
LVPS	Low Voltage Power Supply
lwIP	light-weight IP stack
MATLAB	A data processing environment
ML	maximum likelihood
MMS	Magnetospheric Multiscale
MR	Medium Range
MSS	Maximum Segment Size for TCP packets on a given network
NaN	Not a Number, flag for marking invalid data
NASA	National Aeronautics and Space Administration
NEMI	Noise Equivalent Magnetic Induction
NVIDIA	Name of a Graphics Card Manufacturer
OMB	Orthogonal Mounted Boom, a coordinate system of MMS
OSC	Oscillator
PC	Personal Computer
PHY	Physical Layer Tranceiver
PPS	Pulse Per Second, the MMS time standard signal
Preamp	Pre-Amplifier
PSD	Power Spectral Density
PT100	Resistor with positive temperature coefficient and nominal value of 100 Ω
RBSP	Radiation Belt Storm Probe, NASA mission for research in the Van-Allen belts
RFC	Request for Comment (many of them have become network standards)
RFID	Radio-Frequency Identification
RJ45	Registered Jack 45, the standard jack for network cables
ROI	Region of Interest
RS232	Recommended Standard 232, a serial standard interface
SCM	Search-Coil magnetometer
SDP	Spin plane Double Probe
SDRAM	Synchronous Dynamic Random Access Memory
SITL	MMS Scientist in the loop, responsible for selecting burst data for download
SNR	Signal-to-Noise Ratio
SPEDAS	Space Physics Environment Data Analysis Software, used for download and analysis of MMS data
SRAM	Static Random Access Memory
STAFF	Spatio-Temporal Analysis of Field Fluctuations (CLUSTER instrument)
TAI	Temps Atomique International (world-wide Atomic Clock Standard)
TCP	Transmission Control Protocol (network protocol for the internet)
TCP/IP	Transmission Control Protocol/Internet Protocol
THEMIS	Time History of Events and Macroscale Interactions during Substorms
TVS	Transient Voltage Supressor
UDP	User Datagram Protocol (another network protocol)
uIP	micro IP stack
UNH	University of New Hampshire

USB	Universal Serial Bus
UTC	Coordinated Universal Time
VGA	Video Graphics Adapter

F. References

Publications and Books

Al-Araji, S.R., Hussain, Z.M., Al-Qutayri, M.A.: Digital Phase Lock Loops, *Springer US*, 2006, ISBN 978-0-387-32863-8, http://dx.doi.org/10.1007/978-0-387-32864-5

Alexandrova, O., Mangeney, A., Maksimovic, M., Lacombe, C., Cornilleau-Wehrlin, N., Lucek, E.A., Decreau, P.M.E., Bosqued, J.-M., Travnicek, P., Fazakerley, A.N.: Cluster observations of finite amplitude Alfvén waves and small-scale magnetic filaments downstream of a quasi-perpendicular shock, *Journal of Geophysical Research: Space Physics* (2004), Vol. 109 Iss. A5, http://dx.doi.org/10.1029/2003JA010056

Alexandrova, O., Chen, C.H.K., Sorriso-Valvo, L., Horbury, T.S., Bale, S.D.: Solar Wind Turbulence and the Role of Ion Instabilities, *Space Science Reviews* (2013), Vol. 178 Iss. 2, pp. 101-139, https://doi.org/10.1007/s11214-013-0004-8

Allegacio, 2018: blog "Robottini: Little robots with Arduino", retrieved 2018/03/08 http://robottini.altervista.org/kalman-filter-vs-complementary-filter

Angelopoulos, V.: The THEMIS Mission, Space Science Reviews (2008), Vol. 141, p. 5, https://doi.org/10.1007/s11214-008-9336-1

Argall, M.R., Caide, A., Chen, L., Torbert, R.B.: A method for combining search coil and fluxgate magnetometer data to reveal finer structures in reconnection physics, *American Geophysical Union, Fall Meeting 2012*, abstract id. SM21B-2259, 2012, accessed 2018/03/08, http://adsabs.harvard.edu/abs/2012AGUFMSM21B2259A

Argall, M.R., Fischer, D., Le Contel, O., Mirioni, L., Torbert, R.B., Dors, I., Chutter, M., Needell, J., Strangeway, R., Magnes, W., Russell, C.T.: The Fluxgate-Searchcoil Merged (FSM) Magnetic Field Data Product for MMS, available on *arxiv.org* (publication pending), https://arxiv.org/abs/1809.07388

Auster, H.U.: How to Measure Earth's Magnetic Field, Physics Today (2008), Vol. 61 Iss. 2, pp. 76-77, https://doi.org/10.1063/1.2883919

Balogh, A., Dunlop, M.W., Cowley, S.W.H., Southwood, D.J., Thomlinson, J.G., Glassmeier, K.H., Musmann, G., Lühr, H., Buchert, S., Acuña, M.H., Fairfield, D.H., Slavin, J.A., Riedler, W., Schwingenschuh, K., Kivelson, M.G.: The Cluster Magnetic Field Investigation, *Space Science Reviews* (1997), Vol. 79, pp. 65-91, https://doi.org/10.1023/A:1004970907748

Barbe, K., Pintelon, R., Schoukens, J.: Welch Method Revisited: Nonparametric Power Spectrum Estimation Via Circular Overlap, *IEEE Transactions on Signal Processing* (2010), Vol. 58 Iss. 2, pp. 553-565, https://doi.org/10.1109/TSP.2009.2031724

Baumjohann, W., Treumann, R.A.: Basic Space Plasma Physics, *Imperial College Press*, 1997, ISBN 978-1-84816-894-7, http://dx.doi.org/10.1142/P850

Benmouyal, G.: Frequency-domain characterization of Kalman filters as applied to power system protection, *IEEE Transactions on Power Delivery* (1992), Vol. 7 Iss. 3, pp. 1129-1138, https://doi.org/10.1109/61.141823

Bruno, R., Telloni, D., DeIure, D., Pietropaolo, E.: Solar wind magnetic field background spectrum from fluid to kinetic scales, *Monthly Notices of the Royal Astronomical Society* (2017), Vol. 472, pp. 1052-1059, http://dx.doi.org/10.1093/mnras/stx2008

Burch, J.L., Moore, T.E., Torbert, R.B., Giles, B.L.: Magnetospheric Multiscale Overview and Science Objectives, *Space Science Reviews* (2016), Vol. 199, pp. 5-21, https://doi.org/10.1007/s11214-015-0164-9

Carreira, F.P.N.d.F.C., Calado, J.M.F., Cardeira, C.B., Oliveira, P.J.C.R.: Complementary Filter Design with Three Frequency Bands: Robot Attitude Estimation, *2015 IEEE International Conference on Autonomous Robot Systems and Competitions* (2015), pp. 168-173, http://dx.doi.org/10.1109/ICARSC.2015.33

Chaston, C., Bonnell, J., McFadden, J.P., Carlson, C.W., Cully, C., Le Contel, O., Roux, A., Auster, H.U., Glassmeier, K.H., Angelopoulos, V., Russell, C.T.: Turbulent heating and cross-field transport near the magnetopause from THEMIS, *Geophysical Research Letters* (2008), Vol. 35 Iss. 17, http://dx.doi.org/10.1029/2008GL033601

Chen, C.H.K., Horbury, T.S., Schekochihin, A.A., Wicks, R.T., Alexandrova, O., Mitchell, J.: Anisotropy of Solar Wind Turbulence between Ion and Electron Scales, *Physical Review Letters* (2010), Vol. 104 Iss. 25, p. 255002, https://link.aps.org/doi/10.1103/PhysRevLett.104.255002

Cornilleau-Wehrlin, N., Chauveau, P., Louis, S., Meyer, A., Nappa, J.M., Perraut, S., Rezeau, L., Robert, P., Roux, A., De Villedary, C., De Conchy, Y., Friel, L., Harvey, C.C., Hubert, D., Lacombe, C., Manning, R., Wouters, F., Lefeuvre, F., Parrot, M., Pinçon, J.L., Poirier, B., Kofman, W., Louarn, Ph.: The Cluster Spatio-Temporal Analysis of Field Fluctuations (STAFF) Experiment, *Space Science Reviews* (1997), Vol. 79, pp. 107-136, https://doi.org/10.1023/A:1004979209565

Costello, W.J.: A Frequency Domain Analysis of the Linear Discrete Kalman Filter., Thesis ADA085058 *M.S. in Operations Research-Naval Postgraduate School*, Monterey, California (1980), http://hdl.handle.net/10945/17598

da Silva, A.L., da Cruz, J.J.: Fuzzy adaptive extended Kalman filter for UAV INS/GPS data fusion, *Journal of the Brazilian Society of Mechanical Sciences and Engineering* (2016), Vol. 38 Iss. 6, pp. 1671-1688, https://doi.org/10.1007/s40430-016-0509-7Del Moral, Pierre: Nonlinear filtering: Interacting particle resolution, *Comptes Rendus de l'Académie des Sciences - Series I - Mathematics* (1997), Vol. 325 Iss. 6, pp. 653-658, https://doi.org/10.1016/S0764-4442(97)84778-7

Ergun, R.E., Tucker, S., Westfall, J., Goodrich, K.A., Malaspina, D.M., Summers, D., Wallace, J., Karlsson, M., Mack, J., Brennan, N., Pyke, B., Withnell, P., Torbert, R., Macri, J., Rau, D., Dors, I., Needell, J., Lindqvist, P.-A., Olsson, G., Cully, C.M.: The Axial Double Probe and Fields Signal Processing for the MMS Mission, *Space Science Reviews* (2016), Vol. 199, pp. 167-188, https://doi.org/10.1007/s11214-014-0115-x

Escoubet, C.P., Schmidt, R., Goldstein, M.L.: CLUSTER - Science and Mission Overview, *Space Science Reviews* (1997), Vol. 79, pp. 11-32, https://doi.org/10.1023/A:1004923124586

Fischer, D., Magnes, W., Hagen, C., Dors, I., Chutter, M.W., Needell, J., Torbert, R.B., Le Contel, O., Strangeway, R.J., Kubin, G., Valavanoglou, A., Plaschke, F., Nakamura, R., Mirioni, L., Russell, C.T., Leinweber, H.K., Bromund, K.R., Le, G., Kepko, L., Anderson, B.J., Slavin, J.A., Baumjohann, W.: Optimized merging of search coil and fluxgate data for MMS, *Geosci. Instrum. Method. Data Syst.* (2016), Vol. 5 Iss. 2, pp. 521-530, https://doi.org/10.5194/gi-5-521-2016

Fuselier, S.A., Lewis, W.S., Schiff, C., Ergun, R., Burch, J.L., Petrinec, S.M., Trattner, K.J.: Magnetospheric Multiscale Science Mission Profile and Operations, *Space Science Reviews* (2016), Vol. 199, pp. 77-103, https://doi.org/10.1007/s11214-014-0087-x

Han, F., Harada, S., Sasada, I.: Fluxgate and Search Coil Hybrid: A Low-Noise Wide-Band Magnetometer, *IEEE Transactions on Magnetics* (2012), Vol. 48 Iss. 11, pp. 3700-3703, https://doi.org/10.1109/TMAG.2012.2196762

Hars, Laszlo: Frequency Response Compensation with DSPs, *John Wiley & Sons, Inc.* (2003), pp. 395-406, http://dx.doi.org/10.1002/9781118316948.ch39

Haykin, S.: Adaptive Filter Theory, 4th Ed., *Prentice-Hall, Inc.*, 2002, ISBN 0-13-090126-1, https://www.pearson.com/us/higher-education/program/Haykin-Adaptive-Filter-Theory-5th-Edition/PGM24418.html (link to 5th edition)

Higgins, W.T.: A Comparison of Complementary and Kalman Filtering, *IEEE Transactions on Aerospace and Electronic Systems* (1975), Vol. AES-11 Iss. 3, pp. 321-325, https://doi.org/10.1109/TAES.1975.308081

Hinkley, D.V.: On the ratio of two correlated normal random variables, *Biometrika*, 1969, Vol. 56, Iss. 3, pp. 635-639, https://doi.org/10.1093/biomet/56.3.635

Hogenauer, E.: An economical class of digital filters for decimation and interpolation, *IEEE Transactions on Acoustics, Speech, and Signal Processing* (1981), Vol. 29 Iss. 2, pp. 155-162, https://doi.org/10.1109/TASSP.1981.1163535

Jan, 2018: blog "Creativity in Automation & More", retrieved 2018/03/08, http://www.pieter-jan.com/node/11

Janosek, Michal: Parallel Fluxgate Magnetometers, *Springer International Publishing Cham*, 2017, ISBN 978-3-319-34070-8, https://doi.org/10.1007/978-3-319-34070-8_2

Kalman, R.E.: A New Approach to Linear Filtering and Prediction Problems, *Journal of Basic Engineering* (1960), Vol. 82, pp. 35-45, http://dx.doi.org/10.1115/1.3662552

Keesman, K.J.: System Identification - An Introduction, *Springer London*, 2011, ISBN 978-0-85729-521-7, http://dx.doi.org/10.1007/978-0-85729-522-4

Kay, S.M.: Fundamentals of Statistical Signal Processing, Volume I: Estimation Theory, *Prentice Hall* (1993), ISBN 978-0-13345-711-7, https://www.pearson.com/us/higher-education/program/Kay-Fundamentals-of-Statistical-Processing-Volume-I-Estimation-Theory/PGM50476.html

Kepko, E.L., Khurana, K.K., Kivelson, M.G., Elphic, R.C., Russell, C.T.: Accurate determination of magnetic field gradients from four point vector measurements. I. Use of natural constraints on vector data obtained from a single spinning spacecraft, *IEEE Transactions on Magnetics* (1996), Vol. 32 Iss. 2, pp. 377-385, https://doi.org/10.1109/20.486522

Kiyani, K.H., Chapman, S.C., Sahraoui, F., Fauvarque, O., Khotyaintsev, Y.V.: Enhanced Magnetic Compressibility and Isotropic Scale Invariance at Sub-ion Larmor Scales in Solar Wind Turbulence, *The Astrophysical Journal* (2013), Vol. 763, p. 10, https://doi.org/10.1088/0004-637X/763/1/10

Khurana, K.K., Kepko, E.L., Kivelson, M.G., Elphic, R.C.: Accurate determination of magnetic field gradients from four-point vector measurements. II. Use of natural constraints on vector data obtained from four spinning spacecraft, *IEEE Transactions on Magnetics* (1996), Vol. 32 Iss. 5, pp. 5193-5205, https://doi.org/10.1109/20.538622

Lagrange, J.L.: Lecons elementaires sur les mathematiques donneesa l'ecole normale, *Gauthier-Villars* (1795), Vol. 7, pp. 183-287, retrieved 2018/03/09, http://sites.mathdoc.fr/cgi-bin/oeitem?id=OE_LAGRANGE__7_183_0

LaValle, 2018: “Occulus Developer Blog”, retrieved 2018/03/08
https://developer.oculus.com/blog/sensor-fusion-keeping-it-simple/

Le Contel, O., Leroy, P., Roux, A., Coillot, C., Alison, D., Bouabdellah, A., Mirioni, L., Meslier, L., Galic, A., Vassal, M.C., Torbert, R.B., Needell, J., Rau, D., Dors, I., Ergun, R.E., Westfall, J., Summers, D., Wallace, J., Magnes, W., Valavanoglou, A., Olsson, G., Chutter, M., Macri, J., Myers, S., Turco, S., Nolin, J., Bodet, D., Rowe, K., Tanguy, M., deÂ la Porte, B.: The Search-Coil Magnetometer for MMS, *Space Science Reviews* (2016), Vol. 199, pp. 257-282, https://doi.org/10.1007/s11214-014-0096-9

Leurent, 2018: blog “Quora”, retrieved 2018/03/08
https://www.quora.com/What-is-a-complimentary-filter-How-does-it-differ-from-a-Kalman-filter

Lindqvist, P.-A., Olsson, G., Torbert, R.B., King, B., Granoff, M., Rau, D., Needell, G., Turco, S., Dors, I., Beckman, P., Macri, J., Frost, C., Salwen, J., Eriksson, A., Åhlén, L., Khotyaintsev, Y.V., Porter, J., Lappalainen, K., Ergun, R.E., Wermeer, W., Tucker, S.: The Spin-Plane Double Probe Electric Field Instrument for MMS, *Space Science Reviews* (2016), Vol. 199, pp. 137-165, https://doi.org/10.1007/s11214-014-0116-9

Magnes, W., Pierce, D., Valavanoglou, A., Means, J., Baumjohann, W., Russell, C.T., Schwingenschuh, K., Graber, G.: A Sigma-Delta Fluxgate Magnetometer for Space Applications, *Measurement Science and Technology* (2003), Vol. 14 Iss. 7, p. 1003, https://doi.org/10.1088/0957-0233/14/7/314

Magnes, W., Oberst, M., Valavanoglou, A., Hauer, H., Hagen, C., Jernej, I., Neubauer, H., Baumjohann, W., Pierce, D., Means, J., Falkner, P.: Highly Integrated Front-End Electronics for Spaceborne Fluxgate Sensors, *Measurement Science and Technology* (2008), Vol. 19 Iss. 11, p. 115801, https://doi.org/10.1088/0957-0233/19/11/115801

Mao, G., Drake, S., Anderson, B.D.O.: Design of an Extended Kalman Filter for UAV Localization, *Information, Decision and Control* (2007), pp. 224-229, https://doi.org/10.1109/IDC.2007.374554

Mauk, B.H., Blake, J.B., Baker, D.N., Clemmons, J.H., Reeves, G.D., Spence, H.E., Jaskulek, S.E., Schlemm, C.E., Brown, L.E., Cooper, S.A., Craft, J.V., Fennell, J.F., Gurnee, R.S., Hammock, C.M., Hayes, J.R., Hill, P.A., Ho, G.C., Hutcheson, J.C., Jacques, A.D., Kerem, S., Mitchell, D.G., Nelson, K.S., Paschalidis, N.P., Rossano, E., Stokes, M.R., Westlake, J.H.: The Energetic Particle Detector (EPD) Investigation and the Energetic Ion Spectrometer (EIS) for the Magnetospheric Multiscale (MMS) Mission, *Space Science Reviews* (2016), Vol. 199, pp. 471-514, https://doi.org/10.1007/s11214-014-0055-5

Musmann, G.: Fluxgate Magnetometers for Space Research, *Books on Demand*, 2010, ISBN 9783839137024, https://www.bod.de/buchshop/fluxgate-magnetometers-for-space-research-9783839137024

OlliW, 2018: blog “OlliW’s Bastelseiten”, retrieved 2018/03/08
http://www.olliw.eu/2013/imu-data-fusing/

Oppenheim, A.V., Schafer, R.W., Buck, J.R.: Discrete-Time Signal Processing, 2nd Ed*., Prentice-Hall, Inc.*, 1998, ISBN 0-13-754920-2, https://www.pearson.com/us/higher-education/program/Oppenheim-Discrete-Time-Signal-Processing-3rd-Edition/PGM212808.html (link to 3rd edition)

Osder, S.S., Rouse, W.E., Young, L.S.: The Design of Digital-Adaptive Controllers for VTOL Aircraft, *Sperry Tech.* (1973), Vol. 1 Iss. 3, pp. 168-173, https://archive.org/details/NASA_NTRS_Archive_19760014127

Pollock, C., Moore, T., Jacques, A., Burch, J., Gliese, U., Saito, Y., Omoto, T., Avanov, L., Barrie, A., Coffey, V., Dorelli, J., Gershman, D., Giles, B., Rosnack, T., Salo, C., Yokota, S., Adrian, M., Aoustin, C., Auletti,

C., Aung, S., Bigio, V., Cao, N., Chandler, M., Chornay, D., Christian, K., Clark, G., Collinson, G., Corris, T., DeÂ LosÂ Santos, A., Devlin, R., Diaz, T., Dickerson, T., Dickson, C., Diekmann, A., Diggs, F., Duncan, C., Figueroa-Vinas, A., Firman, C., Freeman, M., Galassi, N., Garcia, K., Goodhart, G., Guererro, D., Hageman, J., Hanley, J., Hemminger, E., Holland, M., Hutchins, M., James, T., Jones, W., Kreisler, S., Kujawski, J., Lavu, V., Lobell, J., LeCompte, E., Lukemire, A., MacDonald, E., Mariano, A., Mukai, T., Narayanan, K., Nguyan, Q., Onizuka, M., Paterson, W., Persyn, S., Piepgrass, B., Cheney, F., Rager, A., Raghuram, T., Ramil, A., Reichenthal, L., Rodriguez, H., Rouzaud, J., Rucker, A., Saito, Y., Samara, M., Sauvaud, J.-A., Schuster, D., Shappirio, M., Shelton, K., Sher, D., Smith, D., Smith, K., Smith, S., Steinfeld, D., Szymkiewicz, R., Tanimoto, K., Taylor, J., Tucker, C., Tull, K., Uhl, A., Vloet, J., Walpole, P., Weidner, S., White, D., Winkert, G., Yeh, P.-S., Zeuch, M.: Fast Plasma Investigation for Magnetospheric Multiscale, *Space Science Reviews* (2016), Vol. 199, pp. 331-406, https://doi.org/10.1007/s11214-016-0245-4

Robert, P., Cornilleau-Wehrlin, N., Piberne, R., de Conchy, Y., Lacombe, C., Bouzid, V., Grison, B., Alison, D., Canu, P.: CLUSTER-STAFF Search Coil Magnetometer Calibration - Comparisons with FGM, *Geosci. Instrum. Method. Data Syst.* (2014), Vol. 3 Iss. 2, pp. 153-177, http://dx.doi.org/10.5194/gi-3-153-2014

Roux, A., Robert, P., Le Contel, O., Angelopoulos, V., Auster, U., Bonnell, J., Cully, C.M., Ergun, R.E., McFadden, J.P.: A mechanism for heating electrons in the magnetopause current layer and adjacent regions, *Ann. Geophys.* (2011), Vol. 29 Iss. 12, pp. 2305-2316, https://doi.org/10.5194/angeo-29-2305-2011

Russell, C.T., Zhang, T.L., Delva, M., Magnes, W., Strangeway, R.J., Wei, H.Y.: Lightning on Venus inferred from whistler-mode waves in the ionosphere, *Nature* (2007), Vol. 450, p. 661, http://dx.doi.org/10.1038/nature05930

Russell, C.T., Anderson, B.J., Baumjohann, W., Bromund, K.R., Dearborn, D., Fischer, D., Le, G., Leinweber, H.K., Leneman, D., Magnes, W., Means, J.D., Moldwin, M.B., Nakamura, R., Pierce, D., Plaschke, F., Rowe, K.M., Slavin, J.A., Strangeway, R.J., Torbert, R., Hagen, C., Jernej, I., Valavanoglou, A., Richter, I.: The Magnetospheric Multiscale Magnetometers, *Space Science Reviews* (2016), Vol. 199, pp. 189-256, https://doi.org/10.1007/s11214-014-0057-3

Schafer, R.W., Rabiner, L.R.: A digital signal processing approach to interpolation, *Proceedings of the IEEE* (1973), Vol. 61 Iss. 6, pp. 692-702, https://doi.org/10.1109/PROC.1973.9150

Schreier, R., Pavan, S., Temes, G.C.: Understanding Delta-Sigma Data Converters*, John Wiley & Sons, Inc.*, 2017, ISBN 9781119258308, http://dx.doi.org/10.1002/9781119258308

Simon, Dan: Optimal State Estimation, *John Wiley & Sons*, Inc., 2006, ISBN 9780471708582, http://dx.doi.org/10.1002/0470045345

Smith, J.O.: Spectral Audio Signal Processing, *W3K Publishing*, 2011, ISBN 978-0-9745607-3-1, online book version accessed 2018/03/08, http://ccrma.stanford.edu/~jos/sasp/

Smith, J.O.: Physical Audio Signal Processing, online book, 2018, accessed 2018/03/08, https://ccrma.stanford.edu/~jos/pasp/

Stoica, P., Moses, R.: Spectral Analysis of Signals, Prentice Hall, New Jersey, 2005, ISBN 0-13-113956-8, out of print, copy retrieved from author's page 2018/03/08, http://user.it.uu.se/~ps/SAS-new.pdf

Tietze, U., Schenk, C.: Halbleiter-Schaltungstechnik, *Springer, Berlin, Heidelberg, New York*, 2002, ISBN 3-540-42849-6, https://doi.org/10.1007/978-3-662-07639-2

Tooley, C.R., Black, R.K., Robertson, B.P., Stone, J.M., Pope, S.E., Davis, G.T.: The Magnetospheric Multiscale Constellation, *Space Science Reviews* (2016), Vol. 199, pp. 23-76, https://doi.org/10.1007/s11214-015-0220-5

Torbert, R.B.: Observing the Electron Diffusion Region with MMS, Yosemite 2010 Interdisciplinary Workshop on Magnetic Reconnection (2010), http://yosemite2010.swri.edu/talks/Torbert.pdf

Torbert, R.B., Vaith, H., Granoff, M., Widholm, M., Gaidos, J.A., Briggs, B.H., Dors, I.G., Chutter, M.W., Macri, J., Argall, M., Bodet, D., Needell, J., Steller, M.B., Baumjohann, W., Nakamura, R., Plaschke, F., Ottacher, H., Hasiba, J., Hofmann, K., Kletzing, C.A., Bounds, S.R., Dvorsky, R.T., Sigsbee, K., Kooi, V.: The Electron Drift Instrument for MMS, *Space Science Reviews* (2016), Vol. 199, pp. 283-305, https://doi.org/10.1007/s11214-015-0182-7

Torbert, R.B., Russell, C.T., Magnes, W., Ergun, R.E., Lindqvist, P.-A., LeContel, O., Vaith, H., Macri, J., Myers, S., Rau, D., Needell, J., King, B., Granoff, M., Chutter, M., Dors, I., Olsson, G., Khotyaintsev, Y.V., Eriksson, A., Kletzing, C.A., Bounds, S., Anderson, B., Baumjohann, W., Steller, M., Bromund, K., Le, Guan, Nakamura, R., Strangeway, R.J., Leinweber, H.K., Tucker, S., Westfall, J., Fischer, D., Plaschke, F., Porter, J., Lappalainen, K.: The FIELDS Instrument Suite on MMS: Scientific Objectives, Measurements, and Data Products, *Space Science Reviews* (2016), Vol. 199, pp. 105-135, https://doi.org/10.1007/s11214-014-0109-8

Torkar, K., Nakamura, R., Tajmar, M., Scharlemann, C., Jeszenszky, H., Laky, G., Fremuth, G., Escoubet, C.P., Svenes, K.: Active Spacecraft Potential Control Investigation, *Space Science Reviews* (2016), Vol. 199, pp. 515-544, https://doi.org/10.1007/s11214-014-0049-3

Vörös, Z.: Magnetic reconnection associated fluctuations in the deep magnetotail: ARTEMIS results, *Nonlin. Processes Geophys.* (2011), Vol. 18 Iss. 6, pp. 861-869, https://doi.org/10.5194/npg-18-861-2011

Waring, E.: Problems concerning Interpolations, *The Royal Society* (1779), Vol. 69, pp. 59-67, http://www.jstor.org/stable/106408

Welch, G.F.: HISTORY: The Use of the Kalman Filter for Human Motion Tracking in Virtual Reality, *Presence* (2009), Vol. 18, pp. 72-91, https://doi.org/10.1162/pres.18.1.72

Young, D.T., Burch, J.L., Gomez, R.G., De Los Santos, A., Miller, G.P., Wilson, P., Paschalidis, N., Fuselier, S.A., Pickens, K., Hertzberg, E., Pollock, C.J., Scherrer, J., Wood, P.B., Donald, E.T., Aaron, D., Furman, J., George, D., Gurnee, R.S., Hourani, R.S., Jacques, A., Johnson, T., Orr, T., Pan, K.S., Persyn, S., Pope, S., Roberts, J., Stokes, M.R., Trattner, K.J., Webster, J.M.: Hot Plasma Composition Analyzer for the Magnetospheric Multiscale Mission, *Space Science Reviews* (2016), Vol. 199, pp. 407-470, https://doi.org/10.1007/s11214-014-0119-6